

DISSERTATION

A NEW MEASUREMENT OF THE
 $2S_{1/2}$ - $8D_{5/2}$ TRANSITION IN ATOMIC HYDROGEN

Submitted by

Adam D. Brandt

Department of Physics

In partial fulfillment of the requirements

For the Degree of Doctor of Philosophy

Colorado State University

Fort Collins, Colorado

Summer 2021

Doctoral Committee:

Advisor: Dylan C. Yost

Jacob L. Roberts

Stuart B. Field

Azer P. Yalin

Copyright by Adam D. Brandt 2021

All Rights Reserved

ABSTRACT

A NEW MEASUREMENT OF THE $2S_{1/2}$ - $8D_{5/2}$ TRANSITION IN ATOMIC HYDROGEN

High-precision spectroscopy of simple atoms provides input data that can be used to extract fundamental constants and to test Standard Model theory. Hydrogen, the simplest element, has played a historically significant role in the development of fundamental theory and, more recently, provides important data for the proton radius puzzle. In this thesis, we will describe a new measurement of the $2S_{1/2}$ - $8D_{5/2}$ transition on a cryogenic hydrogen beam. We will overview the measurement scheme and experimental apparatus, then present analysis and systematic characterization important to the spectroscopy. Finally, we will present our preliminary determination of the proton radius and the Rydberg constant using our value for the $2S_{1/2}$ - $8D_{5/2}$ combined with the previously measured 1S-2S transition.

ACKNOWLEDGEMENTS

Before I entered graduate school, I don't think I fully appreciate how much work completing a Ph. D. would entail, which is almost certainly a common experience amongst those in the scientific community. Speaking of community, without the group people around me during my Ph.D. I would have never been able to half of what I did, and for that I owe a world of thanks.

First, for giving me a home to grow up in and all the love and support a man can ever need, I would like to thank my parents. My mother's near limitless work ethic and selflessness is amongst the most admirable traits I have ever seen anywhere, and I hope she has passed down at least half of her work ethic to me. To my father I owe my outlook and the ability to find humor in life, which has been critical for keeping my sanity. Undoubtedly, the hard work of being a parent is at the very least comparable to the trials of making an experiment work, and to you two, I owe everything. Of course, I would be amiss to not mention my wonderful older sister Becky, who has in many ways inherited the wonderful work ethic of our mother. You always set the example by which I saw myself when I was young, and drove me to work harder.

Without the guidance of Dylan, none of the work detailed in this thesis would have been possible. I entered into an empty lab (with a mostly empty brain), and had the opportunity to build it up alongside you for which I am very grateful. Your physical intuition and scientific approach have had and will continue to have a profound effect on how I approach physics. I have always appreciated your sense of humor and your ability to quickly get to the meat of a topic. I wish you continued success and happiness in your scientific and personal endeavors.

Two graduate students joined this empty lab alongside me, Samuel Cooper (Scoop) and Zak Burkley. Cory Rasor joined us in short order, and together the four of us have built the infrastructure of the laboratory. The three of you have been excellent colleagues, and I am happy to have had many, (*many*) hours of working alongside you all. Scoop, you and I have been roommates, office mates, and lab mates for 7 years now— thank you for putting up with me.

To Jacob Roberts, I would like to thank you for being an excellent scientist and a similarly excellent human being. The class I have had the opportunity to take a class from you (many moons ago now) was probably the most engaging class I have taken. Similarly, we have had many joint-group meetings together, and you are a well of excellent advice, keen insight, and sound ethical principles; thank you.

There are many other individuals to thank. Robert Mayanovic (who will almost always be DrM to me regardless of my own title) was a key figure in my early research career. He made sure I had the opportunities to succeed when I was just a wee undergraduate. Thank you to Bob Adame for teaching me how to not get terribly mangled in the machine shop and for being a real master of the art. To the my committee I thank you for your time and your input. I am grateful for all the faculty members I have taken the classes from: Jake Roberts, Mark Bradley, Kristen and Norm Buchannan, David Krueger, Marty Gelfand, and Siu Au Lee. Thank you to the front office workers, Kristin, Amber, Alicia, Wendy, Sharon, Vanay, and Veronica who always made sure I was on track with the graduate school.

I am so happy to have met my wonderful group of friends I have made here in Fort Collins: Weston and Annalise Maughan (The Dr.'s Maughans), Pascal Jundt, Chase Calvi and Jaz Donkoh, Samuel Cooper, Emmett Randel, August Demann, Matt Harrison, Hannah Berry, and Cory Rasor. Without you subjecting you all to my horrendous puns, jokes-in-poor-taste, and general buffoonery, I don't know if I would have made it.

Finally, I would like to thank Julie Barnum. You have been there for me, and always told me I can do the thing even when I wasn't sure. Your unconditional support has been a wonderful blessing in my life— you make sure to ask me about how my research is going even though I know you don't want to hear me blather about laser woes. Thank you for pushing me to try new things and expand my palette.

-Adam

P.S. Thanks to my cat, Kami, for being a cat and very cute. You really did it.

TABLE OF CONTENTS

ABSTRACT	ii
ACKNOWLEDGEMENTS	iii
LIST OF FIGURES	vii
Chapter 1	Motivation 1
1.1	Outline of Thesis 5
Chapter 2	Overview of the $2S_{1/2}$ - $8D_{5/2}$ Measurement 7
2.1	The 243 nm Laser System 10
2.1.1	High-powered 972 nm source 10
2.1.2	Frequency doubling stages 12
2.1.3	243 nm power enhancement 16
2.1.4	Frequency stabilization and control 19
2.2	The Spectroscopy Laser System 21
2.3	Overlap Geometries 25
2.4	The Atomic Beam and Spectroscopy Chamber 26
2.4.1	Cryogenic Hydrogen Beam Generation 26
2.4.2	Time-of-flight detection 28
2.4.3	Vacuum Chamber and the Spectroscopy Region 31
2.4.4	The Metastable Detector 33
2.5	Conclusion 36
Chapter 3	The Frequency Comb and Stable-Laser System 38
3.1	Introduction 38
3.2	Mode-locked laser oscillators 43
3.3	Frequency comb oscillator I 47
3.4	Frequency comb oscillator II 50
3.4.1	Amplification, Supercontinuum generation, and f_0 detection 54
3.4.2	Phase-locking and RIN Servo 58
3.4.3	Comb Spectra for comparison to Ti:Sapphire spectroscopy laser 65
3.5	Operation of the frequency comb 67
3.5.1	Day-to-day operation 67
3.5.2	Mode-locking the oscillator 70
3.5.3	Aligning the oscillator 73
3.6	The Ultra-Stable Cavity and Laser 75
3.6.1	Introduction 75
3.6.2	Optical Cavity Basics, Revisited 76
3.6.3	Pound-Drever-Hall Locking 79
3.6.4	Design of the Ultra-stable Cavity 83
3.6.5	The Stable Laser 87
3.6.6	USC Performance 88
3.7	Conclusion 91
Chapter 4	Fitting Lineshapes and Extrapolations 93
4.1	The two-level atom 93

4.2	Derivation of Line Fit Function	96
4.2.1	Two-photon processes	96
4.2.2	Density matrix introduction	98
4.2.3	Fitting Function for two-level atom	100
4.2.4	Fitting Function	102
4.3	Functional behavior of the ac-Extrapolations	103
4.3.1	The ac-Stark shift	103
4.3.2	Effect of spatial distribution in ac-extrapolation	105
4.4	Conclusion	106
Chapter 5	The Numeric Model	107
5.1	Introduction	107
5.2	The 2S-8D Transition	108
5.2.1	Inclusion of systematic effects in model	110
5.2.2	DC-Electric Fields	115
5.2.3	Density matrix model	121
5.3	Applications of the Numeric Model	122
5.3.1	Fitting modeled ac-extrapolations	123
5.3.2	ac-extrapolations in the presence of a dc-field	126
5.4	Conclusion	128
Chapter 6	$2S_{1/2}$ - $8D_{5/2}$ Spectroscopy	129
6.1	ac-Stark Shift Extrapolations	130
6.2	dc-Stark Shift Mitigation and Characterization	137
6.3	Correcting extrapolated frequencies for the dc-Stark effect	140
6.4	Minor Systematics	143
6.4.1	Residual Magnetic Fields	143
6.4.2	Pressure Systematics	147
6.4.3	Frequency Calibration	154
6.4.4	Second-Order Doppler Shift	164
6.4.5	Blackbody Radiation	165
6.4.6	Hyperfine Structure	166
6.4.7	Cross-Damping	166
6.4.8	Incoherent Line Pulling	170
6.4.9	Residual First Order Doppler shifts	171
6.4.10	4 th Order ac-Stark Shift	172
6.4.11	Recoil Shifts	172
6.4.12	Light Force Shift	173
6.4.13	Photodiode Offsets	174
6.4.14	Parasitic Etalons	174
6.5	Preliminary $2S_{1/2}$ - $8D_{5/2}$ Results	174
6.6	Conclusion	178
Summary and Outlook	179
Bibliography	183

LIST OF FIGURES

1.1	Determining r_p and R_∞ requires measuring two transitions. Here are a selection of pertinent determinations of the proton radius when combined with the 1S-2S result [1]. The blue and pink bands represent the 1σ error bars of r_p in the CODATA2014 and updated muonic hydrogen value respectively.	4
2.1	Principle of measurement. The measurement is essentially a two-laser experiment, needing 243 nm radiation to drive the 1S-2S transition and 778 nm radiation to drive the 2S-8D transition. Atoms in the 8D state preferentially decay into the ground state via P states, about 5% decay into the 2S manifold. Since driving the 2S-8D transition drives atoms out of the 2S state, the total flux of 2S hydrogen decreases when performing spectroscopy.	7
2.2	A schematic depiction of our measurement subsystems. USC: Ultra-stable cavity. OSA: Optical spectrum analyzer. ECDL: Extended-cavity diode laser. TA: Tapered amplifier. Diff. Pump: Differential pumping manifolds.	8
2.3	Power build up in a simple cavity. Mirrors have reflectivities R_1 and R_2 respectively, and it is assumed there are no losses aside from transmission.	14
2.4	Differential pumping manifold, units in inches	17
2.5	Inside of the mirror cubes. a) Input coupler mirror cube. b) High reflector mirror cube with PZT's and feedthrough	18
2.6	This figure is reproduced from [2]. Frequency stabilization system a) 972 nm ECDL and PDH lock to external Fabry-Perot cavity. The ECDL is first stabilized to the Fabry-Perot (FP) cavity via a PDH lock. Sidebands on the 972 nm light are generated by phase modulation with an intracavity EOM and the lock is maintained by actuating the ECDL cavity length. Once the ECDL is stabilized to the FP, the FP cavity length is actuated to stabilize the 972 nm-comb beat note. b) Beat note between frequency comb and ECDL.	20
2.7	Coherent-799 Ti:Sapphire Oscillator vertical ring oscillator. PZT Mirror: PZT mounted mirror, Wavelength Tuning: Thin/thick etalon pair and birefringent filter, OC: Output coupler, Iso.: Optical Isolator, OSA: Fiber to optical spectrum analyzer, Beat Note: PM fiber to beat note with frequency comb	22
2.8	Example Ti:Sapphire-Comb locked beat note. Resolution bandwidth 10 kHz	23
2.9	Optical setup preceding 778 nm power enhancement cavity. EOM: Electro-optic modulator, $\lambda/2$: Half-wave plate, PBS: Polarizing beamsplitter, PD: Reflection photodetector	24
2.10	Top-down view of the beam overlaps	25
2.11	Microwave cavity and hydrogen disassociation	27
2.12	This figure is reproduced from [3], with permission of AIP Publishing. a) Dimensions of chopper wheel b) Kernel function for chopper wheel.	29
2.13	This figure is reproduced from [3], with permission of AIP Publishing. a) Ground state time-of-flight data and fit. b) Metastable time-of-flight data and fit	30

2.14	Top-down view of the spectroscopy chamber geometry. 8" CF cubes house the mirrors for the 778 cavity (not shown). The atomic beam traverses through the long axis of the vacuum chamber, shown as a beam through the center. The relative orientation of the 778 nm and 243 nm light beams through the chamber are also shown.	32
2.15	Faraday cage geometry and magnetic shields within. The Faraday cage is 16" x 3" x 4", and the magnetic shields are 8" and 3.5" long respectively. The magnetic shields are centered on the 778 nm-atomic beam overlap.	33
2.16	Image of Faraday Cage inside of vacuum chamber with no optics a) back plate off, showing magnetic shields b) back plate on, with metastable detector attached	34
2.17	Biasing of CEM. Also shown, photoelectron rejection grid and ground as dashed lines. The resistors R, R', and R'' have resistances of 20 kOhm, 2 MOhm, and 18 MOhm respectively.	35
2.18	Housing of the metastable detector.	36
3.1	Simple picture demonstrating phase evolution of carrier frequency between pulses . . .	39
3.2	Linear cavity mode-locked oscillator	47
3.3	Linear oscillator spectral output. Spectral output ~ 15 nm	48
3.4	Example of figure-8 style oscillator. WDM: Wavelength-division multiplexer. OC: Output coupler. Iso.: Optical isolator. BS: Beamsplitter	51
3.5	Example of second oscillator design spectral output. Typical width at half-maximum ~ 40 nm	52
3.6	Frequency comb oscillator design two, based off of "figure-9" architecture. PBS: polarizing beamsplitter. WDM: Wavelength division multiplexer. FR: Faraday rotator. SAM: Saturable absorbing mirror. PZT: Piezoelectric transducer. BS: Beamsplitter. . .	53
3.7	Comb Amplification and Supercontinuum generation. Iso: Isolator. LD: Pump laser diode. 50/50: Beamsplitter. PC: Fiber polarization controller. HNLF: Highly nonlinear fiber.	56
3.8	f -to- $2f$ Inteferometer	58
3.9	a) Schematic of RIN servo b) In-loop Relative Intensity noise power spectral density .	62
3.10	[Reprinted] with permission from [4] © The Optical Society. a) Composite lock schematic. b) Amplitude response transfer functions c) Phase response transfer functions	63
3.11	[Reprinted] with permission from [4] © The Optical Society. Linear oscillator beatnotes with composite lock on vs only frequency lock. a) f_0 beatnote with the composite lock on (black) vs off (blue). b) f_b beatnote with the composite lock on (black) vs off (blue). Note that the composite lock reduces noise across the comb spectrum, indicated by the reduction in phase noise on f_0 and f_b which are in disparate parts of the comb spetrum.	64
3.12	Linear vs figure-9 cavity f_0 locks. The reduction in fast frequency noise is expected due to quantum timing jitter's relation to the intracavity pulse duration.	65
3.13	750-780 nm Doubling Stage. The PPLN is on translation stage and heated mount for adjustment of the doubled spectra. Some adjustment of the HWP is necessary when switching between 778 nm and 750 nm comparison	66

3.14	a) Primary frequency comb electronics, including oscillator and main amplifying laser diode drivers and RIN servo. b) Comb temperature controls and electronics for Ti:Sapphire comparison. LDD: Laser diode driver. HV Driver: High-voltage driver for the intracavity PZT's. The laser diode temperature controllers are not labeled, and do not require adjustment for operation. Adjustment of the comb plate temperature is required most days.	68
3.15	a) f -to- $2f$ interferometer setup. b) Doubling stage for comparison to the spectroscopy laser.	69
3.16	Top down view of the frequency comb oscillator. Coarse adjustment knob underneath aluminum plate. Refer to Fig. 3.6 for a schematic depiction of the cavity	71
3.17	Simple cavity with common cavity parameters indicated. L : Cavity length. z_R : Rayleigh range, distance from focus of Gaussian beam in which the w parameter increases by $\sqrt{2}$. w_0 : Beam waist, width of Gaussian beam at focus.	78
3.18	Cavity reflection as a function of frequency (in terms of cavity FSR).	79
3.19	Phase Modulated Sidebands ($f = \pm\Omega$) on a carrier frequency ($f = 0$).	81
3.20	Example of typical PDH-lock. a) A usable PDH experimental setup. PD: Photodiode. LP: low-pass filter. PS: Phase shifter. b) An example error signal generated for PDH locking, note that the cavity linewidth is $\approx \frac{1}{20}$ the dither frequency in this example.	82
3.21	Ultra-stable cavity spacer geometry. Optical cavity is 10 cm long.	84
3.22	Zerodur spacer mount. Key holes are for keep the viton balls in place and also allow for possible trapped gas volumes to vent. a) Top view. b) Bottom view.	85
3.23	Heat shields and cavity mounting assembly in different views. a) Overhead side view. b) Side view along optical axis. c) Top-down view. The lids to the heat shields are omitted from this picture for clarity.	86
3.24	Ultra-stable cavity and comb interfacing. The in-fiber EOM puts 10 MHz sidebands on the 1554 nm laser for PDH lockig to the ultra-stable cavity. 90% of the stable laser output is used for beat note detection with the optical frequency comb. Note that unrelated comb fiber optics are omitted for clarity.	89
3.25	Ultra-Stable Cavity Allan Deviation	90
4.1	Some Example of two-level dynamics. The population in state 2 is plotted vs time. Black shows behavior on resonance and red is off resonant a) No Decay b) With decay ($\Omega \sim 10\gamma$)	96
4.2	Qualitative density matrix time evolution examples, $\Omega > \gamma$ a) Larger γ (black) vs smaller γ (red) b) No detuning (black) vs detuning (red) c) Closed two-level system (black) vs 50% branching ratio (red)	99
4.3	The level structure of the $2S_{1/2}$ and $8D_{5/2}$ states. The lifetime of the 8D state determines the linewidth of each hyperfine manifold ($F = 2, 3$) which is 572 kHz, leaving the 8D hyperfine structure unresolved.	102
5.1	Beam Geometry a) Top-down view of the beam overlaps b) Side view of the beam overlaps.	112
5.2	Splitting of the $n = 8$ manifold (considering fine-structure) assuming z -oriented electric field.	116

5.3	Structure of the $n = 8$ manifold. Note that the 8D lines have a linewidth of 572 kHz and the 8F states have a linewidth of 285 kHz.	118
5.4	$2S_{1/2}$ - $8D_{5/2}$ modeled lineshape in electric fields, single velocity class and metastable spatial class. Lorentzian overlaid only for visual reference. a) 3 mV/cm field. b) 6mV/cm field. c) 9mV/cm field. d) 12mV/cm field.	120
5.5	The magnitude of the dc-Stark shift on the $2S_{1/2}$ - $8D_{5/2}$ transition. Shift is given by difference between expected resonance frequency (zero dc-field) and the resonance frequency when fit with Eq. (4.39), assuming a perpendicular field.	121
5.6	Fitting modeled data in the low intensity limit. a) Sample modeled line fit with Eq. (4.39) for 5 W, 600 μm 778 nm beam diameter, 550 μm spatial distribution. b) Expected shot noise (black) vs fit residuals (red). Shot noise estimated for 10^4 counts/gate, our typical count rate.	124
5.7	Model data with spatial distribution and velocity distribution a) 550 μm metastable spatial spread lineshapes fit with Eq. (4.39). b) Modeled ac-extrapolations for three spatial distributions fit with cubic function. Black: 450 μm spread. Red: 550 μm spread. Blue: 750 μm spread. c) Extrapolated ν_c as a function of minimum dip % used in ac-extrapolation. Black: 450 μm spread. Red: 550 μm spread. Blue: 750 μm spread.	125
5.8	Cross talk check between ac and dc Stark effect. a) Two modeled ac-extrapolations of 550 μm and 750 μm metastable spatial distribution sizes under the influence of a 4 mV/cm electric field. b) The two extrapolations zero-field resonances as a function of minimum metastable extinction fraction (dip %) used in the ac-extrapolation.	126
6.1	3D fits for outlier detection and the corresponding 3D fit residuals below. a) Before removal of outliers and b) After removal of outliers	133
6.2	Sample individual line scans shown at two different probe powers, x -axis is laser frequency and relative a) Low probe power, $\approx 17\%$ dip b) High probe power, $\approx 50\%$ dip	134
6.3	Example of extrapolation data, July 9, 2020. a) Frequency extrapolation data. Note that the plot is in terms of laser frequency, and zero is relative the previous measurement of the $2S$ - $8D$ resonance frequency [5]. While difficult to perceive by eye, the data is fit with a cubic function $\nu(V) = a + bV + cV^3$. b) Metastable quenching parameter (α in Eq. 4.39) as a function of photodiode voltage. Fit with a polynomial of the form $\alpha(V) = aV^2 + bV^3 + cV^4$	135
6.4	Side by side comparison of extrapolated ν_c from the cubic fit and using the numeric model directly. Black: Cubic extrapolation. Red: Numeric model extrapolation. Values displayed are dc-Stark shift corrected	136
6.5	$2S_{1/2}$ - $12D_{5/2}$ modeled lineshape in perpendicular electric fields. a) 3 mV/cm field b) 6mV/cm field	138
6.6	a) An example $12D_{5/2}$ line fit model, electric field magnitude 3 mV/cm with 50 kHz of Lorentzian broadening. b) $2S$ - $8D$ line example fit with our standard fit function (red) and the electric fields model (black). The distortion of the line quantifies the magnitude of the electric field.	139
6.7	<i>In situ</i> measurement of electric fields for each measurement day with batch means and statistical variances overlaid. Blue - July, Red - September, Green - November. Electric field is assumed to be perpendicular to the light field.	140

6.8	Stark corrected extrapolated resonance frequencies. Mean statistical uncertainty overlaid, 1.2 kHz.	141
6.9	Level structure of the 2S-8D transition a) No external magnetic field b) small external field applied. Red lines correspond to σ^+ transitions and black lines are π transitions	145
6.10	General collision between species 1 (perturbed) and species 2 (perturber)	148
6.11	Collisional cross sections for broadening (black) and shifts (red)	153
6.12	The frequency metrology subsystem. USC: ultra-stable cavity, DDS: direct-digital synthesizer, 972 ECDL: 972 nm external-cavity diode laser, GPS: Global positioning system timebase corrections	155
6.13	Example of f_r data collected in a day with an offset subtracted. The individual f_r measurements are displayed in black and the low-passed data is in red (low-pass corner of ≈ 1 mHz)	156
6.14	Ti:Sapphire-Frequency Comb beat note, 3 kHz resolution bandwidth	160
6.15	a) 972 nm ECDL-Frequency comb beatnote 1 kHz resolution bandwidth b) Comparison of convolved line (red) with 1S-2S measured lineshape (black)	161
6.16	Frequency counting of NIST WWVB 5 MHz signal. a) Counted by the FS740 frequency counter. b) Counted by the HP 53131A	161
6.17	Calculated Allan deviation of the FS740 from data presented in Fig. 6.16 a).	162
6.18	An example of the Allan deviation of f_r during spectroscopy compared to Allan deviation of the FS740. The Allan deviations are in reasonable agreement until averaging times of about 1000 s, after which the drift of the USC becomes apparent.	163
6.19	A selection of result determination of the proton radius when combined with the 1S-2S transition [1], with our determination circled.	177

Chapter 1

Motivation

Atomic spectroscopy of gases, particularly atomic hydrogen, has played a crucial role in the development of early atomic theory, and later, the development of Quantum Electrodynamics [6]. Just before the beginning of the 20th century, the Rydberg formula accurately described the emission spectra of the hydrogen atom – this formula was given theoretical justification in 1913 by Niels Bohr, the first quantum theory of the atom [7]. Bohr's model of the atom, requiring discrete energy levels, was interpreted as electron standing waves around the nucleus in 1923 by Louis de Broglie [8]. The development of matrix mechanics by Heisenberg (and others) and wave mechanics by Schrödinger marked the beginning of quantum theory as it is more generally known today [9].

As spectroscopy became more sensitive, previously unresolved features in the hydrogen spectrum came into view, pushing atomic theory forward. For instance, the fine structure of hydrogen, where certain emission lines are actually closely spaced doublets, was not explained by Bohr's theory or wave mechanics without including relativity. However, Dirac's development of quantum theory did properly account for the fine structure of the hydrogen atom. A similar story may be told of hyperfine structure, which led Wolfgang Pauli to propose the existence of nuclear spin. Again this story of refinements in spectroscopic precision of hydrogen leading to refinements in fundamental theory continued in the 1940's. The Lamb shift [10] (the splitting of the $2S_{1/2}$ and $2P_{1/2}$ states) and the unexpectedly large magnetic moment of the electron were not explainable by Dirac's theory. Quantum electrodynamics (QED) was developed to properly describe these discrepancies, and the formalism of QED later became the backbone of the Standard Model developed in the 1960's – the current model describing three of the four fundamental forces of the universe. Although the Standard Model has been very successful, it currently only explains 5% of all known constituents of the known universe. Because of this, the search for physics beyond the standard model continues.

The study of the hydrogen atom is particularly attractive due to its simple nature. Its simplicity makes it one of the best systems, along with simple exotic atoms or ions [11–17], to compare directly to fundamental theory through precision spectroscopy [18–21]. The energy levels of the hydrogen atom can be written

$$E_{nlj} = hcR_\infty \left(-\frac{1}{n^2} + f_{nlj}(\alpha, \frac{m_e}{m_p}, \dots) + \delta_{l0} \frac{C_{NS}}{n^3} r_p^2 \right), \quad (1.1)$$

where R_∞ is the Rydberg constant, and f_{nlj} are relativistic and QED corrections [22, 23]. The last term, $\delta_{l0} \frac{C_{NS}}{n^3} r_p^2$, is the perturbation of S states (zero angular momentum states) due to the finite size of the proton. This effect is much stronger for the S states than for states with angular quantum number $l \neq 0$ because S state wavefunctions are nonvanishing at the origin. In Eq. (1.1), both r_p and R_∞ are free parameters and therefore pairs of transitions must be measured to determine them. Increasingly precise spectroscopic measurements in hydrogen have led to determinations of the Lamb shift, R_∞ , and the proton radius [1, 23–31]. The Rydberg constant is now one of the most well-known fundamental constants, known to 6 parts in 10^{12} , and is used as a metric in the global adjustment of constants [22, 32]. Theoretical calculations of hydrogen’s energy eigenstates can be made to extreme accuracy [18, 19, 33, 34]. This makes hydrogen and hydrogen-like systems ideal candidates for testing bound state QED theory as well as potentially probing physics beyond the standard model, as deviations from theory are smoking guns for unexplained phenomena [20]. There are proposals suggesting probing for physics beyond the standard models by investigating such systems [20, 35–37]. For instance, there are proposed new forces which can couple the nucleus and electron in an atom. If the new force is mediated by a massive boson, then spectroscopic measurements probe a particular mass range of the new particle [35].

Of particular interest is the decade-long proton radius puzzle, which arises from the disparate determinations of the proton charge radius [22, 29, 31, 34, 38–42]. The proton radius, r_p , obtained by averaging of hydrogen spectroscopic measurements and electron-proton scattering measurements, has a value of 0.8751(61) fm, corresponding to a relative uncertainty of about 7×10^{-3} [22]. The proton radius has also been determined by measuring the Lamb shift in muonic hydrogen – a

hydrogen atom where the electron has been replaced by the ≈ 206 times heavier muon. The value of S wavefunction overlap at the origin scales as $1/a_0^3$, where

$$a_0 = \frac{4\pi\epsilon_0\hbar^2}{me^2} \quad (1.2)$$

is the Bohr radius. In muonic hydrogen, this Bohr radius is reduced by the ratio of the muon mass to the electron mass, so the wavefunction overlap is drastically increased. This makes muonic hydrogen *much* more sensitive to the finite size of the proton radius, and the resulting determination of the proton size from the muonic hydrogen Lamb shift measurement is 0.84087(39) fm – a fractional uncertainty of about 4.6×10^{-4} . The 4% difference between these two determinations of the proton size is about a 4σ discrepancy, and this 4σ discrepancy has been come to be known as the proton radius puzzle. Interestingly, recent results from Garching [29] and Toronto [31] are in relatively good or excellent agreement with the muonic proton radius, and a recent 1S-3S measurement in Paris [30] is in excellent agreement with the CODATA2014 value. The mystery deepens as another recent 1S-3S measurement from Garching is 2.1σ discrepant with the Paris determination, and nearly 2σ discrepant with the muonic proton radius [23]. It is worth noting, at the time of this writing, that the current CODATA suggested value of r_p is $r_p = 0.8414(19)$ fm. However, we are highlighting the historical development of the proton radius puzzle, in which the CODATA2014 value played a significant role.

Fig. 1.1 displays this proton radius puzzle and a selection of recent determinations of the proton radius in hydrogen. While there are several potential routes in this investigation, the historical determinations of the 2S-8S and 2S-8D lines strongly pull the value of the CODATA2014 proton radius due to their relatively small measurement uncertainty compared to the available measurements at the time, which are not all displayed in Fig. 1.1. This fact alone makes them compelling candidates for re-investigation and ultimately improved precision. Furthermore, these transitions are two-photon transitions (meaning the Doppler effect can be canceled to first-order), are at a experimentally convenient wavelengths (750 nm -780 nm), and have narrow natural linewidths. These measurements were completed just prior to the turn of the millennia, and several important

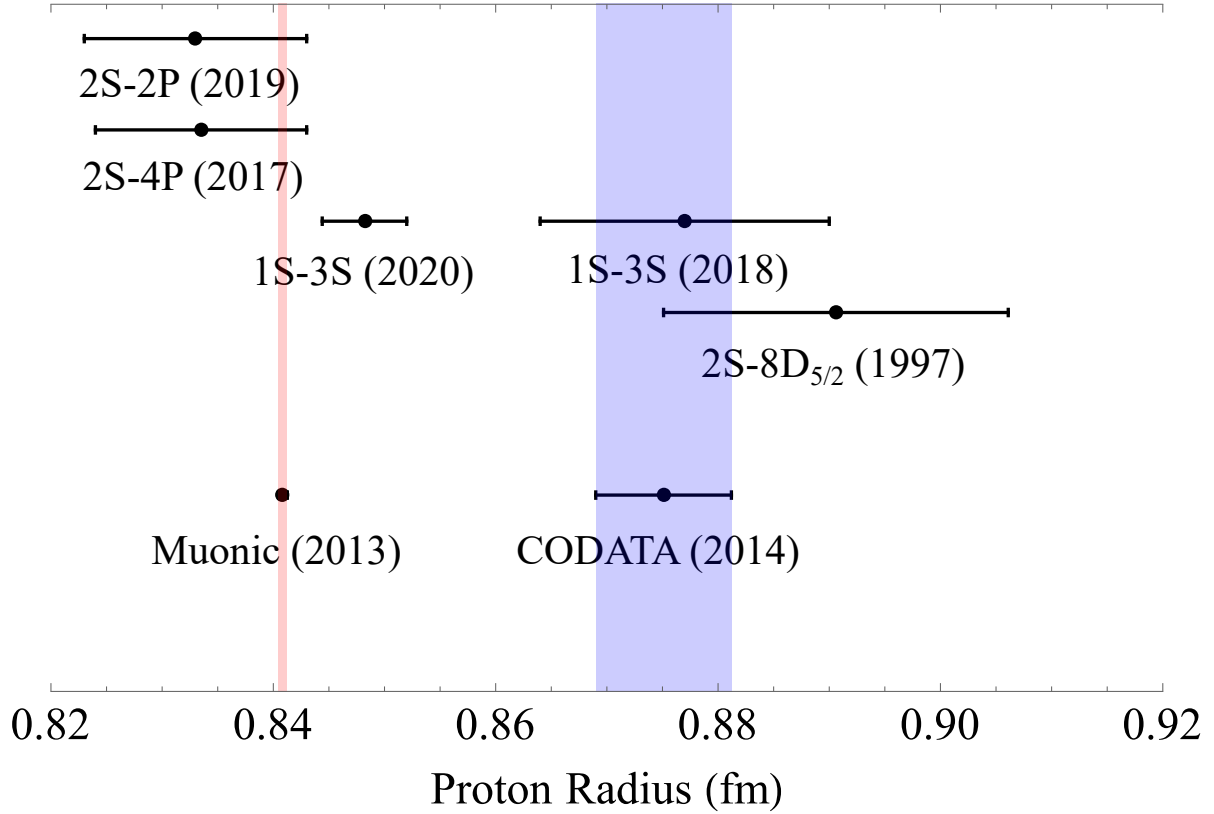


Figure 1.1: Determining r_p and R_∞ requires measuring two transitions. Here are a selection of pertinent determinations of the proton radius when combined with the 1S-2S result [1]. The blue and pink bands represent the 1σ error bars of r_p in the CODATA2014 and updated muonic hydrogen value respectively.

technical advances have occurred since – primarily the optical frequency comb and the improvement in UV-laser technology allowing for optical excitation to the 2S state. These technological advances have ultimately improved the possible precision.

A source of 2S hydrogen atoms is a necessary condition to drive the 2S-8D transition. Previously, metastable hydrogen (2S hydrogen) was generated primarily through collisions with electron beams, leading to relatively hot atom beams [25,43–45]. Advances in UV-laser technology, in part due to efforts in our lab at CSU, have led to the ability to generate significant power at 243 nm (the resonance frequency of the two-photon 1S-2S transition) allowing for more efficient optical excitation into the 2S state [2,46–48]. Optical excitation has several advantages over electron bombardment. Most obviously, optical excitation leaves the trajectory of the hydrogen atoms largely unaffected compared to bombardment, allowing for cryogenic beams of metastable hydro-

gen. This greatly reduces velocity related systematics, which can be rather involved to quantify in some experimental situations [49]. Additionally, it opens up the possibility for different experimental geometries, as the requisite optical power to drive the 2S-8D lines will be reduced as the metastable atoms are correspondingly slower.

Optical frequency combs, first generated just after the turn of the millennia, have revolutionized the world of optical frequency metrology [50–59]. Time, and therefore frequency, is defined through the 9.2 GHz hyperfine transition in the ground state of Cesium-133. In order to report absolute frequency measurements, one must reference to the Cesium standard in some way [60]. This is non-trivial for optical frequencies due to the huge difference in optical frequencies and the RF frequency of the absolute time standard. This issue was previously addressed by the use of highly complicated frequency chains and atomic references, which were cumbersome to operate [61–63]. The frequency comb removed the need of these complicated frequency chains, turning what used to take an entire lab to do into a couple of lasers and vastly simplified optical frequency metrology.

In this thesis, we will discuss our infrastructure to re-measure the $2S_{1/2}$ - $8D_{5/2}$ transition in hydrogen, with an emphasis on the construction of an optical frequency metrology system with a erbium-fiber, mode-locked oscillator at its core. We will also discuss $2S_{1/2}$ - $8D_{5/2}$ spectroscopy and systematic characterization. Finally, we discuss these preliminary spectroscopy results in the context of the proton radius puzzle, and will assign a value of the proton radius and Rydberg constant by combining our results with the most recent determination of the 1S-2S transition frequency [1].

1.1 Outline of Thesis

In Chapter 2 we give an overview of the experimental setup, describing each of the major subsystems (excepting the frequency metrology system) in detail. These different subsystems are the 243.1 nm radiation source, the Ti:Sapphire laser, the cryogenic atomic beam, and our detector. In Chapter 3, we describe the creation of an optical frequency comb, stable laser, and ultra-stable cavity. In Chapter 4, the functions used to fit the measured lines and associated ac-extrapolations are derived. In Chapter 5 the numeric model used to quantify systematics and verify our fitting

procedure is described. Chapter 6 presents the data acquisition method, data analysis, systematics characterization, and final results of the 2S-8D spectroscopy. We then summarize our results, and present some of the possibilities for future work.

Chapter 2

Overview of the $2S_{1/2}$ - $8D_{5/2}$ Measurement

Our measurement of the $2S_{1/2}$ - $8D_{5/2}$ transition occurs in a cryogenic beam and the spectroscopy is essentially a three step process once the cryogenic beam is generated. Once the beam of cold, ground state hydrogen is generated, we drive ground state atoms into the metastable $2S$ state. We then drive the $2S$ - $8D$ transition, moving population out of the $2S$ state and into the $8D$ state. Finally, the remaining metastable atoms are counted by a channel electron multiplier-based detector. This process is schematically depicted in Fig. 2.1, and is superficially similar to the method employed by the Paris group [25, 26, 43–45] in the previous determinations of the $2S$ - $8D$ transitions. In this scheme, we expect to see dips in the metastable counts as $2S$ - $8D$ transition is driven. Fig. 2.2 shows a general schematic overview of the different systems involved.

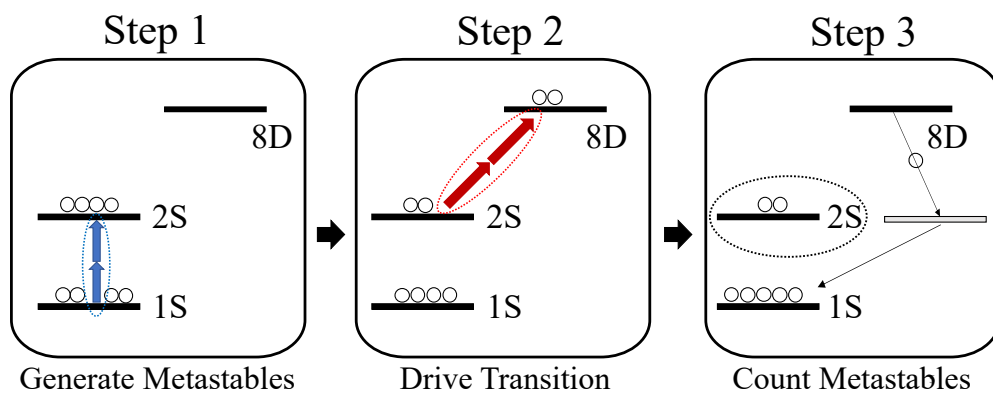


Figure 2.1: Principle of measurement. The measurement is essentially a two-laser experiment, needing 243 nm radiation to drive the $1S$ - $2S$ transition and 778 nm radiation to drive the $2S$ - $8D$ transition. Atoms in the $8D$ state preferentially decay into the ground state via P states, about 5% decay into the $2S$ manifold. Since driving the $2S$ - $8D$ transition drives atoms out of the $2S$ state, the total flux of $2S$ hydrogen decreases when performing spectroscopy.

Hydrogen is electrically neutral and is the lightest element. Magnetic trapping of hydrogen is possible, though the process has many technical challenges [64]. Furthermore, conventional laser cooling techniques, a possible route to reduce velocity-dependent systematics, are technically

difficult because the 1S-2P transition, the natural cooling transition of hydrogen, requires Lyman- α radiation, which is notoriously difficult to produce. While there is a demonstration of laser cooling atomic hydrogen with Lyman- α radiation [65], this technique is not easy to implement, requiring magnetically trapping a spin polarized gas that was first cooled with dilution refrigeration. A very recent demonstration of laser cooling anti-hydrogen via the 1S-2P transition has been published as well [17]. There is also a proposal to drive the 1S-2S transition as the cooling scheme [66], though it is also rather technically involved.

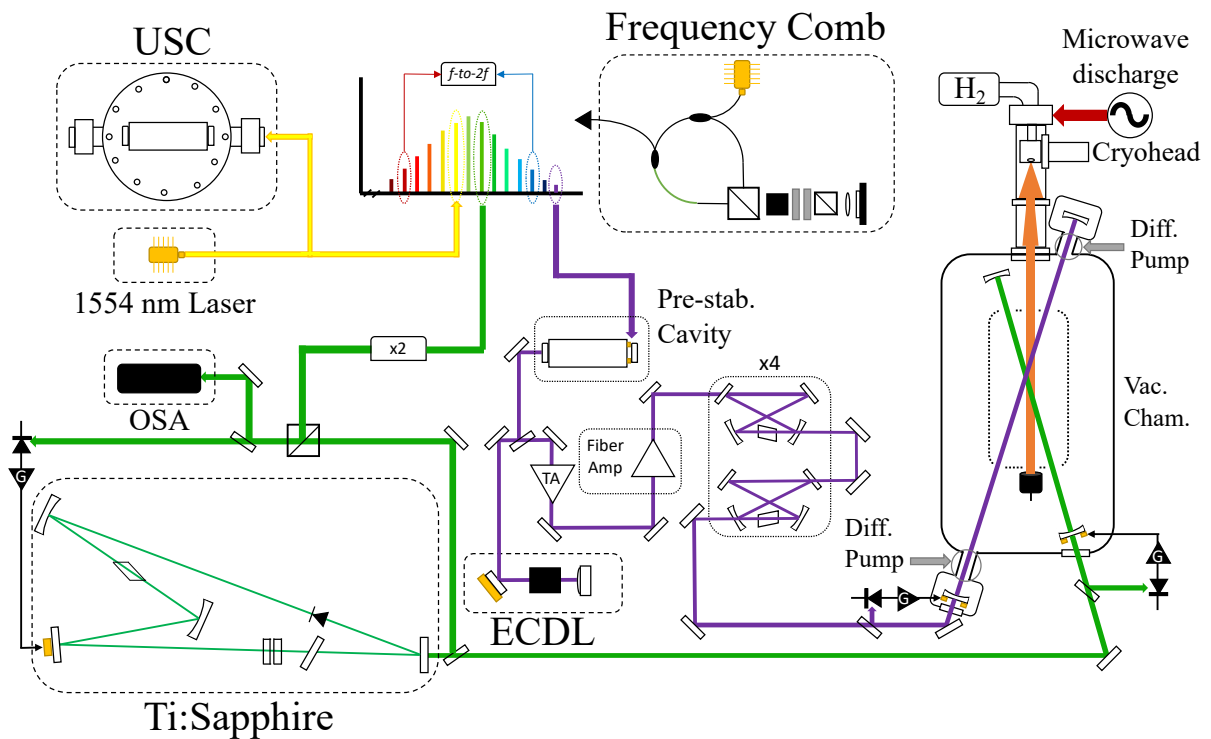


Figure 2.2: A schematic depiction of our measurement subsystems. USC: Ultra-stable cavity. OSA: Optical spectrum analyzer. ECDL: Extended-cavity diode laser. TA: Tapered amplifier. Diff. Pump: Differential pumping manifolds.

Performing spectroscopy on a cryogenic beam of hydrogen atoms is an attractive option as the generation of cryogenic hydrogen beams is not too cumbersome. The approach is described in [67]. To produce an atomic hydrogen beam, molecular hydrogen gas is dissociated into hydrogen atoms in a microwave discharge, and the hydrogen atoms collide with a nozzle that is cooled to

4.5 K via contact with a cryostat. This nozzle effusively emits the hydrogen atoms, which are collimated into a beam by a pair of skimmers [3]. The collimated hydrogen beam is oriented along our spectroscopy vacuum chamber where we drive the 1S-2S transition to generate a beam of metastable hydrogen. The 2S-8D transition is then driven in this metastable hydrogen beam.

Both the 1S-2S and 2S-8D transitions are two-photon transitions. While there are substantial benefits to performing spectroscopy on two-photon transitions [24] (primarily removing the Doppler effect to first order) driving these transitions requires substantially larger optical intensities than their one-photon counterparts [68]. Since two-photon transitions typically require large optical intensities to drive substantial population, the light is commonly resonantly enhanced through optical cavities – an approach we also take here. Once the atomic hydrogen beam is in the spectroscopy vacuum chamber, the atoms interact with power enhanced 243 nm and 778 nm light. For a variety of technical reasons, the power enhancement cavities of the 243 nm and 778 nm light are kept in vacuum. These two optical cavities are aligned so that their modes are overlapped with the cryogenic beam of hydrogen atoms. The metastable excitation laser is a twice-amplified, frequency quadrupled 972 nm diode laser, and the spectroscopy laser is a Coherent-799 Ti:Sapphire ring laser.

Finally, once the hydrogen beam has passed through the metastable excitation and spectroscopy fields, the remaining metastable atoms are detected by quenching the 2S atoms and counting the resultant Lyman- α emissions. Quenching the metastable atoms is very straightforward. A stray electric field or a collision with a wall is sufficient to quench the 2S atom. There are a variety of options to detect the resulting Lyman- α decay; we have opted to use a channel electron multiplier (CEM). A Lyman- α photon causes an electron emission off of the inner surface of the CEM. These photoelectrons are guided down the channels within the CEM, colliding with the inner walls and causing secondary emission events. The cascading secondary emissions result in a current pulse at the end of the channel electron, which can be counted. The total number of metastable counts in a 1 s gate time is recorded as a function of the spectroscopy laser frequency and power, generating our absorption spectroscopy signal.

While the 2S-8D transition is a two-laser experiment in essence, in reality the measurement requires the simultaneous operation of several subsystems. During a measurement, the absolute frequency of the Ti:Sapphire laser during each 1 s metastable counting gate must be set, stabilized, and recorded. Similarly, the metastable excitation laser frequency is stabilized during an entire scan of the 2S-8D transition. Each power enhancement cavity requires its own servo electronics to stay on resonance, and must remain locked during measurements. The stabilization and absolute frequency calibration of our two-laser experiment is mediated via phase-locked loops with our in-house, optical frequency comb. The frequency comb itself is referenced to a highly stable optical resonator and GPS-trained time standard.

In this chapter, we describe the different subsystems necessary to measure the $2S_{1/2}$ - $8D_{5/2}$ transition, except the optical frequency comb (which will be described in Chapter 3). We will begin with the generation and stabilization of the 243 nm light used to drive the 1S-2S transition. Then, we will give an overview of the spectroscopy laser system generating the 778 nm light. Finally, we will briefly describe the generation of the cryogenic hydrogen beam, spectroscopy vacuum chamber, and the metastable atom detector. We will also describe how the velocity distribution of the hydrogen beam was characterized.

2.1 The 243 nm Laser System

Since we wish to populate the 2S state optically, we require a high-powered 243 nm radiation source. While the development of the 243 nm radiation source can be found in [2, 48, 69], we will quickly outline the laser system as a whole: 243 nm radiation is generated by frequency quadrupling a high-powered 972 nm source, which is then power enhanced in an in-vacuum, resonant optical cavity. These subsystems are described in the following sections.

2.1.1 High-powered 972 nm source

The high-power 972 nm laser system is in a master oscillator, power amplifier (MOPA) configuration. Our oscillator is an extended-cavity, diode laser (ECDL) in Littrow configuration; meaning

the output of the ECDL is the zero order diffracted peak off of the intracavity diffraction grating. The ECDL consists of a QPHOTONICS:QLD-980-300S diode collimated with a aspheric lens, a 1200/mm diffraction grating mounted on a translation stage to allow for tuning of the cavity length, and an electro-optic modulator (EOM) to provide fast actuation. Coarse tuning of the ECDL wavelength can be achieved by adjustment of the diffracting grating angle, and fining tuning is typically achieved via a mixture of adjusting the pump current, diode temperature, and cavity length. We achieve about 30 mW of output power at 972.5 nm from the oscillator. This output goes through two stages of amplification before the first frequency doubling stage.

A tapered-amplifier (TA), which are commonly used in a MOPA configuration with ECDLs (see for instance [46, 47, 70]) is the first stage of amplification for the 972.5 nm source. The TA is a DILAS TA-0976-3000 in F-configuration mounted on a gold-plated copper block for heat dissipation. This is mounted onto a larger frame, which is then water cooled to prevent long-term temperature drift. Typically, the TA is run to produce about 2.3 W of optical power, and has a somewhat variable spatial mode quality pending on the input coupling. We have noticed some instabilities of the TA, and there tends to be a coupling between the TA and ECDL that we have attempted to minimize with two stages of optical isolation. There is a broad amplified spontaneous emission pedestal from the TA, and the output is astigmatic. This astigmatism is corrected with a cylindrical lens and the amplified spontaneous emission (ASE) is largely filtered by a 4 nm optical bandpass filter to reduce parasitic amplification in the next stage.

Our second stage of gain employs Ytterbium fiber [48]. Ytterbium (Yb) fiber amplifiers are commonly employed for generating large amount of power in the NIR [71–73]. However, the Yb-gain media preferentially operates in the $>1 \mu\text{m}$ wavelength region where the emission/absorption cross-sections are more favorable [74, 75]. This makes using Yb-fiber as our second stage of amplification at 972 nm unique due to the challenge of operating the Yb-fiber in high inversion and gain competition at $1 \mu\text{m}$ and 976 nm, where the cross sections are more favorable.

To combat these challenges presented by the Yb-gain medium, we have utilized several techniques (see [69] for an in-depth review). A high population inversion throughout the fiber must

be maintained to prevent absorption at our desired wavelength of 972.5 nm, so the fiber amplifier lengths are kept short, ~ 10 -11 cm. By choosing a fiber with a smaller cladding-to-core ratio, the relative gain at 972.5 nm vs 1032 nm is improved [76, 77]. By angle polishing the fiber ends the Fresnel reflections at the fiber tips back into the fiber are heavily reduced, which mitigates ASE in the 976/1030 nm region. Finally, we heavily seed the fiber amplifier with the 2.3 W of 972.5 nm light generated in the first stage of amplification. With this, we are able to generate up to 10 W of 972.5 nm light after the fiber amplifier. After this second stage of amplification, we have a pair of frequency doubling stages [48].

2.1.2 Frequency doubling stages

Light traveling in a medium causes a polarization response in that medium. In many cases, the response of that media is isotropic and linear, meaning the polarization wave in the medium has the same frequency as the electric field and the amplitude of the polarization wave is proportional to the electric field amplitude. However, at high intensities the response becomes nonlinear and may be expanded in a power series of the electric field [78],

$$\mathcal{P}(t) = \epsilon_0 \left(\chi^{(1)} \mathcal{E}(t) + \chi^{(2)} \mathcal{E}^2(t) + \chi^{(3)} \mathcal{E}^3(t) + \dots \right), \quad (2.1)$$

where \mathcal{E} is the incident electric field, $\chi^{(i)}$ is the i^{th} order of susceptibility, ϵ_0 the permittivity of free space, and \mathcal{P} is the polarization. From this, we can see that in large electric fields the nonlinear terms can contribute strongly. If one considers that the electric field is of the form $\mathcal{E} = A e^{i\omega t}$, the higher order terms of Eq. (2.1) are the harmonics of the fundamental light frequency, ω . There are a large number of applications exploiting the nonlinear responses of certain materials; second-harmonic generation is one of them – a $\chi^{(2)}$ process [78, 79]. In order to have a nonzero $\chi^{(2)}$ susceptibility, the medium cannot have inversion symmetry. Such a feature is difficult to achieve in gases or optical fibers, but is possible in crystals.

Certain design considerations must be taken into account to achieve high second-harmonic conversion efficiency [80, 81]. One of the most important considerations is to maintain the co-

herent addition of harmonic waves throughout the crystal. Perhaps a more illustrative description is that the second harmonic generated at the front of the crystal must be in phase with the second harmonic generated in the middle of the crystal, and at the back face. This condition is called phase-matching, and will not generally be fulfilled due to dispersion – the fundamental and the second harmonic will see a different index of refraction in the crystal [80,82]. There are various ways to achieve phase-matching: critical, non-critical, and quasi-phase matching [83]. Critical phase-matching is achieved by adjusting the angle between the crystal axes with the light polarization. Non-critical phase-matching does not require sensitive adjustment of the crystal orientation, and instead the birefringence of the crystal is adjusted by temperature. Non-critical phase-matching is less sensitive to alignment and does not exhibit spatial walk-off, which is the misalignment of the k -vectors of the fundamental and the harmonic light. Quasi-phase matching is a technique where a crystal that typically is used in a critical phase-matching configuration is instead used in a non-critical phase matching configuration, and can be achieved, for instance, by periodically flipping the orientation of the nonlinear crystal so that destructive interference is avoided. In other words, instead of the harmonic being perfectly in-phase throughout the crystal, destructive interference is prevented throughout the crystal by the periodic flipping of the crystal axes [83].

Inspection of Eq. (2.1) indicates that we expect a stronger nonlinear response for larger electric field intensities. A straightforward way to drastically increase the field intensity without further amplification is through power enhancement in a resonant optical cavity. Consider a pair of mirrors with an incoming electric field amplitude \mathcal{E}_0 as shown in Fig. 2.3. If the input mirror has a transmission of T and the second mirror have a reflectivity of R , then the field amplitude \mathcal{E}_1 after bouncing on the back mirror is $\mathcal{E}_1 = \sqrt{1 - R_1}\sqrt{R_2}\mathcal{E}_0$. After two bounces on either mirror, the field amplitude would be $\mathcal{E}_2 = \sqrt{1 - R_1}(\sqrt{R_1R_2})^2\mathcal{E}_0$. The total field inside requires consideration of all possible reflections of the mirror faces, and so we see that this is merely an infinite geometric series which has the solution

$$\mathcal{E}_{tot} = \frac{\sqrt{1 - R_1}}{1 - \sqrt{R_1R_2}}\mathcal{E}_0. \quad (2.2)$$

Note that we have neglected the phase shifts of the field during propagation through the optical cavity. When the cavity length is some integer multiple of the laser wavelength, the phase terms disappear and (2.2) is the solution. As an example, if both mirrors have a reflectivity of 99%, the field amplitude is 10 times larger, an intensity enhancement of 100. The cavity depicted in Fig. 2.3 has standing waves as its resonant modes, but there are also cavity arrangements that have traveling waves as their resonant modes. There are reasons to prefer standing waves or traveling waves depending on the application. In the case of second harmonic generation, a traveling wave is preferable so that all of the harmonic light is generated along a single k -vector.

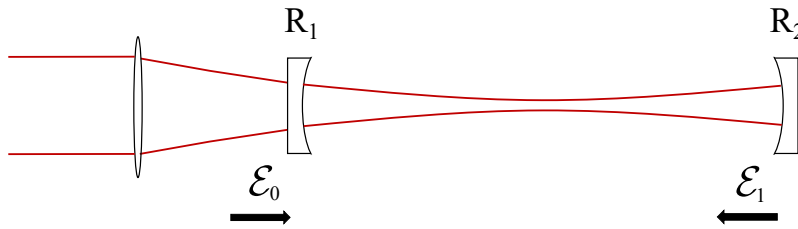


Figure 2.3: Power build up in a simple cavity. Mirrors have reflectivities R_1 and R_2 respectively, and it is assumed there are no losses aside from transmission.

Both the $972 \rightarrow 486$ nm and $486 \rightarrow 243$ nm doubling cavities are in bow-tie configurations, and use a lithium triborate (LBO) and a cesium lithium borate (CLBO) nonlinear crystal respectively. The LBO doubling cavity utilizes type-I, non-critical phase matching, as the birefringence of LBO is highly temperature dependent, which also has the benefit of eliminating spatial walk-off, improving the resultant 486.3 nm beam quality. Unfortunately, the crystal temperature required for phase-matching at 486.3 nm is quite high, >250 °C, requiring the design of an appropriate crystal-oven. Historically, the LBO crystal was uncoated and Brewster cut. We have recently switched to an AR-coated LBO crystal, which has yielded more consistent 486.3 nm conversion efficiency. We attribute the performance improvement to the reduction of 486.3 nm Fresnel reflections at the output crystal face and the previous crystal's damage/contamination. While we have seen 486.3 nm powers up to 4 W with the Brewster-cut crystal, we have not tested the maximum power output

of the AR-coated LBO crystal. For the spectroscopy, we typically run the Yb-fiber amplifier to generate 6 W of IR light and generate 2.5 W of 486.3 nm radiation.

Generation of 243.1 nm radiation is achieved in a second bow-tie frequency doubling cavity. This UV-generating cavity uses a 10 mm Brewster-cut cesium lithium borate (CLBO) crystal and is type-I critically phase matched. While the phase matching is largely tuned by the crystal angle, the crystal is still kept in an oven at 150 °C since CLBO is hygroscopic. For this reason, the crystal oven is also continuously purged with dry nitrogen gas. The phase matching can be finely tuned with variations in the crystal temperature; self-heating effects also can derate the 243.1 nm power generation if the crystal oven temperature is not suitably adjusted. Typically, up to 600 mW of 243.1 nm power is generated from 2.5 W of 486.3 nm input power, with about 80% mode-matching to the CLBO cavity.

Locking both frequency doubling cavities is achieved by actuating the cavity lengths via intra-cavity PZT's. The error signal for both optical cavities is created by sideband generation at 3.64 MHz on the 972.5 nm light with an EOM. Since the LBO doubling cavity has linewidths on the order of 50 MHz, the sidebands are transmitted and not reflected at the input coupler, and therefore constitute a dither lock instead of a Pound-Drever-Hall (PDH) lock [84]. The sidebands themselves are frequency doubled, since they are not filtered by the LBO doubling cavity, and are also present on the 486.3 nm light. In this way, further modulation of the 486.3 nm light for locking the CLBO doubling cavity is unnecessary.

By the time the 243 nm radiation reaches the final power enhancement cavity, significant attenuation (up to 50%) of the UV-power has occurred. At each optic following the CLBO cavity, there is loss exceeding the specification of the optic. While we believe there is some damage due to the large UV powers, we also attribute some fraction of this loss to the build-up of cracked hydrocarbons on the optical faces. There is evidence in the literature that UV-light can disassociate organic compounds and these compounds can accumulate on surfaces where there is significant optical power [85, 86]. This hypothesis is also supported by the fact that the optical surfaces in question are discolored and this discoloration can be largely removed by thorough cleaning. The loss on the

optics is also significantly reduced from this cleaning, but the in-atmosphere optics do not seem to entirely recover. We employ typical solvents for cleaning the optical surfaces: methanol, isopropyl alcohol, and water. It is possible a more aggressive solvent would better remove the film and would lead to improved recovery.

2.1.3 243 nm power enhancement

While there were previous demonstrations of getting up to 1 W of 243 nm radiation in power enhancement cavities [29], it was not yet demonstrated that intracavity powers of >10 W of 243 nm radiation were achievable at the outset of this project. The primary technical difficulties are that the performance capabilities of optical coatings at 243 nm are substantially worse than their visible and NIR counterparts and that the coatings degrade due to the UV radiation. This degradation of the coatings is attributed to two sources: the contamination of the surfaces with hydrocarbons [86] and the depletion of oxygen in the optical coatings [87]. However, we have demonstrated that we are able to achieve > 30 W of 243 nm radiation for greater than 1 hour without degradation in vacuum [88].

Our initial demonstration of the large UV-build up without severe degradation of the mirror coatings hinged on two technical details: the partial pressure of oxygen near the mirror surfaces needs to be about ~ 1 Torr and the surrounding vacuum chamber needed to be as free from contaminants as possible. This first demonstration was done in a test vacuum chamber and was not a part of the 2S-8D spectroscopy vacuum chamber [88], so the UV-power enhancement cavity needed to be adapted to the spectroscopy geometry and vacuum chamber. There are some additional design constraints to make the UV-enhancement amenable to our spectroscopic needs. First and foremost, the pressure in the spectroscopy volume needs to be below 1×10^{-6} Torr. Vacuum chambers flex when they are evacuated, moving the mirrors forming the optical cavity within the chamber. Even if this did not totally destroy the resonant modes of the cavity, it introduces a randomness to our experimental geometry which is unacceptable. Therefore, our design constraints indicate that we need 1) a large pressure differential between the 243 nm cavity mirrors and the spectroscopy vac-

uum chamber proper and 2) the optical cavity alignment needs to be adjustable once the vacuum chamber is pumped down.

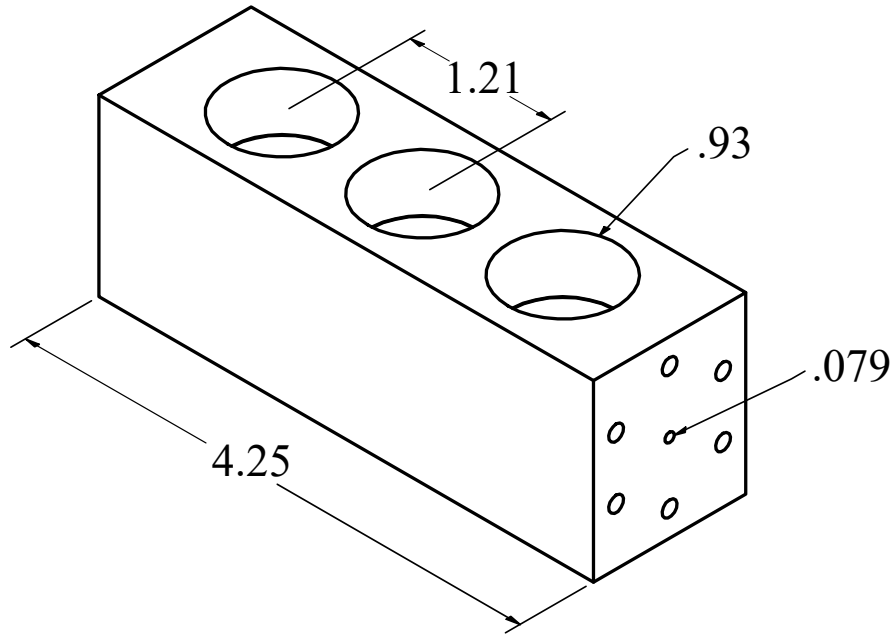


Figure 2.4: Differential pumping manifold, units in inches

To address the requirement of the large pressure differential, we have opted to house our cavity mirrors in hollowed aluminum vacuum cubes external to the main vacuum chamber. These cubes are brought to rough vacuum and O_2 is leaked into the cubes to stay at a pressure of $\sim 300 - 400$ mTorr. The cubes are connected to the spectroscopy vacuum chamber through a series of differential pumping stages. A three stage manifold, shown in Fig. 2.4, bridges the relatively high pressure inside of the cubes ($\sim 10^{-2}$ Torr) to the relatively low pressure in the vacuum chamber ($< 10^{-6}$ Torr). The aperture through the center of the manifold is large enough to support a stable cavity mode without substantial loss. The three .93" apertures are individually pumped, and low conductance through aperture allows for substantial decoupling between the high pressure and low pressure side. The faces of the manifold support a 1.33" conflat flange with fluorocarbon (rubber) gaskets.

To improve the overall stability of the optical cavity, the cubes are quite large and rest on 1.5" of lead. The mirrors inside are mounted onto large copper bases to further increase the weight of the assembly. Small viton rings separate the copper bases from the aluminum cube to provide a high loss interface between the mirror and cube. We have opted to mount the cube and lead assembly on tip-tilt stages to allow for articulation of the cubes once the chamber is evacuated. A miniature translation stage is mounted to the high reflecting mirror copper base. The translation stage allows for μm adjustment of the cavity length with a discrete PZT stack (Thorlabs PK2JA2P1). We found substantial improvement of the mirror lifetime when we thoroughly cleaned all the components inside of the cubes: including removing anodization of translation stages and removing large amounts of the grease of the bearings. Fig. 2.5 shows the inside of the cubes with the 243 nm mirrors, note that the copper is not in contact with the cube walls.

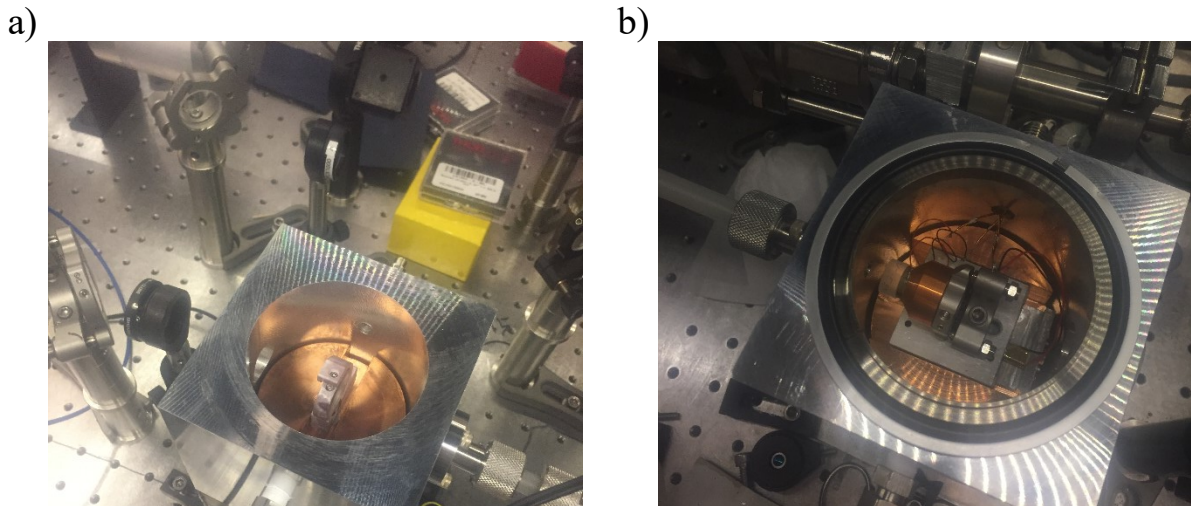


Figure 2.5: Inside of the mirror cubes. a) Input coupler mirror cube. b) High reflector mirror cube with PZT's and feedthrough

The 243 nm cavity is dither locked, with the error signal generated by modulating the 243 nm cavity length with an intracavity piezoelectric (PZT). The modulation frequency is typically in the ~ 450 kHz range, and the transmission of the cavity through the high reflector is monitored by a buffered silicon photodiode. Actuation of the cavity length is achieved by two PZT's, the fast

PZT (that is also applying the dither) attached to the mirror directly, and a slower PZT that drives the translation stage. A pair of 1 m radius of curvature (ROC) mirrors form the cavity, and are separated close to 1.8 m apart giving a free spectral range of about 85 MHz. This forms a cavity waist of about 150 μm with a Rayleigh range of 30 cm. We have recently switched to CaF_2 coated mirrors, which have tentatively been shown to be more resilient against UV-damage due to the lack of an oxide base layer.

2.1.4 Frequency stabilization and control

The 1S-2S transition has an exceedingly narrow natural linewidth of about 1 Hz [1]. While we have not recovered such narrow lines since the 1S-2S line is transit time broadened, the resonance is still quite narrow at our transit time limited width of ~ 100 kHz, see section 6.4.3 for more detail. Therefore, we desire that the 243 nm radiation is highly coherent to achieve maximal metastable flux. Because of the nonlinear processes involved with the excitation of the 2S state (two frequency doubling stages and a two-photon transition) the phase noise requirements of the 972 nm light are very stringent. As a very simple explanation, let us represent the 972 nm light, $\mathcal{E}_{972}(t)$ with a plane wave with a little phase noise, $\beta(t)$,

$$\mathcal{E}_{972}(t) = Ae^{-i\omega t + i\beta(t)}. \quad (2.3)$$

The 486 nm light, $\mathcal{E}_{486}(t)$ produced in the first frequency doubling stage is proportional to $(\mathcal{E}_{972})^2$, so

$$\mathcal{E}_{486}(t) = \chi^{(2)} A^2 e^{-2i\omega t + 2i\beta(t)}. \quad (2.4)$$

We can see that the phase noise in the 486 nm field is apparently double that of the 972 nm field. Each following stage of frequency doubling would exasperate this issue.

Furthermore, aside from just excitation efficiency concerns, finding the narrow 100 kHz transit-time broadened 1S-2S transition is quite difficult if our laser is not stable over long time scales and our frequency calibration is not sufficiently precise.

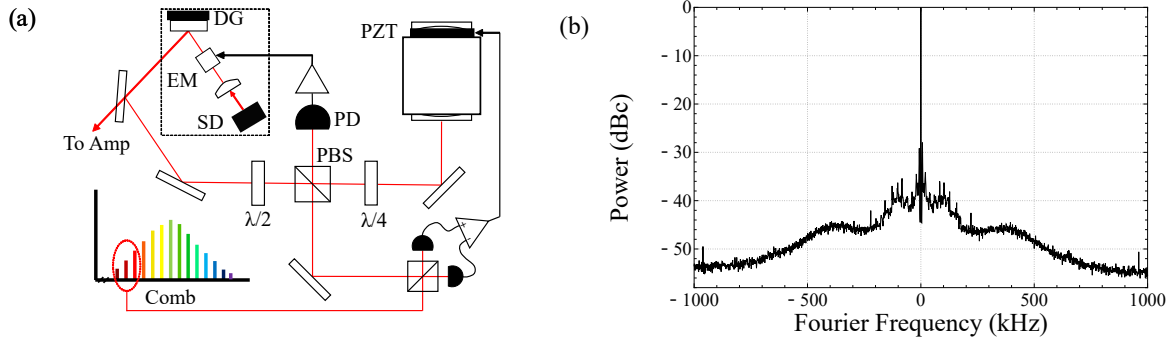


Figure 2.6: This figure is reproduced from [2]. Frequency stabilization system a) 972 nm ECDL and PDH lock to external Fabry-Perot cavity. The ECDL is first stabilized to the Fabry-Perot (FP) cavity via a PDH lock. Sidebands on the 972 nm light are generated by phase modulation with an intracavity EOM and the lock is maintained by actuating the ECDL cavity length. Once the ECDL is stabilized to the FP, the FP cavity length is actuated to stabilize the 972 nm-comb beat note. b) Beat note between frequency comb and ECDL.

Our 972 nm frequency stabilization and measurement system is shown in Fig. 2.6. The frequency stabilization of the 972 nm ECDL begins by PDH locking to the external Fabry-Perot (FP) cavity [84]. The FP cavity finesse is about 1000. Sidebands for the PDH lock are generated by an EOM in the ECDL, and the 972 nm oscillator frequency is actuated by feedback to the cavity length of the ECDL with the EOM and by actuating the PZT which controls the diffraction grating. Further information on PDH locking can be found in Chapter 3.6.3. The 972 nm ECDL is phase-locked to a tooth of the optical frequency comb by actuating the pre-stabilization cavity length – one of the cavity mirrors is mounted on an annular ring attached to the spacer. Phase locking the 972 nm ECDL light with the frequency comb allows us to further stabilize the ECDL frequency, and simultaneously allows for setting the absolute frequency of the ECDL. By adjusting the beat frequency between the ECDL and the frequency comb, we control the absolute frequency of the 972 nm light. The beatnote between these two systems is shown in Fig 2.6 (b).

It is important to estimate the linewidth of the 972 nm oscillator once stabilized to the frequency comb. The linewidth of a laser can be determined by the phase noise of the system, which is quantified as the spectral phase noise density, S_ϕ [89]. Phase noise in a beat note manifests itself as sideband noise around a coherent spike in the frequency domain. In situations with low phase noise, S_ϕ can be approximated by the sideband noise on the beat note, noting that both the negative

and positive sideband noise contributes to S_ϕ . Laser linewidth can be estimated from the phase noise spectral density through,

$$1 \text{ rad}^2 \approx \int_\gamma^\infty S_\phi df, \quad (2.5)$$

where γ is the FWHM laser linewidth of the system [89].

A beat note between two lasers indiscriminately reports the combined phase noise of both laser systems. Therefore, if we were to estimate the ECDL linewidth using only the S_ϕ suggested by the beat note, we would overestimate that laser linewidth. To separate the comb noise from the ECDL laser noise, we investigate the in-loop error signal of the ECDL-cavity lock and the f_0 beat note of the comb. Because the f_0 beat note is generated with light close to 972 nm (f_0 is generated with light near 1010 nm), it provides a good measure of the expected phase noise of the comb in that region. Therefore, comparison of the ECDL-comb beatnote to the f_0 beatnote allows us to determine where comb noise is overrepresented. By investigation of the in-loop error signal, and conversions from voltage to frequency excursions (see [69]), along with the f_0 beat note comparison, we estimate that the ECDL linewidth is <1 kHz. For reference, the dominant contributor of noise above 100 kHz is from the frequency comb – fast frequency excursions are heavily suppressed on the ECDL from the PDH lock to the pre-stabilization cavity.

2.2 The Spectroscopy Laser System

The 2S-8D transition is centered near 778 nm region, which is well suited for solid-state Titanium:Sapphire lasers. The large gain bandwidth of Ti:Sapphire lasers also allows for probing higher lying 2S-nL transitions, such as the 12D state at 750 nm we used to quantify the presence of stray electric fields, which we will discuss in Chapter 6.2. Therefore, we use a Coherent-799 Ti:Sapphire ring laser to probe the 2S-8D and 2S-12D transitions in our experiment. A schematic of this oscillator can be found in Fig. 2.7.

The Coherent-799 is a vertically oriented ring oscillator mounted to a large Invar rod. The laser is set for single-mode operation by a birefringent filter in conjunction with a pair of tunable etalons. Similarly, the lasing frequency of this oscillator is grossly tuned by adjustment of the birefringent

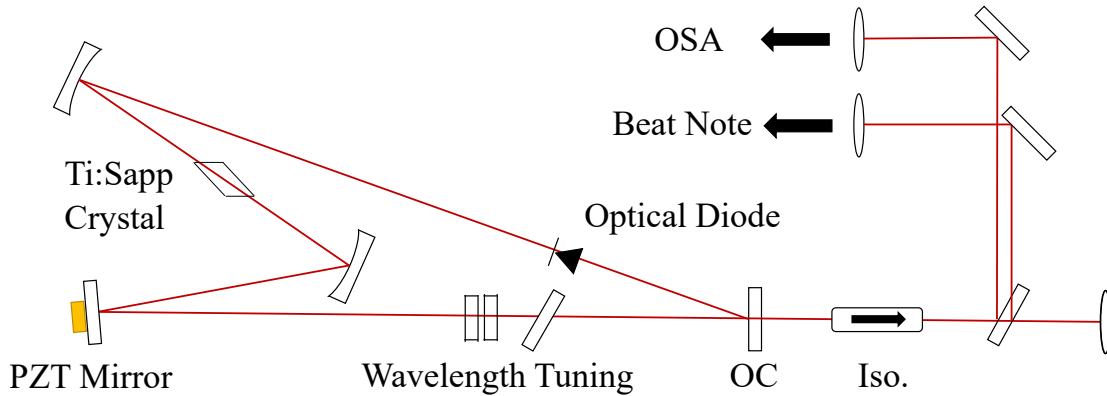


Figure 2.7: Coherent-799 Ti:Sapphire Oscillator vertical ring oscillator. PZT Mirror: PZT mounted mirror, Wavelength Tuning: Thin/thick etalon pair and birefringent filter, OC: Output coupler, Iso.: Optical Isolator, OSA: Fiber to optical spectrum analyzer, Beat Note: PM fiber to beat note with frequency comb

filter, with finer control by adjustments of the thin etalon, thick etalon, and the cavity length respectively. The cavity length is adjusted via a intracavity PZT mounted to the backside of a mirror. An optical diode is in place to promote traveling-wave modes inside of the cavity, which further reduces the chance of mode-hops and promotes single-mode stability. The Ti:Sapphire crystal is pumped by up to 8.25 W of 532 nm light from a Sprout-D diode pumped, solid state laser system. We can extract up to 750 mW of 778 nm light from the oscillator, which then travels through a Faraday isolator, and a nominal amount of power is picked off for characterization by an optical spectrum analyzer and comparison to the frequency comb. The remaining power is coupled to a single-mode, polarization maintaining (PM) fiber, where it is guided to the spectroscopy chamber for resonant power enhancement.

While much of the Ti:Sapphire oscillator is stock to the 799, we have made a few key modifications to improve the temperature and frequency stability of the system. As the wavelength tuning of the 799 is in part set by the exact mode-spacing of the thin/thick etalon pairs (which are tuned mostly by angle), temperature variations of the oscillator can cause mode-hops as the laser system heats and cools with the environment. To combat this issue, we have attached water cooling lines to the etalon pair, as we have found that our lab generally heats up through the day and cools overnight.

Similarly, since we want a highly stable light source as our spectroscopy laser, we have taken steps to reduce both the intrinsic noise on the system as well as our ability to servo remaining fluctuations. We have found the majority of the noise present on our Ti:Sapphire system is from acoustic and vibrational coupling. Therefore, this system is isolated from the environment by setting the system on extra metal feet with vibration dampening rubber (Sorbothane) underneath. The entire oscillator is also within a box lined with acoustic dampening foam. Originally, the 799 cavity length was also adjustable by an intracavity PZT, however, we found this original PZT/mirror mounting to be insufficient for coherent phase-locking to our frequency comb, as it was too slow. We have since replaced the original intracavity PZT with one suitable for fast feedback, and greatly reduced the mass of the PZT mounted mirror.

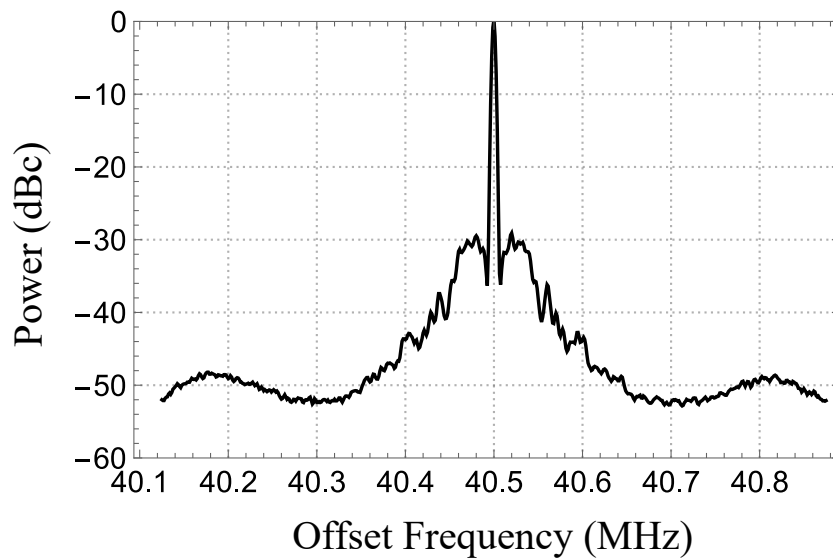


Figure 2.8: Example Ti:Sapphire-Comb locked beat note. Resolution bandwidth 10 kHz

Like the 972.5 nm ECDL, the absolute frequency of the Ti:Sapphire is determined and set by phase-locking to our frequency comb. The absolute frequency of the Ti:Sapphire is scanned by adjusting the beat frequency between the frequency comb and the Ti:Sapphire. The error signal for this lock is created by heterodyning the 799 output with comb oscillator's frequency doubled output. The resultant error signal actuates on the 799's intracavity PZT to stabilize its cavity length.

An example of a locked beatnote between the comb and the 799 is shown in Fig. 2.8. We estimate a laser linewidth < 1 kHz at the fundamental, a more detailed calculation of the contribution of laser noise to the spectroscopy can be found in section 6.4.3.

The 778 nm power enhancement cavity, which is within the vacuum chamber proper, is formed by a pair of 99.7% reflective mirrors and is about 75 cm long, leading to a cavity resonance width of about 200 kHz. Much like the 243 nm build up cavity, the mirror must be adjustable once the chamber is sealed. Fortunately, as compared to UV, 778 nm light is much less damaging to optics, and the mirrors do not require an oxygen purge to prevent degradation. Instead, the mirrors are on vacuum-compatible piezomotor mirror mounts. The cavity is PDH-locked by feedback on the cavity length by a pair of PZTs: one on the mirror mount and the other on a translation stage. Sidebands are generated at 7.5 MHz by an EOM (far larger than the resonance width) and the input power to the 778 nm enhancement cavity can be controlled by way of a zero order $\lambda/2$ waveplate and polarizing beam splitting cube. Controlling the power this way, instead of varying the Ti:Sapphire oscillator pump power, mitigates the chances of mode-hops due to thermal effects in the Ti:Sapphire crystal. The optical setup preceding the 778 nm power enhancement cavity is shown in Fig 2.9. Transmission through the 778 nm cavity is monitored by a silicon photodiode to measure the relative power inside of the 778 nm cavity. During spectroscopy, we typically have between 10 W and 50 W of 778 nm light inside of the cavity.

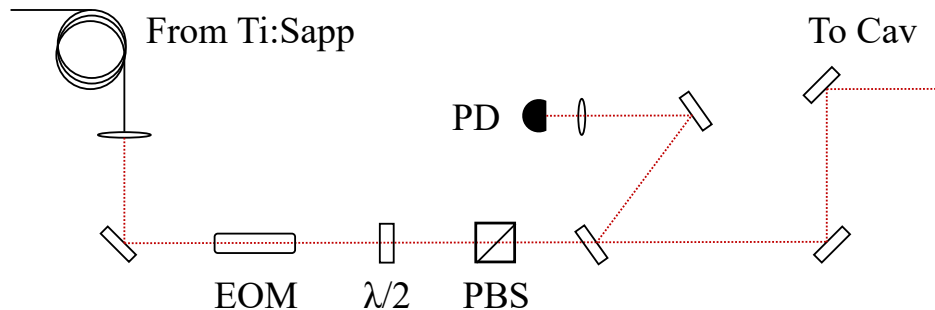


Figure 2.9: Optical setup preceding 778 nm power enhancement cavity. EOM: Electro-optic modulator, $\lambda/2$: Half-wave plate, PBS: Polarizing beamsplitter, PD: Reflection photodetector

2.3 Overlap Geometries

Fig. 2.10 gives a top-down schematic view of the beam overlaps in the vacuum chamber. The standing modes formed by the 243 nm cavity and 778 nm cavities are 6° from collinear with the atomic beam. Our metastable beam divergence is set by the overlap between the 243 nm beam and atomic beam overlap, the separation between the nozzle and the overlap, and the nozzle aperture. The 778 nm/atom overlap and 243 nm/atom overlap are separated by 15 cm, and the metastable detector is 15 cm past the 778 nm/atom overlap. Due to the rather small angles permitted by the differential pumping manifold, the 243 nm beam trajectory is well-defined while the 778 nm beam trajectory is not. As indicated by the dotted line in Fig. 2.10, the spectroscopy region is housed within a Faraday cage which contains apertures to for the three beams (two optical and one atomic). These apertures lightly constrain the geometric orientation of the 778 nm modes, but the apertures are larger than the possible trajectories of the 243 nm beam. Therefore, some alignment of the 778 nm cavity to maximize the metastable-spectroscopy is required when the chamber is first evacuated. This alignment is purely vertical – a horizontal misalignment of the cavity modes to the atomic beam is not geometrically possible.

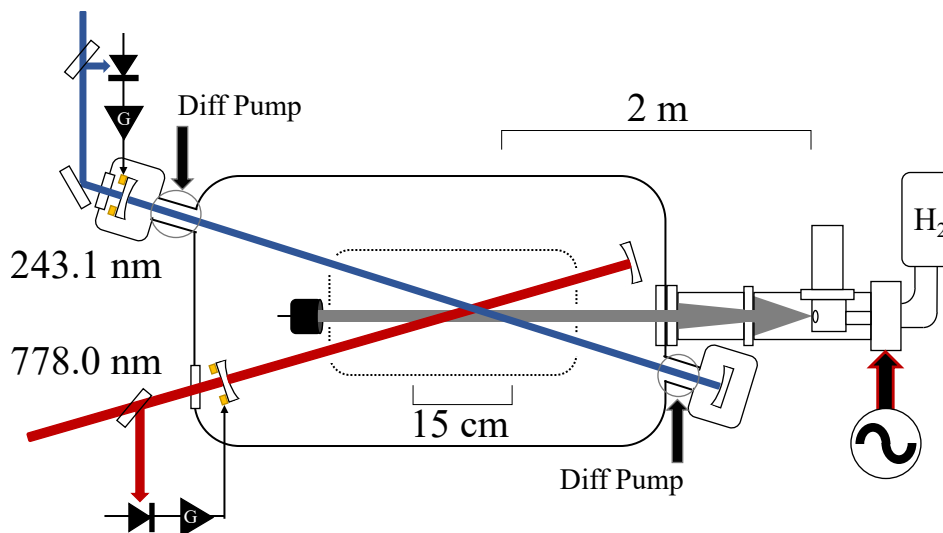


Figure 2.10: Top-down view of the beam overlaps

2.4 The Atomic Beam and Spectroscopy Chamber

Having described the 243 nm and 778 nm laser systems used to drive the 1S-2S and 2S-8D transitions, we will now describe the creation of the cryogenic hydrogen beam and the characterization of the hydrogen beam velocity distribution. Afterwards, we will describe spectroscopy vacuum system which contains both the 243 nm and 778 nm optical cavities described previously. Finally, we will describe the metastable atom detector.

2.4.1 Cryogenic Hydrogen Beam Generation

An early demonstration of a cryogenic beam of hydrogen atoms was shown in [67]. This work was originally motivated by the desire to study the possibility of hydrogen as a weakly interacting Bose gas. While a Bose-Einstein condensate of atomic hydrogen has successfully been created [90, 91], we primarily wish to use a cryogenic hydrogen source in the context of precision atomic spectroscopy. The recipe to create a cold atomic beam is 1) disassociate molecular hydrogen 2) cool atomic hydrogen by collisions with cold surfaces and 3) define a beam with appropriate nozzle geometry and apertures.

The flow of molecular hydrogen into our discharge is controlled by a gas regulator and an Alicat mass flow controller. The discharge itself is maintained by a microwave cavity surrounding a conductance-limited, quartz tube. Our discharge cavity (Ophos Instruments) is based on the Evenson design [92], and is driven by an amplified voltage-controlled oscillator (VCO) (Mini-Circuits ZX95-2390A-S+ and ZHL-100W-242+ VCO). The quartz tube is air cooled, and the aperture is limited to 500 μm and the discharge is typically maintained at 40 W of RF power. About 1 W of power is reflected once the discharge is initiated. We have found that the discharge can be initiated and maintained in a relatively large pressure range on the high pressure side of the discharge (.2-2 Torr) but we typically run the discharge at 400 mTorr during spectroscopy experiments, which is a compromise between larger atomic flux and a larger heat load on the cryogenic nozzle. At most temperature ranges, the atomic flux seems to maximize around 1 Torr, with diminishing returns at

pressures larger than that. We estimate an atomic flux of about 10^{17} atoms/s when operating at a H_2 backing pressure of 800 mTorr.

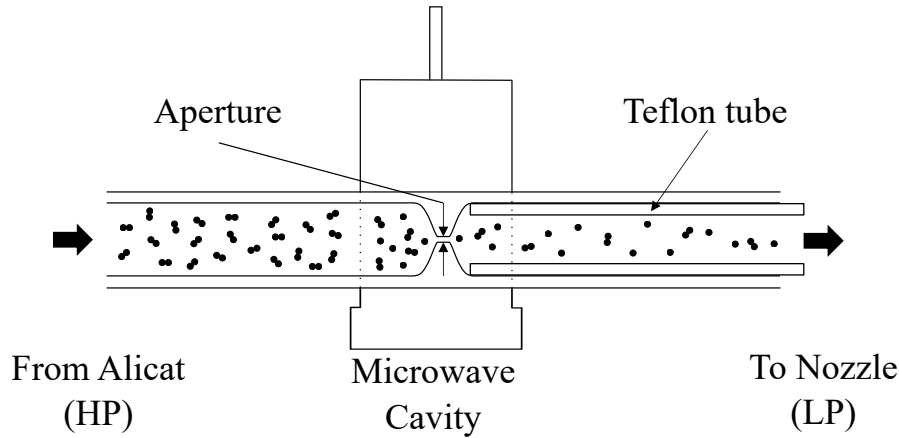


Figure 2.11: Microwave cavity and hydrogen disassociation

On the low pressure side of the hydrogen discharge, a Teflon tube delivers the now-atomic hydrogen to the cold nozzle. Teflon was found in [67] to inhibit the recombination of hydrogen atoms into molecular hydrogen on surfaces. Our beam nozzle design is extensively discussed in [3], but we will review the general points here. The cold nozzle head is directly attached to a closed cycle, Grifford-McMahon cryostat, and the temperature of the nozzle is monitored by a silicon diode (Lakeshore Cryotronics DT-670). To improve performance, two concentric aluminum heat shields surround the nozzle to reduce radiative heating originating from the nearby vacuum chamber walls. The nozzle is machined aluminum, though we have tested copper, and found lower recombination rates in the aluminum nozzle. As for the geometry of the nozzle itself, it has been found that forcing at least one-collision with the nozzle surface greatly improved thermalization of the beam.

Following the nozzle a pair of skimmers, aluminum cones with an axial aperture, define the resulting atomic beam extent and divergence. The distance between the nozzle output and second skimmer is 450 mm, and the skimmer aperture is 4.9 mm, resulting in a 11 mrad beam divergence. Between the two skimmers is a chopper wheel, which can be used for time-of-flight measurements

on the atomic beam. Time-of-flight measurements allow for direct velocity characterization of metastable hydrogen, allowing for robust determination of the second-order Doppler shifts in our spectroscopic measurements.

2.4.2 Time-of-flight detection

Time-of-flight measurements to determine the velocity distribution of either atomic or metastable hydrogen requires modulating the atomic beam directly. The chopper wheel is a singly-segmented, mass-balanced aluminum wheel driven by a dc-motor. Dimensions of the chopper wheel and the kernel function are shown in Fig. 2.12. A rotary position encoder provides a timing signal every revolution of the chopper wheel for synchronization. A quadrupole residual gas analyzer (RGA) is used to detect ground state hydrogen atoms, and our metastable atom detector is used to detect 2S hydrogen atoms.

Regardless of which type of hydrogen species is detected (ground state or metastable), the signal-to-noise ratio of a single chopped event is not sufficient. Therefore, many such traces are averaged together. In the case of ground state hydrogen detection, about 128×500 total traces are averaged together for a single data set, amounting to a few hours of integration time. In the case of the metastable beam detection, we use a channel electron multiplier in pulse counting mode. In order to generate time-of-flight signals, the pulse height is standardized with a latch circuit and then low-passed to turn the digital pulse train into a psuedoanalogue signal. This psuedoanalogue signal is averaged over many chopped events as well – analogous to the ground state detection.

Due to the nature of the finite chopper opening window, and the dynamics of the detection, it is necessary that the time-of-flight signal is compared to a velocity distribution via a model. For instance, the expected Maxwellian-velocity distribution must be transformed into a time-domain signal and convolved with a chopper kernel to be compared to our time-of-flight signal. The flux distribution of ground state hydrogen is expected to be $P(v) \propto v^3 e^{-\beta v^2}$, where $\beta = m/(2k_b T)$. However, there are a number of reasons to expect that our Maxwellian flux distribution to be modified however. For instance, detection by the RGA requires ionization of the hydrogen atom. Since

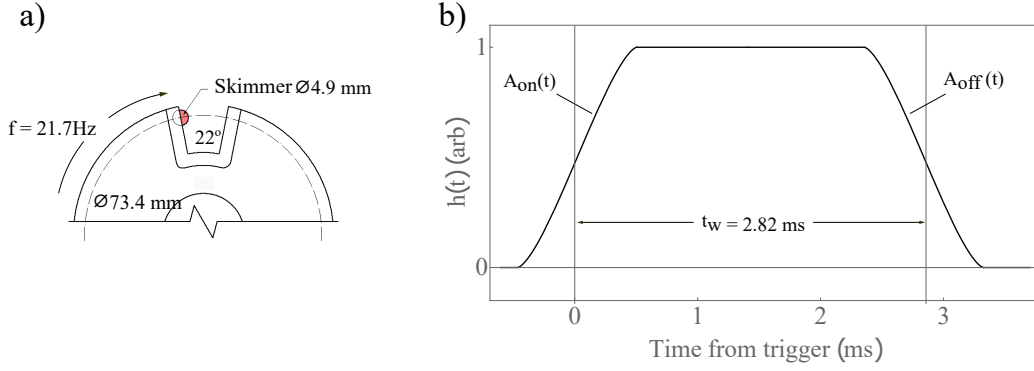


Figure 2.12: This figure is reproduced from [3], with permission of AIP Publishing. a) Dimensions of chopper wheel b) Kernel function for chopper wheel.

the probability of ionization is proportional to the interaction time, the prefactor transformation of $v^3 \rightarrow v^2$ is necessary. In the case of the metastable detection, there is an even stronger deviation from the Maxwellian distribution. These deviations arise due to the interplay between atomic velocity with excitation probability to the 1S-2S state, ionization of the 2S state by the 243 nm radiation, and the metastable detection itself. The metastable detector has a pair of electrodes at the face of the CEM to repel photoelectrons, which can quench slow moving metastable atoms. The net effects of these considerations is that the detected metastable velocity distribution is shifted towards faster atoms, so we model the metastable beam distribution as

$$P(v) = Av^4 e^{-\beta v^2}, \quad (2.6)$$

with the extra power of v in the prefactor preferentially moving the distribution to larger velocities. We have also tried more exotic flux distributions for the metastable beam, but these distributions are not strictly rigorous and are rather utilitarian in nature, for instance $P(v) = Av^{3.5} e^{-(v_c/v)^2} e^{-\beta v^2}$ with v_c some cutoff velocity determined by fit. We find a good fit with a cutoff velocity of about 245 m/s for the data shown in Fig. 2.13 b).

Numerical deconvolution methods do not produce unique solutions, and some solutions exhibit strange oscillatory behaviors that are nonphysical. We therefore only do convolution and not deconvolution in our modeling; we assume a velocity distribution and convolve it with our chopper

kernel, varying the temperature until we reach good agreement. At the time of this writing, our apparatus is somewhat unique amongst other high precision measurements in hydrogen in that we can characterize our velocity distribution by modulating the atomic beam directly. We display the results of the time of flight measurements and fittings in Fig 2.13. In the case of ground state hydrogen, we have found good thermalization (as evidenced by the close match of the modeled line with the measured line), but the analysis indicates that the beam is closer to 6.5 K than the 5 K measured on our silicon diode. We explain this discrepancy due to the heat load of the gas on the inner surfaces of the nozzle, and also due to heating from recombination.

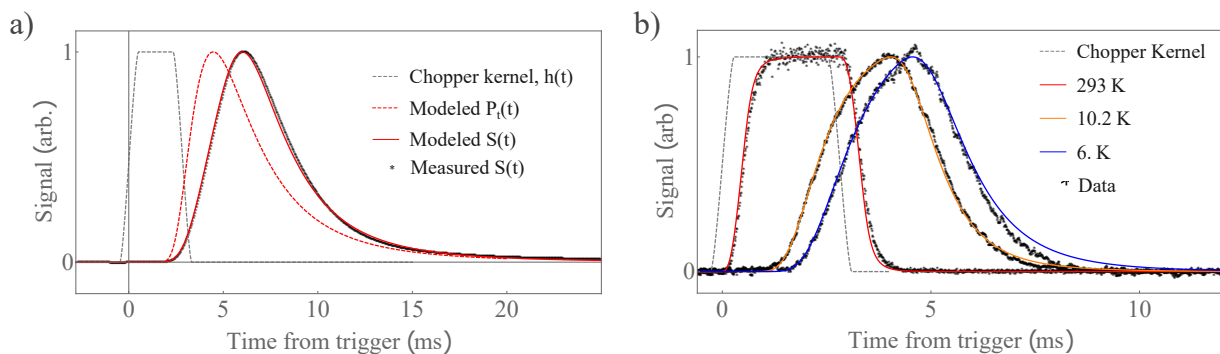


Figure 2.13: This figure is reproduced from [3], with permission of AIP Publishing. a) Ground state time-of-flight data and fit. b) Metastable time-of-flight data and fit

At this point it is worth mentioning that the time-of-flight measurements were taken when the hydrogen discharge was in a different configuration. At the time of the measurements, the high pressure side of the discharge was substantially more complicated with many tubing joints, and the pressure was dictated by two regulators and a leak valve. Since then, we have moved to a substantially simpler backline, with the pressure regulated by the Alicat as described previously. Furthermore, the backline is now kept at 10 PSI, whereas before the entire backline was held below atmospheric pressure. This change has led to a couple of notable improvements. For instance, the nozzle is able to be cooled down to 4.4 K (as indicated by the silicon diode) as opposed to the previous minimum of 5 K. Previously, the nozzle seemed to freeze over relatively quickly (10 min) when held at cryogenic temperatures. Either hydrogen ice or contaminant gases may clog up the

nozzle aperture, reducing hydrogen flux over time. Since the backline change, this freezing has drastically reduced – from freezing over in 30 minutes to taking 6 hours or longer to freeze over instead. These improvements are largely attributed to a reduction in contaminant gas, which we believe arose from leaks of atmospheric gas into the discharge and nozzle. It is our expectation that further time-of-flight measurements would indicate that we may reach sub-6.5 K thermalized atomic beams due to the reduced heatload and freezing of the nozzle surfaces.

2.4.3 Vacuum Chamber and the Spectroscopy Region

The spectroscopy vacuum chamber was designed with flexibility and ease of access in mind. Aside from that, we have a few design considerations to consider for the 2S-8D spectroscopy: the chamber must house two power enhancement cavities, reach relatively low base pressure, and shield the spectroscopic volume from external fields.

The spectroscopy chamber is composed of two 8"-CF, 6-way cubes, a 5-way cross, and a spacer nipple. All are Conflat 8" so that hands can more easily work inside of the vacuum chamber. The spectroscopy chamber is connected to the cryogenic nozzle by a CF to quick-connect 1" stainless steel tube. The vacuum chamber and cryogenic beam generation vacuum chambers are able to be decoupled by a manual stainless ball-valve. On the opposite side of the chamber, another CF to quick-connect adapter is available to couple to specialized chambers, such as the RGA chamber or the future 2S hyperfine splitting measurement chamber. Both of the CF to quick-connect adaption flanges on the faces of the chamber have also been machined to support windows for the 243 nm and 780 nm radiation. Once the differential pumping manifolds for the 243 nm mirror cubes were created, the 243 nm windows were replaced by KF 25 flanges, and .5" stainless steel tubing connect the vacuum chamber to the 1.33" CF flanges on the manifold faces.

The 8" cubes house the 778 nm cavity mirrors, and there are several electrical feedthroughs on the cube flanges to support the necessary electronics contained within the spectroscopy chamber. To improve the stability of the 778 nm cavity, the mounts are held on a 1" thick stainless steel disc breadboard, with another 1" thick stainless disc below. Much like the 243 nm copper mounts, the

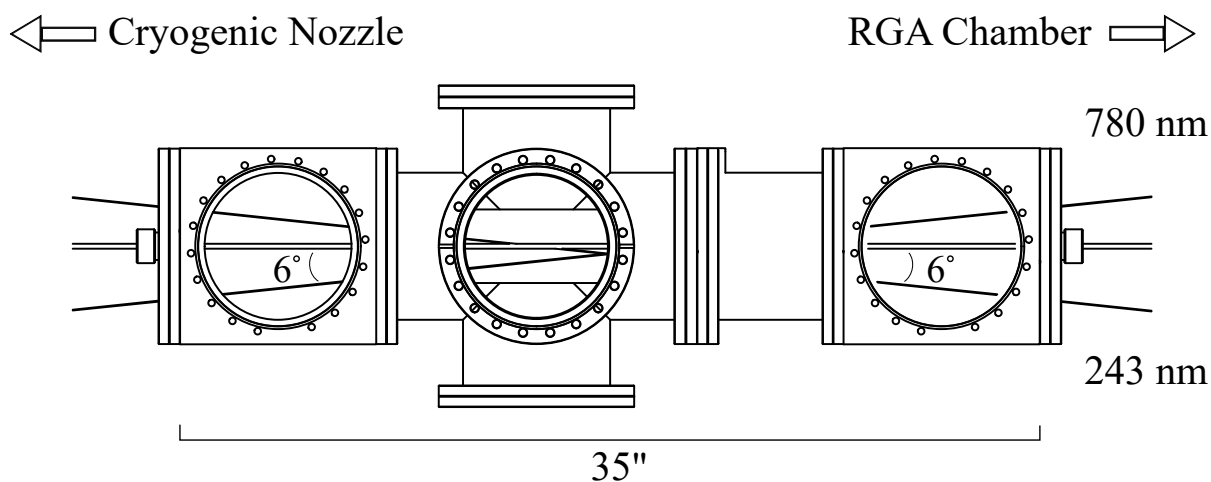


Figure 2.14: Top-down view of the spectroscopy chamber geometry. 8" CF cubes house the mirrors for the 778 cavity (not shown). The atomic beam traverses through the long axis of the vacuum chamber, shown as a beam through the center. The relative orientation of the 778 nm and 243 nm light beams through the chamber are also shown.

stainless steel discs are lightly decoupled from the vacuum chamber through viton rings. Furthermore, extra copper masses, amounting to about 40 lbs total, are added on top of the stainless steel circular breadboard to further increase the effective mass of the mirror mounting assembly. There is a custom machined aluminum breadboard that spans the distance between the cubes. On this breadboard is an aluminum Faraday cage. The outer dimensions of the Faraday cage are 4" tall by 3" wide, and about 18" long. Faceplates to this Faraday cage contain three apertures for the two light beams and the atomic beam. The back plate is machined to rigidly hold the metastable beam detector. Inside the Faraday cage are two concentric magnetic shields, which are centered on the 778 nm-atomic beam overlap volume. Every surface within the Faraday cage, including the magnetic shields and spacers, is coated with two graphite coatings: the base layer aerodag and the second layer aquadag.

It generally takes at least 2 days of pumping to reach pressure suitable to begin spectroscopy on the $2S_{1/2}$ - $8D_{5/2}$ line, with longer pumping preferable to further mitigate pressure effects. An ion-gauge attached to the 5-way cross provides an estimate of the pressure in the spectroscopic volume, but we believe that the pressure within the Faraday is generally much higher than in

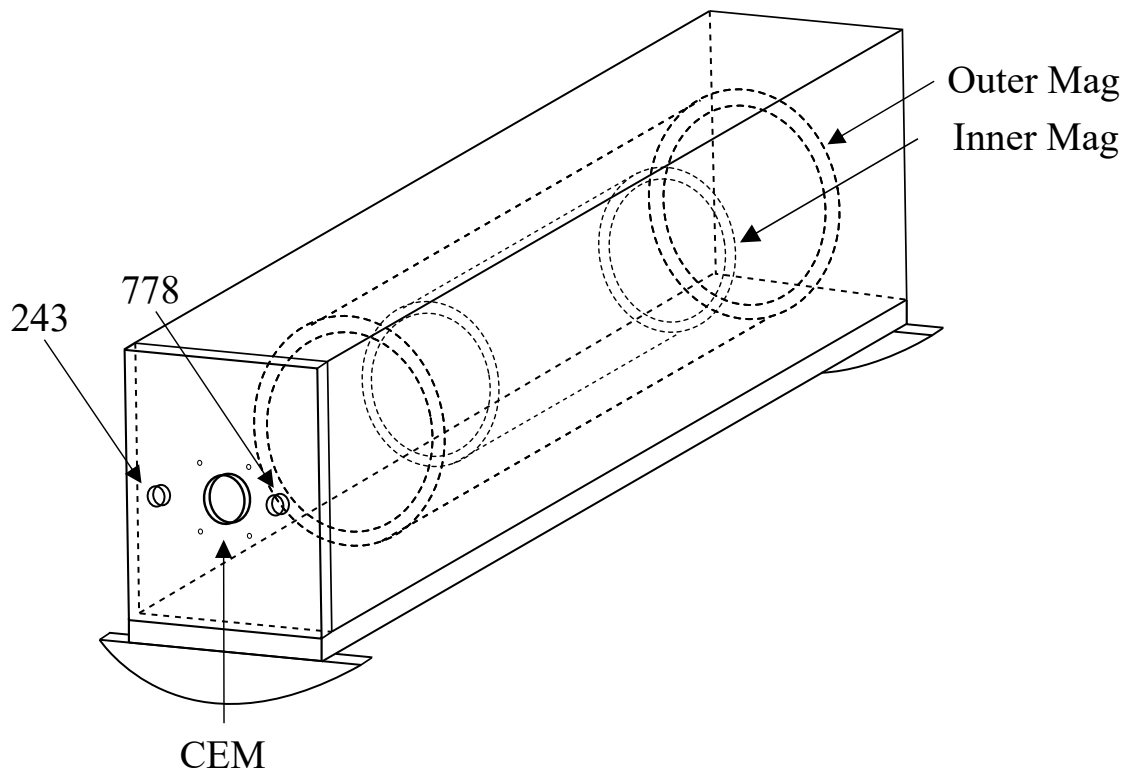


Figure 2.15: Faraday cage geometry and magnetic shields within. The Faraday cage is 16" x 3" x 4", and the magnetic shields are 8" and 3.5" long respectively. The magnetic shields are centered on the 778 nm-atomic beam overlap.

the surrounding volume. We have tried baking the vacuum chamber externally to try to improve the base pressure. Additionally, we have experimented with heating the breadboard holding the Faraday cage directly, reaching temperatures of about 130° C for the breadboard. It is currently believed that the graphite coatings inside of the Faraday cage. We can reach base pressure as low as 9×10^{-8} Torr as read by the ion gauge, but currently believe that we do not reach below 5×10^{-7} within the magnetic shields. The base pressure in the vacuum chamber proper appears to be limited by the conductance of the differential pumping manifolds.

2.4.4 The Metastable Detector

The lifetime of the 2S state is on the order of 1 second, though the lifetime of the metastable atoms can be drastically reduced in the presence of an additional electric field. While the 2S and

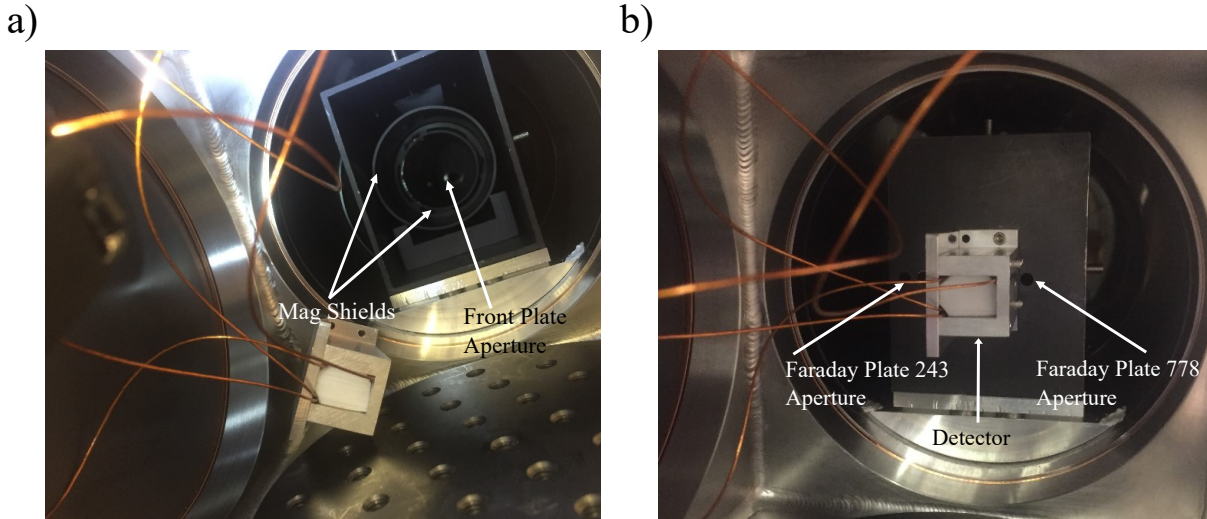


Figure 2.16: Image of Faraday Cage inside of vacuum chamber with no optics a) back plate off, showing magnetic shields b) back plate on, with metastable detector attached

2P states are not degenerate due to the Lamb shift, the 1 GHz splitting is not so large and external electric fields can easily shorten the lifetime of the 2S state. For instance, an electric field of 1 mV/cm modifies the lifetime of the 2S state to only $400 \mu\text{s}$. This is the basic principle by which we quench the remaining metastable atoms after interaction in the spectroscopic volume, and decay of the 2P leads to an emission of a Lyman- α photon. Detecting and counting these Lyman- α photons is the basis of our metastable detection.

Our detector is a Burle Magnum channel electron multiplier (Channeltron 5901, Magnum) used in pulse counting mode. In pulse counting mode, the output pulse number will be roughly constant over a large range of bias voltages, which we typically run between 2.5 kV and 2.8 kV. The output is capacitively coupled to a Mini-Circuits amplifier and the resultant ~ 100 mV pulses are counted by a Hewlett-Packard 53131A frequency counter in totalize mode. Besides amplification, the Mini-Circuits amplifier also has the rather important task of operating as a buffer between the CEM output and our more valuable electronics – more than one amplifier has been sacrificed. The wiring of the CEM is shown in Fig. 2.17.

As shown in Fig 2.17, the channeltron is biased in multiple locations to function properly. To make this detector a rigid assembly, we have opted to create a housing that holds the CEM,

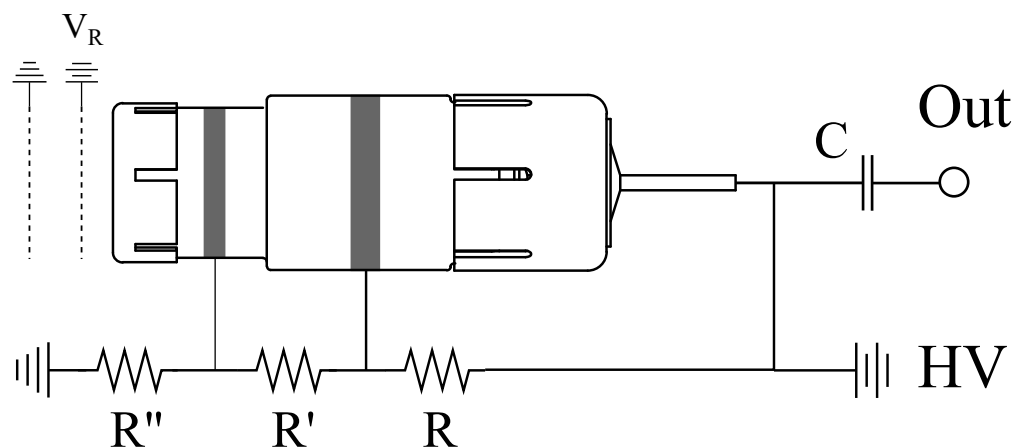


Figure 2.17: Biasing of CEM. Also shown, photoelectron rejection grid and ground as dashed lines. The resistors R, R', and R'' have resistances of 20 kOhm, 2 MOhm, and 18 MOhm respectively.

electrodes, and grids. On the Faraday cage back face plate, the CEM housing is rigidly attached, and the atomic beam is axial with the CEM. The mounting of the metastable detector housing is shown in Fig. 2.16 and the design of the CEM housing is shown in Fig. 2.18. This housing is composed of three components: a face plate, the housing proper, and a lid. A Teflon clamp rigidly holds the CEM in place and the electrodes are copper foil rings. The rejection grid attached to the face plate in front of the CEM face is held at -1.5V and plays the important role of rejecting a large fraction of photoelectrons from entering the detector which constitute our background signal; this results in an attenuation of ~ 1000 . These photoelectrons are generated from scattered 243 nm radiation, and the work function of graphite is apparently quite close to 4 eV [93], hence the relatively small required rejection voltage of 1.5 eV. We do not believe a substantial fraction metastable atoms are quenched due to the rejection grid, but it is possible that some fraction of 2S atoms decay between the rejection grid and the CEM face due to the 100 V potential difference between the CEM face and rejection grid. The grounded grid in front of the rejection grid serves the purpose of shielding the spectroscopic volume from the detector voltages. Both grids are gold-plated tungsten wire meshes (50 \times 50 per inch, .001" wire diameter). These grids have large open areas, but the ratio of the distance from the spectroscopic volume to the fundamental grid spacing is about a factor of 4000, so we do not expect substantial field leakage to the spectroscopy region.

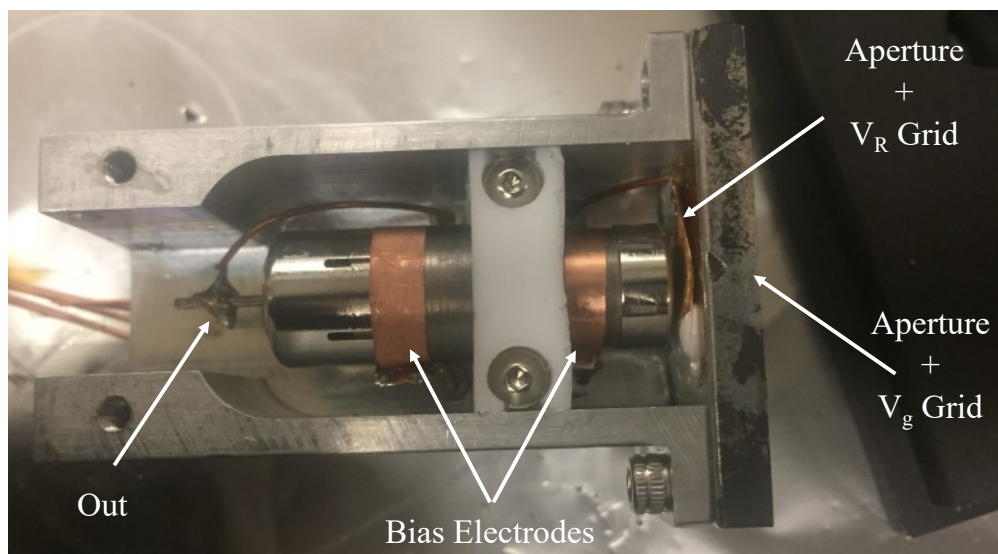


Figure 2.18: Housing of the metastable detector.

It is perhaps worthwhile to mention that the design of the metastable detector went through many iterations before we settled on a configuration that worked. Our original designs suffered from profoundly large background counts, up to 10^6 counts/s. The first designs were configured such that the detector was above a pair of quench electrodes. However, substantial scattered 243 nm radiation reached surfaces near the face of the detector, resulting in backgrounds that are too large as compared to the emission rate of the Lyman- α photons of interest. This is how we settled on a metastable detection configuration that relies on the collision of the metastable atoms directly into the face of the CEM. The pair of apertures (to which the grids are attached) on the face of housing greatly restrict the possible trajectories into the CEM, essentially only coaxial trajectories are permitted. These apertures are 1/4" in diameter, and are made of copper foil with the grids soldered directly on them.

2.5 Conclusion

The infrastructure for 2S-8D spectroscopy, excepting the frequency metrology system, has been described, which includes: the metastable excitation laser, the spectroscopy laser, the generation of the cryogenic beam of hydrogen, the detector, and their overlap within the spectroscopy vacuum

chamber. Both the metastable excitation laser and the spectroscopy laser require frequency stabilization and precise control to perform the spectroscopy as described. Additionally, the absolute frequency of the 778 nm laser must be determined. Both of these tasks require the use of our optical frequency metrology system, which includes the frequency comb, ultra-stable cavity, and GPS-trained Rb-timebase, which we will describe in the following chapter.

Chapter 3

The Frequency Comb and Stable-Laser System

3.1 Introduction

Since their inception, frequency combs have found a diverse array of applications in AMO experiments [51, 53–56, 58–60, 94, 94–101]. While we will not name all such applications, they have been used for high fidelity microwave generation [102], providing phase control in ultra-short pulses for attosecond physics [103], providing frequency bridges in atomic clocks [104, 105], and also directly as spectroscopy lasers [96, 106, 107]. In high precision applications, frequency combs often perform the critical function of being a frequency “flywheel”, turning the large hundreds of Terahertz optical frequencies of spectroscopic experiments and atomic clocks into the relatively small MHz to GHz radio frequencies. These radio frequencies, in turn, can be directly measured, and counted, by the well-engineered RF electronics that were developed in the previous century, allowing for extraordinarily high levels of experimental precision. (e.g., up to 10^{-18} in atomic clock comparisons). In this work, while the frequency comb plays the role of the frequency “flywheel”, it also serves another important function as well: it is the stable local oscillator our other laser systems are trained to, and thus provides frequency stability to the other laser systems in our experiment. Before discussing our frequency comb system in particular, we will review the basics of frequency comb theory.

The frequency comb is a laser whose output is a series of evenly-spaced, Dirac-Delta-like teeth in frequency space. Generally, such an output is generated from phase-stabilized mode-locked laser oscillators – though comb structures can be generated by other methods as well (e.g. microresonators [108, 109]). In the time domain, the output of a mode-locked laser consists of periodic pulses with a fixed phase relationship between subsequent pulses. A carrier frequency with a periodic envelope function may be ascribed to this pulse train. In general, the carrier phase

velocity and the group velocity of the pulse are different, and the phase of the carrier underneath the envelope evolves in time.

We can make a few arguments to defend the appearance of a comb spectrum in frequency space from a pulse train. Since the pulse train is a periodic function in time, we can use a Fourier Series expansion to describe our spectrum. Fourier series use discrete frequency components, so the resultant transform must be composed of a series of delta functions in frequency space. As frequency and time are inversely related, the smallest separation in frequency space corresponds to the largest temporal separation, which is the pulse to pulse separation, τ_s . The minimum spacing between two frequency components is $1/\tau_s$. From the convolution theorem, we know that the Fourier transform of the envelope function, $A(t)$, determines the relative distribution of power of these discrete frequency components. Stated simply, the frequency spectrum, $\tilde{E}(\omega)$, generated by a pulse train will have the form,

$$E(\omega) = \sum_n \delta(\omega - n/\tau_s) \tilde{A}(\omega), \quad (3.1)$$

which is indeed a series of equally spaced comb “teeth”.

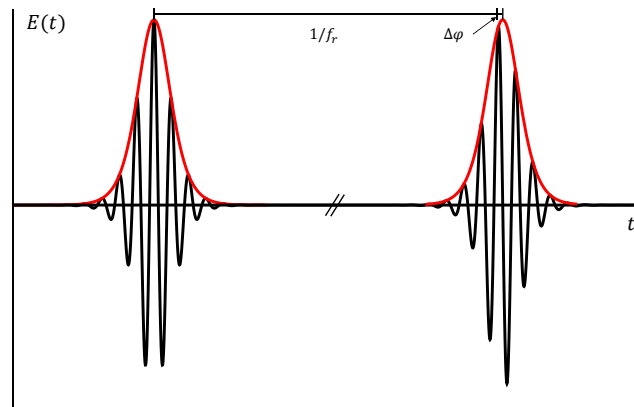


Figure 3.1: Simple picture demonstrating phase evolution of carrier frequency between pulses

Here we present a slightly more rigorous derivation. Given a pulse train, we may describe the electric field of at a particular point in space by

$$E(t) = \sum_n A(t - n\tau_s) e^{i\omega_c t} e^{in(\Delta\phi - \omega_c \tau_s)}, \quad (3.2)$$

where τ_s is the pulse to pulse time separation, ω_c is the carrier frequency, and $\Delta\phi$ is the pulse/envelope carrier pulse to pulse phase shift, see Fig. 3.1. Taking a Fourier transform of this we find,

$$\tilde{E}(\omega) = \sum_n \tilde{A}(\omega - \omega_c) e^{i(n\Delta\phi - n\omega\tau_s)}. \quad (3.3)$$

Regardless of the exact nature of \tilde{A} , this sum is significant when the terms in the above series add coherently, that is, when $\omega\tau_s = \Delta\phi + 2\pi k$. Thus,

$$\omega_k = (\Delta\phi + 2\pi k)/\tau_s, \quad (3.4)$$

or, in its most well known form

$$f_k = kf_r + f_0, \quad (3.5)$$

where f_k corresponds to the frequency of the k^{th} comb tooth, f_r is the repetition rate, and f_0 is the carrier offset. From our derivation, it follows that f_r is given by $1/\tau_s$ and that f_0 arises due to the evolving phase shift between the envelope and the carrier frequency. It should be noted that there is some subtlety in the choice of k and f_0 . One could choose that f_0 is either optical frequency (where $k=0$ corresponds to the first comb tooth that contains optical power), or that $k=0$ corresponds to the extrapolated comb structure to zero frequency. Generally, the second convention is taken. It should be noted that, in most cases, optical power will be in the $k \approx 10^6$ range. Generally, f_r is on the order of 100 MHz, though >GHz repetition rate combs do exist [110, 111], and $f_0 \leq f_r$ by definition.

The simplicity of Eq. 3.5 is significant. Experimental determination of only two radio frequencies allows one to characterize the entire optical spectrum of the comb. Many applications of the

frequency comb become apparent when examining Eq. 3.5. For instance, since each comb tooth is precisely known, the comb itself can be used as a broadband, high precision, spectroscopy laser. In addition, the comb can be used to precisely determine the frequency of another laser or emission spectra by comparison to the frequency comb – such as in the astro-comb application [110]. Perhaps most importantly, the comb structure provides a link between the optical domain (where all of the comb teeth actually lie) and the RF domain (f_r and f_0).

This link between the RF and the optical allows absolute frequencies to be determined in optical frequency measurements, as absolute frequency measurements requires comparison to the cesium time standard [60, 94], an RF frequency. Historically, absolute frequency measurement required long frequency chains; complicated sets of lasers and RF oscillators that are compared to different standards [61, 63]. Such chains involved many processes to generate appropriate bridges between standards such as mixing to produce sum and difference components, frequency doubling, etc. These experimental setups were very cumbersome, often requiring entire labs dedicated to just these frequency referencing schemes. In contrast, the frequency comb itself provides RF frequencies to compare to time standards.

The frequency comb's function of linking disparate ranges of the electromagnetic spectrum extends beyond the linking of the optical and the RF. Indeed, owing to the frequency combs generally broad spectral output, which can be extended even further by e.g., second harmonic generation, etc., it can also provide a bridge from disparate frequency regimes of the optical spectrum as well [112, 113]. Concretely, any set of lasers whose output is within frequency range of the frequency comb's output can be compared by reference through the frequency comb. This is particularly desirable when multiple highly coherent laser systems are required. It is possible to transfer the stability of a highly coherent oscillator to a less coherent oscillator by phase-locking techniques [114, 115]. The requirement for this coherence transfer is that the oscillators to be phase locked must be directly comparable, that is, spectrally close. The frequency comb once again provides a bridge that can close this gap. Therefore, a single highly coherent laser source, in conjunction with a frequency comb, can be used to stabilize other laser systems where such per-

formance is desired. The only caveat is that the frequency comb itself must be low-noise enough to not disrupt this coherence transfer.

Measuring and stabilizing the the two free comb parameters, f_r and f_0 , is required for most applications of the frequency comb, including coherence transfer and absolute frequency metrology. The measurement of f_r is quite straightforward – one merely has to provide a portion of the comb’s output to a sufficiently fast photodetector. Detection of f_0 is somewhat more involved. Historically, the frequency comb breakthrough occurred when the first mode-locked oscillator with a phase-stabilized f_0 beat note was reported. Detection of f_0 usually requires a technique called self-referencing, in which one part of the frequency comb is heterodyned with itself. The most common technique is the “ f -to- $2f$ ”, though there are other self-referencing techniques that use different combinations of generated harmonics to similar effect [50, 116, 117].

The f -to- $2f$ self-referencing technique works in the following way. Assume that we have at least an octave of spectral bandwidth output from the frequency comb. Then, on the red side of the frequency comb spectrum we have the m^{th} comb tooth given by

$$f_m = m f_r + f_0. \quad (3.6)$$

At the same time, since we have an octave of bandwidth, on the blue side of the frequency comb, we have the $2m^{\text{th}}$ comb tooth given by

$$f_{2m} = 2m f_r + f_0. \quad (3.7)$$

If we frequency double the m^{th} tooth and heterodyne it with the $2m^{\text{th}}$, we find

$$2f_m - f_{2m} = 2m f_r + 2f_0 - (2m f_r + f_0) = f_0. \quad (3.8)$$

While the f -to- $2f$ self-referencing technique is the most common method to detect f_0 in mode-locked laser based frequency combs, it does come with its own set of experimental challenges. Namely, the generation of sufficient optical bandwidth to perform this technique.

As stated previously, many optical frequency combs are generated by a phase stabilized mode-locked laser oscillator, e.g. [118, 119]. The gain bandwidth employed in such oscillators must be sufficiently broad to support < 1 ps pulses. There are two gain mediums that are commonly employed for this purpose: Ti:Sapphire crystals, and erbium-doped fibers. While the historical development of the frequency comb from passively mode-locked lasers is intimately linked to passively mode-locked Ti:Sapphire oscillators, in the past decade fiber-based passively mode-locked lasers have become common. This is in large part due to their reduced cost, alignment-free operation, and reduced sensitivity to their environment. In particular, Er-doped fiber based lasers are particularly attractive [100, 101, 120, 121], as they operate in the 1.3-1.5 μm range, where there is a large selection of fiber optic components to support the telecom industry. A downside of Er-fiber based frequency combs is that the gain bandwidth of Er-fiber does not support an octave of bandwidth, which can be directly produced from a Ti:Sapphire oscillator [122]. Due to this, mode-locked er-fiber oscillators require substantial subsequent amplification and non-linear spectral broadening methods to generate sufficient bandwidth for f -to- $2f$ interferometry.

In the 2S-8D measurement, we require both a 778 nm spectroscopy laser and a 243 nm laser in which the absolute frequency of both laser systems is well known and stabilized. We therefore require a frequency comb with sufficiently low noise to stabilize these two laser systems. Additionally, the comb itself must be referenced to an absolute frequency standard. In the following sections, we will discuss the development of such an erbium-fiber based frequency comb to perform this vital role in our experiment.

3.2 Mode-locked laser oscillators

The design of mode-locked laser oscillators is a rich field of study, and there are many distinct methods to achieve mode-locking [123]. Mode-locking occurs when high intensity pulses expe-

rience larger round-trip cavity gain, or less round-trip loss, than continuous-wave laser radiation (cw) [124]. Broadly, there are two ways to achieve this pulse-favoring behavior – actively, where the cavity/loss gain is intentionally modulated, or passively, where the cavity dynamics naturally favor pulsed operation via a nonlinearity. As an example of active mode-locking, one can modulate an intracavity Pockels cell at the cavity repetition rate to create very high loss except for a short window of time. However, modern optical frequency comb designs are typically based on passively mode-locked laser oscillators. This is in part due to the fact that passively mode-locked lasers typically generate shorter pulses, and therefore larger spectral bandwidths, than their active counterparts. The minimum pulse duration possible in a given oscillator design is in part set by the modulator (active) or nonlinear (passive) response time.

A simple method of self-starting passive mode-locking is through the use of semiconductor-based saturable absorbers (SA) [125–128]. A saturable absorber is a medium in which the absorption is reduced at large optical intensities. These SA's can be used in transmission or in reflection (called a saturable absorbing mirror, SAM). Once saturated, these semiconductor-based saturable absorbers have a relaxation time before the absorption returns to its unsaturated value (typically in the range of 1-10 ps). These SAM's can be particularly simple to use, sometimes only requiring the replacement of an intracavity mirror with the SAM. One might expect that the pulse duration to be comparable to the relaxation time of the SA, that is, typically a couple of picoseconds. However, the use of these saturable absorbers can actually lead to pulse durations substantially shorter than their relaxation time [129].

The qualitative explanation for this is that the saturable absorber preferentially absorbs the leading edge of the pulse [127]. Therefore, the pulse is effectively delayed – the leading edge is attenuated, shifting the center of mass of the pulse backwards in time. This delay is important for preventing the growing power of the continuum behind the pulse, which could experience gain due to the saturable absorbers slow recovery time. Since the pulse is delayed, but the continuum behind the pulse is not, the pulse slowly assimilates power from the continuum. Another way to visualize this is that the pulse and the light behind the pulse effectively experience different

repetition rates, but the saturable absorber loss modulation is matched with the timing of the pulse. Because of this, the continuum experiences more loss over many round trips than the pulse. There are other stabilizing effects possible in the cavity dynamics of a mode-locked laser. One that is particularly important for generating sub-picosecond pulses is the presence of solitonic pulse shaping [126, 127, 130].

A soliton is a wave-packet whose envelope is stationary in time. Typically, a pulse will spread out in time due to linear effects such as dispersion. However, if nonlinear effects reach a certain magnitude, the effects of dispersion can be balanced by nonlinear effects, such as self-phase modulation, to produce a pulse that is stable in time [78]. The stability of solitons is quite interesting. For example, perturbations to the pulse energy do not necessarily destabilize the soliton, as the pulse can shed excess energy once the balance between linear and nonlinear effects are disrupted [126, 127]. For a soliton pulse to be supported, the pulse must experience self-phase modulation and dispersion. Self-phase modulation (SPM) is a nonlinear effect in which the index of refraction is intensity dependent. Suppose that the index of refraction, n , has the form

$$n(\omega) = n_0(\omega) + n_2 I, \quad (3.9)$$

where n_0 is the familiar linear, frequency-dependent index of refraction, n_2 is the nonlinear index, and I is the intensity of the light. This intensity dependent index of refraction is due to the Kerr effect. Suppose we have a pulse of light in such a nonlinear medium. Then, fluctuations in intensities couple to phase changes via the nonlinear index. The instantaneous frequency of the light after propagation through a nonlinear medium of length L is then

$$\omega(t) = \omega_0 - \frac{2\pi L}{\lambda_0} \frac{\partial n}{\partial t}, \quad (3.10)$$

where ω_0 and λ_0 is the angular frequency and wavelength of the light in vacuum. Assuming a Gaussian pulse, we find

$$\omega(t) = \omega_0 - \frac{4\pi I_0 n_2 L}{\lambda_0 \tau^2} e^{-t^2/\tau^2} t, \quad (3.11)$$

where τ is the pulse width, I_0 is the maximum intensity, and n_2 the nonlinear index. Near the vicinity of the peak intensity, where this effect is most pronounced, it is linear, and thus SPM produces an approximately linear frequency chirp (it has the form $\omega(t) = a + bt$). Since both self-phase modulation and dispersion apply chirps to the pulse, approximately linear in both cases, properly signed dispersion can cancel the effect of SPM. Since n_2 is typically positive, anomalous dispersion is required for the cancellation.

Once soliton mode-locking is initiated, the saturable absorber parameters do not need to be finely tuned, as the solitonic shaping effects do a lot of the heavy lifting. The function of the saturable absorber is simply to prevent the energy shed by the soliton from building up in the cavity, which would be destabilizing to the mode-locking [126, 127]. The stability offered by this soliton plus saturable absorber combination is very desirable for robust mode-locking.

An important consideration, aside from easily achievable and robust mode-locking, is the noise performance of mode-locked laser oscillators [52, 131–134]. Since the mode-locked laser forms the basis of the frequency comb structure, the noise characteristics of this comb structure are intimately linked with the oscillator. There are several sources of technical noise on any laser system. For instance, vibrations on the mirrors in the cavity will introduce phase noise on the light. While we are interested in minimizing these sources of technical noise, there is also noise that is intrinsic the function of the laser itself – so called "quantum noise". This noise is typically due to amplified spontaneous emission (ASE) [135]. Spontaneous emission manifests itself as both intensity noise on the pulse and as phase noise on the pulse.

The contribution of amplified spontaneous emission to intensity noise is relatively clear, the spontaneous emission, being random, adds noise to the intensity profile of the pulse. The direct contribution to phase noise is via timing jitter – the spontaneous emission distorts the intensity profile sufficiently to shift the center of the pulse producing variation in the pulse-to-pulse timing. This direct contribution of quantum fluctuations to timing jitter scales with the square of the pulse duration [130, 132, 135]. This is a relatively straightforward result since it is easier to define the center of a short pulse. Spontaneous emission also indirectly couples to timing jitter via intra-

cavity dispersion, an effect referred to as Gordon-Haus jitter [136]. For intrinsically low noise performance oscillators, a short pulse and low intracavity dispersion is required.

3.3 Frequency comb oscillator I

The design of our first frequency comb oscillator used the principles outlined above as guidelines. Since fiber based combs are an economically viable option, and semiconductor saturable absorbers are typically allow for easy mode-locking, we decided to base our oscillator design on this architecture. Since soliton shaping effects make the mode-locking more robust, and ultimately allow for the shortest pulse generation, we also knew that the intracavity fiber must be anomalously dispersive. The other design consideration was to minimize the total length of fiber inside of the oscillator. At the time, this was to reduce certain nonlinear effects related to noise performances, namely amplitude-to-phase noise conversion and Gordon-Haus jitter.

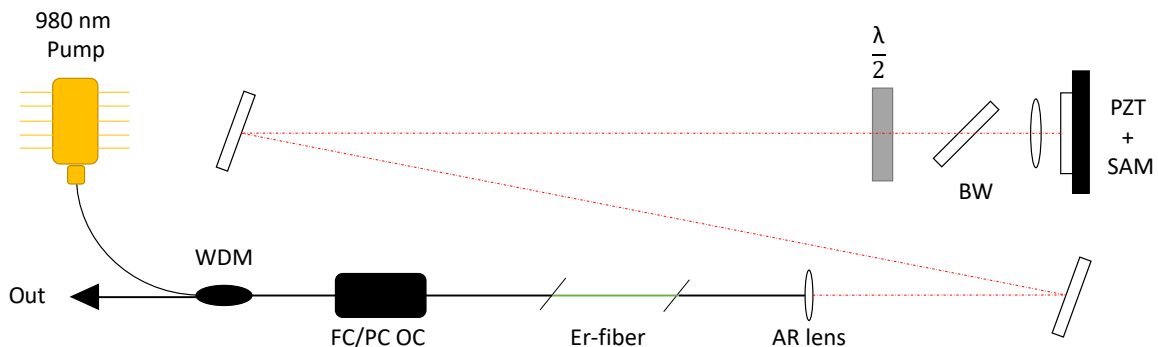


Figure 3.2: Linear cavity mode-locked oscillator

Our first oscillator to be fully realized as a frequency comb, detailed in [4], was a linear cavity, saturable absorber mode-locked laser (see Fig. 3.2). The saturable absorber was a BATOP, 2 ps lifetime, 15% modulation depth, 10% non-saturable loss, saturable absorbing mirror. The cavity featured all anomalously dispersive fiber (Corning SMF-28), with a round trip cavity dispersion of $\approx -7000 \text{ fs}^2$ to promote soliton mode-locking. The erbium-doped gain fiber (nLight ER80) was pumped by about 500 mW of 980 nm (Gooch and Housego AC1409-0700-0976) light through

a custom coated 80% reflective FC/PC connector. We found that the the half-wave plate and Brewster window were critical for stabilizing the polarization of the intracavity pulse. Without the polarization control, there was strong periodic amplitude modulation on the pulse train at some fraction of the repetition rate. The laser oscillator output was about 10 mW with 16 nm of spectral bandwidth, which corresponds to 160 fs transform limited pulses, assuming a sech^2 distribution.

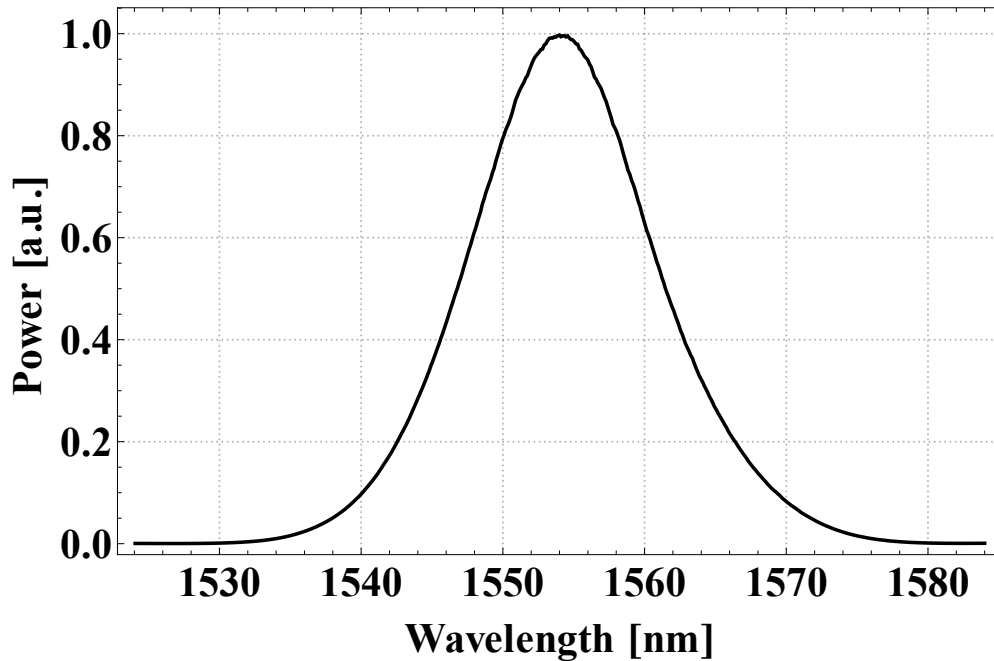


Figure 3.3: Linear oscillator spectral output. Spectral output ~ 15 nm

In the development of this frequency comb, some non-obvious design requirements started to appear. For instance, linear cavities are somewhat sensitive to etalon effects and parasitic back reflections. Back reflections are especially troublesome when establishing stable mode-locking. This required careful alignment of optics and the use of AR-coated lenses. As stated previously, broader spectral output is preferable (an a indicator of shorter pulse duration). Typically, one can achieve shorter pulse duration by reducing the intracavity dispersion. In the case of erbium-doped fiber, and optical fibers in general, dispersion can be tailored by adjusting the core-cladding ratio. Therefore, normal dispersion Er-fiber is easily obtained. We attempted this strategy to further broaden the spectral output of the oscillator, but instead found narrower spectral output (8-10 nm).

This was an unexpected result, and stems from the fact the a soliton is only truly a stable wave packet in anomalously dispersive media. In general, the laser cavity is not a purely anomalously dispersive media, there are sections of free space propagation. The soliton period, which is the distance a soliton propagates where nonlinear phase shifts become substantial, provide the length scale for the soliton behavior. The soliton period can be written as

$$z_s = \frac{\pi\tau}{2\gamma E_p}, \quad (3.12)$$

where τ is the pulse duration, γ is the self-phase modulation coefficient (rad/(W*m)), and E_p is the pulse energy [137]. From this, We see that shorter, higher energy pulses have much shorter periods. If the period of the perturbation is much less than the soliton period, the soliton behavior can be well described by the average parameters (e.g. dispersion) during its evolution and the disturbances are smoothed over. In our case, the presence of alternating dispersion signs was on the order of the soliton period, and to compensate, we believe the dynamics of the laser system favored longer pulses to lengthen the soliton period. Therefore, in an effort to minimize the dispersion in the cavity, and still maintain stable soliton mode-locking, we instead used very short sections of fiber in the cavity, eventually achieving the 16 nm output shown in Fig. 3.3. We also found that coupling the pump light into the cavity through the output coupler can disrupt the pump diode. The original output coupler was a stock 50/50 coated fiber tip near 1550 nm, and a fraction of pump light incident upon the OC was reflected back into the pump diode, destabilizing its operation. Therefore, we used a custom coated OC with high transmission at 980 nm. However, we eventually found a fiber isolator in between the pump and cavity output coupler was required for optimal performance.

Soon after the development of this laser oscillator, and the required generation of f_0 that followed, a new technique to mode-lock erbium-fiber lasers was reported [138, 139]. This new technique seemed to produce short pulses, up to 40 nm of spectral bandwidth, and correspondingly had very good noise characteristics [138, 139]. This led to the development of our second design for a Er-fiber mode-locked oscillator.

3.4 Frequency comb oscillator II

As stated previously, the minimum pulse duration achievable in a mode-locked oscillator is linked to the nonlinear response time of the cavity. If shorter optical pulses are desired, then utilizing a faster nonlinear technique is typically beneficial. In the case of semiconductor saturable absorbers, the relaxation time of the saturable absorber effectively limits on the minimum achievable pulse durations possible, even if that pulse duration is much shorter than the relaxation time. For instance, in Kerr-lens mode-locked systems, pulse durations on the order of 5 fs are possible, as the nonlinearity responds almost instantly to the circulating fields in the oscillator [140]. In the case of the Er-fiber lasers, leveraging the Kerr effect can also be utilized to initiate mode-locking.

An early application of directly utilizing the Kerr effect to initiate mode-locking was the “figure-eight” cavity [141], see Fig. 3.4. The right handed loop in Fig. 3.4 is referred to as a nonlinear loop mirror. The loop is asymmetric for light split at the 50/50 beamsplitter; one direction is amplified first and travels through a length of fiber and the other travels through fiber first and then is amplified. This asymmetry causes a relative phase shift, through the nonlinear index of the fiber, between light light traversing in opposite directions. This relative phase shift determines the fraction of light that exits that particular port of the beamsplitter. This arrangement can be set such that if the light is in phase when recombined, it is incident upon the exit port of the optical isolator in the left hand loop, causing high loss factor. When the light is π out of phase, the light is sent entirely through the other port of the beamsplitter, so the isolator does not attenuate the power. Therefore, for increasing phase shifts, up to π , the loss in the cavity is reduced. Since, the nonlinear index causes increasingly large phase shifts as a function of intensity, pulse formation is favored.

This design of the figure-eight laser has a few technical issues. First, in order to generate sufficiently large phase shifts in the right hand arm, long lengths of fiber are required, which results in low repetition rate mode-locked lasers. Second, such oscillators proved to be somewhat difficult to optimize, as such oscillators do not function in cw-operation. This led to the development of nonreciprocal phase shifters, an intracavity device that allows for tuning of the relative phase of

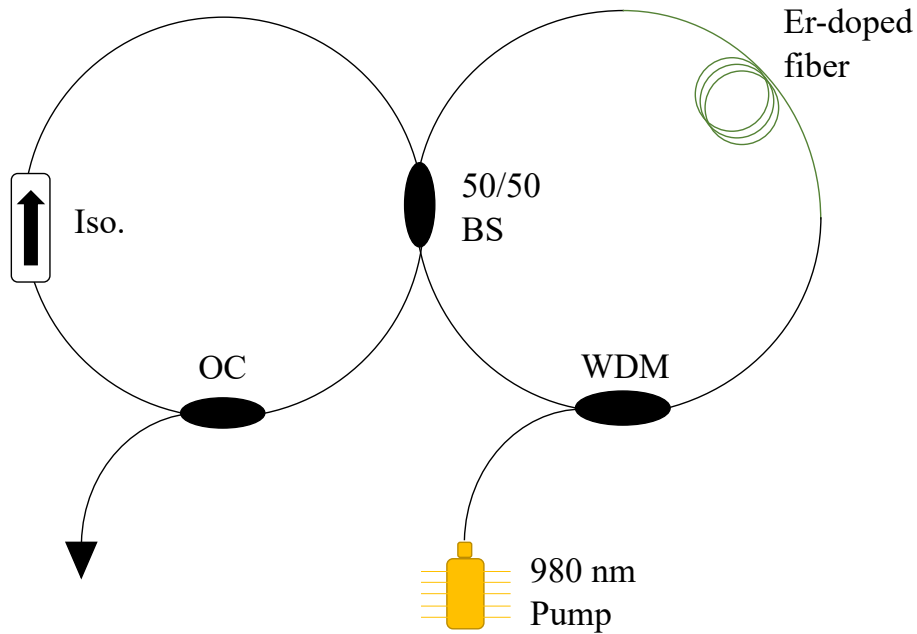


Figure 3.4: Example of figure-8 style oscillator. WDM: Wavelength-division multiplexer. OC: Output coupler. Iso.: Optical isolator. BS: Beamsplitter

the pulses directly [142]. In short, one can set the relative phase between the counter propagating light to be anywhere between 0 and π radians, allowing for preferred cw or pulsed operation. Additionally, fiber lengths do not need to be as long to achieve the low-loss π phase shift in pulsed operation. In general this allows for tuning of the pulse energy (and duration). Lastly, such oscillators have proven difficult to accommodate all polarization maintaining (PM) fiber designs which are less susceptible to environmental perturbations (though there has been a demonstration of PM figure-8 style oscillator [143]).

The figure-8 design was eventually usurped by the development of a slightly modified design [138, 139], with Menlo Systems trademarking their architecture as the “figure-9”. The pertinent change is the removal of the “left loop” in Fig. 3.4 with a linear arm and the incorporation of a nonreciprocal phase bias [142]. These figure-9 style oscillators have been shown to be self-starting, and accommodate all PM-fiber designs, unlike their figure-8 counterparts. Additionally, the spectral output of these designs have been shown to greatly exceed semiconductor saturable

absorber mode-locked oscillators (>40 nm of spectral bandwidth at 1550 nm [138]), indicating the potential for superior phase noise performance, see [125, 134].

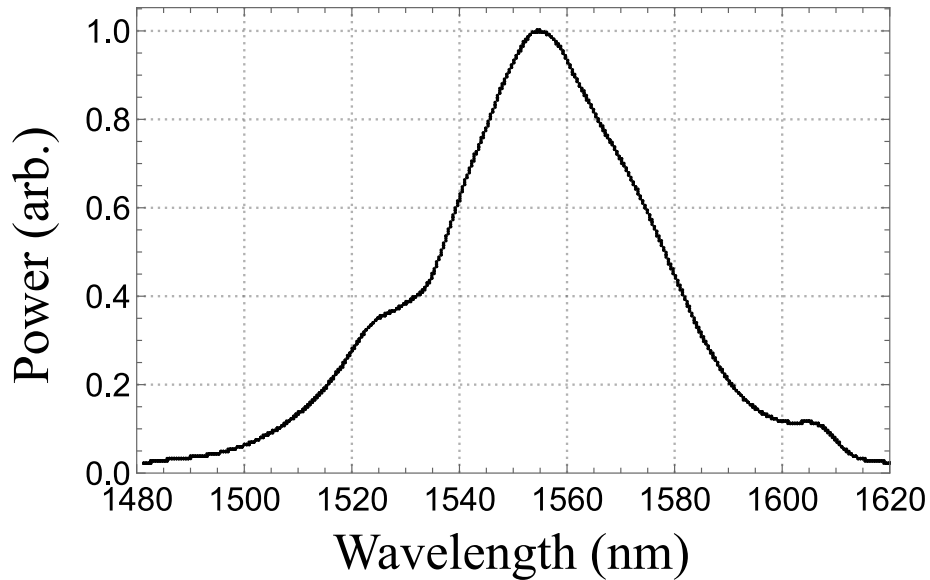


Figure 3.5: Example of second oscillator design spectral output. Typical width at half-maximum ~ 40 nm

Our second, and current, frequency comb oscillator is based upon this figure-9 configuration (see Fig. 3.6). Our particular design is not PM-fiber in the nonlinear amplifying loop, and requires waveplates to properly guide the counter propagating beams into the linear arm. The nonlinear amplifying loop itself is composed of all anomalously dispersive fiber, 40 cm of which is Er-doped gain fiber (nLight Er80). The oscillator is pumped with about 300 mW of 980 nm power (Gooch and Housego AC1409-0700-0976) and outputs about 10 mW through a 90/10 beamsplitter fiber optic. As shown in Fig. 3.5 the spectral bandwidth is about 40 nm when operating optimally. The repetition rate is about 137.5 MHz, and is grossly adjustable via a translation stage underneath a optic mount in the nonlinear loop; it is finely adjusted by tuning the temperature of the plate the fiber loop rests upon. In the linear arm we have our nonreciprocal phase bias which is composed of a 45° Faraday rotator, a half and quarter zero-order wave plate, and a polarizing beamsplitter (PBS 2 in Fig. 3.6). Finally, a semiconductor saturable absorbing mirror (SAM) mounted to a

is traveling in either direction of the loop. For further simplicity, let us ignore the half-wave. Then, light that exits the loop into the linear arm is polarized at 45° . This 45° polarized light transmits through the Faraday rotator, becoming vertically or horizontally polarized. The linearly polarized light transmits through the quarter waveplate to become circularly polarized and is then incident upon PBS 2. Since we have circularly polarized light, the loss at PBS 2 is 50%. Now instead let us assume there is a $\pi/2$ phase shift between light traveling in one direction of the loop relative to the other. Then, instead of circularly polarized light incident at PBS 2, it will be either horizontally or vertically polarized depending on the orientation of the quarter wave plate. Therefore, by correct orientation of the quarter waveplate, you can achieve very low loss at PBS 2. In this case, you have made it so increasing nonlinear phase shifts, between zero and $\pi/2$ radians, provide lower loss in the cavity, promoting mode-locking. The half waveplate primarily adjusts the splitting ratio between the two directions in the loop, reducing or increasing the relative phase shift between the two directions.

3.4.1 Amplification, Supercontinuum generation, and f_0 detection

In order to generate sufficient spectrum for the f_0 detection and locking, as well as spectrum for phase locking to the 972 nm and 778 nm lasers, amplification stages and nonlinear broadening mechanisms must be employed on the mode-locked oscillator output. While broadening occurs within the amplification stages, largely through the effect of self-phase modulation [144], this broadening typically can only reach ≈ 100 nm of optical bandwidth at 1550 nm. In order to reach the required octave of bandwidth for f_0 generation, which corresponds to $1 \mu\text{m}$ of optical bandwidth, other additional nonlinearities must be utilized. This typically involves the presence of a specific kind of optical fiber, known as highly nonlinear fiber (HNLF) [145]. For other laser systems, such as Ti:Sapphire based comb systems, a photonic crystal fiber is used instead [146]. Finally, after the required bandwidth is generated, a Michelson-style interferometer with a frequency doubling arm is used to detect the f_0 beat note. Within the amplifiers, broadening stages, and f_0 interferometer, there are several taps to provide comb-light for other subsystems.

Fig. 3.7 depicts the amplification stages, continuum generation, and other fiber optic components necessary for the operation of the frequency comb. Immediately after the output of the oscillator, there are two fiber-coupled optical isolators, providing 60 dB of isolation from back-reflections which can destabilize the operation of the oscillator. Then 50% of the light is tapped off for amplification, while the remaining 50% is used for the intensity noise servo and f_b note locking, which are described in a later section. After the first stage of amplification, 1% of light is tapped off and amplified for a frequency doubling stage for generation of 780 nm light, and the other 99% is amplified once more before being sent to the HNLF and f_0 interferometer. All fiber that is not directly labeled is SMF-28 (a standard fiber for telecom applications).

The amplification stages are composed of one bidirectionally pumped 2 m section and another 1 m forward pumped section. The 2 m bidirectionally pumped erbium-doped fiber amplifier (EDFA) is composed half of normally dispersive ER110 and anomalously dispersive ER80. The second amplification stage is again normally dispersive. These alternating dispersion sections have been found to assist in generating the largest possible supercontinua in the HNLF. By alternating the dispersion of fiber in the EDFAs, the chirp of the pulses is controlled, allowing for larger possible nonlinearities in the HNLF. It is worth mentioning that while solitons are supported in anomalous dispersion regimes, a fundamental soliton is in general not supported for arbitrary pulse energies, and so the net dispersion of the optical path must be considered.

After the second stage of amplification, the polarization of the pulses are controlled via a two-paddle polarization controller. Since SMF-28 is not polarization maintaining, strain induced on fiber can rotate the polarization of the light with the fiber. Strain on non-PM fiber induces birefringence, causing the polarization to rotate. By adjusting the relative bend and angle in these paddle controllers you approximate the action of a waveplate, and can control the resulting polarization state of the light. This paddle is composed of 2 loops of fiber in the first paddle, and 3 in the second loop. The approximate total length of SMF-28 fiber between the last stage of amplification and HNLF is 75 cm. This length of fiber must be carefully chosen for continuum generation. The output spectrum after the HNLF ranges from about 950-2150 nm. Note that the upper wavelength

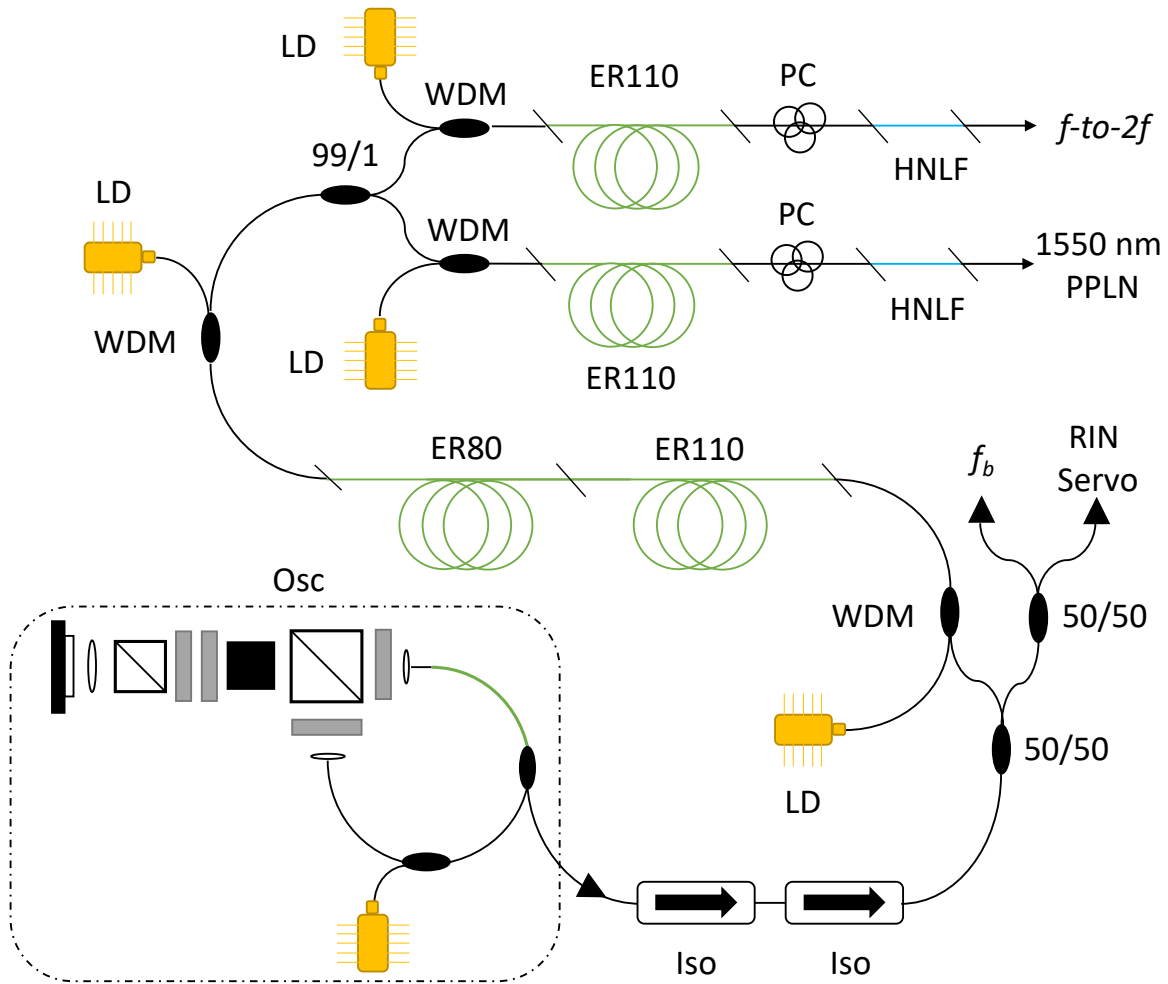


Figure 3.7: Comb Amplification and Supercontinuum generation. Iso: Isolator. LD: Pump laser diode. 50/50: Beamsplitter. PC: Fiber polarization controller. HNLF: Highly nonlinear fiber.

limit is estimated by the achievable SHG from the f -to- $2f$ interferometer, as our optical spectrum analyzer does not reach past 1800 nm.

The highly nonlinear fiber is a 25 cm section of -5.6 ps/nm/km fiber from OFS. This HNLF polarization maintaining, requiring appropriate input polarization state for proper continuum generation, as the two core axes have differing birefringence. We have also tested a HNLF with dispersion -2.3 ps/nm/km, but we have found that this fiber did not generate large enough spectra for f_0 detection. These HNLF fibers are flourine doped, and feature a large nonlinear coefficient with small dispersion coefficients to minimize chirp through the HNLF (to contrast, the dispersion

of regular SMF-28 fiber is about 18 ps/nm/km). The dominant mechanisms by which the continuum is generated in the first part of the HNLF is through self-phase modulation and four-wave mixing, both $\chi^{(3)}$ processes. Later, the pulse train breaks into several pulses in a process known as soliton fission [147], and these solitons themselves undergo several nonlinear processes. These processes include the previously mentioned four-wave mixing and SPM [78, 146], but also include Raman-scattering effects, self-frequency shifting, and the coupling of dispersive wave light with the solitons generated in the soliton fission process [148].

After the supercontinuum is generated by the HNLF, the f_0 beat note is generated and detected via the f -to- $2f$ technique. The layout of the f -to- $2f$ interferometer is schematically depicted in Fig. 3.8. The output of the HNLF is collimated and split into two arms via a dichroic mirror. The long wavelengths are transmitted through the dichroic mirror to the frequency doubling arm of the interferometer and the shorter wavelengths are reflected. The two arms are recombined at a 50/50 beamsplitter, and coupled into a 980-PM fiber to ensure good spatial overlap. Since the light is a pulse train, it is also crucial that the frequency doubled pulse train and the fundamental pulse train must be temporally overlapped as well. With this aim, the fundamental pulse train contains a delay arm (two 45° mirror mounted on a translation stage). The delay arm is adjusted to maximize the signal-to-noise on the f_0 beat note. If the pulse trains are not well temporally overlapped, there will be no f_0 beat note. Just before the fiber coupling for the f_0 beat note, there is a long pass optical filter set at a slight angle to reflect light below $1 \mu\text{m}$. This light below $1 \mu\text{m}$ is composed only of the fundamental light, and is used for phase-locking the 976 nm laser system to the comb.

The frequency doubling arm in the interferometer contains a periodically poled lithium niobate crystal (PPLN). Periodically poled crystals are frequently used for nonlinear conversion pulsed laser systems due to their enhanced acceptance bandwidth and the large optical intensities do not necessarily require resonant enhancement to achieve appreciable second-harmonic power. Proper fundamental light polarization is required to have maximize conversion efficiency, and the resultant doubled light is of the same polarization state as the pump.

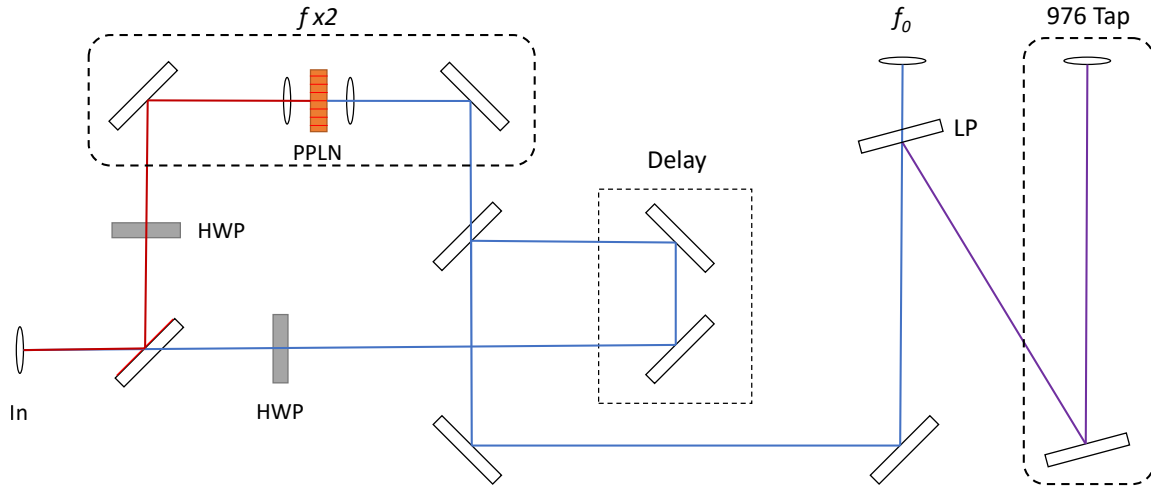


Figure 3.8: f -to- $2f$ Interferometer

The quasi-phase matched frequency is set by the poling period of the PPLN; that is, the distance between the poled regions of the nonlinear media. Additionally, there is some acceptance bandwidth for quasi-phase matching. This bandwidth is inversely proportional to the crystal length, as dispersion effects becomes more important for longer crystal lengths. Typical PPLN crystals are manufactured with several poling periods transversely arranged across the crystal length, so gross tuning of the phase-matching is achievable with a single crystal. Fine tuning of crystals can be achieved with temperature adjustment, as thermal expansion changes the poling period. Our PPLN for f_0 generation (Covesion MSHG2100-0.5-xx) contains poling periods for frequency doubling fundamental light from 1925-2250 nm light. The crystal temperature is set by actuating current to a resistive heater (Thorlabs HT15W) inside of the crystal mount, and the whole assembly is on a translation stage to tune between poling periods. The frequency doubled 3 db bandwidth is about 15 nm broad, and centered at 1010 nm.

3.4.2 Phase-locking and RIN Servo

As mentioned, in order for the frequency comb to function as an absolute frequency reference and as a flywheel for coherence transfer, the two comb parameters, f_r and f_0 must be detected and

stabilized. In this section we will describe the stabilization of these comb parameters, as well as the phase-locks between the frequency comb and the other laser systems.

While it seems natural to detect and lock f_r directly, which only requires a fraction of the comb's output on a photodiode, this approach has technical downsides [149]. The first downside is that f_r is a RF frequency, and any frequency noise on this frequency, whether due to electronic noise or to instability in the RF reference f_r is locked to, is written back onto the actual optical frequencies of the comb by a factor of k^2 , where k is the comb tooth index number as described in Eq. 3.5 [150]. This k^2 dependence arises from an f^2 dependence between phase and frequency noise. As of now, the only oscillators that have sufficient stability for our application are in the optical domain. Second, both comb parameters must be locked simultaneously, and the feedback on f_r and f_0 should be as uncoupled as possible. Examination of Eq. 3.5 shows that by adjusting one parameter of the comb will invariably affect the other [151]. Let β be an arbitrary parameter of the comb, such as the cavity length or pulse energy. Then variation of β yields

$$\delta f_k = \frac{\partial f_0}{\partial \beta} + k \frac{\partial f_r}{\partial \beta}. \quad (3.13)$$

Given that any lock requires measuring and stabilizing a particular f_k , we desire that the lock meant to stabilize f_0 primarily feeds back on f_0 and the lock meant to stabilize f_r does not influence f_0 much. By stabilizing a comb tooth in the optical domain, that is $k \approx 10^6$, instead of f_r directly, $k = 1$, the sensitivity to variations in f_r is improved by about a factor of a million. Therefore, it is typical that stabilization of f_r is often achieved instead by the stabilization of a beat note between the frequency comb and a highly coherent optical reference, which we will label f_b for convenience. This highly coherent optical reference allows for the coherence transfer described previously.

The creation of the highly coherent optical reference at 1555 nm, which we will call the stable laser, is detailed in Chapter 3.6.5. A portion of the frequency comb oscillator output is tapped for generating f_b between the comb and the stable laser, as shown in Fig. 3.7. This comb-tap and some portion of the stable laser output are overlapped in a fiber optic 50/50 splitter, and f_b is detected on

a fiber-coupled photodiode. The photodiode output is then amplified and band-pass filtered at 19-23 MHz, and the resultant signal is mixed with a 20 MHz signal from a quartz-oscillator stabilized direct-digital synthesizer (DDS). The difference frequency component is then used to generate an error signal, and this error signal is amplified in a loop filter and feeds back onto two intracavity PZT's inside of the frequency comb oscillator. The f_0 beat note is actuated by tuning the oscillator pump diode current, which in turn varies the circulating pulse's energy. This energy modulation varies the f_0 beat frequency by way of varying the total phase shifts the pulse experiences in one round trip of the cavity (see Eq. 3.4). Similar to f_b , the detected f_0 beat frequency is detected by a photodiode, amplified, band-pass filtered (27-33 MHz), mixed with a DDS signal to generate an error signal, loop filtered, and sent to the oscillator pump diode to actuate its output power.

While perhaps not immediately obvious, the performance of the f_0 beat phase lock is often the limiting factor in a given frequency comb's coherence. While both f_b (or f_r) and f_0 experience technical and other noise originating in the oscillator, extra noise is written onto f_0 beat note due to amplification and spectral generation, with the proliferation of noise in the supercontinuum generation being particularly problematic [152]. Nonlinear processes change the relative distribution of power in the coherent signal to the power in the noise of that signal, with more power being distributed from the coherent signal to noise. In addition, not only is there a strong presence of $\chi^{(3)}$ effects in the supercontinuum generation, generation of the f_0 beat frequency requires another $\chi^{(2)}$ process (second harmonic generation). With that in mind, it is advantageous to take steps to minimize the intrinsic phase noise originating in the oscillator.

A prominent source of phase noise, especially in fiber laser systems, is the conversion of amplitude noise to phase noise via the Kerr effect (Eq. 3.9) [153]. The nonlinear index of a medium, which is substantially larger in fiber than in air, couples fluctuations in intensity to fluctuation in the index of refraction, and therefore, the round trip phase shifts a pulse will experience. The origin of this amplitude-to-phase noise is the subject of some of the work we and a group at JILA have completed [4, 154]. We found that while some amplitude-to-phase noise has origins in relative intensity noise (RIN) from the pump diode (technical noise) [150], there are other sources of noise.

Some of these sources include amplified spontaneous emission (ASE), fluctuations in cavity loss, vacuum field fluctuations, and gain medium dipole fluctuations. All of these other noise sources have quantum mechanical origins, and cannot be removed by only reducing the RIN of the oscillator pump diode. Because of this, the strategy for best reducing the amplitude-to-phase noise is directly measuring and reducing the intensity noise of the frequency comb as opposed to just reducing the intensity noise due to the oscillator pump diode [4].

As indicated in Fig. 3.7, a portion of the oscillator output is used for the RIN servo, which functions to detect and reduce the amplitude noise of the comb. By actuating the pump diode current in such a way to cancel the oscillator intensity noise, the intensity noise can be reduced. A schematic depiction of the RIN servo and the resulting reduction in intensity noise is shown in Fig. 3.9. Inspection of Fig. 3.9 part b) indicates that the feedback bandwidth of this servo is on the order of 550 kHz. This is not a trivial feat, as the feedback bandwidth is in some part limited by the oscillator cavity dynamics. When the amplitude response transfer function for the comb oscillator was measured, we found that it largely acted as a single pole low pass filter, with its corner at ≈ 100 kHz. In order to achieve a stable feedback system (i.e., one that does not oscillate), careful tuning of the RIN servo transfer function was necessary. In particular, the servo acts dominantly as a proportional-derivative controller (more accurately a PD^2 as there are two differentiation corners) to ensure good phase at unity gain, stabilizing the loop against problematic oscillation. The amplitude noise added by the servo bump at around 650 kHz is largely inconsequential compared to the overall reduction in noise, especially given that the correlation between amplitude and phase noise has an extra factor of f^{-2} [135].

Since both the f_0 phase lock loop and the RIN servo loop both feedback onto the oscillator pump diode, these two signals are summed just prior to feedback on the pump diode. Because both systems feedback on the same degree of freedom, consideration of the net transfer function is necessary. While the RIN servo has a relatively large feedback bandwidth of 550 kHz, the frequency lock alone (consisting of the f_0 detector, error signal generation, and loop gain electronics) has a smaller feedback bandwidth of about 50 kHz. There is a limit to the maximal potential feedback

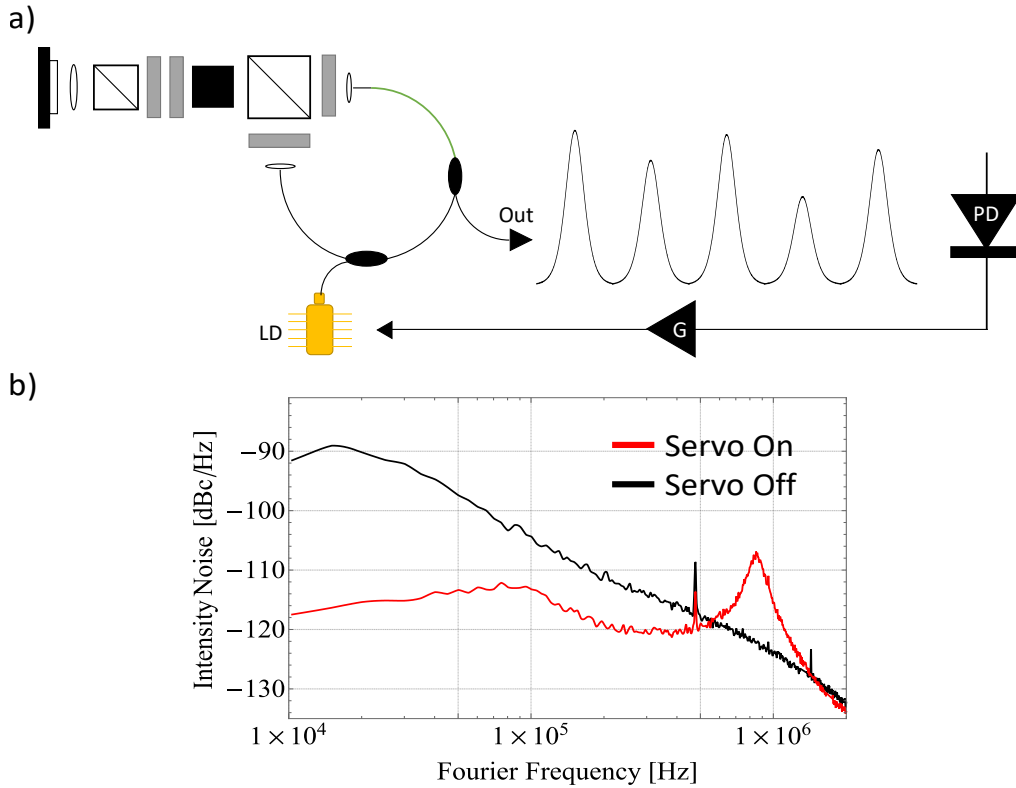


Figure 3.9: a) Schematic of RIN servo b) In-loop Relative Intensity noise power spectral density

bandwidth of the frequency locking loop, and reaching feedback bandwidths much beyond 50 kHz using the frequency lock alone is challenging. Good phase at unity gain is a requirement for stable negative feedback loops. This means that while single pole roll off (a phase of 90°) is acceptable, higher order roll off leads to unstable feedback loops (180° phase). In the case of the frequency lock, there are two poles intrinsic to the feedback loop: the 100 kHz low pass corner due to the cavity dynamics, and an overall integration factor. This intrinsic integration factor arises because the loop detects a frequency, but feeds back on a phase – the two naturally being related to each other via an integral or derivative respectively. However, the RIN servo does not contain this intrinsic integration factor, so ideally there is only a single pole roll off at fast feedback frequencies. The RIN servo’s improved phase at unity gain can then be leveraged to stabilize the frequency lock feedback loop, since the two are actuating the same degree of freedom.

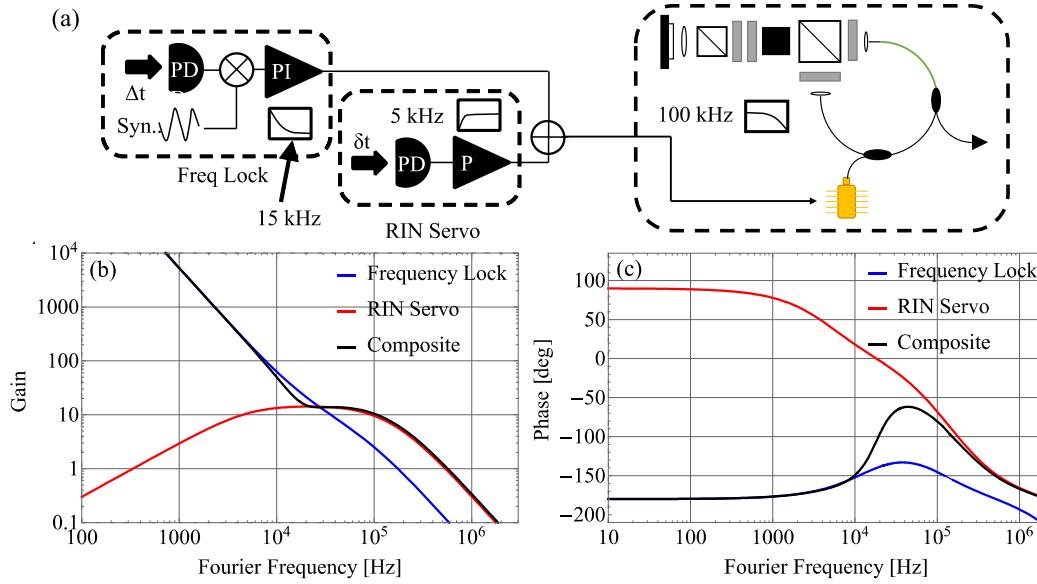


Figure 3.10: [Reprinted] with permission from [4] © The Optical Society. a) Composite lock schematic. b) Amplitude response transfer functions c) Phase response transfer functions

To illustrate this point a bit more concretely, we constructed a simple toy model. For simplicity, we will consider the frequency lock loop to be a PI loop (with an extra integration factor discussed above) and the RIN servo to be a proportional loop (with an active high-pass corner at 5 kHz). These two functions are summed, and a 100 kHz corner low-pass due to the oscillator dynamics is applied. Estimated line delays are also added to the RIN servo and frequency lock functions as well. This is schematically depicted in Fig. 3.10 with the resulting amplitude and phase responses. We can see that the composite lock has the large potential gain of the frequency lock loop at low feedback frequencies and the phase at unity gain is determined by the RIN servo. What this allows is an overall increase of the frequency lock gain without disrupting the phase at unity gain of the composite system. By increasing the overall gain of the frequency lock, we achieve an overall reduction in the phase noise, as demonstrated in [4]. A requirement for this composite locking technique is the high correlation of the amplitude fluctuations and phase fluctuations, which is met in erbium fiber mode-locked oscillators. If applied in conjunction with fast frequency actuators, such as loss modulation as demonstrated in [119], we believe this technique could further increase the feedback bandwidth of these locks as the intrinsic line delays required for f_0 detection

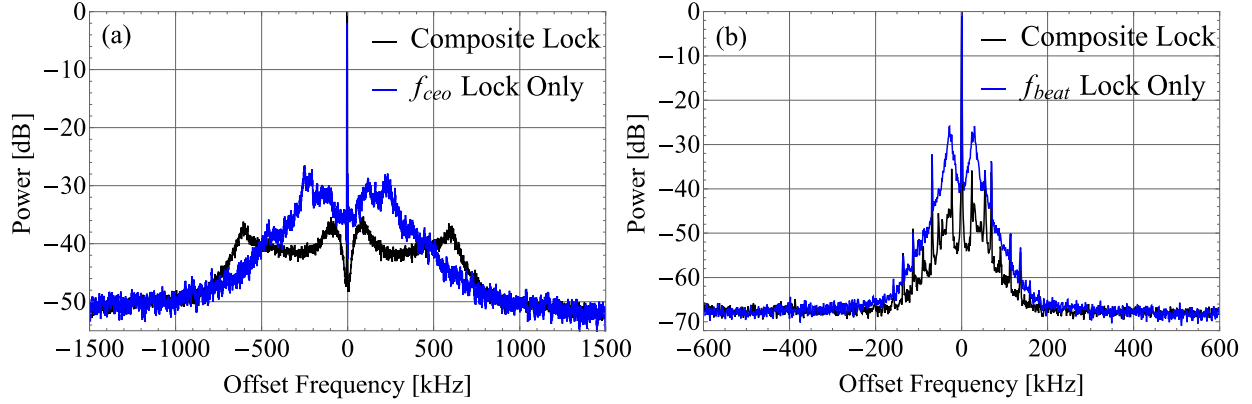


Figure 3.11: [Reprinted] with permission from [4] © The Optical Society. Linear oscillator beatnotes with composite lock on vs only frequency lock. a) f_0 beatnote with the composite lock on (black) vs off (blue). b) f_b beatnote with the composite lock on (black) vs off (blue). Note that the composite lock reduces noise across the comb spectrum, indicated by the reduction in phase noise on f_0 and f_b which are in disparate parts of the comb spectrum.

are greater than intensity noise detection since f_0 detection requires amplification, supercontinuum generation, and an interferometer while intensity noise detection does not. Additionally, the utilization of this composite locking scheme does not remove the fact that we are still reducing intensity noise, improving the phase noise performance of the entire comb structure. The results of utilizing this composite locking scheme as opposed to just using a frequency lock is shown in Fig. 3.11. Since the phase noise on both relevant beat notes is reduced, our claim that the phase noise across the entire comb structure is well-supported.

While we originally formulated this composite locking technique on the frequency comb feedback with the linear cavity mode-locked oscillator, we have also applied this technique to the figure-9 style oscillator, with similar results. However, as mentioned previously, intrinsic phase noise due to timing jitter is proportional to the pulse duration squared of the circulating intracavity pulse. While we do not have an autocorrelator to directly characterize the pulse, we expect the pulse duration is still roughly inversely proportional to the pulse duration and the figure-9 style oscillator can generate pulses with 40 nm of spectral bandwidth as opposed to the 16 nm spectral bandwidth of the linear cavity oscillators. A comparison of the locked f_0 is listed in Fig. 3.12, with

corresponding integrated phase noise of 127 mrad and 270 mrad for the figure-9 and linear cavity oscillators respectively.

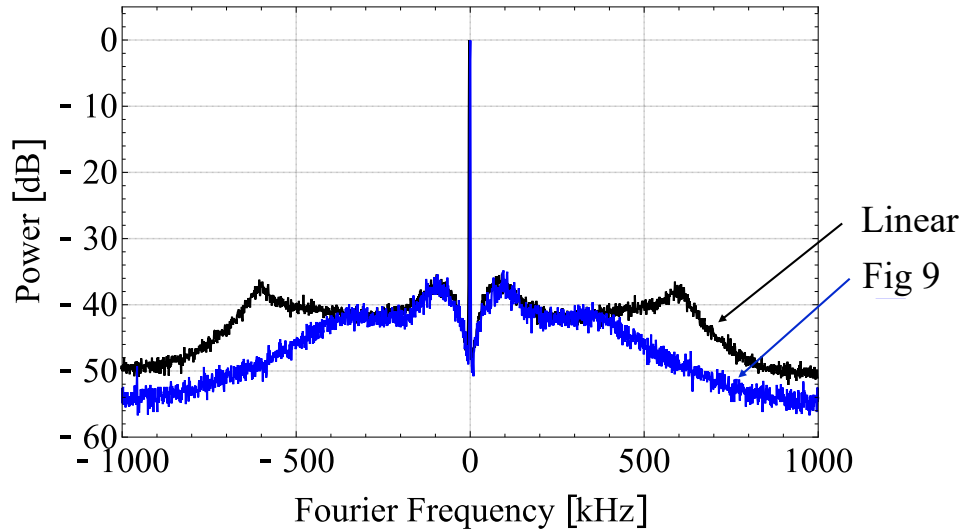


Figure 3.12: Linear vs figure-9 cavity f_0 locks. The reduction in fast frequency noise is expected due to quantum timing jitter's relation to the intracavity pulse duration.

3.4.3 Comb Spectra for comparison to Ti:Sapphire spectroscopy laser

Unlike for the 976 nm light for referencing the comb to the 976 nm ECDL, the comb does not generate sufficient spectrum out of the HNLF to reference to the Ti:Sapphire laser at the relevant wavelengths. Fortunately, given that the 2S-8D/S and 2S-12D/S transitions are in the 750-780 nm range, generating these wavelengths only requires one stage of second harmonic generation with on fundamental light of 1500-1560 nm, which is quite close to the oscillator output. As indicated in Fig 3.7, a 1% tap before the second stage of amplification extracts some light for this second harmonic generation stage.

In order to have sufficient intensity for the 750-780 nm light generation, the power from the 1% tap has its own amplification stage. We have found that in order to have sufficient power at 1500 nm, we also require a short section of HNLF (about 8 cm), after this amplification stage for spectral broadening. Similar to the supercontinuum generation for the f -to- $2f$ interferometer,

careful control of the polarization state before the HNLFF is necessary for proper spectral broadening. Additionally, depending on whether the 2S-8D transition or the 2S-12D transition is being probed, the amount of amplification before the HNLFF is different for optimal power in the doubled light. Since 780 nm is within the oscillator output spectrum, less spectral broadening is necessary and therefore less amplification. Conversely, when probing the 2S-12D line, there must be much more amplification in order to move sufficient power to the 1500 nm band in the HNLFF. Small adjustments to the pre-HNLFF polarization states must also be adjusted to maximize power in either band.

The frequency doubling crystal for 750-780 nm generation is also a PPLN, albeit with different poling periods than that for 1 μm generation (MSHG17.40 μm +/-0.5-3). This PPLN is also mounted to an aluminum piece that is heat controlled by a resistive heater for fine tuning of the poling period, all of which mounted to a translation stage for transverse adjustment. Fig. 3.13 depicts this doubling stage. A half wave plate before the PPLN ensures correct polarization for efficient doubling efficiency, and a pair of lenses for focusing into the PPLN and recollimating the doubled light are used. The frequency doubled light is coupled into a 630-PM optical fiber (Thorlabs P3-630PM) and sent to the Ti:Sapphire laser system. Typically we generate about 1.5 mW of 780 nm light total and 600 μW of 750 nm light. The coupling efficiency to the 630-PM fiber is about 70%, and the light should be visible to naked eye at the output of the PM fiber.

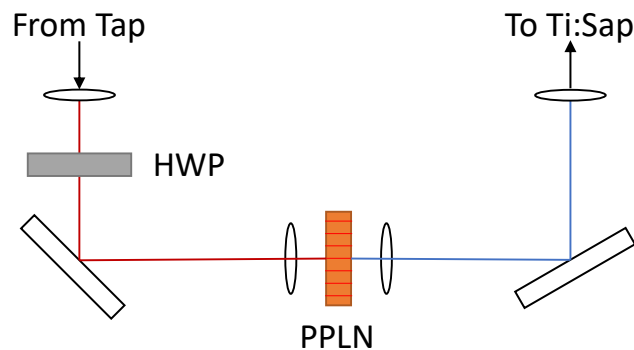


Figure 3.13: 750-780 nm Doubling Stage. The PPLN is on translation stage and heated mount for adjustment of the doubled spectra. Some adjustment of the HWP is necessary when switching between 778 nm and 750 nm comparison

3.5 Operation of the frequency comb

As of the time of this writing, the current, non-PM figure-9 styled oscillator requires occasional realignment and re-initialization of mode-locking due to the rather large temperature drifts that our laboratory experiences as the seasons change. Additionally, the wax adhering the PZT+SAM to the copper mount occasionally needs to be reset, as the adhesive can fail over long time scales. To aid in future users of this oscillator, and the frequency comb system as a whole, this section will include a tutorial operating the frequency comb on a day-to-day basis and for mode-locking the oscillator.

3.5.1 Day-to-day operation

Operating the comb for most day-to-day applications is relatively straightforward, and requires only a few steps for the comb to be operational. Most of the operations on the frequency comb are to achieve one of few goals: detect and lock f_0 , lock the comb to the ultra-stable cavity, set the repetition rate, and generate spectrum for locking the 972 nm and 778 nm laser systems. In most of these cases, the comb can be made operational without opening the box to the frequency comb; most can be achieved just through the electronics controlling the comb system.

The comb-oscillator is kept running all the time, but the rest of the comb system is not. The laser diode driver for the oscillator pump diode is a Thorlabs LDC220C with a current limit set at 1350 mA. At the time of writing, the oscillator pump diode is typically run in the 500-600 mA range. There is an acceptable range of about 100 mA in which the oscillator will remain mode-locked without cw-breakthrough; going above will result in cw-breakthrough and below will result in cessation of mode-locking. Typically, running the comb closer to the cw-breakthrough threshold is safer than running low, and the performance is also improved. The first order of business is to generate an f_0 beat note, which requires turning the fiber amplifier on. There are three pump diodes associated with the fiber amplifier for f_0 detection. The approximate settings for good operation are .5-.6 A on LDD1, 1.1 A (max) on LDD2, and .9 A on LDD3 as labeled in Fig 3.14 a). Typically,

the rightmost laser diode driver current is tuned to around .9 A until the best signal-to-noise ratio of the f_0 beat note is achieved (typically around 30 dB at 1 MHz resolution bandwidth).

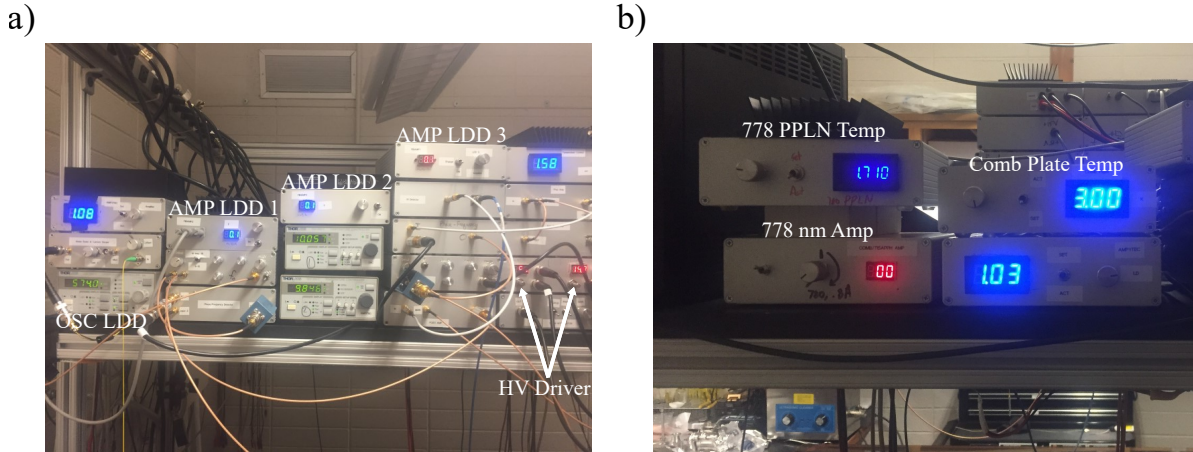


Figure 3.14: a) Primary frequency comb electronics, including oscillator and main amplifying laser diode drivers and RIN servo. b) Comb temperature controls and electronics for Ti:Sapphire comparison. LDD: Laser diode driver. HV Driver: High-voltage driver for the intracavity PZT's. The laser diode temperature controllers are not labeled, and do not require adjustment for operation. Adjustment of the comb plate temperature is required most days.

Once a ~ 30 dB SNR f_0 beatnote is generated, we need to set f_0 close to 30 MHz. The f_0 beat frequency can be tuned with the oscillator driver current. For a positive beat note, an increase in current should correspond to an increase in f_0 frequency (the beat note should move right on the RFSA). If, as one turns up the oscillator pump current, extra features on the f_0 begin to appear, for instance extra beat frequencies, this means that cw-breakthrough is beginning to occur and f_0 cannot be locked. If further tuning of f_0 is required, adjustment of the comb-plate temperature in the oscillator can shift the f_0 beat frequency as well. The display is in hundreds of Kelvin, 3.00 means 300K, and a tuning range of 297-303 is reasonable; a temperature change of 1 K is sufficient to move f_0 about 30 MHz.

The other most common operation is the setting of the oscillator repetition rate. The oscillator contains two intracavity PZTs to actuate the cavity length. Fine adjustment of the repetition rate can be achieved by changing the high voltage driver DC offsets, with about 700 Hz change in repetition rate being comfortable. It should be noted that the comb-stable laser phase lock actuates

the PZT attached to the SA in the linear arm, which corresponds to channel 1 (left channel) on the high voltage driver. This PZT has a safe voltage range of about 75 V, which displays up to about 22.5 on the HV driver (Corresponding to 75 V on the PZT). The other HV driver channel is connected to a PZT on a translation stage used for the coarse repetition rate adjustment, the small green object as shown in Fig. 3.16. This PZT can safely be operated 0-150 V, the full range of the HV driver, and is currently not active in the comb-stable laser feedback loop. The best practice is to do most of the fine tuning of the repetition rate with changing the DC offset in channel 2 of the HV driver. As in the case of the f_0 beat frequency setting, it is possible a much larger change of the repetition rate is required than what the PZT's can offer. In that case, coarse adjustment of the cavity length can be achieved by tuning a translation stage in the oscillator. The translation stage is attached to one of the mirror mounts holding a GRIN lens in the loop. Reaching the translation stage requires grabbing underneath of the heated aluminum plate. 10 kHz tuning of the repetition rate is easily achieved with this coarse tuning knob. It is advised to practice caution when using this knob, since some fibers are nearby.

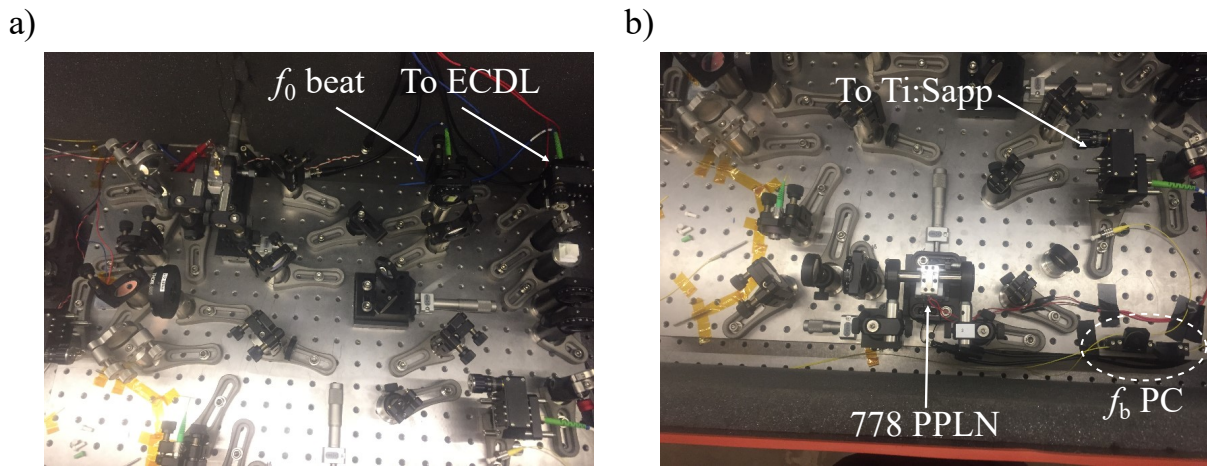


Figure 3.15: a) f -to- $2f$ interferometer setup. b) Doubling stage for comparison to the spectroscopy laser.

Generating the spectra for the comb-ECDL beat note is achieved when the f_0 beat note reaches 30 dB signal-to-noise ratio. Power below 1 μ m is picked off from the f_0 interferometer and coupled

into a PM-fiber, which is sent to the 972 nm laser system. Occasional realignment of this fiber coupling is necessary. For the 778 nm or 750 nm beat note with the Ti:Sapphire, a tap off of the main frequency comb amplification stage is sent to a separate amplification and HNLf section, as shown in Fig 3.7. This smaller amplifier+spectral generation stage is sent to a small frequency doubling stage. This frequency doubling stage is composed of a heated PPLN on a translation stage to change the poling period. The poling period of this PPLN can be finely tuned by adjusting the temperature of the PPLN mount. Unfortunately, temperature readings are in kOhms, it is a Thorlabs platinum temperature sensor, but a "temperature" of ~ 1.7 for 780 and ~ 1.5 for 750 is about right. If the LDD for the smaller amplifier section is set to 1 A, it will work for either wavelength. When switching between doubling for 750 nm and 780 nm, it is likely that a few tweaks to the amplifier subsection must be made. First, the poling period must be changed. In addition, the waveplate in the doubling arm will probably need to be adjusted, and the polarization state of the light going into the smaller HNLf section will likely need light adjustment using the polarization paddle controllers. It is likely that one will need to monitor the spectral output of the PPLN while making these changes. Unattaching the fiber for the Ti:Sapphire-comb beat note on the other side of the lab and plugging it into the OSA on that side is most convenient; a long USB cable connecting to the comb laptop is sufficient.

3.5.2 Mode-locking the oscillator

If the mode-locking of the oscillator has broken, there are certain steps to restart the mode-locking. First, if the amplifier pump diodes are running, turn them off. When the comb first breaks mode-locking, it typically operates in a pseudo q-switched regime. This q-switching can be damaging to the fiber optics, so turning off unnecessary fiber amplifiers is a precaution to protect against potential damage. If the oscillator was recently mode-locking, and there is no reason to believe that the oscillator has been strongly misaligned/etc since the mode-locking has broken, there is a straightforward procedure to restart the mode-locking, which I will outline below.

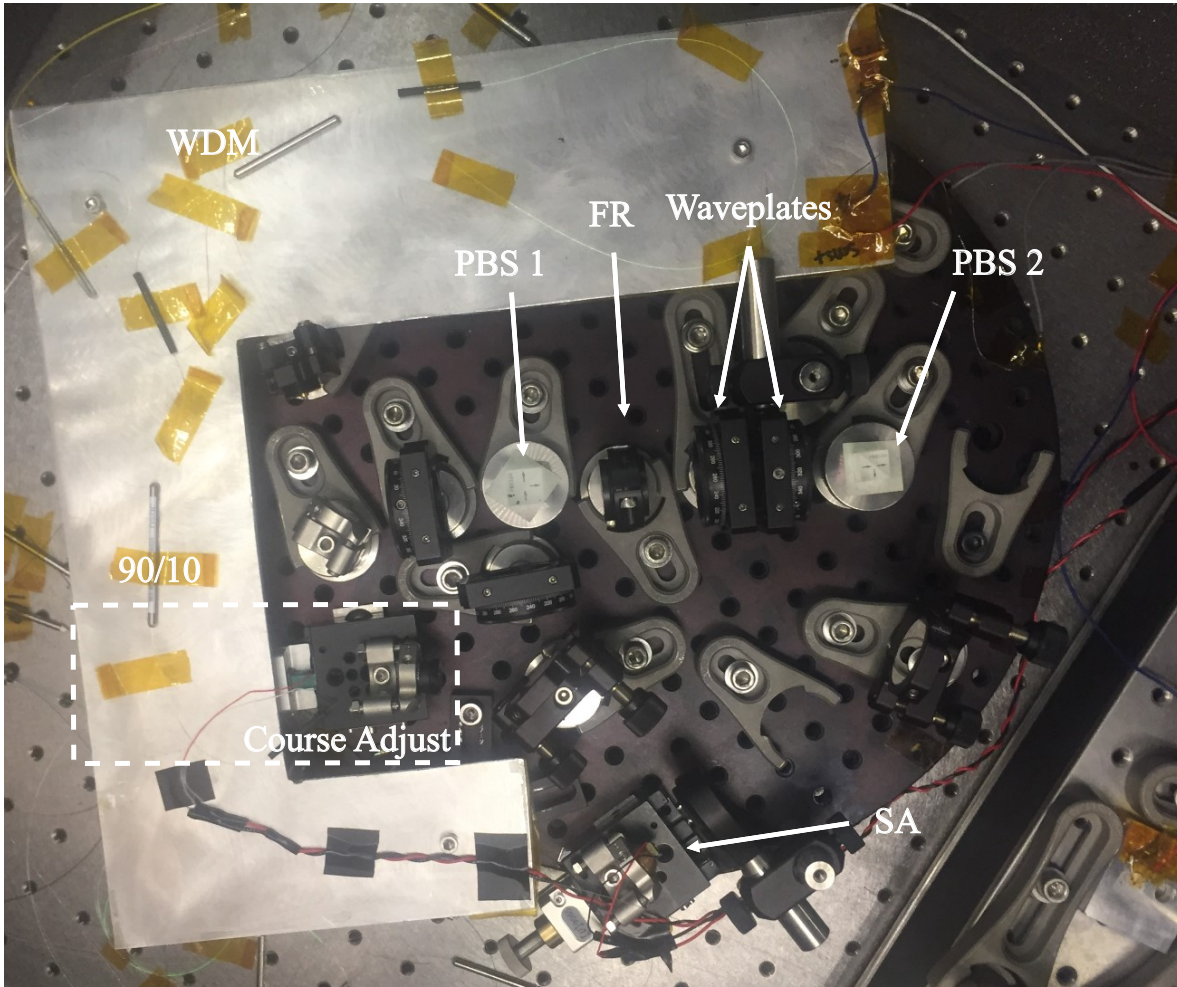


Figure 3.16: Top down view of the frequency comb oscillator. Coarse adjustment knob underneath aluminum plate. Refer to Fig. 3.6 for a schematic depiction of the cavity

It is very helpful if the OSA is employed during the mode-locking procedure. The tap used for the stable-laser comb beat note is readily available to use for this purpose, just disconnect the 1555 coupling to the fiber optic beamsplitter. Additionally, the tap used for the RIN servo may be used to monitor the oscillator output power. It is suggested that the RIN servo is not engaged when trying to initiate mode-locking. The oscillator pump diode can be run in up to 1350 mA of current, though the typical operation current is in the range of 500-600 mA when mode-locked. It has been found that initialization of mode-locking is easiest at larger pump powers, generally in the 1300 mA range. First, verify that the $\lambda/4$ waveplate is set to 172° as marked on the mount (looks relatively close to 45° from vertical by eye) and turn up the pump diode to 1300 mA. The operation

of the oscillator is highly sensitive to the orientation of the waveplates, setting the $\lambda/2$ waveplate to 58° you should see an output power close to 1.8-2 mW from the RIN tap. It is worthwhile to lightly optimize the power output by adjusting the alignment of the cavity. Walking the beams and large adjustments typically are not necessary – tuning the mirror in the linear arm or one of the mirrors in the ring is sufficient. The waveplates in the loop may also need to be lightly tuned to minimize the power loss on PBS1.

Once this light power optimization has been done, it is possible the comb will have mode-locked with substantial cw-breakthrough. A sudden increase in the oscillator power output, or a sudden broadening of the spectrum as seen by the OSA both indicate that mode-locking has begun. If mode-locking has not initiated at this point, verify that the setting of the linear-arm waveplates are 172° and 58° for the quarter and half waveplate respectively. Then, the focusing distance to the SA may be adjusted slightly, about a quarter turn or less, may aid in initializing the mode-locking. If left in this configuration, the oscillator generally will mode-lock itself within 5 minutes. Once you have a mode-locked laser, you need to turn down the oscillator pump diode driver to a much lower current. The oscillator usually mode-locks in this high-pump setting into a multiple-pulse regime which is unsuitable for our purposes. It is highly recommended that the spectrum on the OSA is monitored as you turn down the pump power at this point. As the pump current is turned down, the oscillator's spectral bandwidth should decrease then suddenly change and increase again. This should happen 2-3 times before reaching a pump current of about 450 mA. The single-pulse operation generally is achieved once the pump current is as low as 450 mA, and the spectral output is typically larger than what was observed in the high pump current regimes. At this point, if the waveplates have not been turned, the oscillator is likely still operating with substantial cw-breakthrough, usually at 1530 and at 1560 nm. By turning the $\lambda/2$ waveplate closer to 45° , the spectrum of the comb should start drastically increasing and the cw-breakthrough should also diminish. At this point, alternately tune the pump current and the waveplate orientation until you are able to reach cw-breakthrough free operation and also have a spectral output of about 40 nm. Once this is achieved, note the maximal operating pump current without cw-breakthrough

as to avoid it during normal operation (though the f_0 beatnote starts looking very problematic once cw-breakthrough arises, so it is noticeable).

Here is a step-by-step summary of this procedure is from above:

1. Turn off all laser diode drivers in frequency combs system to prevent damages to optical components
2. Disconnect RIN servo, and use tap for monitoring oscillator output power
3. Use comb-stable laser tap for monitoring the oscillator spectral output on the OSA, disconnect stable laser from beamsplitter, you don't need to see it on the OSA
4. Set the waveplates in the linear arm to 172° and 58° for the quarter and half waveplates respectively
5. Set the oscillator laser diode driver to 1300 mA
6. (Optional) Lightly optimize the power output of the oscillator. Power outputs from 1.8-2.2 mW are normal
7. Wait or make slight adjustments until mode-locking initializes
8. Turn down the laser diode driver, observing the mode-locking regime changes on the OSA, until single-pulse operation is achieved. This is typically around 450 mA.
9. Adjust the $\lambda/2$ waveplate towards 45° , an increase of the oscillator bandwidth should be apparent. Going too far will break the mode-locking
10. Adjust the current and $\lambda/2$ in tandem to achieve 40 nm of oscillator bandwidth with no cw-breakthrough

3.5.3 Aligning the oscillator

In the case that the oscillator has been sufficiently misaligned, the former strategy outlined above will not work. In that case, realignment of the oscillator will be necessary. A difficulty in

the design of the current oscillator is ensuring the overlap of the two possible paths in the linear arm; it is possible to have beam trajectories that do not overlap in the linear arm but are coupled into the opposite GRIN lens. One of our main strategies will be to ensure that these two beam paths are overlapped in the linear arm.

In the case of total realignment, it is suggested that once again the comb-stable laser tap is used to monitor is the oscillator spectral output on the OSA and the RIN servo tap is used to monitor the power output of the oscillator. First, one needs to ensure that at least one of the loop arms is able to be well coupled back into itself upon reflecting off the SA in the linear arm. One should remove the Faraday rotator and quarter wave plate from the linear arm. The fiber loop has two branches, which will be referred to as the pump arm and the weak arm. The pump is the GRIN lens where the unabsorbed 980 pump light is dumped, and is also the side closest to the erbium fiber. Block the weak arm GRIN lens and observe the ASE spectrum from the comb on the OSA. Maximize the ASE signal – this signal provides evidence that the pump arm retraces back onto itself upon reflection on the SA, a necessary condition for mode-locking.

Next, overlap the weak arm with the pump arm on PBS 1 and along the linear arm. Unfortunately, the weak arm ASE signal is very dim. Once it is believed that reasonable overlap is made, lasing should occur. Turn the oscillator into a ring cavity by reinserting the Faraday rotator only. If the cavity begins to lase at this point, optimize the power by adjusting the weak arm lens and mirror knobs *only*. Then, optimize the ring cavity power by turning the *in-loop* waveplates. It might be more straightforward to instead minimize the power dumped through PBS 1 with the waveplates. Note that PBS 1 should dump two beams – one is the 1550 nm light from the oscillator and the other is 980 nm pump light.

Once the ring laser power has been relatively optimized, return the $\lambda/4$ wave plate into the linear arm, between the Faraday rotator and the $\lambda/2$ waveplate. Likely, the maximal power output achievable by the oscillator has been substantially reduced, this is expected as the cavity can no longer operate in a ring-configuration (remember that the output coupler of the oscillator is directional as it is a 2×1 90/10 beamsplitter). With the $\lambda/4$ waveplate in place, one should pay attention

to the power dumped by PBS 2. Observe the beam dumped by PBS 2 while the oscillator is lasing while turning the linear arm waveplates. If there are two clearly offset, distinct beam dumped from PBS 2, the pump and weak arms are not overlapped in the linear arm, and achieving mode-locking will not be possible. Overlap the beams transmitted through PBS 2. When the overlap is good, a rotationally symmetric interference pattern should appear as the linear arm waveplates are adjusted. Once this symmetric interference pattern is achievable, follow the steps in the mode-locking initiation guide.

Here, we present a quick summary of cavity alignment steps:

1. Remove Faraday rotator and $\lambda/4$ waveplate from the linear arm
2. Align the pump arm so that it can retroreflect back into itself by blocking the weak arm and maximizing the ASE signal.
3. Overlap the weak arm beam path with the pump arm, the beam will be very dim so it may be somewhat difficult. Lasing should occur when reasonable overlap is achieved
4. Turn the cavity into a ring cavity by reinserting the Faraday rotator. Optimize the ring cavity power output by walking the weak arm lens and mirror. Minimization of the transmitted power through PBS 1 may also be required.
5. Place the $\lambda/4$ waveplate into the linear arm and observe the interference pattern transmitted through PBS 2. Make sure this pattern is rotationally symmetric.
6. Begin the mode-locking protocol outlined in the previous section.

3.6 The Ultra-Stable Cavity and Laser

3.6.1 Introduction

As our frequency comb is intended to function both as a absolute frequency reference and as a coherent stable oscillator to train our other light sources to, we require that the comb itself has the required coherence. As indicated previously, due to the nature of locking the two comb

parameters, f_r and f_0 , the current best method to achieve this level of performance is to lock a comb tooth within the optical spectrum instead of f_r directly. At the same time, the current best stable oscillators (RF or optical) each are based on optical sources that are referenced to very high finesse (or Q) optical resonators [84, 155–158].

Ultra-stable cavity designs start with optical cavities with very large quality factors ($Q \approx 10^{10}$ or greater) that are then highly environmentally isolated. Such high Q -factors correspond to a cavity finesse between 100000 and 300000 and mirror losses on the order of 20 ppm. These optical cavities are typically made of a ≈ 10 cm monolithic piece of Ultra-low expansion (ULE) Corning glass, but have been also constructed out of single-crystal silicon or sapphire substrates, with a bore through the long axis of the substrate (called the spacer) and mirrors optically contacted to the ends of the spacer [159–162]. This monolithic optical resonator is then mounted to reduce the effect of vibrations, and put in ultra-high vacuum to reduce air current disturbances. Finally, the temperature of these cavities is held very constant to prevent the effects of thermal fluctuations. The length stability of an optical resonator is intimately connected to the frequency stability of the resonator, and we aim for frequency stability at the level of one Hz, or 10^{-15} precision. By

$$\frac{\delta f}{f} = \frac{\delta L}{L}, \quad (3.14)$$

we find that this requires a length stability on the order of 10^{-16} m, or about 1/10th the size of a proton! Most impressively, the performance limiting effect for many of these ultra-stable cavity systems is due to the Brownian motion of the mirror coatings surfaces [163, 164].

3.6.2 Optical Cavity Basics, Revisited

The most simple optical cavity consists of two mirrors facing each other, aligned so that there exists at least one resonant mode between them. In the simple case of plane waves, the two mirrors may be flat, and the resonance condition merely requires that the distance between the two mirrors leads to constructive interference for an arbitrary number of round trips, that is, the cavity length, L , is a half integer multiple of the light's wavelength, λ . This is given by

$$L = m(\lambda/2). \quad (3.15)$$

Rewriting in terms of the fundamental frequency spacing, called the free spectral range (FSR), we find

$$FSR = \frac{c}{2nL} \quad (3.16)$$

with n being the index of refraction of the media separating the two mirrors. The eigenmodes of light propagating in free-space are not plane waves, but instead the Hermite-Gaussian modes (TEM modes). This changes the true resonance condition of our optical resonators slightly, as Hermite-Gaussian beams experience a phase shift as compared to a plane wave phase evolution called the Gouy phase shift. The modified cavity resonances due to this extra phase term is

$$f_{mpq} = \frac{c}{2nL} \left(m + (1 + p + q) \frac{\Delta\psi}{\pi} \right), \quad (3.17)$$

where $\Delta\psi$ is the Gouy phase shift through the cavity, and the indices p and q track higher order Hermite-Gaussian modes (TEM_{pq}).

While the spacing between resonant modes of an optical cavity are determined by the cavity length (see Eq. 3.16), the widths of these resonances are determined by the reflectivity of the mirrors and the cavity length. The width of these resonances is set by the lifetime of the radiation inside of the cavity (that is, the time it takes the light to leak out of the cavity through the mirrors). Clearly, for lower cavity loss, it takes more time for the light to leave the cavity. Finesse, F , is one metric to quantify how frequency discriminant an optical cavity is and is given by

$$F = \frac{FSR}{\Delta\nu_{1/2}} \approx \frac{2\pi}{\text{Loss}}, \quad (3.18)$$

where $\Delta\nu_{1/2}$ the width of a resonance and Loss is the round trip power loss. As we can see, the finesse relates the width of a cavity resonance to the spacing between resonances, and is determined only by the cavity loss.

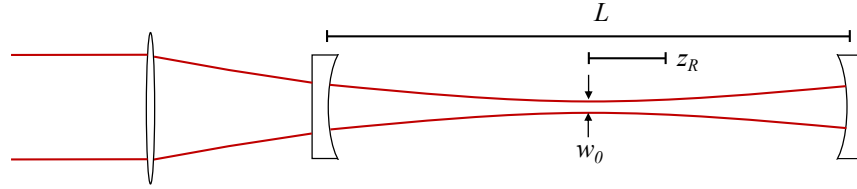


Figure 3.17: Simple cavity with common cavity parameters indicated. L : Cavity length. z_R : Rayleigh range, distance from focus of Gaussian beam in which the w parameter increases by $\sqrt{2}$. w_0 : Beam waist, width of Gaussian beam at focus.

It is possible, given the cavity mirrors' radii of curvature and separation distance(s), to determine the resonant spatial modes for an optical cavity. The most straightforward approach is to generate the appropriate ABCD matrix for one round trip through the cavity and determine the corresponding eigenvectors. These eigenvectors describe beams that are unchanged after one round trip, and therefore correspond to the resonant spatial modes. The overlap integral between the incoming beam to the cavity and the resonant modes of the cavity determines how efficiently the resonant modes are driven, typically called mode-matching [165]. If the input beam is not well spatially matched, or is off the frequency resonance, no power may build up inside of the cavity, and the power is reflected off the cavity. The nominal reflectivity of an example optical cavity, as a function of frequency, is shown in Fig. 3.18. This example cavity has a finesse of $F \approx 8$ and has loss aside from mirror transmission, causing the reflectivity to not quite reach zero on resonance. This picture also assumes perfect mode matching with only a single spatial mode of the cavity; imperfect mode-matching would lead to multiple resonances being excited through a scan of one free spectral range.

While the example shown in Fig. 3.18 shows an optical cavity with only a finesse of about 8, there exist optical cavities with a finesse of up to 800,000. Assuming a nominal cavity length of about 15 cm, this would lead to an FSR of about 1 GHz, and a corresponding resonance linewidth of only 1 kHz. Remembering that optical frequencies are in the 10^{14} to 10^{15} Hz, these resonances are quite narrow. If a laser was referenced to one of these resonances, merely keeping it within the linewidth of a cavity resonance, this represents a laser stability on the order of 10^{-12} . In reality, it

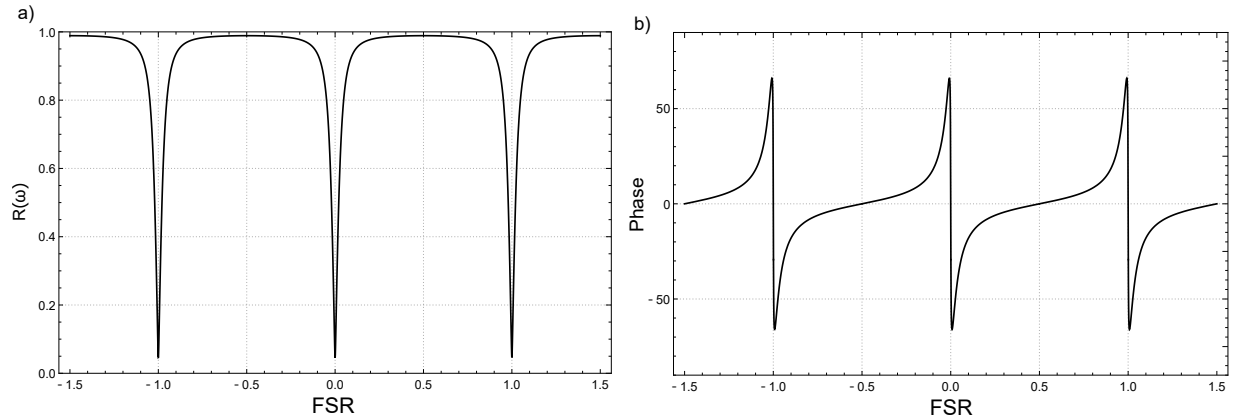


Figure 3.18: Cavity reflection as a function of frequency (in terms of cavity FSR).

is possible to stabilize a laser such that its frequency excursions are much less than the linewidth of the resonance referenced.

3.6.3 Pound-Drever-Hall Locking

As mentioned, the narrow optical resonances offered by high finesse cavities offer a compelling reference to stabilize lasers [158]. While there are a large variety of specific techniques to lock a laser to a frequency reference, all require the creation of an error signal and a method to actuate the laser frequency or phase. An error signal is simply a signal that tracks how close the desired signal is to a setpoint, i.e., the difference between the laser frequency and a cavity resonance. Many of the most commonly employed methods to generate error signals involve either frequency (or phase) modulation of the laser. Perhaps the most powerful of these modulation techniques is the Pound-Drever-Hall method [84]. A key feature of the Pound-Drever-Hall (PDH) locking scheme is the use of high modulation frequencies – that is, modulations frequencies that are well beyond the linewidth of the resonance.

An excellent review of the PDH locking technique can be found in [166]. A conceptually simple frequency modulation method to lock a laser to a cavity resonance would be to “slowly” (that is, modulate at some frequency much less than the linewidth of the resonance) dither the laser frequency around the resonance. Examining Fig. 3.18, we see that when the laser is slightly off resonance, there is some small phase shift on the rejected light. The total reflected light power

is composed partially of rejected light and some amount of leakage light out of the cavity. In general, these two beams will interfere. The phase of the rejected light depends on which side of the resonance the light is on, allowing for proper feedback to minimize this frequency difference. There are drawbacks to this “dither” locking method. First and foremost, potential modulation frequencies are limited to well below the cavity linewidth itself. This is especially problematic if using a high finesse optical cavity, which can have linewidths as low as a few kHz. At frequencies this low, technical noise in the form of RIN on the laser itself, vibrations in the environment, and electronic noise floors can be substantial. Additionally, the feedback bandwidth is limited by the modulation frequency as well, degrading ultimate performance limit, or preventing locks from being achieved altogether. For this reason, it is attractive to instead modulate the laser at high frequency, where these technical issues can be circumvented.

While we have been mostly discussing modulating the frequency of the laser for these locking techniques, it is typically much easier to modulate the phase of the light at high frequency via the use of electro-optic modulators (EOM). Fortunately, this does not pose a problem, as phase and frequency modulation are intimately linked. In the case of sinusoidal modulation the two are equivalent, as phase and frequency are related by a derivative. A phase modulated at frequency Ω electric field has the form

$$E(t) = Ae^{-i(\omega t + \beta \sin(\Omega t))} \quad (3.19)$$

with ω the angular frequency of the laser light and β the depth of the phase modulation. This expression may be expanded in terms of Bessel functions giving us

$$E(t) = Ae^{-i(\omega t + \beta \sin(\Omega t))} = AJ_0(\beta)e^{-i\omega t} + Ae^{-i\omega t} \sum_n (J_n(\beta)e^{-in\Omega t} + (-1)^n J_n(\beta)e^{in\Omega t}) \quad (3.20)$$

where J_n are Bessel functions of the first kind. For small modulation depth, only the $n = 0, 1$ terms are significant and our field reduces to

$$E(t) \approx AJ_0(\beta)e^{-i\omega t} + AJ_1(\beta)e^{-i(\omega + \Omega)t} - AJ_1(\beta)e^{i(\omega - \Omega)t} \quad (3.21)$$

Therefore, there are sidebands at frequencies $\omega \pm \Omega$ that have opposite signs from one another. For modulation frequencies well above the cavity linewidth, these sidebands are totally reflected and unaffected. However, the carrier phase (that is, the J_0 term) is affected when reflected near the resonance frequency and interferes with the unaffected sidebands. This interference between the reflected carrier light and the sidebands allows us to determine where the laser frequency is with respect to the resonance frequency.

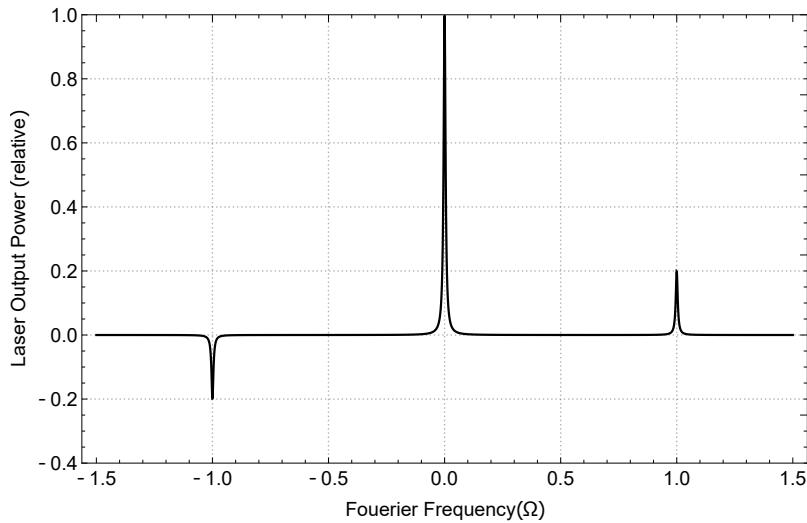


Figure 3.19: Phase Modulated Sidebands ($f = \pm\Omega$) on a carrier frequency ($f = 0$).

A basic Pound-Drever-Hall locking scheme is depicted in Fig. 3.20. The output of a laser is phase-modulated with an EOM and sent to the reference cavity. The reflected beam is deflected to a photodiode, by way of a polarizing beam splitter and quarter-wave plate. The photodiode signal, which has a carrier frequency of Ω is demodulated by mixing with the EOM modulation signal and low-passed to leave only the difference signal in the mixing process. An ideal error signal generated in this process is shown Fig. 3.20 b). This error signal is then conditioned by a loop filter and actuates the laser frequency. A phase shift between the photodiode signal and the EOM modulation signal is usually necessary to generate error signals akin to Fig. 3.20 b). Typically, the proper phase shift is determined by varying the phase shift experimentally until the error signal resembles Fig. 3.20 b).

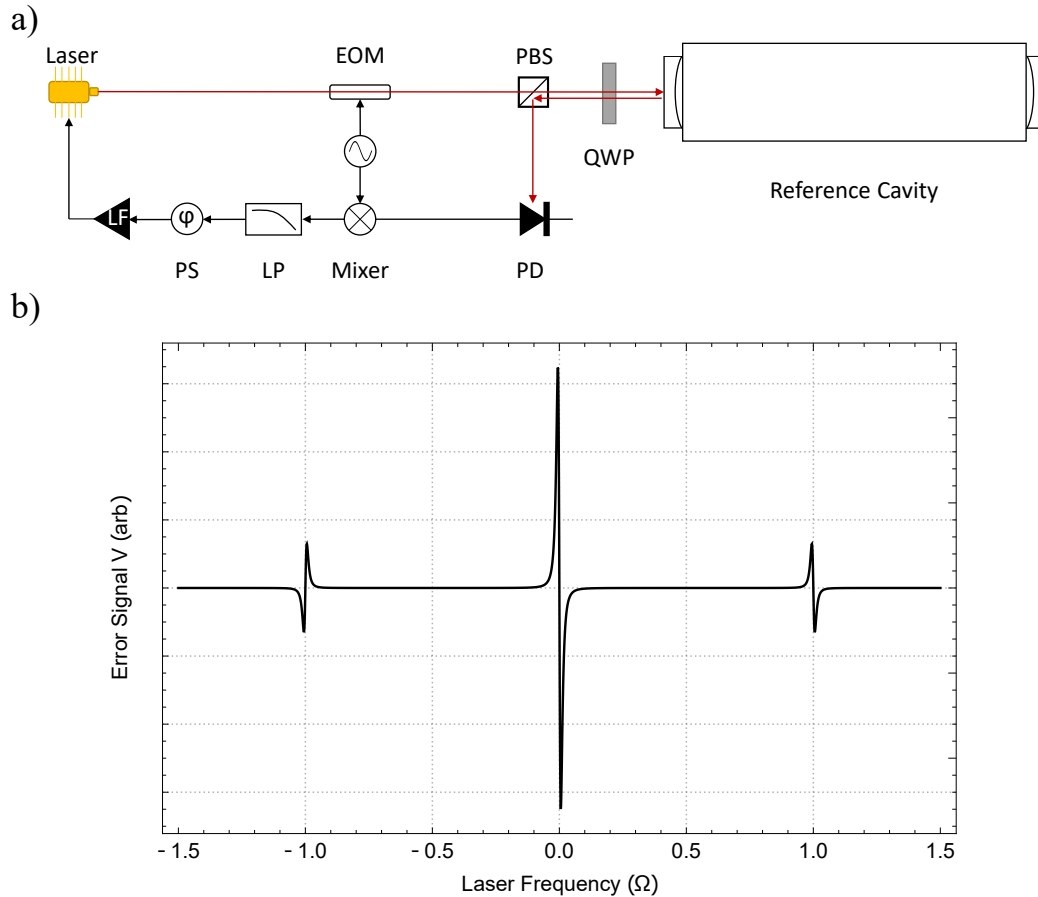


Figure 3.20: Example of typical PDH-lock. a) A usable PDH experimental setup. PD: Photodiode. LP: low-pass filter. PS: Phase shifter. b) An example error signal generated for PDH locking, note that the cavity linewidth is $\approx \frac{1}{20}$ the dither frequency in this example.

To accurately determine the linewidth of a PDH-locked laser to one of these reference cavities requires two independently locked lasers. The two lasers are compared by measuring the heterodyne beatnote and measuring the fluctuations in the beat frequency. However, it is possible to estimate the performance of the PDH locked laser in a much more straightforward way. By examining the PDH error signal, we can see that the peak of the error signal height corresponds to the maximal slope of the cavity resonance. This occurs near one-half the resonance width. Therefore, the full height of the error signal (maximum-minimum voltage) roughly corresponds to a frequency excursion of the resonance width $\Delta\nu_{1/2}$. This full error signal height can be compared to the root-mean-square voltage of the locked error signal, and the linewidth of the laser, $\delta\nu_{laser}$, can be estimated by

$$\frac{\delta V_{rms}}{\Delta V_{max}} \approx \frac{\delta \nu_{laser}}{\Delta \nu_{1/2}}. \quad (3.22)$$

3.6.4 Design of the Ultra-stable Cavity

The frequency stability achievable with a PDH-locked laser is dependent on the length stability of the cavity the laser is referenced to (as indicated in Eq. 3.14). To maximize the length stability of these cavities several steps are taken. First, the cavity spacer is designed and mounted in such a way to reduce the effect of vibrations [167]. The mirrors are optically contacted to the spacer directly. Second, the cavity is made out of a material which is highly impervious to thermal expansion and shielded from external temperature fluctuations [155]. Finally, the cavity is placed in high vacuum, to further reduce thermal fluctuation and remove the index of refraction variations associated with air currents and pressure changes.

To minimize the effect of vibration, the stable cavities are generally made monolithic [156]. This is achieved by optically contacting the mirrors that form the cavity with a glass spacer, forming an effective single piece of glass. The glass spacer is machined with a bore through the center to support the cavity mode, and a venting hole is bored into the spacer as well. The spacer is designed to be either mounted vertically or horizontally. We choose a horizontal orientation so that the cavity modes are parallel to the ground as it allows for easier mounting and optical access. In this configuration, the spacer is machined so that there is a mounting plane just under the vertical mid-plane of the spacer, giving a “mushroom” shaped cross-section (see Fig. 3.21). Our particular cavity spacer is 10 cm long with a 5 cm diameter. The mirrors mounted to this spacer are a flat-50 cm concave radius of curvature pair, each with thickness of 1/4" and 1" diameter. Our monolithic glass spacer and mirrors piece are all ULE glass – occasionally fused silica mirrors with a ULE cap on the back are used in other similar cavity designs.

While to first-order a monolithic optical cavity is insensitive to vibrations, as both mirrors move in tandem with one another, the cavity spacer is not perfectly rigid. Therefore, vibrations can couple to length of the optical cavity by causing deformations in the spacer as a result of the changing stress in the material. The established method to minimize these vibration-induced deformations is

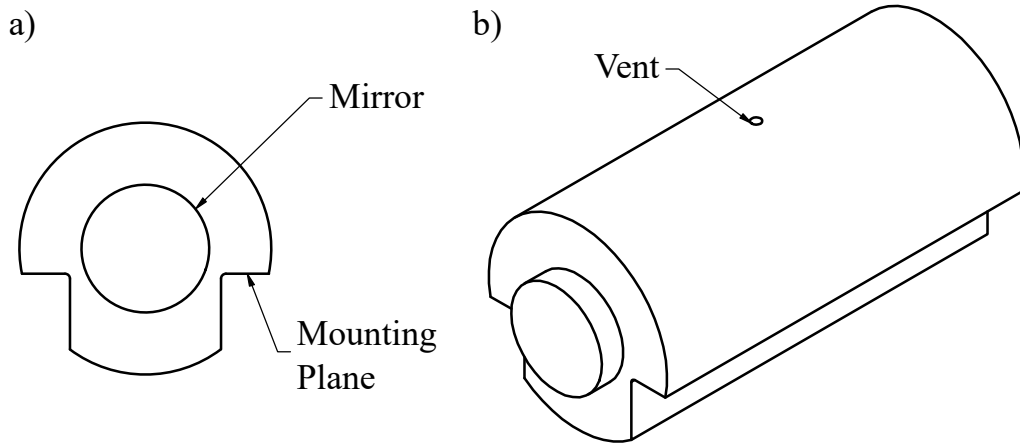


Figure 3.21: Ultra-stable cavity spacer geometry. Optical cavity is 10 cm long.

to carefully engineer the exact geometry of the cavity spacer and hold the cavity at specific points along the spacer. By mounting the cavity in specific locations, the resulting deformations to cavity can be set such that the length fluctuations are minimized. Typically, finite-element analysis is used to determine the location of these mounting points for a given cavity/spacer geometry. In our case, we purchased our cavity (including the spacer and optically contacted mirrors) from Stable Laser Systems.

The cavity itself rests on soft viton 1/4" balls. A "tub" shaped piece of Zerodur glass has been machined with key slots to prevent the viton balls from shifting from the optimal support point. The Zerodur piece itself rests upon three 1/4" viton balls, also held in place with slots on the bottom of the tub. Viton, being a soft rubber that is suitable for vacuum application, was chosen partially to ensure a more even distribution of the load on each support point as well to decouple the system from external vibration. The Zerodur piece is shown in Fig. 3.22.

As mentioned, the cavity is composed of a material that is largely insensitive to thermal fluctuations. Commonly, the material employed is Corning Ultra-low Expansion glass (ULE). This material boasts a thermal expansion coefficient around $10^{-7}/\text{K}$. The thermal expansion of a material can be written as

$$\Delta L/L = \alpha(T)\delta T + \alpha'(T)(\delta T)^2 + \dots \quad (3.23)$$

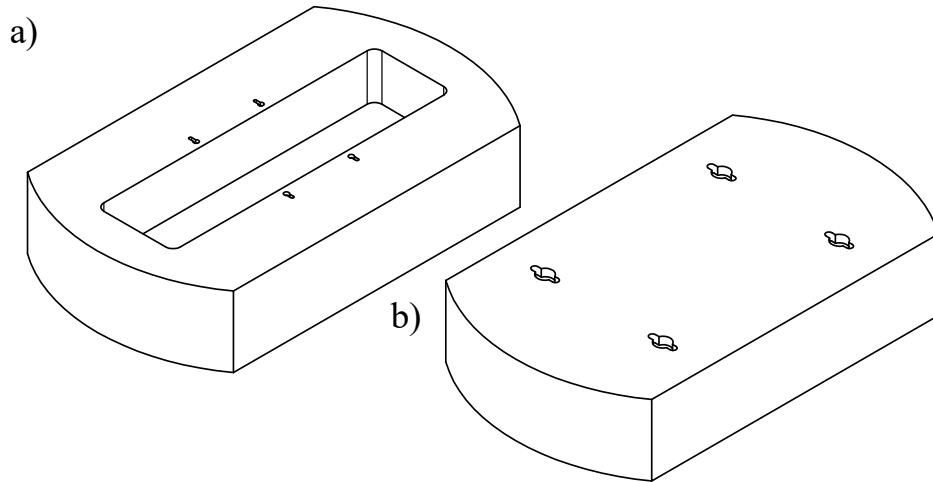


Figure 3.22: Zerodur spacer mount. Key holes are for keep the viton balls in place and also allow for possible trapped gas volumes to vent. a) Top view. b) Bottom view.

For ULE glass there exists a temperature T such that $\alpha(T) = 0$, often called the zero crossing point. This zero crossing temperature can vary between $0\text{ }^{\circ}\text{C}$ and $35\text{ }^{\circ}\text{C}$ from batch to batch of ULE glass, which are in the range of convenient experimental working temperatures. If the optical cavity is held at a zero crossing temperature, thermally induced length fluctuations are strongly suppressed. This is a common practice for these ultra-stable cavities, and we have followed suit. The sign of the instantaneous coefficient of thermal expansion for ULE glass flips sign as it goes through the zero crossing, allowing for a relatively straightforward determination of the zero crossing. For instance, one merely has to record the a resonance frequency for a given temperature, then change the cavity temperature. As the temperature is swept, a quadratic temperature dependence of the resonance frequency is found, and the zero crossing corresponds to the extrema of that parabola. We have determined that our zero crossing temperature is quite near $32.1\text{ }^{\circ}\text{C}$.

To further improve the temperature stability of the optical cavity, we have placed the cavity within a pair of aluminum heat shields that are only lightly thermally coupled to one another. These heat shields are closed-can shaped, and have apertures in the side for the optical beam path. The outer heat shield temperature is monitored with an AD590 transducer, and a thermo-electric device (Thorlabs TEC3-2.5) with Indium foil on either side is pressed onto the outer head shield to

actuate the outer heat shield temperature. We have found that the thermal time constant between the outer heat shield and the cavity to be about 24 h. The entire assembly, including the heat shields, Zerodur "tub", and stable cavity, are placed within a cylindrical vacuum chamber. We use a Thorlabs laser diode temperature controller (TED200C) to read the AD590 temperature and provide feedback to the outer heat shield TEC. As is, the integration time constant of this device is too low, and to prevent oscillation the integration on this device is turned off. This reduces the stability of the setpoint, and currently the temperature reading of the outer heat shield can vary by about ± 0.01 °C over the span of a day.

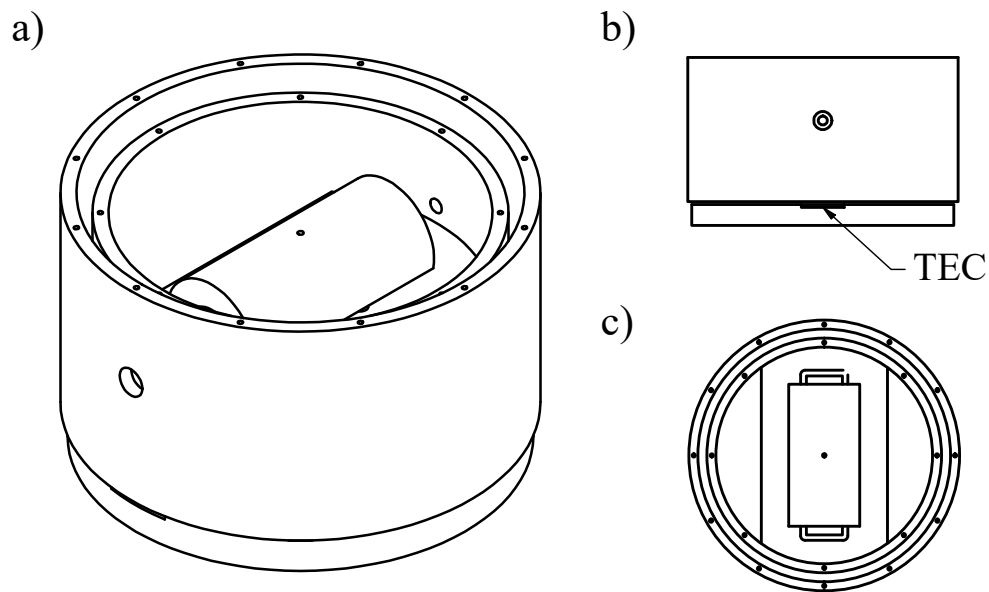


Figure 3.23: Heat shields and cavity mounting assembly in different views. a) Overhead side view. b) Side view along optical axis. c) Top-down view. The lids to the heat shields are omitted from this picture for clarity.

The vacuum chamber is a 5-11/16" tall, 10" Conflat flange, nipple with four symmetrically distributed around the mid-plane of the nipple. For optical access, wedged AR-coated windows are Torr-sealed to bored 2.75" CF flanges on two of the four ports. Electrical feedthroughs for the AD590 and the thermoelectric device are on another one of the ports, and the last port is for the vacuum pump. While the vacuum chamber is initially pumped out with a turbo vacuum pump, the

vibrations could be disruptive to the performance of the cavity. Therefore after the initial pump down, the vacuum chamber is then further pumped by a 20 liter/s ion pump (Duniway DGD-020-5125-M). Our chamber has reached a pressure of about $1 * 10^{-8}$ Torr, as measured by the ion pump controller and a cold cathode (or inverted magnetron) gauge (Kurt Lesker CCPG-H2-3). As mentioned above, we require the index of refraction variation to cause length variations below 10^{-15} . We can estimate the magnitude of pressure fluctuation this corresponds to by assuming the index variation is linear with pressure variation. Then,

$$n(P) \approx 1 + .00029 \frac{P}{P_0} \quad (3.24)$$

with P_0 the pressure at atmosphere. Then the fractional frequency stability and fractional index stability are linked by

$$\frac{\delta f}{f} = \frac{\delta n}{n}. \quad (3.25)$$

So,

$$10^{-15} \approx .00029 \frac{\delta P}{P_0}, \quad (3.26)$$

which corresponds to pressure fluctuations of about $3 * 10^{-9}$ Torr, or just over 10% fluctuations of our base pressure, which would be detectable and are not realistic fluctuations over day time scales. The entire vacuum chamber is mounted on a passive vibration damping platform Minus-K stage (175-BM8). To reduce the current required by the outer heat shield TEC to heat to 32.1 °C, the vacuum chamber is wrapped in heat tape and kept near the zero crossing temperature as well. Finally, the entire assembly is in a sound dampened enclosure to aid in temperature stability and reduce acoustic source vibrations.

3.6.5 The Stable Laser

The laser system we currently reference to our ultra-stable cavity is a 1554 nm Orion laser module from RIO. The laser is a Bragg-grating stabilized, external cavity diode laser that is fiber coupled outputting 10 mW of optical power at 1554.5 nm. This laser module is temperature and

current tunable for setting the gross wavelength, and is controlled via a command module on a laptop connected via USB. The free running linewidth of the laser module is specified to be <2 kHz, though we have not verified this directly, and we do not believe it was determined via heterodyne. Immediately after the output of the Orion laser, we have a fiber coupled 200 MHz acousto-optic modulator (AOM), with an EOM crystal (Lithium Niobate w/ polarizer, Thorlabs LN65S) to apply 10 MHz sidebands to the light immediately after (using a 4-5 V Vpp signal). The output is then split with an in-fiber 90/10 beamsplitter; one tap is for comparison to the frequency comb and the other is for referencing the ultra-stable cavity. For comparison to the frequency comb, the Orion output and frequency comb tap are combined on a two-port 50/50 beamsplitter and sent to a balanced photodetector. A two-paddle polarization controller on the comb tap is used to optimize the signal to noise on this beat frequency, and does not drift if the fibers are not disturbed.

For the PDH-locking, the 90% tap is used. The beam is collimated before passing through a $\lambda/2$ wave-plate and polarizing beamsplitter pair to control the total light power incident on the cavity. After the beamsplitter, a $\lambda/4$ wave-plate follows, and the reflected power is directed to a photodetector for locking. The transmission out of the cavity is also monitored with a photodiode. The reflected light photodiode signal is mixed with the EOM 10 MHz modulation signal (Mini-circuits ZAD-1+). The resultant error signal is filtered, conditioned, and actuates the laser frequency by feedback onto the diode current and EOM for slow/fast feedback respectively. The feedback bandwidth of the PDH lock is estimated to be about 300 kHz. While searching for cavity resonances (which are 1.5 GHz apart), we sweep the Orion laser frequency at 8 Hz with the AOM.

3.6.6 USC Performance

As mentioned, the cavity spacers and mirrors were purchased from Stable Laser Systems. We were provided with the measured reflectivities of the mirrors, and from this we calculate a cavity finesse of $F \approx 300,000$. During the initial locking of the cavity, we did a simple ring down measurement and found good agreement with the calculated finesse from the given mirror reflectivities.

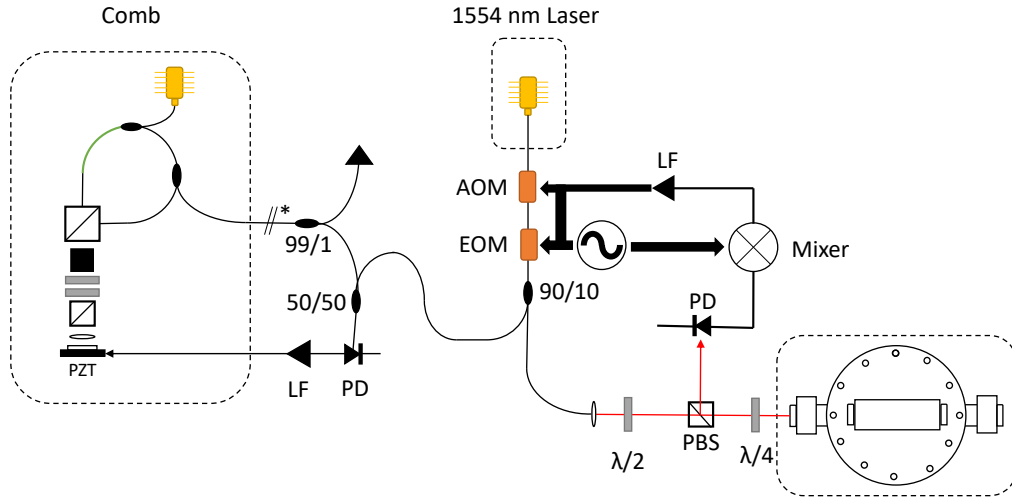


Figure 3.24: Ultra-stable cavity and comb interfacing. The in-fiber EOM puts 10 MHz sidebands on the 1554 nm laser for PDH lockig to the ultra-stable cavity. 90% of the stable laser output is used for beat note detection with the optical frequency comb. Note that unrelated comb fiber optics are omitted for clarity.

The performance of the ultra-stable cavity is quantified by measurement of the frequency comb repetition rate while it is phase-locked to the stable laser. The typical metric to quantify the stability of a clock or oscillator, such as a laser, is the Allan variance [54, 89, 94]. Allan variance has an advantage over traditional statistical analysis methods when quantifying these systems; oscillators frequently have very slow frequency drifts associated with them. If a standard deviation was taken of the measured oscillator frequency, in general the estimator would diverge due to these unmitigated drifts. The Allan variance estimates the point-to-point scatter of a data set for a particular time interval. Put another way, the Allan variance can quantify the variance of an oscillator if measured every second, every 10 s, and so on. As one might expect, a general feature of the Allan variance is that it decreases with increasing measurement time until the frequency drifts becomes noticeable over the measurement time, at which point the Allan variance will start to increase.

The Allan variance is a special case of M-sample variance, where M is taken to be two samples and there is no dead time between measurements of the oscillator frequency. M-sample variance, $\sigma_y^2(M, T, \tau)$ may in general be calculated as

$$\sigma_y^2(M, T, \tau) = \frac{1}{M-1} \left[\sum_{i=1}^{M-1} y_i^2 - \left(\sum_{i=1}^{M-1} y_i \right)^2 \right] \quad (3.27)$$

where M is the number of points per sample, T is the time between each sample, τ is the gate time for each sample, and y_i is the average fractional frequency during that gate [168]. To calculate the Allan variance, we set $M = 2$ and $T = \tau$ and find the average:

$$\sigma_y^2(2, \tau, \tau) \rightarrow \sigma_y^2(\tau) = \frac{1}{2} \langle (y_{i+1} - y_i)^2 \rangle \quad (3.28)$$

The Allan deviation, $\sigma_y(\tau)$ is related to the Allan variance as $\sigma_y(\tau) = \sqrt{\sigma_y^2(\tau)}$.

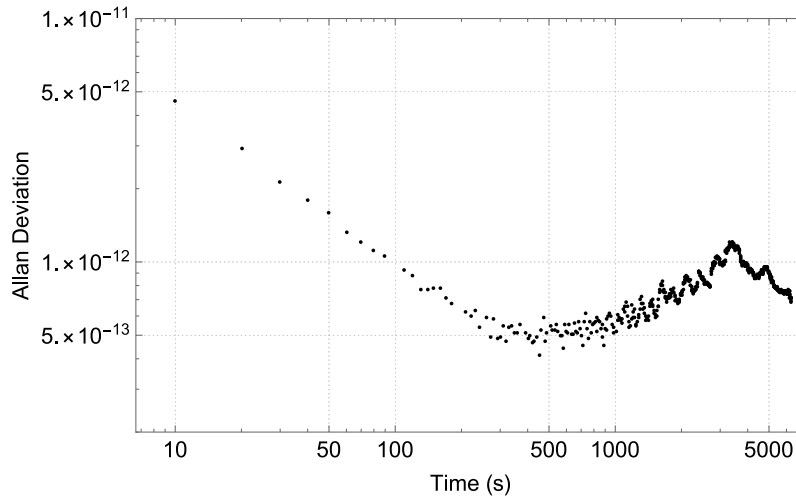


Figure 3.25: Ultra-Stable Cavity Allan Deviation

The Allan deviation of the optical cavity is determined by measuring the frequency comb's repetition rate. This slightly complicates the determination of the frequency stability of the comb-cavity system; the stability of the frequency counter itself must also be considered. Both of our frequency counters, a Hewlett-Packard 53131A and our SRS FS740, are referenced to a GPS-trained Rb-timebase within the SRS FS740. A quoted Allan deviation of the FS740 is available on its data sheet, though we have also directly characterized the Allan deviation of the FS740 (see section 6.4.3). The expected frequency stability of the Rb-timebase is 10^{-12} over averaging times

of 100-1000 s, and we see comparable, though slightly better, performance in these averaging times. In Fig. 3.25, we show the measured Allan deviation of the frequency comb repetition rate which is linked to the stability of the ultra-stable laser. On timescales between 10-1000s, the Allan deviation of the repetition rate is within the specifications of the FS740 timebase, which indicates that the frequency stability of the system is limited by the Rb-timebase over that time. For gate times > 1000 s, the increasing deviation of the repetition rate indicates that the frequency drift of the comb-cavity system becomes significant at those time scales. We attribute these long-term frequency drifts to slow thermal fluctuations and optical cavity settling. This is not atypical if drift compensation is not applied [160].

As it stands, we cannot rigorously quantify the linewidth of the stable-laser + ultra-stable cavity system, nor can we quantify the short-term noise floor of the ultra-stable cavity. Quantifying very narrow linewidth optical sources requires heterodyning between two mutually independent oscillators [157, 169] – we unfortunately do not have access to two ultra-stable cavity + laser systems. We can estimate the linewidth of the stable 1554 nm laser using Eq. (3.22), and find that the 1554 nm laser has a < 100 Hz linewidth when referenced to the cavity. Similarly, the noise floor of the ultra-stable cavity Allan deviation is limited either by the Rb-timebase or the thermal drift of the optical cavity. While it is promising that the noise floor is dominated by the FS740 instead of other sources at short time-scales, it also means that we cannot quantify the contribution of vibrations or thermal noise in our optical cavity. However, the frequency metrology system can make determinations at the 5×10^{-13} level in 500 s, while the most recent determinations of the $2S_{1/2}-8D_{5/2}$ are at the 6×10^{-12} level. This makes our frequency metrology system well-suited for making a competitive measurement of the $2S_{1/2}-8D_{5/2}$ transition.

3.7 Conclusion

In this chapter, we described the creation of a coherent erbium-fiber frequency comb. The two radio frequency comb parameters, f_0 and f_b , are stabilized by self-referencing and phase locking to an ultra-stable laser. The ultra-stable laser is a commercial diode laser at 1554 nm that is

locked to a monolithic ultra-stable cavity. The comb-stable cavity is capable of making frequency determinations at the 5×10^{-13} level, making the system well-suited for a competitive measurement of the $2S_{1/2}$ - $8D_{5/2}$ transition. Having described the experimental infrastructure surrounding $2S_{1/2}$ - $8D_{5/2}$ spectroscopy, we now describe our fitting procedures.

Chapter 4

Fitting Lineshapes and Extrapolations

When fitting and analyzing lineshapes in spectroscopic experiments, there are in general two approaches that can be taken. In one approach, a numeric model can be developed to explicitly track all of the contributing effects within the experiment. This numeric model can then be used to directly fit the measured lines – such an approach was taken by the Paris group in their previous measurement of the $2S$ - $8S/D$ lines [25, 45]. The other approach is to instead fit lineshapes with analytic functions that can be derived from the governing physics making relatively simple considerations, as in the recent $2S$ - $4P$ measurement from the Garching group [29]. We will take the second approach and fit our measured lines with physically well-motivated, simple analytic functions. In Chapter 5, we will check the validity of this approach by comparison with a numeric model.

In this chapter, we begin with a brief overview of the basic theory describing light-atom interactions. With this basic theory, we derive the analytic function that we use to fit $2S_{1/2}$ - $8D_{5/2}$ lines in our measurement directly. The largest systematic effect in the $2S_{1/2}$ - $8D_{5/2}$ measurement is the ac-Stark effect, which produces shifts between 100-300 kHz in our experiment. To determine the unperturbed resonance frequency, we measure the transition at many different light intensities and extrapolate to zero-field, which is also how the previous measurements of the $2S_{1/2}$ - $8D_{5/2}$ were performed [25, 43–45, 170]. We also characterize the functional behavior of these ac-extrapolations analytically, removing the necessity of using a complex numeric model to determine the zero-field resonance frequency.

4.1 The two-level atom

The two-level quantum system and its interaction with a perturbing Hamiltonian is a quintessential atomic physics problem. Treating an atom as a two-level system is a good description when the perturbing Hamiltonian only strongly couples two states, and the others do not

strongly participate. In the case of a laser light field perturbing an atom, the perturbing Hamiltonian is due to the atomic dipole-light field interaction energy. Starting at the two-level atom provides a strong theoretical background to begin our 2S-8D modeling.

We will label the two states of the two-level atom as 1 and 2 for the ground and excited states respectively. The state of that atom in general may then be written as

$$\psi(t) = c_1(t) |\phi_1\rangle + c_2(t) |\phi_2\rangle, \quad (4.1)$$

with ϕ_m 's the basis states for the two-level atom. Schrödinger's equation determines the time evolution of the state ψ ,

$$i\hbar \frac{\partial \psi(t)}{\partial t} = (H_0 + H_p)\Psi(t), \quad (4.2)$$

with H_0 the unperturbed atomic Hamiltonian (with basis states $|\phi_1\rangle, |\phi_2\rangle$), and H_p the perturbing light-matter interaction. The interaction energy, U , between an electric dipole, $\vec{\mu}$, and electric field, $\vec{\mathcal{E}}$, is $U = -\vec{\mu} \cdot \vec{\mathcal{E}}$. This gives us

$$U = -\vec{\mu} \cdot \vec{\mathcal{E}} = -e\mathcal{E}_0 \cos(\omega t)z. \quad (4.3)$$

The eigenstates of H_0 have certain rotational symmetries in the position basis, and therefore only the off diagonal components of H_p are nonzero, e.g. $\langle \phi_1 | z | \phi_2 \rangle$. Thus, the perturbing Hamiltonian has the form

$$H_p = \frac{\hbar\Omega}{2} (e^{i\omega t} + e^{-i\omega t}) (|\phi_1\rangle \langle \phi_2| + |\phi_2\rangle \langle \phi_1|), \quad (4.4)$$

where ω is the laser angular frequency, and Ω is the Rabi frequency given by $\Omega = \beta_{12}(e\mathcal{E}_0/\hbar)$, and β_{12} is the matrix element connecting states 1 and 2. Applying Schrödinger's equation gives

$$i\hbar(\dot{c}_1 |\phi_1\rangle + \dot{c}_2 |\phi_2\rangle) = c_2 \hbar\omega_0 |\phi_2\rangle + \frac{\hbar\Omega}{2} (e^{i\omega t} + e^{-i\omega t})(c_1 |\phi_2\rangle + c_2 |\phi_1\rangle), \quad (4.5)$$

where we have taken the ground state energy as zero for convenience, and $\hbar\omega_0$ is the resonance energy. Since the $|\phi_i\rangle$'s are orthogonal, we arrive at two coupled differential equations given by

$$i\hbar\dot{c}_1 = \frac{\hbar\Omega}{2}(e^{i\omega t} + e^{-i\omega t})c_2 \quad (4.6)$$

$$i\hbar\dot{c}_2 = \frac{\hbar\Omega}{2}(e^{i\omega t} + e^{-i\omega t})c_1 + \hbar\omega_0 c_2. \quad (4.7)$$

We are interested in the population in either state, given by $|c_m|^2$. We may substitute $c'_1 = c_1$ and $c'_2 = c_2 e^{i\omega t}$. Then, we apply the rotating wave approximation, dropping the fast oscillating terms (that is, terms oscillating at $\pm 2\omega$). We are left with our differential equations describing our state amplitudes which are

$$i\dot{c}_1 = \frac{\Omega}{2}c_2 \quad (4.8)$$

$$i\dot{c}_2 = \frac{\Omega}{2}c_1 + (\omega_0 - \omega)c_2, \quad (4.9)$$

where we have dropped the prime notation out of convenience. At this point, it is worth mentioning that our treatment here does not yet include spontaneous emission. We will return to the problem of spontaneous emission in a later section. For now, it is sufficient to mention Schrödinger's equation alone is insufficient to properly account for spontaneous emission. However, if decay does not repopulate $|\phi_1\rangle$ and instead decays into a state that is not included in our pair of differential equations, we may include the effect of spontaneous emission by adding $-i\frac{\gamma}{2}c_2$ to the right hand side of Eq. 4.9, where $\frac{\gamma}{2\pi}$ is the resonance width of the transition.

It is worth noting the general dynamics of the two-level in a few cases. In Fig. (4.1), we have plotted the population in the upper state vs time for a couple of cases. There are some general features to note: detuning leads to faster oscillations, but the amplitude of the oscillation is diminished. In the limiting cases, the time scale of the system is either 1) set by the Rabi frequency ($\Omega \gg \gamma$) or 2) set by the lifetime of the state ($\Omega \ll \gamma$). Common approximations include weak excitation and assume steady state where very little population is driven to the excited state on resonance. In that case, \dot{c}_m 's $\rightarrow 0$ and $c_1 \rightarrow 1$, we find that the steady state population in the

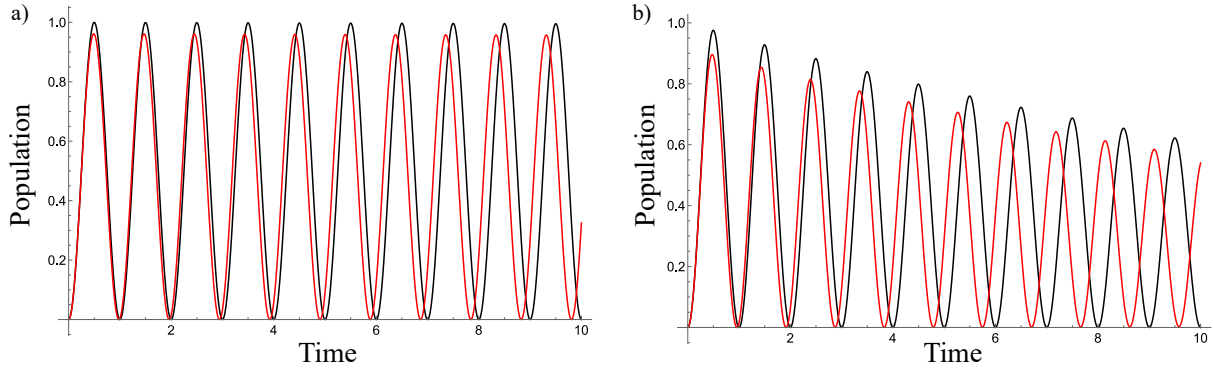


Figure 4.1: Some Example of two-level dynamics. The population in state 2 is plotted vs time. Black shows behavior on resonance and red is off resonant a) No Decay b) With decay ($\Omega \sim 10\gamma$)

excited state is

$$c_2 = \frac{\Omega^2}{\Omega^2 + (\gamma/2)^2} \approx \frac{\Omega^2}{(\gamma/2)^2}, \quad (4.10)$$

where the final approximation is taken because $\Omega \ll \gamma$ is required for $c_2 \ll 1$ to be valid in steady state. The rate of decay out of the excited state must be $\Gamma \sim \frac{\Omega^2}{\gamma}$ by unit analysis.

4.2 Derivation of Line Fit Function

4.2.1 Two-photon processes

We are interested in the dynamics of the $2S_{1/2}$ - $8D_{5/2}$ transition as the metastable $2S$ hydrogen atoms traverse the 778 nm light. Unlike the treatment in the preceding section, which derived a set of coupled differential equations for dipole-allowed (“one-photon”) transitions, the $2S$ - $8D$ transition is not dipole allowed as $\Delta L = 2$. However, the $2S$ - $8D$ transition can be driven via a two-photon processes. Driving a transition in such a way requires much larger light intensities to move substantial population than for a dipole-allowed transition [45, 68]. These transitions are called two-photon transitions, though the quantization of the electromagnetic field is not required for an accurate theoretical treatment. Fortunately, the population dynamics in a two-level system driven by a two-photon processes are quite similar to their one-photon counterparts. The largest differences between the two processes are the calculation of the matrix elements and the two-photon Rabi frequency is proportional to the intensity instead of the electric field amplitude. Of

course, the selection rules for two-photon transitions are also modified, for a derivation of these rules see [171]. Since the two-photon matrix element can be considered as driving all possible two-step pathways that connect states $|\phi_1\rangle$ and $|\phi_2\rangle$ via one-photon processes, it is intuitive that the selection rules require that $\Delta L = 0, \pm 2$. In the case of linearly polarized light, we may consider the light to be along the z axis, leading to selection rules of $\Delta F = 0, \pm 2, \Delta m_F = 0$.

The Hamiltonian describing our new two-photon coupled two-level atom is quite similar to our one-photon Hamiltonian,

$$H = E_1 |\phi_1\rangle \langle\phi_1| + E_2 |\phi_2\rangle \langle\phi_2| + \frac{\hbar\Omega}{2} [e^{-i\omega t} + e^{i\omega t}]^2 (|\phi_2\rangle \langle\phi_1| + |\phi_1\rangle \langle\phi_2|), \quad (4.11)$$

where E_1 and E_2 are coupled to the probe light energy via the ac-Stark effect and the two-photon Rabi frequency, Ω , are defined by

$$E_m = h\nu_m \quad (4.12)$$

$$\Omega(t) = 2(2\pi\beta_{12})I(t), \quad (4.13)$$

where β_{12} is the matrix element connecting states 1 and 2 [68]. We denote ν for real frequencies (measured in Hz) and ω, Ω for angular frequencies. Applying our new Hamiltonian onto a state ψ and using the orthogonality of $|\phi_1\rangle$ and $|\phi_2\rangle$ leaves us with

$$i\dot{c}_1 = \frac{\Omega(t)}{2} (e^{-i\omega t} + e^{i\omega t})^2 c_2 \quad (4.14)$$

$$i\dot{c}_2 = \omega_0 c_2 + \frac{\Omega(t)}{2} (e^{-i\omega t} + e^{i\omega t})^2 c_1 \quad (4.15)$$

where once again ω corresponds to the angular frequency of the light field. We perform a similar substitution as before ($c'_2(t) = c_2(t)e^{2i\omega t}$ and $c'_1 = c_1$). Once again, we apply the rotating wave approximation, dropping instead terms rotating at $\pm 2\omega, \pm 4\omega$, and find

$$i\dot{c}_1 = \frac{\Omega}{2} c_2 \quad (4.16)$$

$$i\dot{c}_2 = \frac{\Omega}{2}c_1 + (\omega_0 - 2\omega - i\frac{\gamma}{2})c_2, \quad (4.17)$$

which is effectively the same result acquired for one-photon processes.

4.2.2 Density matrix introduction

Another formulation to describe quantum mechanical dynamic evolution is through the use of density matrices. Density matrices have the advantage of being able to track statistical ensembles of states. Such a formulation is useful when applying quantum theory to large numbers of states in which the initial preparation of states is not known. In particular, density matrices are attractive if the dynamics of the system involves mixed states instead of only pure states. Inclusion of spontaneous emission is more naturally treated in a density matrix formulation.

A natural starting point is the von Neumann equation, which gives the time evolution of the density matrix ρ ,

$$i\hbar\dot{\rho} = [H, \rho] \quad (4.18)$$

where H is still the Hamiltonian of the system. Solving the von Neumann equation in the context of the two-level atom in a light field leads to a new set of equations:

$$\dot{\rho}_{gg} = -\Omega \text{Im}(\rho_{ge}) \quad (4.19)$$

$$\dot{\rho}_{ge} = -i2\pi(\Delta\nu)\rho_{ge} + i\frac{\Omega}{2}(\rho_{gg} - \rho_{ee}) \quad (4.20)$$

$$\dot{\rho}_{ee} = \Omega \text{Im}(\rho_{ge}) \quad (4.21)$$

where $\Delta\nu$ is the detuning from the (possibly perturbed) resonance and ρ_{gg} , ρ_{ee} , and ρ_{ge} are the population ground state, population of the excited state, and the coherence between $|g\rangle$ and $|e\rangle$ respectively. These set of three equations, and small modifications to them, are called the Optical Bloch Equations (OBE's) [172, 173]. Solving these sets of equations gives identical results as Schrödinger's equation. To include spontaneous emission into the system dynamics, a modification to the von Neumann equation is required,

$$i\hbar\dot{\rho} = [H, \rho] - \mathcal{L}\rho. \quad (4.22)$$

The Lindblad operator, $\mathcal{L}\rho$, accounts for spontaneous emission within the system [174]. Formally, the Lindblad operator is written as

$$\mathcal{L}\rho = \frac{1}{2} \sum_{ij} \gamma_{ij} (S_i^+ S_j^- \rho - 2S_j^- \rho S_i^+ + \rho S_i^+ S_j^-) \quad (4.23)$$

where $\gamma_{ij} = \sqrt{\gamma_i \gamma_j}$ and S_i^+ / S_j^- are projection operators that have the form $|i\rangle \langle j|$ and $|j\rangle \langle i|$ respectively. The differential equations for the two-level atom generated by Eq. 4.22 are:

$$\dot{\rho}_{gg} = -\Omega \text{Im}(\rho_{ge}) + \gamma \rho_{ee} \quad (4.24)$$

$$\dot{\rho}_{ge} = -i2\pi(\Delta\nu)\rho_{ge} + i\frac{\Omega}{2}(\rho_{gg} - \rho_{ee}) - \frac{\gamma}{2}\rho_{ge} \quad (4.25)$$

$$\dot{\rho}_{ee} = \Omega \text{Im}(\rho_{ge}) - \gamma \rho_{ee} \quad (4.26)$$

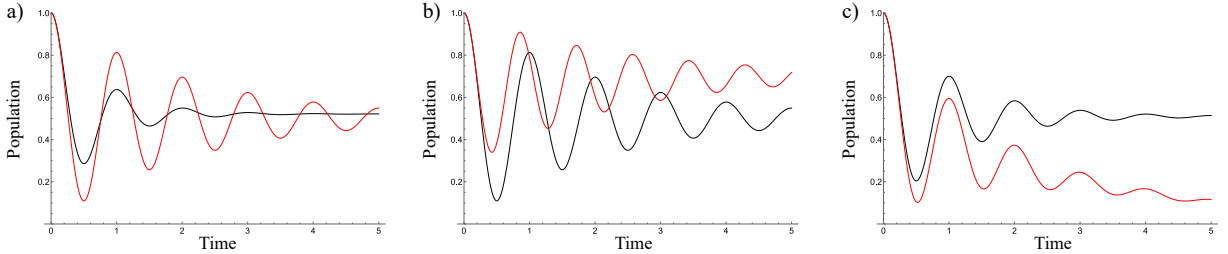


Figure 4.2: Qualitative density matrix time evolution examples, $\Omega > \gamma$ a) Larger γ (black) vs smaller γ (red) b) No detuning (black) vs detuning (red) c) Closed two-level system (black) vs 50% branching ratio (red)

We expect that on resonance in the closed two-level atom, for $\Omega/\gamma \rightarrow \infty$ the population in either state approaches .5 as $t \rightarrow \infty$. Some examples of the dynamical evolution of two-level atom given by Eqs. (4.24-4.26) are shown in Fig. (4.2). It is possible that the two-level system is not closed as treated here, some of the decays could exit the two-level system, modifying the repopulation term in the ground state equations.

4.2.3 Fitting Function for two-level atom

With the basic theory describing the light-atom interaction, we now derive expected functional form of the 2S-8D transition from the optical Bloch equations. Let us investigate the optical Bloch equations (Eqs. (4.24-4.26)) in the weakly driven limit. There is minimal repopulation of the ground state via spontaneous emission in our case, the branching ratio is less than 6% to the ground state, so we will remove the $\gamma\rho_{ee}$ term in the ρ_{gg} equation giving

$$\dot{\rho}_{gg} = -\Omega\text{Im}(\rho_{ge}) \quad (4.27)$$

$$0 = -i2\pi(\Delta\nu)\rho_{ge} + i\frac{\Omega}{2}(\rho_{gg} - \rho_{ee}) - \frac{\gamma}{2}\rho_{ge} \quad (4.28)$$

$$0 = \Omega\text{Im}(\rho_{ge}) - \gamma\rho_{ee}. \quad (4.29)$$

We can solve for ρ_{ee} in terms of the coherence ρ_{ge} . Solving for the coherence we find

$$\rho_{ge} = \frac{1}{(2\pi\Delta\nu)^2 + (\gamma/2)^2} \left(\frac{\Omega}{2}\Delta\nu(\rho_{gg} - \rho_{ee}) + \frac{i\Omega\gamma/2}{2} \right). \quad (4.30)$$

Since the imaginary part of ρ_{ge} determines $2\pi\gamma\rho_{ee}$ and $\rho_{gg} + \rho_{ee} = 1$, we find

$$\rho_{ee} = \frac{\Omega^2/4}{(2\pi\Delta\nu)^2 + (\gamma/2)^2} (1 - 2\rho_{ee}). \quad (4.31)$$

Finally, solving for the excited population we find

$$\rho_{ee} = \frac{\Omega^2/4}{\Omega^2/2 + (2\pi\Delta\nu)^2 + (\gamma/2)^2}, \quad (4.32)$$

which is a Lorentzian function of the detuning, which is a very well-known result. As a connection to classical physics, the response function of a damped harmonic oscillator is also a Lorentzian as a function of the detuning.

In reality, the 2S-8D transition is not exactly matched by the physics we assumed in the derivation of the Lorentzian lineshape. For one, the Rabi frequency Ω is a function of time, and we are

measuring the remaining metastable population in lieu of the fluorescence of the excited state. To acquire a more accurate lineshape, we now solve for the ground state population. The equation governing the ground state is

$$\dot{\rho}_{gg} = -\Omega \text{Im}(\rho_{ge}). \quad (4.33)$$

We now make some simplifying assumptions. First, we assume that the population in the excited state is small and that the coherences adiabatically follow the populations ($\dot{\rho}_{ge} \approx 0$). Then, the time evolution of the ground state is

$$\dot{\rho}_{gg} = -\frac{1}{2} \frac{\gamma \Omega^2}{(2\pi \Delta\nu)^2 + (\gamma/2)^2} \rho_{gg} \quad (4.34)$$

The solution to this linear, first-order ODE is well-known, and is

$$\rho_{gg}(t) = \exp\left(-\int_0^t \frac{1}{2} \frac{\gamma \Omega^2}{(2\pi \Delta\nu)^2 + (\gamma/2)^2} d\tau\right), \quad (4.35)$$

remembering that Ω is a function of time. Note we have implicitly assumed that Ω varies much more slowly than the dynamics set by γ . This assumption is valid within parameter space that we perform this experiment in. This solution is functionally the same as $e^{-\text{Lorentzian}}$ with the amplitude of the Lorentzian dip being given by the intensity of the light. We can see that in the low intensity limit we recover a Lorentzian profile again, which follows our expectations.

In this derivation, we have implicitly assumed that the detuning term, $\Delta\nu$, is time independent. With the presence of the ac-Stark shift, this is not the case. However, we can see that if the ac-Stark effect is less than the linewidth, this approximation is valid. While it is true that at large intensities this approximation breaks down, the low intensity limit is fundamentally more important because we are performing ac-extrapolations – if the fit function produces accurate extrapolations to zero field, small deviations at large intensities can be tolerated. This is later confirmed in Chapter 5 when we compare our analytic functions to a full numeric model.

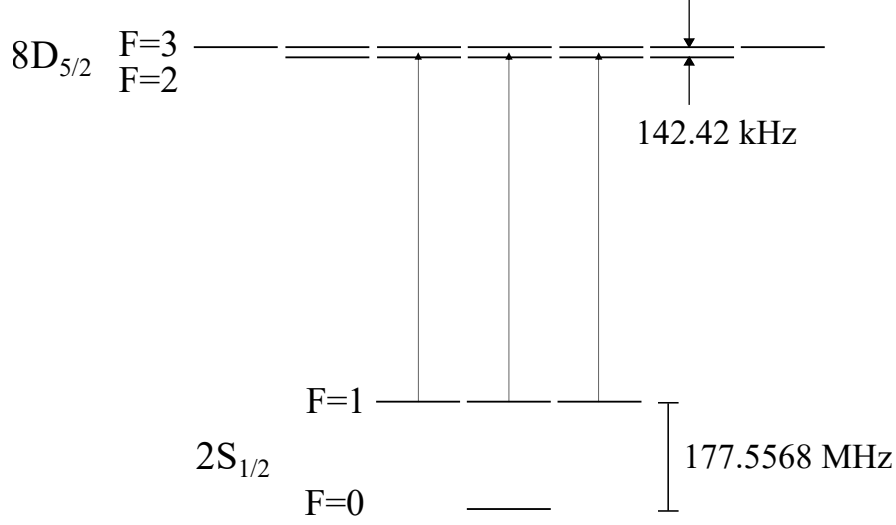


Figure 4.3: The level structure of the $2S_{1/2}$ and $8D_{5/2}$ states. The lifetime of the 8D state determines the linewidth of each hyperfine manifold ($F = 2, 3$) which is 572 kHz, leaving the 8D hyperfine structure unresolved.

4.2.4 Fitting Function

We now determine an appropriate low-intensity Lorentzian-like profile to properly describe our transition. In Fig. 4.3, the level structure of the $2S_{1/2}$ - $8D_{5/2}$ transition is shown. A straightforward approach is to fit with two Lorentzian functions to account for the unresolved hyperfine structure of the 8D manifold.

$$\mathcal{L} = \frac{\alpha_2(\frac{1}{2}\gamma)^2}{(\nu - \nu_2)^2 + (\frac{1}{2}\gamma)^2} + \frac{\alpha_3(\frac{1}{2}\gamma)^2}{(\nu - \nu_3)^2 + (\frac{1}{2}\gamma)^2} \quad (4.36)$$

The ratio of α_2 and α_3 can be constrained by the population driven to the two states, or by the relative strengths of these transitions. We know $\rho_{ee} \propto \Omega^2$, therefore

$$\frac{\alpha_3}{\alpha_2} = \frac{(\Omega_3)^2}{(\Omega_2)^2} = \frac{\sum_{m_F} (\beta_{3,m_F})^2}{\sum_{m_F} (\beta_{2,m_F})^2} = 3.5 \quad (4.37)$$

where the sum over the m_F sublevels is determined by the two-photon selection rules governing the transition. For linearly polarized light, this sets $\Delta m_F = 0$, so the sum is over $m_F = -1, 0, 1$. We can further reduce the free parameters in the fit by applying the hyperfine weighting and splitting to the $F = 3$ and $F = 2$ components. The hyperfine splitting of the 8D state is 142.43 kHz, and

the multiplicity of the $F = 3$ and $F = 2$ states are 7 and 5 respectively. The hyperfine centroid is $5/12 \times 142.43$ kHz below the $F = 3$ state and $7/12 \times 142.43$ kHz above the $F = 2$ state. We can therefore replace ν_2 and ν_3 by a single parameter, ν_c , and α_2, α_3 by α_0 , giving

$$\mathcal{L}(\alpha_0, \nu_c, \gamma) = \alpha_0 \left(\frac{(\frac{1}{2}\gamma)^2}{(\nu + \frac{7}{12}\text{HFS} - \nu_c)^2 + (\frac{1}{2}\gamma)^2} + \frac{3.5(\frac{1}{2}\gamma)^2}{(\nu - \frac{5}{12}\text{HFS} - \nu_c)^2 + (\frac{1}{2}\gamma)^2} \right) \quad (4.38)$$

where ν_c is the hyperfine centroid for our Lorentzian fit.

From our second-order approximation of the lineshape of the two-level atom, Eq. (4.35), we found that the lineshape is more closely matched a functional form of $e^{-\text{Lorentzian}}$. Given that in the three level atom, the equation governing the ground state will have the form $\dot{\rho}_{11} = -\Omega_2 \text{Im}(\rho_{12}) - \Omega_3 \text{Im}(\rho_{13})$, this naturally leads to our three-level fitting function, \mathcal{F} , which is given by

$$\mathcal{F} = A \exp(-\mathcal{L}(\alpha_0, \nu_c, \gamma)), \quad (4.39)$$

where the free parameters are the off-resonant count rate A , the metastable quenching parameter α , the effective centroid frequency ν_c , and the effective linewidth γ .

As an aside, it turns out that the relative weighting of the $F = 3$ and $F = 2$ hyperfine levels is light-polarization independent. Calculation of Eq. (4.37) in the case of circularly polarized light also gives a factor of 3.5. This means that our fitting function is robust against impure polarization states in the absence of external fields. It should be noted that ν_c is related to the hyperfine centroid of the transition. Practically speaking, the $2S_{1/2}$ hyperfine structure must be added to ν_c to report the true centroid frequency of the $2S_{1/2}$ - $8D_{5/2}$ transition.

4.3 Functional behavior of the ac-Extrapolations

4.3.1 The ac-Stark shift

The ac-Stark effect is the shift of the atomic energy levels due to a rapidly oscillating electric field of our spectroscopy laser [175]. This effect can be quite small in one-photon spectroscopy

experiments, but due to the large field intensities required to drive substantial population in two-photon transitions, the ac-Stark shift is our dominant systematic effect [25,43,44]. To give perspective, we have performed a $\approx 10^{-12}$ level measurement on the 2S-8D line. The atomic transition frequency is on the order of 770 THz, and the ac-Stark shifts we will commonly see will be on the order of 200 kHz. That means to accurately quantify this effect, which is our largest systematic shift, we need to understand the effect at the kHz level. Experimentally, this is achieved by performing an extrapolation on the measured resonance frequency vs the excitation power. Each scan of the resonance is fit with Eq. (4.39), and ν_c as a function of probe power (given by a photodiode voltage) forms the data set to be extrapolated. Properly analyzing this extrapolation is critical to our measurement.

The shift due to the ac-Stark effect on state $|n\rangle$ levels can be written as

$$\Delta\nu_{ac}(n) = \beta_{ac}(n)I(t) \quad (4.40)$$

where $\beta_{ac}(n)$ is the ac-Stark coefficient for state $|n\rangle$. In general, β_{ac} is laser frequency dependent, but are constant to a good approximation in the tuning ranges in which spectroscopy is performed for two-photon transitions. For the 2S-8D transition, $\beta_{ac} \approx 4 \text{ mHz}/(\text{W}/\text{m}^2)$ for the 6 hyperfine transitions that contribute in the spectroscopy. While the ac-Stark coefficient appears quite small, the optical intensities driving the 2S-8D transition are quite large. For an order of magnitude estimate, the ac-shifts will be on the order of 100 kHz as the optical intensities seen by the atoms can easily reach $5 \text{ kW}/\text{cm}^2$. Despite the linear shift of the states with intensity, it is perhaps naive to expect that the ac-Stark effect results in a strictly linear shift in the transition resonance with respect to the spectroscopic intensity. The reality of the situation is that while the ac-Stark effect largely results in a linear shift of the transition, this is only valid in certain conditions. For instance, in the case that the ac shifts are comparable to or larger than the linewidth of the transition, $\Delta\nu_{ac} > \gamma$, a time-varying ac-Stark effect can distort the lineshape, leading to nonlinearities in power extrapolations. This requires ac-Stark shifts $\Delta\nu_{ac} > 572 \text{ kHz}$, which is not something observed in our experiment. Furthermore, since we are performing extrapolations to zero field, the contribution of this

distortion become negligible in the low-field limit and therefore is not a concern. Another situation where the ac-Stark effect can exhibit nonlinearities is when atoms sample a distribution of intensity profiles – i.e. some atoms may sample the peak of the intensity profile but others may only sample the wings. In the case of a non-uniform sampled intensity profile, the nonlinearity arising in the ac-Stark shift is largely due to saturation. In certain regimes, atoms along high-intensity sampling trajectories can saturate while atoms sampling the wings of the intensity profile do not. Due to this saturation, atoms along the wings contribute relatively more to the overall signal as compared to when there is no saturation, leading to an effective reduction in the ac-Stark shift at high saturation intensities.

4.3.2 Effect of spatial distribution in ac-extrapolation

We wish to find the functional form of the nonlinearity present in the ac-extrapolations. If the ac-Stark shift is within a linewidth of the transition, the net shift can be considered due to the average intensity profile seen by the atom through the 778 nm beam. In the case of many atomic trajectories contributing to the overall line, the contribution of each trajectory is weighted by the population driven in that trajectory. Such a distribution of atomic trajectories arises from the finite size of the metastable atomic beam and its divergence.

The average ac-Stark shift experienced by the atoms weighted by the population driven is

$$\langle \Delta\nu_{ac} \rangle = \frac{\int (1 - \rho_{gg}(s)) \Delta\nu_{ac}(s) ds}{\int (1 - \rho_{gg}(s)) ds}, \quad (4.41)$$

where s is the transverse distance from the peak of the 778 nm intensity profile. If $\rho_{gg}(s)$ is uniform in s over the bounds of integration, as would be the case if the width of the 778 nm Gaussian beam is much greater than the spread of the metastable beam, investigation of Eq. (4.41) indicates we will find a linear shift with intensity. Relying on the result in the previous section, the population driven to the excited state(s) will be of the form

$$1 - \rho_{gg} = 1 - \exp[-\alpha I_0^2 e^{-ks^2}], \quad (4.42)$$

which follows from Eq. (4.35) and the fact that Ω is proportional to I_0 . We may now consider $\langle \Delta\nu_{ac} \rangle$ in a range of circumstances. First, let us consider the situation where the size of the spatial distribution is comparable to the 778 nm beam width, but the total population driven is small. Then $\rho_{gg} \approx 1 - \alpha e^{-ks^2} I_0^2$, and

$$\langle \Delta\nu_{ac} \rangle = \frac{\int e^{-ks^2} I_0^2 \Delta\nu_{ac}(s) ds}{\int e^{-ks^2} I_0^2 ds}. \quad (4.43)$$

Since we know that $\Delta\nu_{ac}$ is proportional to intensity we find

$$\langle \Delta\nu_{ac} \rangle = \frac{\int e^{-ks^2} I_0^2 (I_0 \beta_{ac} e^{-ks^2}) ds}{\int e^{-ks^2} I_0^2 ds} = I_0 \frac{\int f(s) ds}{\int g(s) ds}, \quad (4.44)$$

where $f(s)$ and $g(s)$ are just spatially dependent functions. In the case of no saturation, the ac-Stark shift is still linear in intensity (or power).

We estimate the effect of saturation by keeping another term in our series expansion of $(1 - \rho_{gg}(s)) \approx e^{-ks^2} I_0^2 - \frac{1}{2} e^{-2ks^2} I_0^4$. Using this two term approximation of $1 - \rho_{gg}$ we find that Eq. (4.41) takes the form

$$\langle \Delta\nu_{ac} \rangle \approx f_1(\Delta s) I_0 - f_2(\Delta s) I_0^3, \quad (4.45)$$

where $f_i(\Delta s)$ are constants that depend on the size of the spatial distribution and the Gaussian beam. Therefore, we find that the nonlinearity introduced in the ac-extrapolation from moderate saturation is cubic. It is also worth noting that this result is not highly dependent on the exact nature of $\rho_{gg}(s)$ – that is the metastable spatial distribution. Therefore, a day's extrapolation, consisting of many measured $\{\bar{V}, \nu_c\}$ pairs, will be fit with a function of the form $\nu_c(V) = \nu_0 + aV + bV^3$, with free parameters (ν_0, a, b) , with ν_0 corresponding to the unperturbed resonance frequency.

4.4 Conclusion

In this chapter, we presented the basic light-atom theory and used it to recover the lineshape expected in 2S-8D spectroscopy. We have also considered the nonlinearity introduced into the ac-extrapolations due to the contribution of different atomic trajectories. This distribution of trajectories dominantly introduces a cubic term in the extrapolation due to the saturation of the transition.

Chapter 5

The Numeric Model

5.1 Introduction

While we have chosen to fit measured lineshapes and the associated generated ac-extrapolations with analytic functions, we have also developed a numeric $2S_{1/2}$ - $8D_{5/2}$ lineshape model. This numeric model primarily serves two purposes. First, the numeric model can be used to verify that the lineshape fitting function and ac-extrapolation fitting function derived in the preceding chapter capture the physics suitably within the appropriate parameter space. Second, the numeric model can be used to identify individual systematic effects. In particular, the numeric model will be used to characterize stray dc-electric fields, which can both distort and shift the $2S_{1/2}$ - $8D_{5/2}$ line.

In reality, we have created two numeric models: one using the based on the state amplitudes and one using density matrices. The density matrix model was made to examine the effect of repopulation of the $2S$ state in the analysis, which we have largely found to be a very minor effect. Due to the relatively cumbersome nature of the density matrix formulation when a large number of states are considered, and the minor contribution of spontaneous emission in the result, we have opted to include the dc-Stark effect in a state amplitude based model. In both models we have included experimental geometry effects (time-varying light interaction and metastable spatial distribution), the ac-Stark effect, second-order Doppler effect, the velocity distribution of the atoms, and ionization out of the $8D$ state. The density matrix approach also includes the repopulation of the $2S$ state via spontaneous emission, and the state amplitude formulation includes the $8F_{5/2}$ states to model the effect of stray electric fields. For the application of testing systematics, either the density matrix or amplitudes formulation may be used. To characterize the presence of stray electric fields, we use the amplitude based model, and we will generally refer to the amplitude formulation as the numeric model.

As mentioned, it is possible to directly fit measured 2S-8D lines with the numeric model. However, the numeric model depends on a number of parameters which are not known precisely and are also not orthogonal degrees of freedom. For instance, the exact ratios of the calculated two-photon matrix elements to the ac-Stark matrix elements can couple to the size of the metastable spatial distribution. Nevertheless, we have checked that our experimental data can be fit with reasonable experimental parameters and produces nearly identical extrapolated line centers as when using the simple analysis presented in the last chapter.

In this chapter, we derive the numeric lineshape model's equations of motion and then add additional effects relevant to the 2S-8D transition. We investigate the accuracy of the derived fit functions by comparison to modeled data. The distortions and shifts arising from the dc-Stark effect and possible couplings to the ac-Stark shift are also investigated.

5.2 The 2S-8D Transition

We need to generate the equations of motion for the 2S and 8D states participating in our spectroscopic experiment. The 2S state is populated via a two-photon excitation. The hyperfine splitting of the 1S and 2S states is large enough and the transit time long enough that we can consider the population in $2S^{F=0}$ to be zero. We assume that our ground state (1S) atoms are equally populated in the $F = 1, m_F = 0, \pm 1$ levels. There is no tensor component when calculating β_{ij} 's for the 1S-2S transition [68], and therefore the $1S_{m_F=\pm 1}^{F=1} \rightarrow 2S_{m_F=\pm 1}^{F=1}$ and $1S_{m_F=0}^{F=1} \rightarrow 2S_{m_F=0}^{F=1}$ matrix elements have the same magnitude. This means that the 2S $F = 1$ hyperfine manifold is equally populated as well. The dynamics of the metastable excitation are completed before excitation of the 2S-8D line. Additionally, the lifetime of the 2S state is $\approx .77$ s so no appreciable decay occurs in the 10^{-3} s after excitation and before detection. The hyperfine splitting of the $8D_{5/2}$ manifold is 142.43 kHz [5] and the natural linewidth of the 8D states is 572 kHz [45], so that the $F = 3$ and $F = 2$ states are not resolved and we must consider both together. We choose to drive the 2S-8D transition with linearly polarized light, which will define the z -axis in the experiment. The two-photon selection rules for linearly polarized light $\Delta L = 2$ dictate that $\Delta m_F = 0$, reduc-

ing the 7 and 5 sublevels of the $F=3$ and $F=2$ hyperfine states respectively to just the $m_F = 0, \pm 1$ sublevels. With these considerations our equations of motion for a given m_F set become

$$i\dot{c}_1 = \frac{\Omega_{12}(t)}{2}c_2 + \frac{\Omega_{13}(t)}{2}c_3 \quad (5.1)$$

$$i\dot{c}_2 = \frac{\Omega_{12}(t)}{2}c_1 + (\omega_{12} - 2\omega + -i\frac{\gamma}{2})c_2 \quad (5.2)$$

$$i\dot{c}_3 = \frac{\Omega_{13}(t)}{2}c_1 + (\omega_{13} - 2\omega - i\frac{\gamma}{2})c_3, \quad (5.3)$$

where c_i corresponds to the amplitude for the $F = i$ state (conveniently we have $F = 1, F = 2,$ and $F = 3$), ω_{ij} corresponds to the angular frequency splittings between states i and j , and we use a corresponding definition for Ω_{ij} . A similar set of three coupled equations, with modified Ω_{ij} 's, exist for each hyperfine sublevel, making 9 total levels to be tracked in this treatment. Fig. (4.3) shows the relevant level structure and the connected states for this two-photon process. The hyperfine splittings and lifetimes of pertinent transitions can be found in Table 5.1.

Table 5.1: A table containing the hyperfine splittings and lifetimes of states used in modeling. A compilation of hyperfine splittings in hydrogen can be found in [5] and the lifetimes of the 8D and 8F states are calculated in [45]. The lifetime and splittings of the F states are important for including the dc-Stark effect.

State	Hyperfine splitting (kHz)	Linewidth (kHz)
2S _{1/2}	177556.8382(3)	.001
8D _{5/2}	142.430(140)	572.4
8F _{5/2}	101.620(100)	284.9
12D _{5/2}	42.20(40)	172
12F _{5/2}	31.10(30)	84

Calculation of $\Omega_{ij}(t)$ is nontrivial due to the calculation of β_{ij} . Unlike their one-photon counterparts, which merely require integrating $\langle \phi_i | \vec{r} | \phi_j \rangle$ and converting to the $|nLJFm_F\rangle$ basis, calculation of β_{ij} for two-photon transitions requires summing over all possible off-resonant pathways, including transitions to virtual states in the continuum. Another approach is to use a Greene's function formalism using Sturmian representations [176] Fortunately, the reduced matrix element for states up to $n = 20$ have been calculated in [68] and the process for recoupling these reduced

matrix elements into the $|nLJFm_F\rangle$ basis is also described. Once β_{ij} is determined, $\Omega_{ij}(t)$ is set by the geometry of the experiment. In our case, the metastable hydrogen beam traverses the excitation field at angle of $\theta \approx 6^\circ$ and the light is Gaussian radially. We may write the time dependence of the radial position as $r(t) = vt\sin(\theta)$ for an atom traversing the Gaussian beam. This gives a time dependent Rabi rate of

$$\Omega_{ij}(t) = 2(2)(2\pi\beta_{ij})I_0\text{Exp}\left(-2\frac{v^2t^2\sin^2(\theta)}{w^2} + 2\frac{s^2}{w^2}\right), \quad (5.4)$$

for atom with velocity v and beam $1/e^2$ width (in intensity) given by w . The extra factor of s allows for offsets from the peak of the Gaussian. Another factor of 2 arises in Eq. (5.4) due to excitation with counter propagating beams.

5.2.1 Inclusion of systematic effects in model

There are several systematic effects that must be considering when modeling the dynamics of the 2S-8D transition. These include the ac-Stark effect, the spatial distribution of metastable atoms, and, to a lesser extent, the second-order Doppler effect, and the velocity distribution.

The ac-Stark Effect

Both the 2S manifold and the 8D manifold are subject to shifts in the presence of an external time-varying electric field. As mentioned previously, the shift on state $|n\rangle$ levels can be written as

$$\Delta\nu_{ac}(n) = \beta_{ac}(n)I(t), \quad (5.5)$$

where $\beta_{ac}(n)$ is the ac-Stark coefficient for state $|n\rangle$. In general, β_{ac} is laser frequency dependent, but can be treated as constant to a good approximation in the tuning ranges in which this spectroscopy is performed (this is generally not true for one-photon transitions). The calculation of β_{ac} requires determining the matrix elements of the dynamic polarizability. These matrix elements are calculated using a Greene's function formalism [176], and the calculation of the scalar and tensor

Table 5.2: ac-Stark coefficients for the states important to the modeling. Coefficients for n up to 20 given in [68]. The scalar ac-Stark coefficients for the 8F states are identical with the 8D states to about 1%.

State	$\beta_{ac}^{(0)}$ (Hz/(W/m ²))	$\beta_{ac}^{(2)}$ (Hz/(W/m ²))
2S	-1.66537×10^{-3}	N/A
8S	1.36562×10^{-3}	N/A
8D	3.03968×10^{-3}	3.03968×10^{-5}
12D	2.83068×10^{-3}	3.17867×10^{-5}

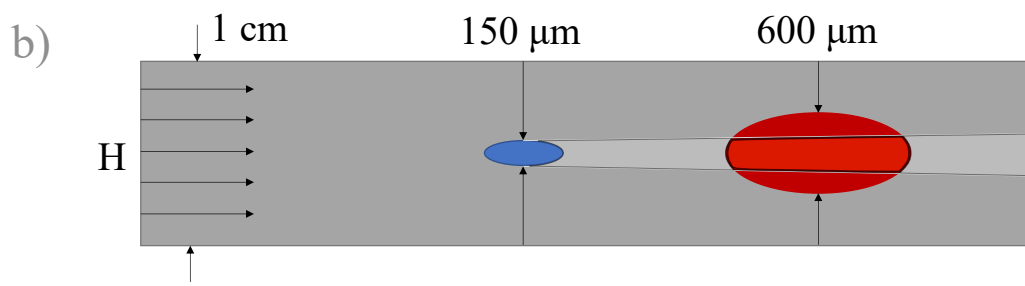
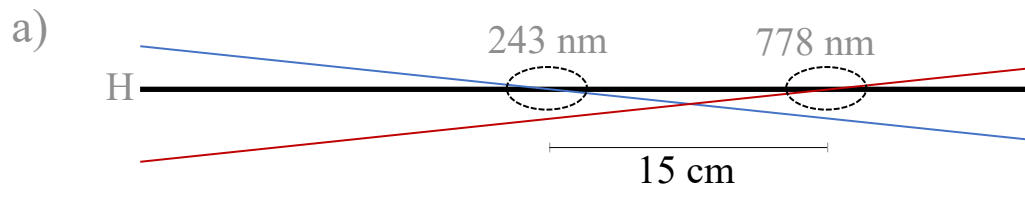
β_{ac} 's, $\beta_{ac}^{(0)}(n)$ and $\beta_{ac}^{(2)}(n)$ respectively, is given in [68]. Perturbations to state $|g\rangle$ from a perturbing potential $U(t)$ in this formalism are calculated as $\langle g|U(t)\frac{1}{E_g-H_0+\hbar\omega_L}U(t)|g\rangle$, and the real part of this matrix element corresponds to the ac-Stark shift on $|g\rangle$. Much like the reduced β_{ij} 's that appear in the calculation of the Rabi rate, determining the proper ac-Stark coefficient requires coupling into the $|Fm_F\rangle$ basis for the D states. Inclusion of the ac-Stark effect in the differential equations of motion introduces a detuning term, $2\pi\beta_{ac}I(t)$, that is added to the ω_{ij} in the amplitude equations of motion. This term requires calculating the total change in the splitting between the 2S and 8D state (so the effective ac-Stark coefficient is given by $(\beta_{ac}(8D) - \beta_{ac}(2S))$). A table of β_{ac} 's used in this modeling can be found in Table 5.2.

As indicated in section 4.3.2, the presence of many atomic trajectories can effectively introduce a nonlinearity in the ac-Stark effect. We therefore must include the many atomic trajectories into the model since the metastable atoms excited by the 243 nm light have an effective spatial distribution. We now turn our attention to the metastable spatial distribution.

Metastable Spatial Distribution

From purely geometric considerations, the metastable hydrogen beam generated by the 243 nm light samples a non-negligible fraction of the total 778 nm intensity profile. As just discussed, this spatial distribution introduces a nonlinearity in the ac-Stark shift power extrapolations and warrants inclusion in the model.

The atom-light interaction volumes are depicted in Fig. 5.1. The hydrogen beam interacts at a distance of 2 m away from the effusive nozzle, and the 243 nm beam diameter is about 150 μm at the overlap, which defines a metastable beam divergence of about 1.5 mrad and a Gaussian



lineshape achieved sampling a spatial distribution over Δs given by $\rho(s)$, $L^s(\omega, \Delta s)$, can be found as

$$L^s(\omega, \Delta s, v) = \int \tilde{L}(\omega, s, v)\rho(s)ds. \quad (5.6)$$

Much like the spatial distribution, the velocity distribution, as determined in 2.4, is included in the model by modeling each velocity class separately and integrating. If the velocity distribution is given by $\rho_v(v)$ the overall lineshape, $L(\omega, \Delta s)$, is given by

$$L(\omega, \Delta s) = \int L^s(\omega, \Delta s, v)\rho_v(v)dv. \quad (5.7)$$

Second-order Doppler shift

A metastable atom's velocity affects the spectroscopy primarily through two effects: the total interaction time with the spectroscopic light and the second-order Doppler shift. Slower metastable atoms require less optical power to drive population to the 8D state, so saturation is more prominent on the slow atoms. The second order Doppler shift (SODS) can couple to the velocity distribution, but, due to the relatively small size of the SODS (less than a kHz), the difference between including the SODS in the differential equation or applying the SODS for the most probable class leads to nearly identical results.

The relativistic Doppler effect causes a frequency shift between the lab frame and the constant velocity frame of the atom.

$$\nu_{2S-8D} = \sqrt{\frac{1 - (v/c)}{1 + (v/c)}}\nu_H \quad (5.8)$$

Where v is the velocity of the atom (moving towards the light source) and c is the speed of light. Typically, the Doppler shift is expanded in powers of (v/c) as

$$\nu_H = \nu_{2S-8D} + (v/c)\nu_{2S-8D} + \frac{1}{2}(v/c)^2\nu_{2S-8D} + \dots \quad (5.9)$$

Since our hydrogen atoms are at ≈ 5 K, they will have a velocity of on the order of 400 m/s, so we expect the first-order term to be on the order of 1 GHz. In a two-photon transition, neither two

“incoming photons” or two “outgoing photons” can contribute in the process, as these processes would be ± 2 GHz detuned from a 572 kHz linewidth transition. Therefore, we expect a heavy suppression of the first-order Doppler effect. The second-order effect does not cancel, and has a magnitude of about 700 Hz for atoms moving at 400 m/s. Therefore, we would have to apply a +700 Hz shift to correct for this effect. Inclusion of this effect in the lineshape model amounts to including the term $\frac{1}{2}(v/c)^2(770.65 \times 10^{14})2\pi$ in the frequency detuning term in the $F = 2$ and $F = 3$ states.

Ionization

Ionization plays a minor role in the dynamics of the 2S-8D transition. An atom, once in the 8D state, can be excited into the continuum via a one step process. Like the Rabi rate and ac-Stark shift, the ionization rate can be modeled as being linear with the intensity

$$\gamma_i(n) = \beta_{ion}(n)I(t), \quad (5.10)$$

where $\beta_i(n)$ is the ionization coefficient for state $|n\rangle$, and is related to the complex part of the dynamic polarizability of the state. The ionization coefficient is about two orders of magnitude down from the ac-Stark coefficient, and thus we can anticipate the largest ionization rates on the order of about 2 kHz, which is a largely negligible effect as there is no direct associated shift. The only possibility for a shift being introduced is via the broadening acting as another “saturation” effect in the ac-Stark extrapolation. This could slightly modify the nonlinearity of the extrapolation. To contrast the small 2-3 kHz of broadening due to ionization at large interrogation intensities, the saturation and power broadening of the transition can easily amount to 300 kHz.

The Differential Equations

We now rewrite the set of differential equations describing the time evolution of our states for a particular m_F sublevel including the extra effects outlined resulting in

$$i\dot{c}_1 = \frac{\Omega_{12}(t, v, s)}{2}c_2 + \frac{\Omega_{13}(t, v, s)}{2}c_3 \quad (5.11)$$

$$i\dot{c}_2 = \frac{\Omega_{12}(t, v, s)}{2}c_1 + (\omega_{12} - 2\omega + -i\frac{\gamma}{2} + \delta_{12}(t, v, s))c_2 \quad (5.12)$$

$$i\dot{c}_3 = \frac{\Omega_{13}(t, v, s)}{2}c_1 + (\omega_{13} - 2\omega - i\frac{\gamma}{2} + \delta_{13}(t, v, s))c_3, \quad (5.13)$$

where

$$\delta_{ij} = 2\pi[\beta_{ac}(j) - \beta_{ac}(i)]I(t, v, s) + \frac{v^2}{2c^2}\omega_{ij}. \quad (5.14)$$

These sets of equations describe the population dynamics for a particular velocity class sampling a particular intensity profile – inclusion of the velocity and spatial distribution requires integration as shown in Eqs. (5.6) and (5.7). Practically, Eqs. (5.11-5.13) are numerically integrated for 51 laser frequencies as if we were scanning the transition with a laser, and this is done for many different 778 nm powers.

5.2.2 DC-Electric Fields

The dc-Stark effect due to the presence of nearby static electric fields is our other primary systematic. Unlike the ac-Stark shift, in which the qualitative behavior of the effect can be analytically approximated, the dc-Stark effect distorts the 2S-8D line in such a way that is not amenable to fitting accurately with approximate lineshapes. To this end, we have also included the dc-Stark effect in the model. While the numeric model primarily plays the role of verifying the accuracy of using Eq. (4.39) and a cubic power extrapolation, it is also used directly to quantify the magnitude of the stray electric fields and the corresponding shift.

With the numeric model, observed distortions in measured lineshapes can be used to quantify the magnitude of the stray electric field. To do so, a measured lineshape is fit with the numeric model directly, with the electric field strength as a fit parameter to match the distortion of the line. With the field strength determined from this model fit, the corresponding dc-Stark shift can be estimated. Since individual scans are fit with (4.39), we wish to quantify the effect of stray electric fields when fitting with that function. We do so by fitting modeled data, which is under the

influence of the measured electric field, with Eq. (4.39) and determining the difference from the dc-Stark free resonance frequency.

Theoretical background

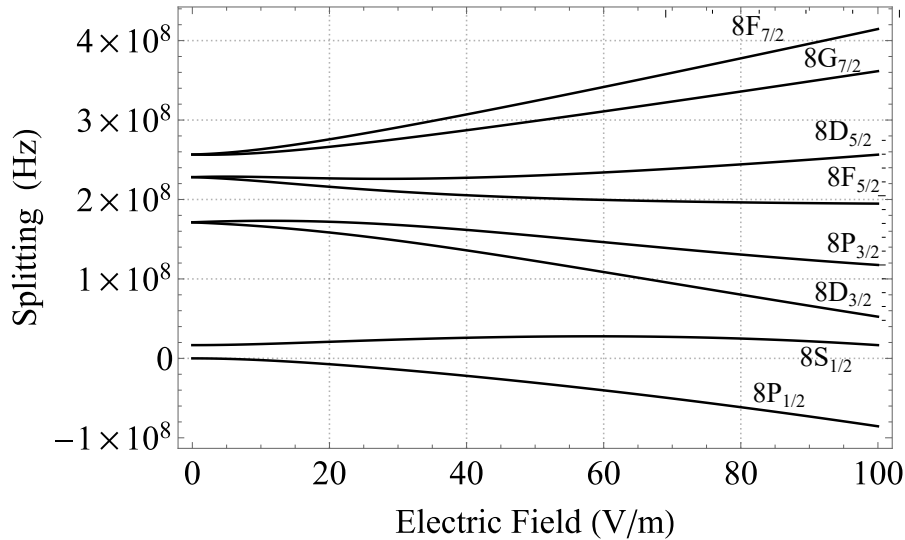


Figure 5.2: Splitting of the $n = 8$ manifold (considering fine-structure) assuming z -oriented electric field.

The dc-Stark effect is the splitting of atomic spectral lines by application of external electric fields [177]. Let us consider the effect of an applied electric field on a hydrogen atom. Treating the external field as a perturbation, we write

$$H = H_0 - \vec{\mathcal{E}} \cdot \vec{\mu}. \quad (5.15)$$

A given n manifold of the hydrogen atom is n^2 degenerate without considering fine-structure effects. This requires degenerate perturbation theory. The general strategy for dealing with the degeneracies is to solve the eigenvalue problem for $H = H_0 + H_p$ in the degenerate subspace (that is, the n manifold in question). Fig. (5.2) shows the splitting of the $n = 8$ manifold, including fine structure effects, using this approach. Unfortunately, the dc-Stark effect in this experiment is a bit more subtle due to the mixing of the $8D_{5/2}$ state with the $8F_{5/2}$ state. This mixing produces

structure in the lineshape that is comparable to the natural linewidth. A treatment of the dc-Stark effect on the 2S-8D transition is outlined in [45], where the dc-Stark effect is broken into two effects: the “linear effect”, which arises due to the distortion introduced by the mixing of the $8D_{5/2}$ and $8F_{5/2}$ states, and the “quadratic effect” which arises from a standard second-order perturbation treatment.

For the quadratic effect, standard second-order perturbation theory indicates the shift introduced to state $|n\rangle$ due to the dc-Stark effect is

$$\Delta E^2(n) = e^2 \mathcal{E}^2 \sum_m \frac{|\langle n | z | m \rangle|^2}{E_n - E_m}. \quad (5.16)$$

A calculation of the shift coefficients for the relevant states to our modeling are given in Tab. 5.3.

Table 5.3: Quadratic Stark shift coefficients for states of interest in this measurement. A similar table can be found in [45]

State	(kHz/(V/m) ²)
$8D_{5/2}$	-5.359
$8F_{5/2}$	-4.528
$12P_{3/2}$	-69.810
$12D_{3/2}$	-68.487
$12D_{5/2}$	-102.944
$12F_{5/2}$	-96.573

The $n = 8$ manifold

We can see from Eq. (5.16) that the Stark effect become much more dominant when there are nearby nearly degenerate states. The Lamb shift, the ~ 1 GHz splitting of the $2S_{1/2}$ and $2P_{1/2}$ states, breaks the degeneracy of the $n = 2$ manifold. However, the size of the Lamb shift decreases as n increases (scaling as $1/n^3$) as the effect is largely dependent on the electron wavefunction overlap at the nucleus [21]. Furthermore, the dipole matrix elements increase with n and the fine-structure splittings also decreases with n , with the $n = 8$ manifolds having splittings as small as

100 kHz for transitions of interest. Therefore, we can anticipate that the Stark effect on the 8D state will dominate the small effect of the electric fields on the 2S state.

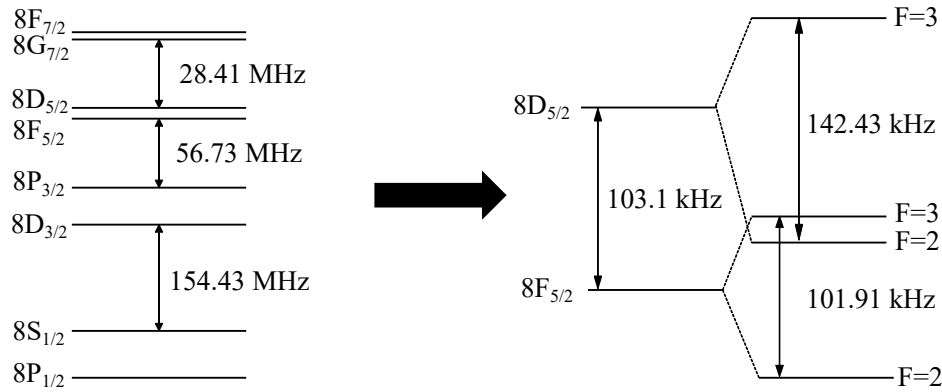


Figure 5.3: Structure of the $n = 8$ manifold. Note that the 8D lines have a linewidth of 572 kHz and the 8F states have a linewidth of 285 kHz.

As indicated previously, the dc-Stark effect also introduces a mixing between the $8D_{5/2}$ and the $8F_{5/2}$ state. From the level structure shown in Fig. (5.3), we can see that the resonances have significant overlap, and both have unresolved hyperfine structure. This means that in the presence of a static field, population is also driven to the $8F_{5/2}$ state via its coupling to the $8D_{5/2}$ state. In order to accurately model the effect of static fields on the lineshape, we must include the mixing between the $8D_{5/2}$ and $8F_{5/2}$ states.

Modification to the 2S-8D lineshape model

We must include the mixing of the 8D and 8F states as well as the quadratic shift introduced by a static electric field. To isolate the shift due to the dc-Stark effect, we will simulate lines under the weakly driven limit. In that case, the density matrix formulation is unnecessary since there will be negligible repopulation due to spontaneous emission, and we have found that the repopulation of the 2S state is a minor effect generally. As such, we modify the amplitude Eqs. (5.11-5.13). We will refer to the F states with an f , alongside g and e for 2S and 8D respectively. This results in a coupled set of differential equations given by

$$\dot{c}_g = -i \sum_e \frac{\Omega_{ge}}{2} c_e, \quad (5.17)$$

$$\dot{c}_e = (i\Delta\omega_e - \frac{\gamma_e}{2})c_e - i\frac{\Omega_{ge}}{2}c_g - \frac{i}{\hbar} \sum_f U_{ef}c_f, \quad (5.18)$$

$$\dot{c}_f = (i\Delta\omega_f - \frac{\gamma_f}{2})c_f - \frac{i}{\hbar} \sum_e U_{fe}c_e, \quad (5.19)$$

$$\Delta\omega_e = \omega - (\omega_e - \delta\omega_{\mathcal{E}}^{(e)}\mathcal{E}^2 + \delta_{ge}(t)), \quad (5.20)$$

$$\Delta\omega_f = \omega - (\omega_f - \delta\omega_{\mathcal{E}}^{(f)}\mathcal{E}^2 + \delta_{gf}(t)), \quad (5.21)$$

where $\delta\omega_{\mathcal{E}}^{(i)}$ is the quadratic Stark shift coefficient for state $|i\rangle$, δ_{ij} is the combined ac-Stark, and second order-Doppler detuning terms given by Eq. (5.14) and U_{ij} is the perturbing matrix element connecting states $|i\rangle$ and $|j\rangle$ (i.e. $-\langle i | \vec{\mathcal{E}} \cdot \vec{\mu} | j \rangle$). In Fig. (5.4), we display a selection of results for the $8D_{5/2}$ line for a variety of electric fields strengths oriented perpendicular to the light field.

Shifts from the dc-Stark shift arise from the quadratic level shift as well as the distortion of the resonance lineshape. Even at relatively small static fields of 3 mV/cm, the $2S_{1/2}$ - $8D_{5/2}$ begins to show a subtle, yet noticeable, distortion. This lineshape distortion can provides indication of the presence of static fields. Additionally, the distortion moves the resonance "center-of-mass" when fit with Eq. (4.39), which manifests as an additional shift with field strength. Evaluation of Eq. (5.16) gives a quadratic shift coefficient of $-53.59 \text{ Hz}/(\text{mV/cm})^2$ for the $8D_{5/2}$ sublevels. The $2S_{1/2}$ - $8D_{5/2}$ line is shifted by 1.286 kHz for a 3 mV/cm field and 4.835 kHz for a 6 mV/cm field, indicating that the shift due to the distortion comprises a large fraction of the total effect (the "quadratic" contribution corresponds to -480 Hz and -1.92 kHz respectively).

Since we intend to fit our real data on the $2S$ - $8D$ transitions with Eq. (4.39), the shift of the resonance is quantified by the difference between the fit ν_c and the expected ν_c given zero static field. In Fig. 5.5, we show the shift on the $2S_{1/2}$ - $8D_{5/2}$ line due to the dc-Stark effect as a func-

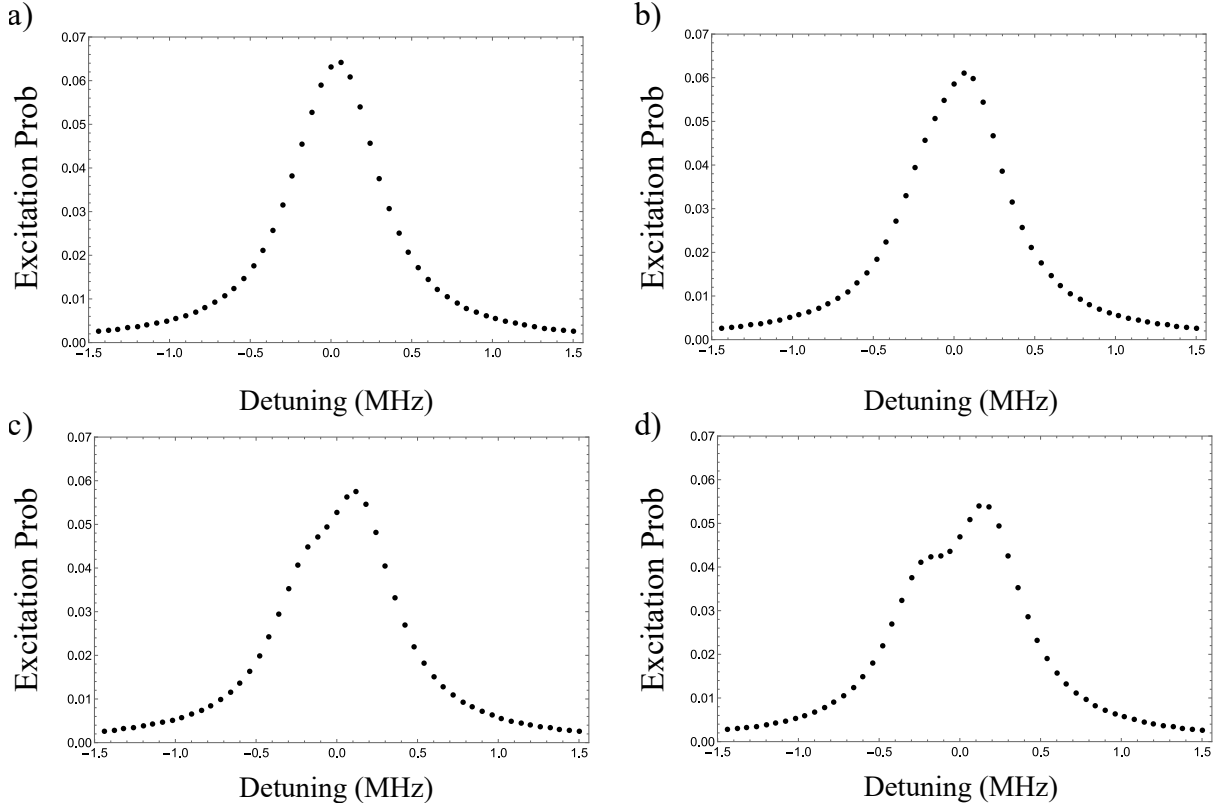


Figure 5.4: $2S_{1/2}$ - $8D_{5/2}$ modeled lineshape in electric fields, single velocity class and metastable spatial class. Lorentzian overlaid only for visual reference. a) 3 mV/cm field. b) 6mV/cm field. c) 9mV/cm field. d) 12mV/cm field.

tion of field strength, assuming the dc-field is perpendicular to the light polarization. There is a dependence of the U_{ef} terms within Eqs. (5.17-5.19) on the orientation of the electric field relative to the excitation polarization. As we will discuss in the next chapter, we have determined that the electric field orientation is largely perpendicular to the light polarization, so we assume a perpendicular field in our modeling as well. We have also created a numeric lineshape model including the dc-Stark effect for the $2S$ - $12D_{3/2}$ and $2S$ - $12D_{5/2}$ transitions, which are more sensitive to the presence of stray electric fields than their 8D counterparts.

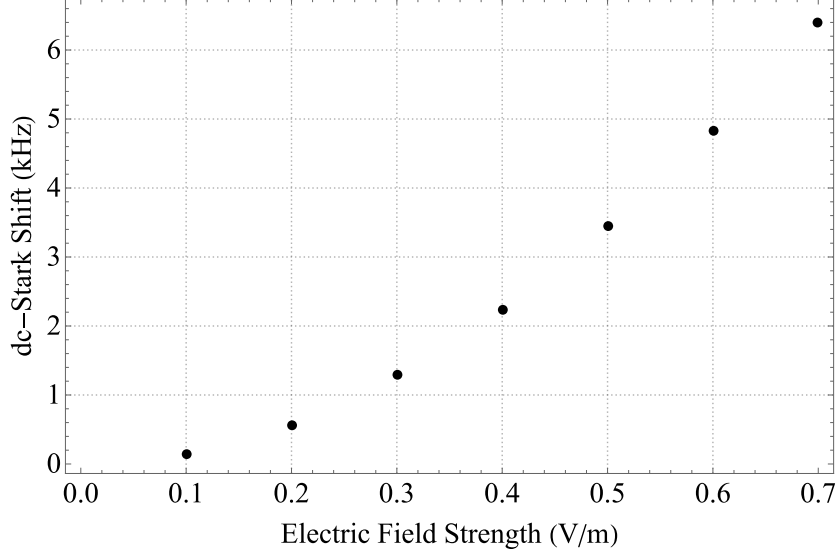


Figure 5.5: The magnitude of the dc-Stark shift on the $2S_{1/2}$ - $8D_{5/2}$ transition. Shift is given by difference between expected resonance frequency (zero dc-field) and the resonance frequency when fit with Eq. (4.39), assuming a perpendicular field.

5.2.3 Density matrix model

As indicated, we have also made a numeric model using density matrices to investigate the repopulation of the 2S state via spontaneous emission. Spontaneous emission is included in the von Neuman equation via the Lindblad operator acting on the density matrix, $\mathcal{L}\rho$, modifying the von Neumann equation to

$$i\hbar\dot{\rho} = [\rho, H] - \mathcal{L}\rho. \quad (5.22)$$

In our case, the effective 3-level atom is not closed— the majority of the decay paths lead back to the 1S state via the decay to the P states.

Inclusion of Branching Ratios

The 8D state largely decays into the nP states via spontaneous emission, which are most likely to decay back into the 1S state. However, some small fraction end up decaying to the 2S state. Furthermore, some of the atoms decay into the $2S_{1/2}^{F=0}$ state, which is largely a dark state. Our metastable detector cannot differentiate between $F = 0$ and $F = 1$ metastable atoms.

The lifetime of a state, and the associated branching ratios with spontaneous emission, can be estimated from Fermi's Golden rule. Fermi's Golden rule in this context can be stated as

$$\Gamma_{i \rightarrow f} = \frac{1}{\hbar} |\langle f | H | i \rangle|^2 g(\hbar\omega) \quad (5.23)$$

where $g(\hbar\omega)$ is the density of states of photons in vacuum and $\langle f | H | i \rangle$ is the dipole matrix element connecting hydrogen states $|i\rangle$ and $|f\rangle$. Summing over all possible dipole allowed decays from the 8D state allows us to estimate the lifetime of the 8D state, and the relative strength of each decay channel compared to the linewidth estimates the branching ratio. The branching ratio back to the 2S state is about 5.13%, with a 2/15 fractional decay rate into the $2S_{1/2}^{F=0}$ state [45]. Our density matrix model takes into account the different branching pathways back into the 2S state, and the relative redistribution of the m_F sublevels.

Inclusion of systematics in density matrix formulation

Since we have derived the equations of motion for the state amplitudes of the 2S-8D transition under the influence of relevant shifts and distributions, we will not repeat them here. It is sufficient to state that the Von Neumann equation is solved for the 2S and 8D manifolds, with the light field perturbation Hamiltonian connecting the $F = 1 \rightarrow F = 2$ and the $F = 1 \rightarrow F = 3$ states and the spontaneous decay back into the 2S manifold with the appropriate branching ratios included. The effect of metastable beam distributions and velocity distributions are still integrated over to generate the lineshape. We have found that the inclusion of 2S repopulation via spontaneous emission is a negligible effect, with zero-field extrapolated frequencies within ± 10 Hz of the values obtained when neglecting spontaneous emission.

5.3 Applications of the Numeric Model

While in principle the numeric model developed in the preceding section can be used to fit measured 2S-8D lineshapes, we only do so as a consistency check. The numeric model has many free running fit parameters: for example, the size and location of the metastable spatial distribution,

the temperature of the atomic beam, and the absolute power and size of the 778 nm beam. Additionally, if fitting with the numeric model is to be perfectly accurate, the ratios of the two-photon matrix elements and the ac-Stark matrix elements need to be known exactly. While we have great confidence in the calculations of [68], we do not want our experimental results to be dependent on these calculations. To circumvent these concerns, we instead fit our measured lines with the analytic function given by Eq. (4.39). Similarly, the extrapolations we generate to determine the zero-field resonance frequency will be fit with a cubic function, as derived in Chapter 4.

5.3.1 Fitting modeled ac-extrapolations

We wish to verify that the lineshape fitting function, Eq. (4.39), adequately approximates a scanned 2S-8D resonance. As mentioned in Chapter 4, the low-intensity limit is fundamentally more important as we are performing these extrapolations to zero-field. In Fig. 5.6, we show modeled data fit with the analytic function in the low intensity limit, and compare the fit residuals to the expected shot noise in our experiment, assuming count rates on the order of $10^4/s$. In this parameter space we expected a reduced chi squared $\chi_k^2 = 1$ for this fit assuming shot noise uncertainty only (since the residuals are dominated by the shot noise to many orders of magnitude in this example). For signal sizes on the order of 10^{10} counts/gate the fit residuals become comparable to the shot noise, though in the experiment, we are typically limited by technical noise and the count rates are much lower. As another consideration, in the low intensity limit, we expect that as $P \rightarrow 0$, $\nu_c \rightarrow 0$ (when ν_c is referenced to the mathematically defined resonance) when fitting modeled data. This may be quickly tested by artificially turning off the ac-Stark shift in the model and fitting a low-intensity line. Doing this, we find a fit $\nu_c = -10 \pm 30$ Hz, which is in excellent agreement at our target precision. There is no appreciable difference between the density matrix formulation or the amplitude formulation in this analysis. From these considerations, we believe using Eq. (4.39) is well-justified.

In section 4.3.2, it is argued that the inclusion of a metastable spatial distribution dominantly introduces a cubic term to the ac-Stark shift extrapolation. We now verify that fitting an ac-

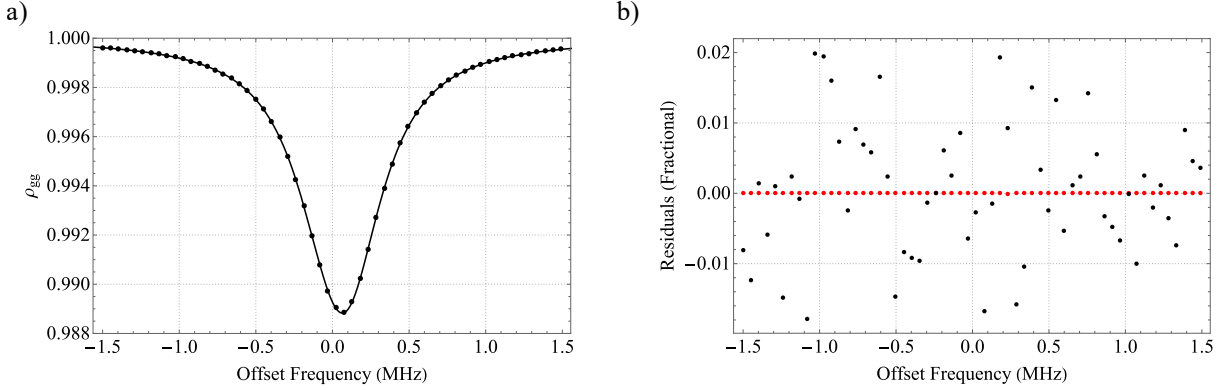


Figure 5.6: Fitting modeled data in the low intensity limit. a) Sample modeled line fit with Eq. (4.39) for 5 W, 600 μm 778 nm beam diameter, 550 μm spatial distribution. b) Expected shot noise (black) vs fit residuals (red). Shot noise estimated for 10^4 counts/gate, our typical count rate.

extrapolation generated from modeled data will accurately reproduce the zero-field resonance frequency to sufficient accuracy. In Fig. 5.7 b), three ac-Stark shift extrapolations with differential spatial distributions are displayed. The spatial distributions used in the model are uniform within some spread, then zero outside of that distance (flat-top distribution). To test the reliability of the cubic extrapolation, we have chosen to model a 450 μm , 550 μm , and a 750 μm sized metastable distribution. A spread of 350 μm is considered to be the absolute minimum of possible distribution size, and is exceedingly unlikely to be achieved in our measurement. Conversely, it is unlikely that distributions much larger than 750 μm are possible from geometric considerations, namely the size of the 778 nm cavity apertures in the Faraday cage constrain the relative angle between the two optical cavity modes. We believe that the most geometrically favored spatial distributions lie within 450-750 μm spreads. For each of the three spatial distributions, a function of the form $\nu_c(P) = a + bP + cP^3$ is used to fit the data, and the data set is composed of pairs $\{P, \nu_c(P)\}$ extracted from fitting with Eq. (4.39). For the 450 μm , 550 μm , and 750 μm distributions in Fig. 5.7, a zero field resonance frequency of -57 ± 22 Hz, 14 ± 5 Hz, and 42 ± 10 Hz are found respectively. Additionally, we have investigated the possibility of other spatial distribution shapes including a Gaussian and a pair of offset Gaussians. In either case, the functional behavior of the ac-extrapolation is still well-approximated by the cubic extrapolation. This is expected as the result in section 4.3.2 did not explicitly rely on the functional behavior of the spatial distribution.

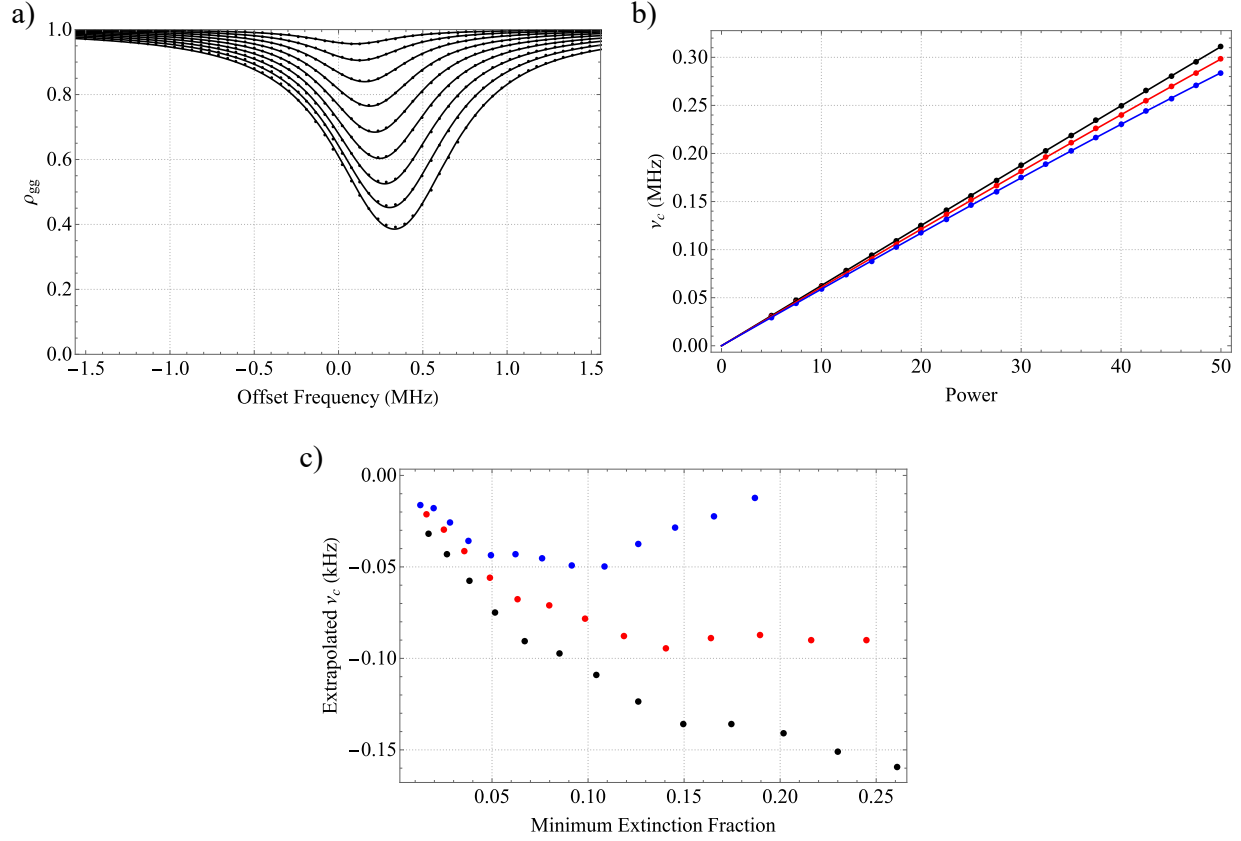


Figure 5.7: Model data with spatial distribution and velocity distribution a) 550 μm metastable spatial spread lineshapes fit with Eq. (4.39). b) Modeled ac-extrapolations for three spatial distributions fit with cubic function. Black: 450 μm spread. Red: 550 μm spread. Blue: 750 μm spread. c) Extrapolated ν_c as a function of minimum dip % used in ac-extrapolation. Black: 450 μm spread. Red: 550 μm spread. Blue: 750 μm spread.

The results from the fits in Fig. 5.7 b) indicate that the cubic extrapolation is accurately reproducing the expected resonance frequency to 1 in 10^{13} if 1% metastable quenching fractions (that is, how large the metastable dips are) are used in the ac-extrapolation. Given our metastable count rates of $\sim 10,000/\text{s}$, fitting lines with very small metastable quenching fractions is unreliable. Our measured extrapolations do not contain scans with less than 15% quenching fraction, we therefore investigate the sensitivity of the ac-extrapolations when including larger minimum dip percentage (metastable quenching fraction) as the lowest data point in the extrapolation in Fig. 5.7 c). If one takes a conservative approach and assumes that a 450 μm and 750 μm metastable spatial distribution are indistinguishable, the uncertainty would amount to ± 100 Hz. A 100 Hz uncertainty corresponds to a 1.3×10^{-13} measurement, which is sufficient at our precision goal.

5.3.2 ac-extrapolations in the presence of a dc-field

Of particular importance is whether the dc-Stark effect strongly perturbs the ac-Stark shift extrapolation. It is conceivable that the distortion of the 2S-8D lineshape could be strongly coupled to the excitation dynamics, varying the effective dc-Stark shift as a function of the population driven to the excited state. This would require a modification of the functional form of the extrapolation rather than just a modification of the extrapolation coefficients, i.e., the ac-extrapolation is no longer cubic with the light intensity. However, in the case of minimal cross-talk between the dc-Stark shift and the ac-Stark shift, the dc-Stark shift may be quantified independently and applied to the extrapolated zero-light field resonant frequency. We now estimate the magnitude of the cross-talk between the two expected leading systematics.

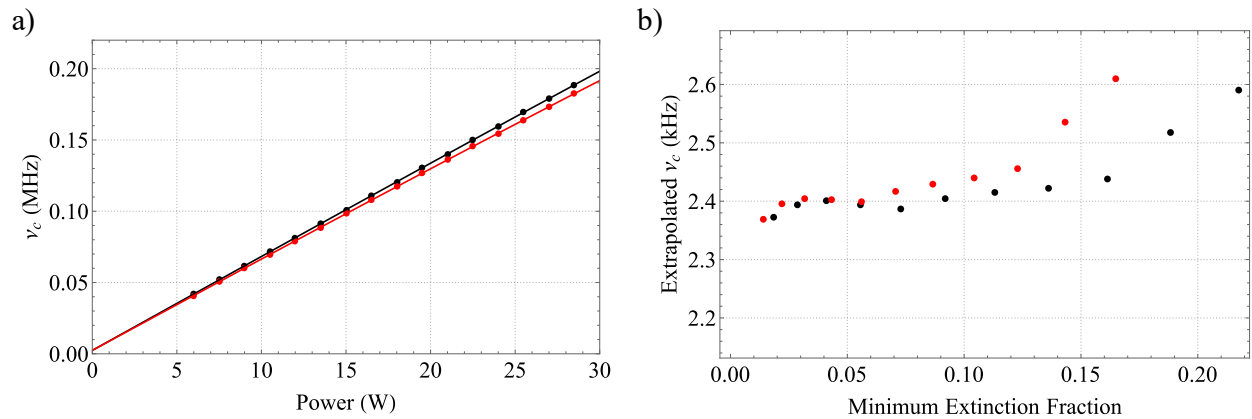


Figure 5.8: Cross talk check between ac and dc Stark effect. a) Two modeled ac-extrapolations of $550 \mu\text{m}$ and $750 \mu\text{m}$ metastable spatial distribution sizes under the influence of a 4 mV/cm electric field. b) The two extrapolations zero-field resonances as a function of minimum metastable extinction fraction (dip %) used in the ac-extrapolation.

The natural check for cross-talk between the systematics is to compare the extrapolated resonance frequency to the expected zero light-field frequency in the presence of an electric field. In Fig. 5.8 a), two modeled ac-extrapolations are shown, both in the presence of a dc-electric field of 4 mV/cm strength, perpendicular to the light polarization. The black data set corresponds to a metastable spatial distribution of $550 \mu\text{m}$ and the red to a $750 \mu\text{m}$ spatial distribution, with both data sets being fit with cubic functions. In Fig. 5.8 b), the extrapolated zero light-field resonance

frequency as a function of the minimum dip size is shown. The expected dc-Stark shift for a 4 mV/cm, perpendicular electric field corresponds to a 2.24 kHz shift. Due to our typical count rates, the population driven out of the metastable state must be $> 10\%$ for a reasonable signal-to-noise ratio in the measured dip. There appears to be a small shift (which we will call a cross-talk shift) of the extrapolated resonance frequency that is dependent on the minimum dip size (metastable extinction fraction) used in the cubic extrapolation. The interpretation of this cross-talk shift is that the distortion of the line due to the dc-Stark effect is slightly modified when saturation and power broadening effects begin to manifest from the excitation. Since a large portion of the dc-Stark shift is due to the distortion of the line, changes in the distortion slightly modify the shift. While this effect is small, limited to a few hundred Hertz, we have investigated the sensitivity of this effect.

To quantify the sensitivity of the cross-talk to stray fields and the metastable spatial distribution, we will determine the cross-talk shift, ν_χ , in a reasonable experimental parameter space. The difference between an extrapolated zero light-field frequency and the expected value due to the dc-Stark shift will be taken to be the value of ν_χ . Three ac-extrapolations are generated using the model for three electric field strengths (3.7 mV/cm, 5.7 mV/cm, and 6.4 mV/cm) with a 550 μm spatial distribution for each. Similarly, three ac-extrapolations are generated for three metastable spatial distribution sizes (450 μm , 550 μm , and 650 μm) under the influence of a 4 mV/cm electric field. In our measurement data set, we have $\approx .15$ as the typical minimum extinction fraction among the different ac-extrapolations, chosen from shot noise signal-to-noise considerations. The cross-talk shift is insensitive to the metastable spatial distribution size parameter s ($\frac{\partial \nu_\chi}{\partial s} \approx .5$ Hz/ μm), but is relatively more sensitive to the size of the electric field. For a metastable spatial distribution parameter of 550 μm and using a minimum dip size of 15%, ν_χ as a function of the electric field is shown in Tab. 5.4. This cross-talk shift is approximately linear in field strength, with a slope of $\frac{\partial \nu_\chi}{\partial \mathcal{E}} = 190$ Hz/(mV/cm) for around a field strength of 5 mV/cm.

The correlation between the ac and dc Stark shifts also modifies the addition of the statistical uncertainties of the extrapolations and the dc-Stark shifts. Uncorrelated systematic uncertainties may be added in quadrature to obtain the total uncertainty. These two systematics are no longer

Table 5.4: ν_χ as a function of field strength. Assuming a 550 μm spatial distribution and a minimum dip size of 15% in the ac-extrapolation.

\mathcal{E} (mV/cm)	ν_χ (kHz)
3.7	.12
5.7	.47
6.4	.64

uncorrelated, and the addition of their statistical uncertainties is modified. The total uncertainty associated with the Stark shifts is then given by:

$$\sigma_T^2 = \sigma_{ac}^2 + \sigma_{dc}^2 + 2 \frac{\partial \nu_\chi}{\partial s} \frac{\partial \nu_\chi}{\partial \mathcal{E}} \sigma_{s\mathcal{E}} \quad (5.24)$$

with

$$\sigma_{s\mathcal{E}} = \frac{1}{N} \sum (\mathcal{E}_i - \bar{\mathcal{E}})(s_i - \bar{s}) \quad (5.25)$$

which resembles the usual addition in quadrature with an additional cross-term [178].

5.4 Conclusion

We have developed an atomic lineshape model for the $2S_{1/2}$ - $8D_{5/2}$ transition in the context of our experimental setup. The model can be used to study systematics in the experiment. In Chapter 4, a physically-motivated analytic function to fit lineshapes and the functional behavior of the ac-extrapolations were derived. The numeric model was used to verify that using the fitting function and cubic extrapolations accurately reproduces the zero-field resonance frequency. The dc-Stark effect was included in the model by adding the 8F states and adding the mixing between the 8D and 8F induced by the stray dc-fields. Aside from the shifts and distortions introduced by the stray fields, cross talk between the two leading systematics is also investigated, revealing a small coupling between the two Stark effects.

Chapter 6

$2S_{1/2}$ - $8D_{5/2}$ Spectroscopy

Due to the large shifts associated with the ac-Stark effect, measuring the unperturbed $2S_{1/2}$ - $8D_{5/2}$ frequency requires performing an extrapolation of the resonance with the probe light intensity. This sets the ac-Stark shift determination apart from the other potential systematics, which are treated as a perturbation to be added to the extrapolated resonance frequency. Extrapolations are generated by scanning over the $2S$ - $8D$ resonance for a given light power many times, then changing the probe power and repeating scans many times within a given day. The probe power is varied pseudorandomly between high and low to help mitigate possible drifts. The other leading systematic in this measurement is the dc-Stark shift, which can shift and slightly distort the lineshape. In this section we will describe how these ac-Stark shift extrapolations are generated, present data generated from these scans, and review the analysis of the extrapolations, including the determination of the dc-Stark effect. Then, we investigate a myriad of potential systematics. Finally, we report our final obtained value of the $2S_{1/2}$ - $8D_{5/2}$ transition frequency and the corresponding proton radius.

The data acquired in the measurement of the $2S$ - $8D$ transition took place on the following dates: 7/09/20, 7/10/20, 7/15/20, 7/17/20, 7/21/20, 7/22/20, 7/24/20, 9/30/20, 10/02/20, 11/02/20, 11/03/20, 11/11/20, 11/13/20, 11/16/20, 11/20/20, 12/02/20, 12/03/20. Throughout the 6 months of data acquisition, the apparatus went through some minor changes as we checked for systematic effects. The primary change to the system is the modification to the 778 nm power enhancement cavity by changing the mirror pair radius of curvatures (ROC). There were three pairs of mirrors: a flat and a 5 m, a flat and a 10 m, and a 5 m and a 10 m. The mirror changes altered the 778 nm beam diameter substantially enough to change the nonlinearity of the power extrapolations. The changes to the apparatus required venting the spectroscopic chamber to atmosphere, which can change the distribution of patch charges/contact potentials within the spectroscopic volume. Primarily due to the potential variation of the dc-electric fields, as noted in the preceding section, we group the data

into batches which coincided with venting the spectroscopy vacuum chamber to atmosphere. The first batch of data is comprised of dates from 7/09-7/24 (flat and a 5 m), the second 9/30 and 10/02 (flat and 5 m), and the third 11/02-12/03 (5 m and a 10 m). The batching is primarily used to apply the proper electric field shifts as determined by the *in situ* field characterization.

6.1 ac-Stark Shift Extrapolations

The spectroscopy laser frequency is set by the beat frequency between the comb and Ti:Sapphire. To scan over the $2S_{1/2}$ - $8D_{5/2}$ resonance we adjusted the beat frequency. The phase-lock between the comb and Ti:Sapphire is further described in Chapter 2. Beat frequencies between the comb and Ti:Sapphire and the comb and 972 ECDL are set by a direct digital synthesizer (DDS), which is externally controlled. The approximate location of the transition is found, and a set of 25 frequency points around this resonance center is generated. A scan range is selected (1.5 MHz in laser frequency), and the set of 25 frequency points are randomly sequenced for each scan of the line since randomization of the frequency sequencing mitigates the effect potential drifts during the scans. At the beginning of each scan, that is one set of 25 frequency points, the 243 nm laser beat frequency is adjusted off-resonance to measure the background count rate caused by photoelectrons generated from the 243 nm light. Then, the scan proper begins.

For each frequency point in the set, the total number of metastable atoms incident upon our detector, the pressure of the hydrogen gas discharge, the 243 nm and 778 nm cavity transmission diode voltages, and the temperature of the cryogenic nozzle during the 1 s gate time are simultaneously monitored and recorded. The photodiode signal's average and variance are recorded for each 1 s gating. After each 1 s gate, the comb-Ti:Sapphire beat note is changed to another frequency in the sequence, with a dead time of 200 ms before starting the 1 s metastable counting gate to allow the locks to settle. The 200 ms dead time is also applied for the background count rate check.

During scans, the frequency comb is self-referenced by f_0 locking and is also phase-locked to the ultra-stable laser and cavity system. The repetition rate of the comb is separately recorded by another program not associated with the line scanning routine, and the repetition rate of the

comb is typically measured in 100 s gate times. The drift of the frequency comb repetition rate is insignificant over 100 s, so corrections to the repetition rate over the 100 s gate time are unnecessary. Both routines apply timestamps for each recorded gate so that the absolute frequency of the spectroscopy participating lasers may be determined and so that cycle slips of the comb may be removed from our data set.

We have found from the numeric model that the nonlinearity of the ac-Stark shift from the metastable spatial distribution is large enough that it cannot be neglected. While linear extrapolations benefit from sampling a large range of intensities, nonlinear extrapolations require it. The reason is not so mysterious; while the nonlinearity is not negligible, it is still much smaller than the linear effect.

As indicated in Chapter 2.2, the power inside of the 778 nm enhancement cavity is set by way of a half-wave plate and a polarizing beamsplitter before the cavity. Making an absolute power measurement, and more so an absolute intensity measurement, is not trivial. However, a relative intensity measurement is straightforward – the relative intensity in the optical cavity is given by the voltage as read by 778 transmission photodiode. We have tested and verified the linearity of our photodetector. We typically discuss the range of intensities as seen by the atoms in terms of the metastable destruction fraction.

A typical days extrapolation samples “dip sizes” ranging from 15%-60% metastable destruction probability (for clarity, a 15% destruction probability means the metastable count rate would be decreased by 15% when the spectroscopy light is on resonance). While we do not explicitly rely on this information for the ac-extrapolation, this corresponds to a power range of ~ 10 -50 W of 778 nm power in the cavity. While generating an extrapolation for the day, the probe light intensity is alternated between high and low, though not in a particular sequence between days, to also help mitigate any potential drifts or other long-term effects. The number of intensities probed each day varies, but typically > 10 intensities constitute each day’s extrapolation, with frequent resampling of the same intensities throughout the day. Each day of data was acquired over the

course of 4-7 hours. Because the signal-to-noise ratio is greater for a 60% dip than for a 15% dip, we correspondingly have more scans at low probe power than at large probe powers.

For each day of data, the logged repetition rate is used to turn each beat frequency between the spectroscopy laser and the comb into an absolute frequency. Each frequency point during a scan has an associated time-stamp so we can apply a time-dependent correction to that beat frequency. This is done by generating an interpolation function of the logged repetition rate. The repetition rate interpolation is generated by first removing lock breaks and cycle slips from the repetition rate data. Lock breaks of the repetition rate breaks all the locks during data acquisition, so there is no issue of potentially free-running spectroscopy laser frequencies during scans. The rep rate data is then low-passed with a time constant of 1000 s to reduce the point-to-point scatter and to generate a smooth interpolating function. The repetition rate is logged on two different frequency counters, and the typical mean offset between the two generated interpolation functions is on the order of 10^{-13} or smaller. We have also found that our extrapolated resonance frequencies are insensitive to this low-pass time constant. For more information on the absolute frequency metrology, see section 6.4.3.

Before fitting each scan with our four-parameter fit function Eq. (4.39), we first remove lock breaks and 243 nm cycle slips, which manifest as far statistical outliers, from the data set. Metastable count rates during a scan are normalized by the 243 nm build up voltage squared, and the far-off resonant metastable normalized count is set to unity. 243 nm cavity lock breaks, where the cavity transmission photodiode voltage drops to nearly zero, appear as count rates far above unity and are removed from the data set. For the 778 nm build up cavity, a similar cut is made – voltages below a certain threshold are removed as they are indicative of a 778 nm cavity lock break. Fig 6.1 shows the data (orange) overlaid with 3D fits (blue) alongside the residuals fitted with a Gaussian below. Both the 3D fit before and after the outlier removal are shown. Lock breaks and 243 nm cycle slips are apparent on Fig. 6.1 a), manifesting as large spikes on rising above the surface for lock breaks and below for cycle slips. In a typical day we remove $< 5\%$ of data points.

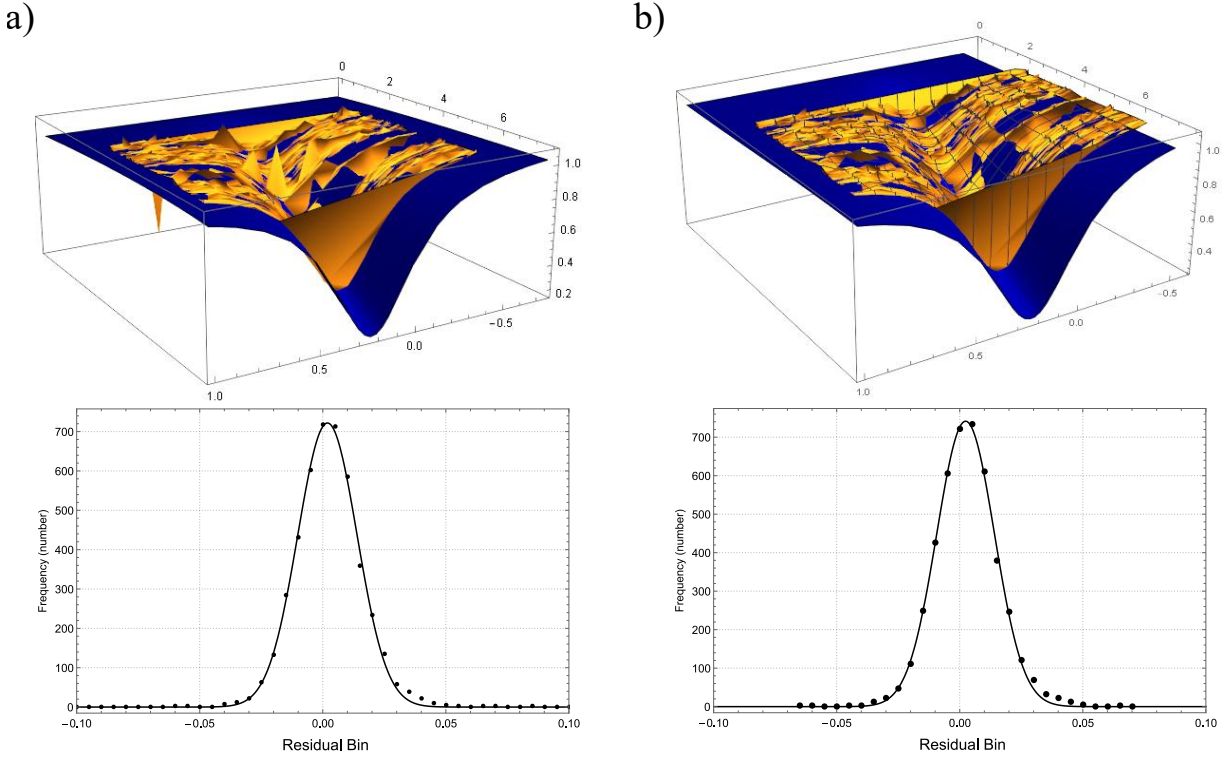


Figure 6.1: 3D fits for outlier detection and the corresponding 3D fit residuals below. a) Before removal of outliers and b) After removal of outliers

After the initial outlier removal is performed, the scans are to be fit with Eq. (4.39). Scans with < 20 out of 25 remaining data points are omitted. Additionally, scans with too large of variation in the 778 nm voltage ($\sigma_V > 100$ mV for a ≈ 5 V scale) are omitted. Each data point in a scan is weighted by the estimated shot noise for that point. In Fig 6.2, we show two examples of a single line scan and its fit. The typical individual line fit has a $\chi_k^2 > 1$ ($\chi_k^2 \approx 1.5$) assuming only shot noise, but this is expected as some technical noise also contributes. The source of this additional technical noise is dominantly variations in the atomic beam flux, which also manifests as scatter in the metastable count rate. The error bars on the four fit parameters are then scaled up to bring the reduced χ^2 to unity on any given single scan to accommodate the contribution of extra technical noise since beam flux is not associated with any shift. Possible density shifts are negligible as we discuss later. Each ν_c is recorded as a function of 778 nm build up voltage. This data is fit to a cubic function of the form: $\nu_c = \nu_0 + aV + bV^3$ to extrapolate to the zero field resonance

frequency, see section 4.3.2. In this cubic extrapolation, each data point corresponding to the fit ν_c of that scan is weighted by the statistical uncertainty of the scan fit, and provides a value $\nu_0 \pm \sigma_\nu$. The final uncertainty for the day's extrapolation, σ_ν , is not scaled in the fitting routine to guarantee a reduced χ_k^2 of 1; we typically achieve a $\chi_k^2 \approx .95$ in a day's extrapolation. The χ_k^2 has a variance of $\sqrt{2/N}$, and a day's data set consists of somewhere close to 200 scans, so a $\chi_k^2 \approx .95$ in a day's worth of data is well-within the expected variance of the estimator.

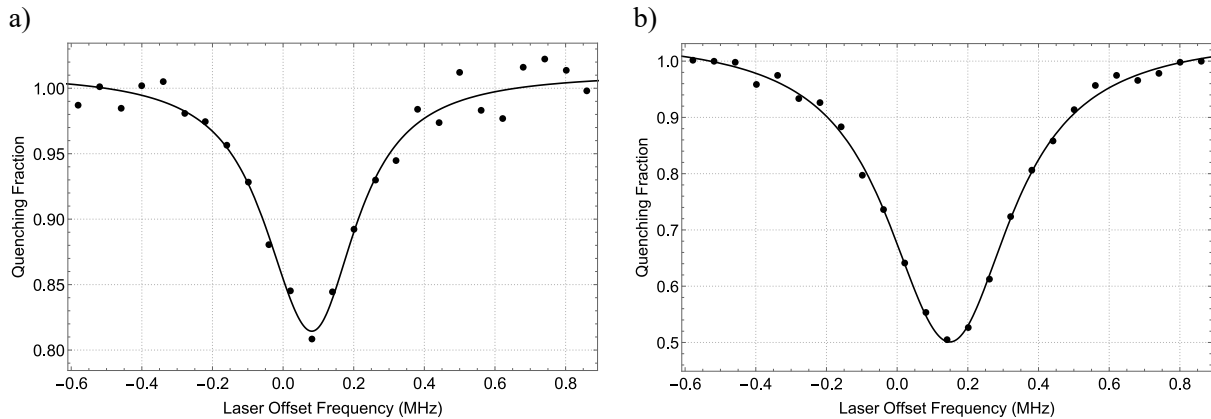


Figure 6.2: Sample individual line scans shown at two different probe powers, x -axis is laser frequency and relative a) Low probe power, $\approx 17\%$ dip b) High probe power, $\approx 50\%$ dip

As a quick aside on the scaling of the various σ_i 's to achieve a reduced χ^2 of unity. When a fitting routine is used to fit a function, frequently the routine only considers the relative magnitude of the weights between the data points when fitting – the absolute magnitudes of the weights are not considered. For example, if the uncertainty (inverse of the weight) of each data point is uniformly increased, the routine's reported fit uncertainty will not be affected. In a sense, the routine is indicating that the assumed uncertainty is incorrect based on the scatter of the data. In our case, we know that the weighting of each data point in a scan is not being properly estimated by shot noise alone, which leads to a reduced χ^2 that is too large (the scatter is too large given just shot noise). Because we know that our measurement is not necessarily shot noise limited, the scaling up of the ν_c uncertainty in a scan is acceptable. However in the case of the extrapolation uncertainty, this scaling is not well justified – the scatter of the data due to technical noise is already taken

into consideration in the initial fits of the scans. We therefore do not allow for the scaling of extrapolation uncertainties.

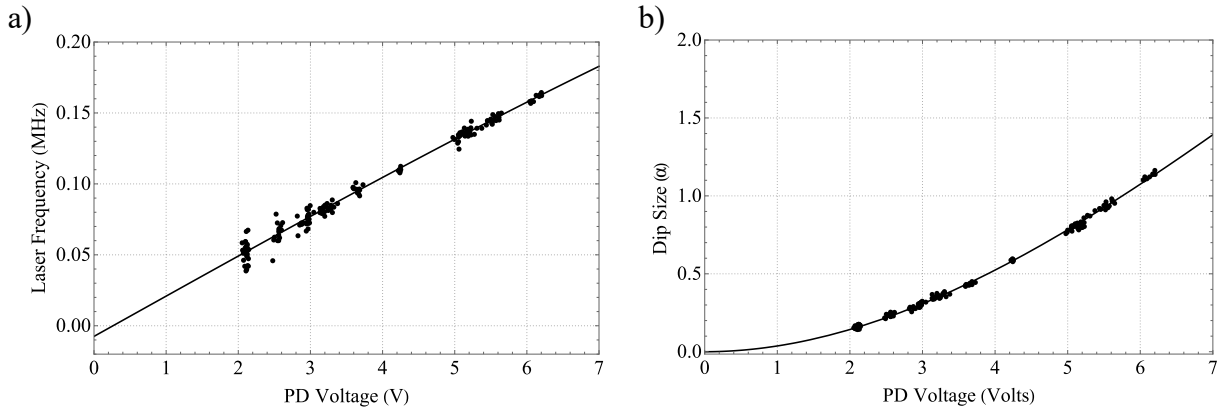


Figure 6.3: Example of extrapolation data, July 9, 2020. a) Frequency extrapolation data. Note that the plot is in terms of laser frequency, and zero is relative the previous measurement of the 2S-8D resonance frequency [5]. While difficult to perceive by eye, the data is fit with a cubic function $\nu(V) = a + bV + cV^3$. b) Metastable quenching parameter (α in Eq. 4.39) as a function of photodiode voltage. Fit with a polynomial of the form $\alpha(V) = aV^2 + bV^3 + cV^4$

An example of a frequency extrapolation fit with a cubic function is shown in Fig. 6.3, with the frequency axis relative to the $2S_{1/2}$ - $8D_{5/2}$ resonant laser frequency as reported in [5]. Both the effective resonance frequency and the dip size are plotted as a function of 778 nm photodiode voltage. Note that the dip size is of the form $e^{-\alpha}$, so dip sizes larger than 1 indicate metastable destruction fractions greater than $1/e$.

As a sanity check, we also extract the zero field resonance frequency using the lineshape model to fit to the extrapolation instead of the analytic cubic function. The density matrix model and the amplitude model produce results within ~ 10 Hz of each other, so this sanity check is robust against model architecture. In fitting with either model, there is an overall voltage to power scaling and a metastable spatial distribution parameter as free parameters in the fit. The model is used to fit both the frequency extrapolation as well as the dip size extrapolation, and we find good agreement between the voltage-to-power scaling and metastable spatial distribution size between the two model fits. Fortunately, the extrapolated zero field resonance as determined by the cubic

fit and the model fit are in excellent agreement from day-to-day, typically much less than 1σ . A side-by-side comparison between the extrapolated resonance frequency as determined by a cubic fit vs using the numeric model directly is shown in Fig. 6.4. A typical σ_ν for a day's extrapolation is on the order of 5 kHz, which some as low as 2 kHz and others as large as 8 kHz. We have found that for extrapolations to be sensible, we require a range of > 200 kHz (atomic) in the ac-Stark shift within a given day. On a day-to-day basis, the numeric model estimates a metastable spatial distribution parameter between $500\text{-}700\ \mu\text{m}$, which is in good agreement with the estimate from our geometric considerations. Days that sample an insufficient range of intensities, aside from being relatively unusable in the frequency extrapolation, also result in nonphysical estimates of metastable spatial distribution parameter when fit directly with the numeric model, e.g. $50\text{-}150\ \mu\text{m}$, which is impossible given our geometry. From this data set, we calculate a mean frequency of 770649561574.90 ± 1.20 kHz, where the weighting for a particular day is given by $1/\sigma_i^2$.

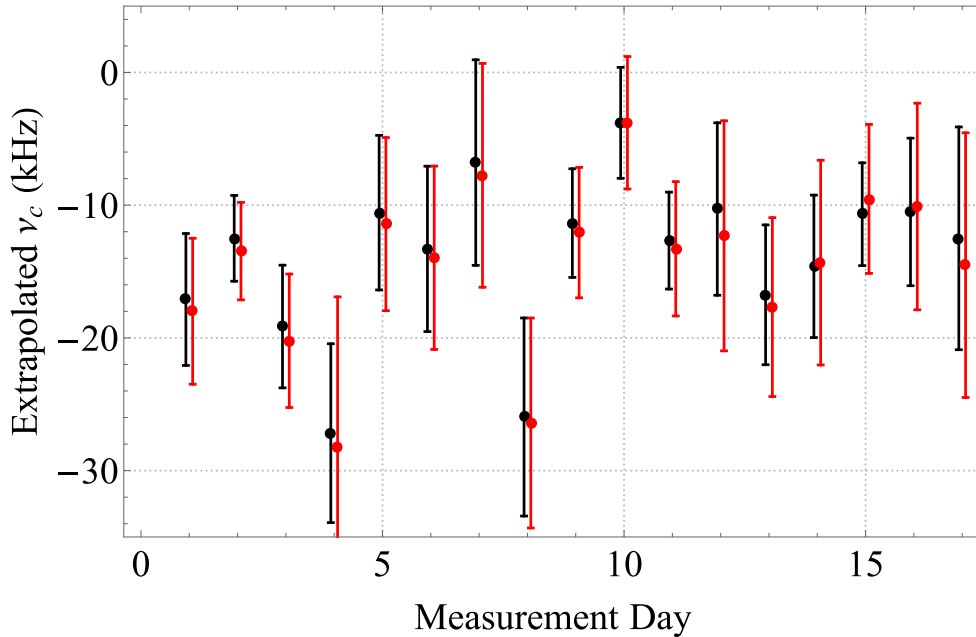


Figure 6.4: Side by side comparison of extrapolated ν_c from the cubic fit and using the numeric model directly. Black: Cubic extrapolation. Red: Numeric model extrapolation. Values displayed are dc-Stark shift corrected

The dip size fraction is either fit with the model or with a polynomial, but mostly it serves as a check for issues with that day's data. For example, nozzle freezing is particularly noticeable on the dip size extrapolation if it occurs; the scatter in the dip size increases. This increased scatter is due to the increased variation in the velocity, but this does not strongly couple to the measured frequency of the line. In addition, we extrapolate the width of the transition as a function of photodiode voltage. The linewidth is fit with a quadratic function, $\gamma = \gamma_0 + a_\gamma V^2$, and the extracted γ_0 provides a good estimate of the linewidth of the transition.

6.2 dc-Stark Shift Mitigation and Characterization

The other primary systematic in our measurement is the shifts and distortions induced by stray dc-electric fields. We have employed a few strategies to mitigate the presence of stray electric fields. The entire 2S-8D spectroscopy is performed in a Faraday cage to shield from potential stray field originating from nearby electronics and wires in the vacuum chamber. We also apply a colloidal graphite coating to all surfaces near the spectroscopic volume [179]; the Faraday cage, magnetic shields, and detector grids facing the spectroscopic volume (essentially everything within the Faraday cage) are all coated. This colloidal graphite coating homogenizes the wall surfaces, reducing the presence of contact potentials. Furthermore, this graphite coating also has the effect of reducing patch charge build up, and is employed in other precision hydrogen measurements [23, 29, 45]. We have chosen to avoid using more active approaches to mitigating stray fields using electrodes for simplicity.

The dc-Stark shift dominantly affects the 8D manifold by mixing the $8D_{5/2}$ states with the nearby $8F_{5/2}$ state, whose hyperfine centroids are only separated by 103 kHz. This mixing both shifts the line and distorts the resultant lineshape. Higher lying n -manifolds exhibit relatively smaller hyperfine splittings and linewidths. These two effects, the increased degeneracy and the narrower linewidths, in addition to the larger dipole matrix elements, make these higher lying n states much more sensitive to stray fields (see Fig. 6.5 as compared to Fig. 5.4). For instance, the $12D_{5/2}$ line has a natural linewidth of 172 kHz and is only separated by 30.7 kHz from the

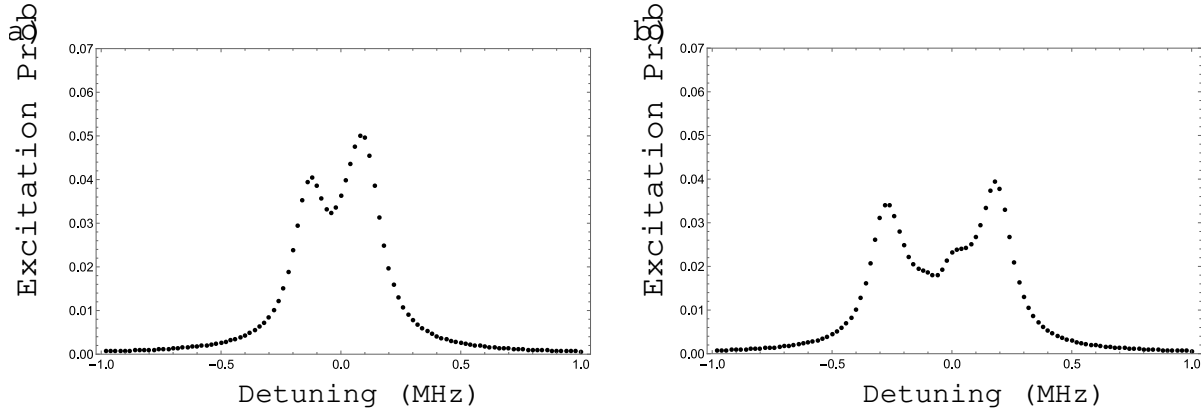


Figure 6.5: $2S_{1/2}$ - $12D_{5/2}$ modeled lineshape in perpendicular electric fields. a) 3 mV/cm field b) 6mV/cm field

$12F_{5/2}$ line, making distortions of the $2S_{1/2}$ - $12D_{5/2}$ much more noticeable for the same stray field as compared to the $2S_{1/2}$ - $8D_{5/2}$ transition. Additionally, investigation of Fig. (5.2) indicates that the $8D_{3/2}$ and $8D_{5/2}$ split in opposite directions, the 12D lines exhibit a similar but stronger effect. This provides an attractive option for quantifying stray electric fields: measure both 12D lineshapes and the relative splitting of these lines [45]. This also provides a consistency test for quantifying field strengths with the numeric model.

Spectroscopy of the 2S-12D lines was performed periodically during the measurement of the 2S-8D line. The primary difference in the two measurements is that we more densely sample the 2S-12D lines during scans (35 frequency points per scan instead of 25) to improve the resolution to potential line distortions. The distortion is dependent on the relative orientation of the stray electric field to the polarization of the excitation field, see section 5.2.2. Therefore, we also varied the excitation field polarization (vertical, horizontal, and $\pm 45^\circ$) for sets of scans on the 12D lines to determine the orientation of the stray field. We have found that the measured lineshapes of the 12D transitions are insensitive to the polarization state of the excitation light field, indicating that the orientation of the stray field is largely parallel to the atomic beam and therefore perpendicular to the light polarization. Fig. 6.6 a) shows $12D_{5/2}$ lineshape averaged over many scans (Aug 14, vertical polarization), the distortion indicating the presence of dc-fields. We have fit this scan with our lineshape model with a parallel field magnitude of $3 \pm .5$ mV/cm and an additional Lorentzian

broadening of 50 kHz, which was likely due to pressure broadening (see section 6.4.2). This extra broadening is included by convolving the modeled lineshapes with a Lorentzian function of appropriate width. Measurements of the $12D_{3/2}$ line collected within the same batch of data collection also are well matched by assuming a 3 mV/cm field.

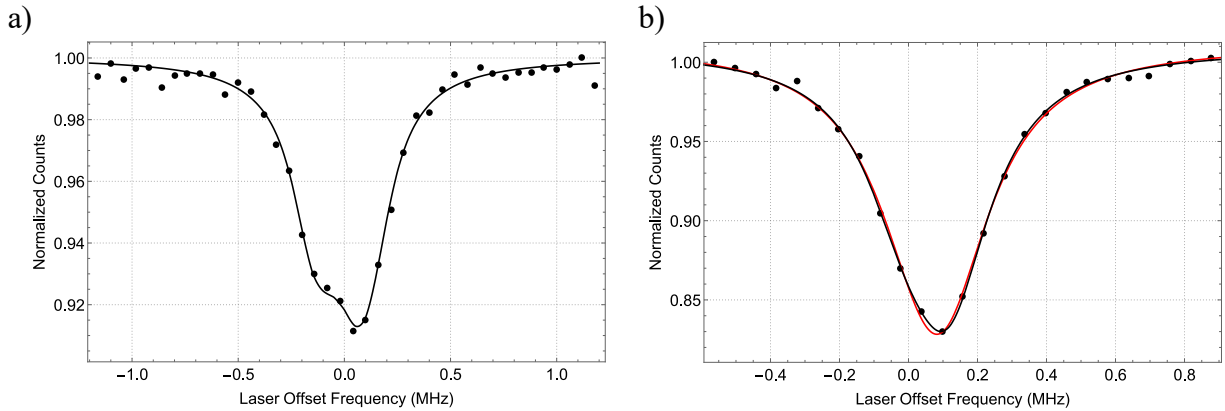


Figure 6.6: a) An example $12D_{5/2}$ line fit model, electric field magnitude 3 mV/cm with 50 kHz of Lorentzian broadening. b) $2S$ - $8D$ line example fit with our standard fit function (red) and the electric fields model (black). The distortion of the line quantifies the magnitude of the electric field.

The dc-fields in the spectroscopic volume are not guaranteed to be constant in the 6 month long data acquisition of the $2S_{1/2}$ - $8D_{5/2}$ transition, we therefore do not assume that the field strength found in the periodic 12D scans is valid for all of our data. We have found that the electric fields are stable from day-to-day if the spectroscopy chamber remains under vacuum. Data on the $2S_{1/2}$ - $8D_{5/2}$ transition was collected in three batches: one in July, September, and November. During these three time periods, we assume that the fields are constant. We estimate the electric field strength for each day of $2S_{1/2}$ - $8D_{5/2}$ data by fitting an averaged lineshape from that day with the numeric model. The averaged line consists of many scans in a similar voltage range, usually chosen in the 15%-30% metastable quenching fraction range. To create a fit, the numeric model generates a large set of lineshapes under a spread of light intensities, electric fields, and additional broadening. An interpolating function for this modeled data set is created, and the day's data is fit to that interpolating function to provide an estimate of the electric field. Fig. 6.6 b) provides an example of an averaged scan fit to the electric field model. The red line is the standard line fitting

function (red), and the slight distortion near the peak is better captured by the model fit (black). In a single scan, this distortion is not visible due to the noise, but does appear when several scans are averaged. The electric field determined for each day is shown in Fig. 6.7 with the corresponding batch averages overlaid. The batch average electric fields are 3.68 ± 0.32 mV/cm, 6.41 ± 0.35 mV/cm, and 5.72 ± 0.26 mV/cm for the July, September, and November batches respectively (blue, red, green respectively). These fields correspond to shifts of $+1.92 \pm 0.32$ kHz, 5.45 ± 0.54 kHz, and 4.43 ± 0.37 kHz respectively.

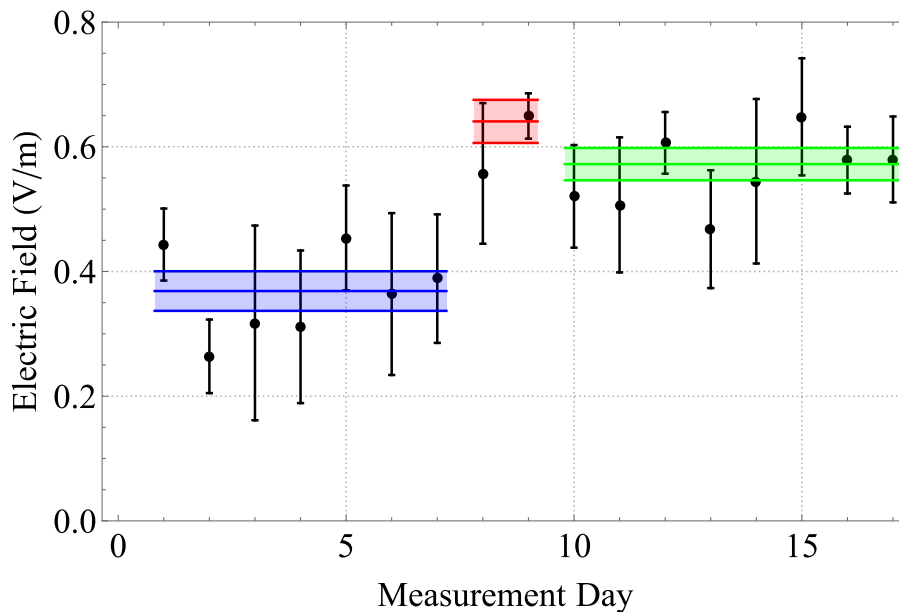


Figure 6.7: *In situ* measurement of electric fields for each measurement day with batch means and statistical variances overlaid. Blue - July, Red - September, Green - November. Electric field is assumed to be perpendicular to the light field.

6.3 Correcting extrapolated frequencies for the dc-Stark effect

For each day's extrapolation, we extract the zero-field resonance frequency, electric field magnitude, and their statistical uncertainties. The zero-field resonance frequency and electric field magnitude are weighted by $w_{\nu,i} = 1/\sigma_{\nu,i}^2$ and $w_{e,i} = 1/\sigma_{e,i}^2$ respectively. The mean electric field magnitude for each batch of data, which will be referred to as July, September and November

batches accordingly, is calculated. An electric field shift is applied to the July, September, and November batch according to that batch's mean field. The small correction due to the dc-Stark effect and the ac-extrapolation cross-talk is also included according to the size of the electric field for each batch. The now corrected zero-field resonance frequencies statistical mean, $\bar{\nu}$, and variance, $\bar{\sigma}_\nu$, is calculated. The variance of the mean frequency is given by $\bar{\sigma}_\nu = (\sqrt{\sum 1/\sigma_{\nu,i}^2})^{-1}$. In Fig. 6.8, we show the dc-Stark corrected extrapolated resonance frequencies in our data set with the mean statistical uncertainty overlaid. The frequency is reported relative to the $2S_{1/2}$ - $8D_{5/2}$ atomic resonance frequency as given by [5].

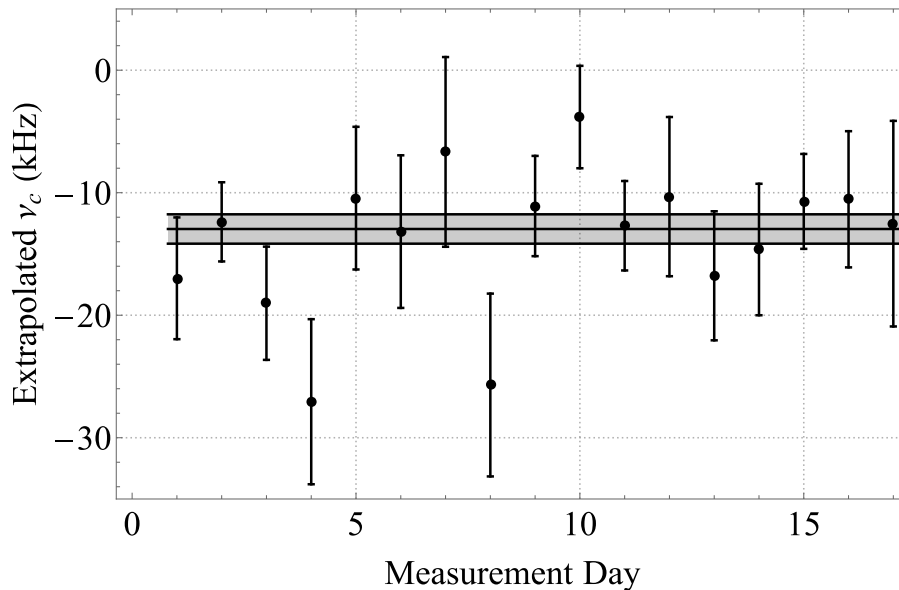


Figure 6.8: Stark corrected extrapolated resonance frequencies. Mean statistical uncertainty overlaid, 1.2 kHz.

The scatter and mean of the electric-field-corrected extrapolated frequencies, $\bar{\nu} = -12.98 \pm 1.20$ kHz, are in excellent agreement with statistical fluctuations. The reduced χ_k^2 of the data set is 1.05, and given that the variance of the χ^2 distribution is on the order of $\sigma_{\chi^2} \sim \sqrt{2/N}$, there is no evidence of an uncontrolled varying and significant systematic. The accuracy of our statistical uncertainty has been further supported with bootstrap Monte-Carlo methods. By generating 10^6 new data sets from randomly sampling our original data set, bootstrapping indicates a statistical

variance of 1.185 kHz is expected, with a negligibly shifted mean. A similar analysis has been performed on the numeric model fit extrapolations, with a reduced χ^2 of .86 and a bootstrap estimated variance of 1.38 kHz, indicating that the model statistical error may be slightly overestimated.

As indicated, electric field corrections are applied in batches instead of applying a correction to each day based off of its measured field individually. For the July batch, this is particularly important as that batch exhibits the smallest line distortions (smallest field), causing some variance in the field estimates. The measured values of the electric field are 3.68 ± 0.32 mV/cm, 6.41 ± 0.35 mV/cm, and 5.72 ± 0.26 mV/cm for the July, September, and November batches corresponding to shifts of $+1.92 \pm 0.32$ kHz, 5.45 ± 0.54 kHz, and 4.43 ± 0.37 kHz respectively. The weighted dc-Stark shift is -3.54 kHz with an uncertainty of ± 0.37 kHz, with the weighting factors given by the statistical contribution of the batches to the mean resonance frequency.

The error quoted above assumes a perpendicular field to the spectroscopy laser. As mentioned in Chapter 5.2.2, the dc-Stark shift and distortion are both dependent on the relative orientations of the dc- and ac-fields. We have found that the stray dc-field must largely be perpendicular to the light field by varying the polarization of the excitation light during 2S-8D and 2S-12D spectroscopy and observing the distortion. However, we cannot totally exclude the possibility of a small component of the dc-field pointing parallel to the spectroscopy laser polarization. To account for this possibility, we have also fit our data with the numeric model assuming a dc-field orientation up to an angle of 35° from perpendicular to the light-field. By varying the dc-field orientation through this range in the data analysis, the weighted dc-Stark shift can vary by 0.52 kHz. Therefore, we include an uncertainty due to the potential variation in the electric field orientation of 0.52 kHz.

Similarly, there are small model corrections due to the cross-talk of the two Stark effects, as discussed in Chapter 5.3.2. Table 5.4 gives the cross-talk shift for the three average dc-fields, which are applied to each batch of data accordingly. The contribution of this cross-talk results in a weighted shift of 0.41 kHz and we assign the full 0.41 kHz shift as the corresponding uncertainty. The systematic shifts associated with the cross-talk effect, the possibility of non-perpendicular fields, and the statistical variance of the dc-field correction are correlated, so we add their uncer-

ainties linearly. Therefore, we find a weighted dc-Stark shift of -3.95 ± 1.28 kHz (including cross-talk).

To summarize, the ac-extrapolations alone give a centroid value of 770649561574.90 ± 1.20 kHz and the dc-Stark effect amounts to a correction of -3.95 ± 1.28 kHz to this extrapolated value. These two effects are correlated and therefore the uncertainties cannot be added in quadrature only – the correlation between them must be considered as discussed in Chapter 5.3.2 [178]. If the two effects are added in quadrature alone, the combined uncertainty of the two Stark effects is 1.75 kHz. When the correlation between the effects is included, the total uncertainty is increased to 1.82 kHz. This gives a dc-Stark corrected $2S_{1/2}$ - $8D_{5/2}$ centroid frequency of 770649561570.95 ± 1.82 . This value is subject to minor corrections due to other potential systematics, for example: residual magnetic fields, offsets in the frequency calibration, pressure-induced shifts, and the second-order Doppler shift.

6.4 Minor Systematics

In this section, we discuss several minor systematics in the measurement. These systematics amount to small corrections – all of them together shift our result less than a kHz.

6.4.1 Residual Magnetic Fields

Static magnetic fields can split atomic lines via the Zeeman effect, the magnetic analogue of the Stark effect [180]. Similar to the Stark effect, the Zeeman effect also played a significant role in the development of early quantum theory, and we will explore the pertinent details of the Zeeman effect to our measurement.

Analogously to the Stark effect, the interaction energy between a magnetic dipole and an external magnetic field is given by

$$U_m = -\vec{\mu}_m \cdot \vec{B}. \quad (6.1)$$

The magnetic moment of the atom, $\vec{\mu}_m$, is the result of the total angular momentum of the atom. The total magnetic moment of the hydrogen atom may written as

$$\vec{\mu}_m = g_L \frac{e}{2m_e} \vec{L} + g_s \frac{e}{2m_e} \vec{S} - g_I \frac{e}{2m_p} \vec{I}, \quad (6.2)$$

where e is the elementary charge, m_e the mass of the electron, m_p the mass of the proton, \vec{L} , \vec{S} , \vec{I} are orbital, electron spin, nuclear spin angular momentum, and g_i 's are the corresponding g -factors for each angular momenta. A very well known and important result is that while $g_L = 1$ in accordance with classical theory, $g_S = 2(1 + \frac{1}{2\pi}\alpha + \mathcal{O}(\alpha^2) + \dots) \approx 2.0023$ and is an expressly quantum mechanical result, with the corrections in a power series of α are Q.E.D. corrections to the Dirac result of $g_S = 2$ [181, 182]. In stark contrast to perturbations due to electric fields (pun intended), hydrogen atoms experience energy shifts due to external magnetic fields in first-order perturbation theory. The shift due to a magnetic field oriented along the z -axis is

$$\Delta E^1 = - \langle \psi | \vec{\mu} \cdot \vec{B} | \psi \rangle = \frac{1}{\hbar} g_F \mu_B m_F B, \quad (6.3)$$

where g_F is the Lande g -factor for the total angular momentum \vec{F} and m_F is the corresponding magnetic sublevel. Note that either \vec{F} or \vec{J} may be a better choice of quantum number depending on the magnitude of the external field – if hyperfine interactions are larger than the Zeeman level shifts \vec{F} is a good quantum number. If the applied magnetic field corresponds to larger interaction energy than the hyperfine interactions, then \vec{J} is a better quantum number and $g_F \rightarrow g_J$ in Eq. (6.3).

2S-8D in a magnetic field

In the absence of circularly polarized light about the orientation of the magnetic field, only the $m_F = 0, \pm 1$ for the 2S and 8D states participate in the spectroscopy due to the two-photon selection rule that $\Delta m_F = 0$ and the fact that the $2S_{1/2}^{F=1}$ is preferentially populated in the metastable excitation. The upper limit for the magnetic field shifts occurs when the magnetic field is parallel with the light excitation field (that is, about the z axis). In that case, let us qualitatively apply Eq. (6.3) to our system. In the case of linearly polarized light (π transitions), the $m_F = 0$ states do not shift and the $m_F = \pm 1$ states shift symmetrically about $m_F = 0$. The participating 2S and 8D both shift, as the g_F factor is different for the different magnetic sublevels. In this case, there is no

associated shift due to the Zeeman effect, only a broadening of the line occurs. Therefore, only in the case of some circularly polarized light (σ transitions, $\Delta m_F = \pm 2$) can a shift occur.

We can quickly estimate the shift of the $8D_{5/2}$. The zero-order estimation of shifts for totally circular polarized light in a magnetic flux density B is $\Delta E \approx 2 \frac{e}{2m_e} B$ as g_F is on the order of 1, which evaluates to $\delta\nu/B \approx 3$ MHz/Gauss. The Earth's magnetic field is about 250 mGauss, so a totally unmitigated field could broaden the 2S-8D line by 750 kHz. As an aside, the original 2S-8D $_{5/2}$ lines were recovered with no magnetic shielding or trimming. The recovered lines had a width of about 1.2 MHz, which is in quite good agreement with this estimate of 3 MHz/Gauss. Of course, the value of 3 MHz/Gauss corresponded to a shift when using totally circularly polarized light. However, the broadening similarly goes as $\Delta\gamma \sim \frac{1}{h}(\Delta E(m_F = 1) - \Delta E(m_F = -1)) \approx 2\mu_B B$.

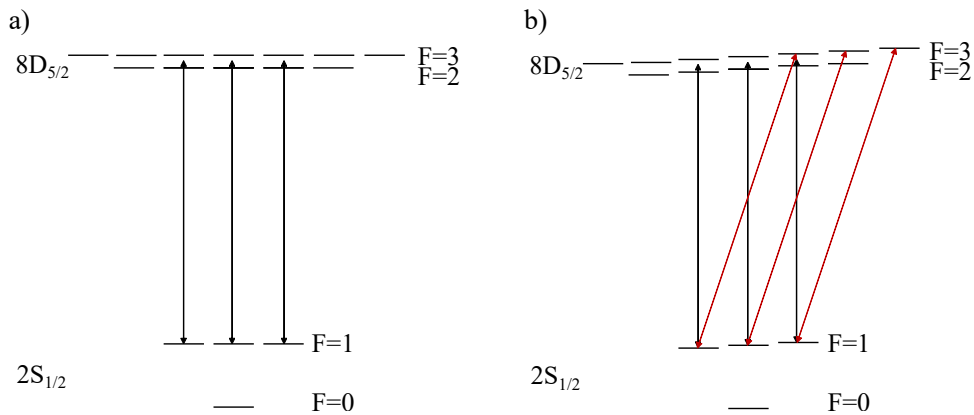


Figure 6.9: Level structure of the 2S-8D transition a) No external magnetic field b) small external field applied. Red lines correspond to σ^+ transitions and black lines are π transitions

Mitigation of Residual Magnetic Fields

There are two commonly employed methods to reduce the effect of Earth's field: field trimming with, e.g., a Helmholtz Coil, or using magnetic shielding. Magnetic shields are composed of a high permeability metal, typically mu-metal. The naive expectation of magnetic fields blocking external fields is incorrect. Instead, the high permeability metal draws the magnetic field lines towards their surface. While this leaves the total magnetic flux the same, the distribution of field lines is greatly

affected. We have opted to use magnetic shields instead of the more "active" approach using trimming coils.

To calculate the attenuation for the magnetic shields, we used Radia, a free-to-use program written for Mathematica [183]. The dimensions, thickness, and relative geometry of our magnetic shields were modeled in Radia using Earth's field as the applied field. Finite element analysis requires careful variation of the meshing and relaxation steps to test for convergence if a highly accurate result is desired. Estimations from Radia for our particular shield configuration estimated an overall field attenuation of about a factor of about 1000. From our estimate in the preceding subsection, an magnetic field attenuation of 1000 corresponds to a ~ 700 Hz shift when using totally circularly polarized light.

Characterization of Magnetic Field Shifts

In order to quantify the potential magnetic field shifts with the magnetic shielding in place, we have performed 2S-8D spectroscopy with σ^+ and σ^- light of similar intensity. The frequency difference between these two lines sets *twice* the maximal field shift possible. The maximal shift possible, combined with information of the relative polarization purity of our spectroscopy light, allows for a determination of the residual Zeeman shifts in our measurement.

The splitting of the σ^+/σ^- spectroscopic lines, once the small correction due to the ac-Stark shift is accounted for, is about 3.7 kHz. This indicates that the maximal potential Zeeman shift, using totally circularly polarized light, is ± 1.85 kHz. This ± 1.85 kHz shift is suppressed by the relative polarization purity of the spectroscopy light. The polarization purity was determined by measuring the maximum polarization extinction ratio of the 778 nm light after the enhancement cavity. The maximal polarization extinction ratio is $R = 1/100$. From this polarization extinction ratio, we can determine the total fraction of light power that is circular (that is, we can determine the ellipticity of the polarization). The fraction of power that is circularly polarized, S , is given by:

$$S = \frac{I_R - I_L}{I_R + I_L} = \frac{2\sqrt{R}}{1 + R} \approx .2. \quad (6.4)$$

The total population driven to states is proportional to the intensity squared (for two-photon transitions). We estimate that the shift is then

$$\delta\nu_B = \frac{\nu_{\sigma^+} - \nu_{\sigma^-}}{2} S^2 \approx 70 \text{ Hz.} \quad (6.5)$$

Since we do not know the orientation of the fields or the handedness of the ellipticity, we assigned no shift due to the magnetic field but apply an uncertainty of 70 Hz. This 70 Hz uncertainty is far below the current measurement precision. Higher order Zeeman effects are negligible. Additionally, we can estimate the magnitude of the residual field in the spectroscopic volume to be $\sim 1.85/3000$ Gauss, or about .6 mGauss.

6.4.2 Pressure Systematics

We have observed in preliminary measurements that the recovered lineshapes of the 8D and 12D transitions are occasionally broader than what our lineshape models predict. In those instances, our modeled lineshapes more closely match our measured lineshapes when we include a small Lorentzian broadening term, on the order of 25 kHz on the 8D line and 50 kHz on the 12D lines (the natural linewidths of these transitions are 572 kHz and 172 kHz respectively). The lines constituting our $2S_{1/2}$ - $8D_{5/2}$ spectroscopy data do not exhibit this broadening. This extra broadening appears to be related to background gas pressure; we found that the extra broadening slowly decreases with the spectroscopy chamber pressure. In this section, we investigate the possibility of potential pressure related systematics.

Interactions between hydrogen atoms and other gases may affect the resultant spectroscopic lineshapes [184–186]. The effects due to pressure related systematics are sensitive to the parameter space involved in the collisions between the perturbing and perturbed (hydrogen atom) gases. A general collision between gas species 1 (perturbed) and 2 (perturber) is shown in Fig. 6.10. The interaction time in a collision is roughly $\Delta t \sim v/b$, where b is the impact parameter of the collision and v is the relative velocity between the pair of atoms/molecules. Given that the lifetimes of

transitions of interest in our spectroscopy experiment are all $>1 \mu\text{s}$, and the collision times are typically on the order of 1 ns, we may treat the collisions under the impact approximation [187].

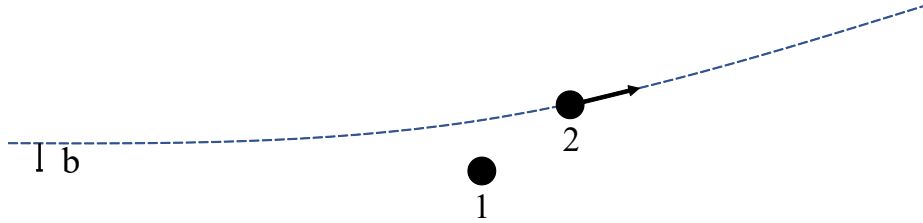


Figure 6.10: General collision between species 1 (perturbed) and species 2 (perturber)

A general result in the impact approximation is that collisions impart a random phase shift on the perturbed atom. The net effect of all the random phase shifts accumulated by the perturbed atom results in a Lorentzian broadening profile and shifts may also occur. Under the impact approximation we investigate the possibilities for collisions between hydrogen atoms (mediated by Van der Waals forces and short lived multipole fields) and collisions between hydrogen atoms and water molecules (the dominant gas load in vacuum).

Hydrogen-Hydrogen Collisions

While any energy eigenstate of the hydrogen atom does not have an intrinsic electric dipole moment associated with it, these hydrogen states can exhibit a transient dipole moment via second-order perturbation theory [188]. These transient dipole moments in hydrogen can induce forces between hydrogen atoms. During a collision, an energy between the two hydrogen atoms may be assigned due to the transient dipole-dipole interaction.

To estimate the effect of atomic hydrogen-hydrogen collisions, we can investigate the Van der Waals interaction between a pair of hydrogen atoms. The Van der Waals Hamiltonian may be written

$$H_V = \frac{e^2}{4\pi\epsilon_0} \frac{x_1x_2 + y_1y_2 - 2z_1z_2}{R^3}, \quad (6.6)$$

where R is the mean interatomic distance and the x_j, y_j, z_j are the electron spatial coordinates with respect to the atomic center for atom j . Since any given state of atomic hydrogen has no intrinsic dipole moment (as mentioned), there are no first order shifts, and the energy shift due to the Van der Waals interaction is given by

$$\Delta E_V(n) = \sum_{m, m \neq n} \frac{|\langle n | H_V | m \rangle|^2}{E_n - E_m} = \frac{C_6}{R^6}, \quad (6.7)$$

with $|n\rangle = |n_1\rangle \otimes |n_2\rangle$ being a product state of atom 1 and atom 2. The phase shift imparted in a collision with relative velocity v and impact parameter b in this way is given by:

$$\phi(b, v) = \frac{1}{\hbar} \int_{-\infty}^{\infty} (\Delta E_e(\sqrt{b^2 + v^2 t^2}) - \Delta E_g(\sqrt{b^2 + v^2 t^2})) dt. \quad (6.8)$$

Resultant frequency shifts and broadening associated with these phase shifts are calculated as:

$$\Delta\omega(v) = \mathcal{N}v \int_0^{\infty} (2\pi b) \sin(\phi(b, v)) db \quad (6.9)$$

and

$$\Delta\gamma(v) = \mathcal{N}v \int_0^{\infty} (2\pi b) (1 - \cos(\phi(b, v))) db, \quad (6.10)$$

where \mathcal{N} is the number density of the perturbing species [189]. It should be noted that these shifts and broadening terms apply for collisions that occur at velocity v , and in general the velocity distribution of the collisions must be taken into account.

We do not expect significant hydrogen-hydrogen interactions to be prominent. For instance, in the recent 2S-4P measurement performed at Garching, hydrogen-hydrogen interactions constituted shifts on the order of ~ 10 Hz for hydrogen densities of 2×10^{15} atoms/m³ [29]. The estimated 10 Hz Van der Waals shift was dominated by the perturbation of the 4P state due to nearby 1S atoms. In our experiment, we estimate that our atomic hydrogen density in the beam is 10^{13} atoms/m³, and therefore believe hydrogen-hydrogen Van der Waals interactions are negligible at the current

level of precision. As an aside, we have also performed spectroscopy on the $2S_{1/2}$ - $8D_{5/2}$ line while varying the hydrogen pressure and found no effect.

There is also the possibility of coherent interactions between hydrogen atoms in mixed states within the spectroscopy excitation volume, and was perhaps prominent in a Ramsey measurement of Rydberg circular states in hydrogen ($n = 27 \rightarrow 28$ and $n = 29 \rightarrow 30$, $l = |n - 1|$) [190]. In that measurement, the shift introduced by this systematic was found to be at the ≈ 10 kHz level, albeit with significant uncertainty. The mechanism of this interaction is relatively straightforward; the beam of Rydberg hydrogen atoms can be treated as a distribution of rotating dipoles, modifying the resonance frequency of the transition via the Stark effect. The size of the shift was estimated by comparing the resonance frequency extracted in high-density beam measurements and low-density beam measurements. In their experiment, they estimate a maximum circular atom density of $10^5/\text{cm}^3$ with a corresponding electric field amplitude of $\approx 2 \times 10^{-5}$ V/m (see section 6.5.1 in [190]).

In our situation, the hydrogen atoms in the state $|\psi\rangle = \frac{1}{\sqrt{2}}(|2S\rangle + |8D\rangle)$ do not have a dipole moment, and instead have a quadrupole moment which in principle can perturb other nearby atoms. There is also the possibility of short lived $\frac{1}{\sqrt{2}}(|2P\rangle + |8D\rangle)$ atoms which do have a dipole moment. The density of $\frac{1}{\sqrt{2}}(|2S\rangle + |8D\rangle)$ mixed state atoms in our experiment is at most $1000/\text{cm}^3$, giving a mean interatomic distance of $\sim 5 \times 10^{-4}$ m. The magnitude of a quadrupole field generated from a $\frac{1}{\sqrt{2}}(|2S\rangle + |8D\rangle)$ at this distance is $\mathcal{E} \sim 10^{-18}$ V/m, which indicates this effect is negligible. The $\frac{1}{\sqrt{2}}(|2P\rangle + |8D\rangle)$ states will be very short lived as the lifetime of the $|2P\rangle$ state is ≈ 1.6 ns. We can expect the density of the atoms in this state is scaled by $(\gamma_{8d}/\gamma_{2p})$, which results in a density reduction of 100. Since the corresponding dipole moment for the $\frac{1}{\sqrt{2}}(|2P\rangle + |8D\rangle)$ is 1000 times smaller than the Rydberg states considered in [190] and our density is about 10^4 times smaller, this effect is negligible in our measurement.

Hydrogen-Water Collisions

Besides hydrogen atoms, the dominant background gas we expect to participate in collisions is water. The outgassing of water from the internal surfaces is well-known to be a large portion of

the gas loads in vacuum chambers. Furthermore, unlike atoms and the rest of gases constituting air (N_2 , O_2 , CO_2 , Ar), the water molecule has an intrinsic dipole moment. This dipole moment of water is about 1.8 Debye ($0.72 ea_0$) [191], and in a collision with a water molecule, a hydrogen atom sees a rapidly varying electric field. This time-dependent electric field can drive transitions in the hydrogen atom. These population dynamics can both quench states (effectively changing the lifetime of those states, causing a broadening) and impart phase shifts to the hydrogen atom.

The interaction potential between the hydrogen atom and the dipole is given as

$$V(t) = -\vec{\mathcal{E}}_w(t, b) \cdot \vec{\mu}_H, \quad (6.11)$$

where \mathcal{E}_w is the external electric field due to a water molecule and μ_H is electric dipole moment of the atom, $\vec{\mu}_H = e(x\hat{x} + y\hat{y} + z\hat{z})$. For simplicity in the following estimate, we may consider the dipole moment of water to be oriented along the \hat{z} direction and the separation between the water molecule and hydrogen atom to be along the $x - y$ plane (trajectories along different paths do not substantially change the result). Thus, the electric field due to the water molecule as seen by the hydrogen atom can be written as

$$\vec{\mathcal{E}}_w(t, b) = \frac{0.72ea_0}{4\pi\epsilon_0} \frac{\hat{z}}{(b^2 + v^2t^2)^{3/2}}, \quad (6.12)$$

where b is the impact parameter of the collision, and v is the relative velocity between the molecule and atom (noting that the dipole field goes as $\mathcal{E} \sim 1/R^3$). We first wish to estimate the quenching of the 8D state due to a collision with a water molecule – i.e. the rate of population being driven out of the 8D state.

We can estimate the population amplitude driven from the 8D state to another state (nL) in a collision via first-order perturbation theory,

$$c_{nL}(b) \approx -\frac{i}{\hbar} \int_{-\infty}^{\infty} \langle nL | V(t', b) | 8D \rangle e^{i\omega t'} dt', \quad (6.13)$$

with $\hbar\omega$ the energy splitting between the states. We expect the electric field given by Eq. (6.12) to be valid when there are not too many other water molecules around (which should quickly average to zero given enough water molecules). For water molecule number densities of $\mathcal{N} \sim 10^{16}/\text{m}^3$, pressures of $10^{-7} - 10^{-6}$ Torr, this distance of validity is $a = (\frac{3}{4\pi\mathcal{N}})^{1/3}$, which is about $40000 a_0$ – a couple of microns. This sets a maximal collisional interaction time of $\Delta t < 5$ ns. Inspection of Eq. (6.13) indicates that only states where $\omega\Delta t < 1$ will have much amplitude driven by the collision. In that case, we are limited to dipole-allowed transitions in the 8D manifold (8P and 8F). Therefore, the population in the 8D state after a collision with impact parameter b can be estimated as

$$\rho_{8D}(b) = 1 - |c_{8P}(s)|^2 - |c_{8F}(b)|^2 \approx 1 - \frac{4}{v^2\hbar^2} \left(\frac{.72e^2a_0^2}{4\pi\epsilon_0} \right)^2 (45^2 + 48^2) \frac{1}{b^4}, \quad (6.14)$$

where we have explicitly evaluated the integrals in Eq. (6.13). There exists a b_c where $\rho_{8D}(b_c) = 0$, that is, the 8D state is totally quenched. The zeroth order estimation of the quench rate due to these collisions is then

$$\Gamma \approx \pi\mathcal{N}v \int_0^{b_c} b db. \quad (6.15)$$

Clearly, some population is also quenched for collisions $b > b_c$, and therefore we estimate the quench rate due to collisions as

$$\Gamma \approx \pi\mathcal{N}v \int_0^{b_c} b db + 2\pi\mathcal{N}v \int_{b_c}^a b(1 - \rho_{8D}(b))db, \quad (6.16)$$

which estimates a quench rate (broadening) of 50 kHz.

We have also employed Monte Carlo simulation of the collisions between hydrogen and water molecules to accurately model the net effect of velocity distributions and the many possible trajectories during the collision with collaborators at the Russian Quantum Center in Moscow [192]. A collision trajectory (relative velocity, impact parameter, orientation) is randomly chosen, then Schrödinger's equation including the relevant states and perturbing Hamiltonian is numerically integrated for that collision. We may make a few qualitative predictions for the results of this simulation. It is expected that these collisions dominantly broaden the line by quenching, and the

collisions will not typically impart large phase shifts without simultaneously strongly quenching the atom. Some simple arguments can be made to support this. The frequency content of the collisional electric field is determined by the inverse of the collision duration, which amounts to ~ 1 GHz for the most probable collisions. The relative splittings of the $n = 8$ states that can be coupled by the collisions are all much less than a GHz. This means that, during a collision, the relative phase difference accumulated between the 8D state and one of the nearby states (e.g. 8F) is very small. States outside of the $n = 8$ manifold do accumulate a large phase difference relative to the 8D state in this time frame, but do not participate strongly in the collision, as Eq. (6.13) indicates. This leaves collisions which are “resonant” with a nearby state (that is the inverse of the collision duration is comparable to an energy splitting) as the source of appreciable phase shifts. Since it is unlikely that there are many collisions slow enough to be nearly resonant as determined by a typical thermal velocity distribution, it is unlikely that substantial phase shifts on the 8D state are accumulated. The net phase shifts potentially accumulated are made even smaller by the fact that the 8D state has states both above and below it, which accumulate oppositely signed phase shifts. We therefore can expect that the potential line shift due to collisions (from accumulated phase shifts) will be much smaller than the broadening of the line due to the collisions.

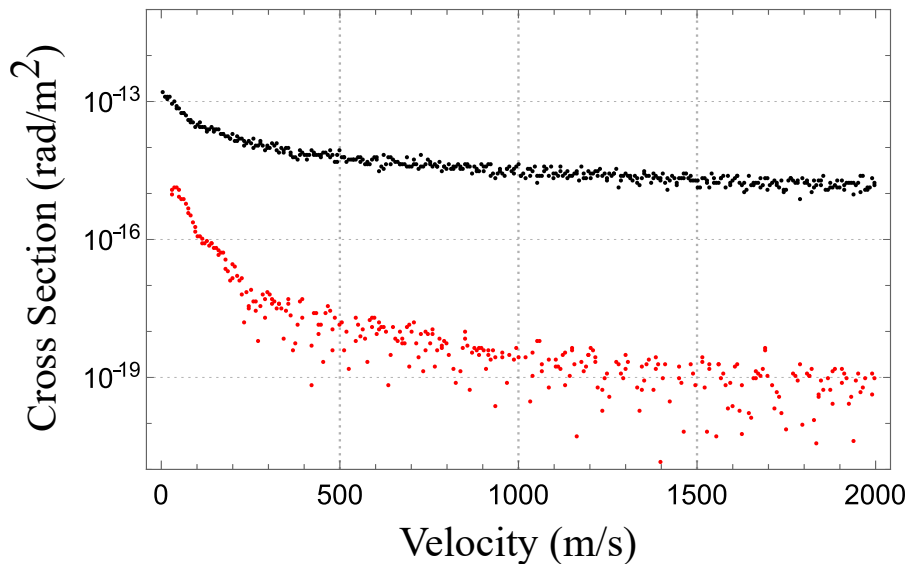


Figure 6.11: Collisional cross sections for broadening (black) and shifts (red)

In Fig. 6.11, we display the cross sections calculated by the Monte Carlo simulation for the broadening and shifts as a function of relative velocity, black and red respectively, on the $8D_{5/2}$ state. The cross sectional shifts are much smaller than the broadening, as we anticipated from our qualitative Fourier arguments. We can calculate the net shift and broadening from these cross sections using Eqs. (6.9-6.10), noting that the integral terms are the cross sections given by the Monte Carlo, and integrating over the collisional velocity distribution. These are given by

$$\Delta\omega = \mathcal{N} \int v \sigma_{\omega}(v) \rho(v) dv \quad (6.17)$$

and

$$\Delta\gamma = \mathcal{N} \int v \sigma_{\gamma}(v) \rho(v) dv. \quad (6.18)$$

Which amount to close 16 GHz/Torr broadening and a 3 MHz/Torr shift on the 8D line and 37 GHz/Torr broadening, 3 MHz/Torr shift on the 12D. Note that the shift has a fractional uncertainty of about 50%, but the shift is orders of magnitude below the broadening. Therefore, while we have seen evidence of pressure broadening on our lines, there are negligibly small shifts associated with them; 50 kHz of broadening corresponds to a ~ 10 Hz shift. Including the Van der Waals interaction between hydrogen atoms in the Monte Carlo simulations show negligible effect. We therefore assign no shift for Van der Waals interactions.

6.4.3 Frequency Calibration

As described in Chapter 3, the optical frequency comb plays the pivotal role in converting the large optical frequencies in the spectroscopy into RF frequencies which can be counted electronically. This alone only provides a precise relative frequency determination however, and a time standard must be referenced to provide an absolute frequency determination [94]. In the following section, we describe the frequency metrology subsystem in the 2S-8D experiment, and investigate potential systematics associated with our frequency calibration.

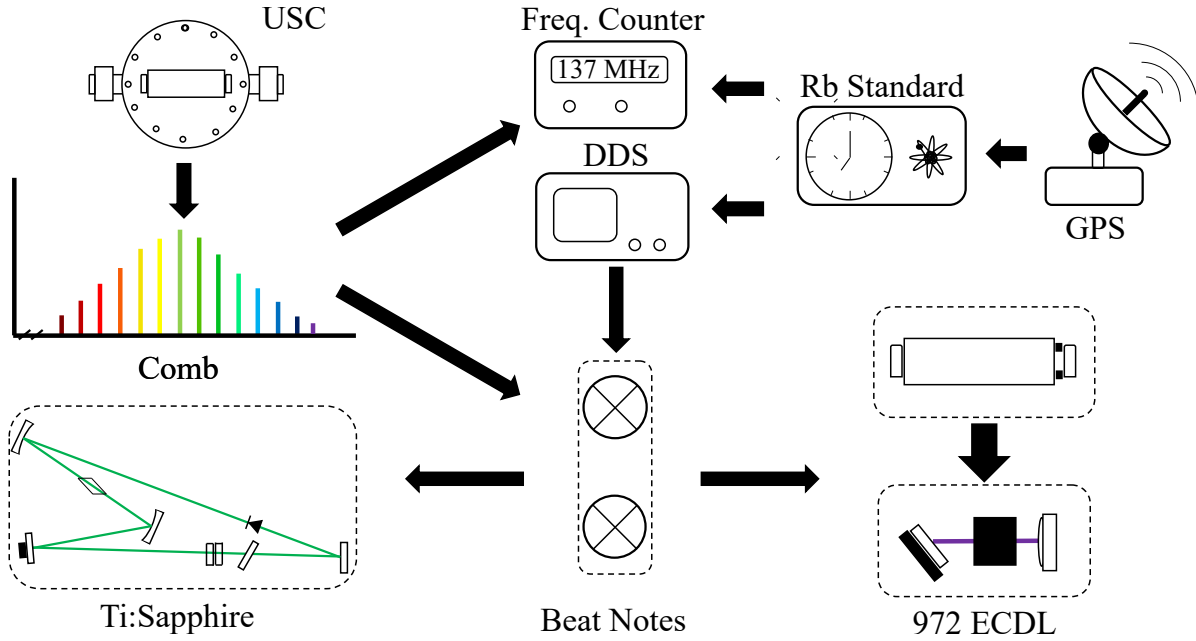


Figure 6.12: The frequency metrology subsystem. USC: ultra-stable cavity, DDS: direct-digital synthesizer, 972 ECDL: 972 nm external-cavity diode laser, GPS: Global positioning system timebase corrections

A GPS-trained, Rb-oscillator provides our absolute frequency reference – Stanford Research Systems, FS740. The FS740 has 10 MHz outputs to reference electronics, and also functions as a frequency counter. The frequency comb is self-referenced, and is also stabilized indirectly to the ultra-stable cavity via a coherent phase-lock to the stable 1554 nm laser. By counting the repetition rate of the comb, and setting the f_0 degree of freedom, we can determine the absolute frequency of any of comb tooth. Similarly, the spectroscopy laser and the metastable excitation laser are coherently phase-locked to the comb. The beat frequencies between the comb and the other laser systems are set by a direct-digital synthesizer, which is also referenced to one of the 10 MHz outputs of the Rb-timebase.

The frequencies of the beat notes with the comb can be converted into absolute atomic frequencies via

$$\nu_{1S-2S} = 8(nf_r + f_0 + f_{\text{beat}}^{972}) \quad (6.19)$$

for the 972 nm laser system and

$$\nu_{2S-8D} = 2(mf_r + 2f_0 + f_{\text{beat}}^{778}) \quad (6.20)$$

for the 778 nm laser system. Throughout the day, f_r is counted by both the Rb-timebase and a Hewlett-Packard 83131A counter in 100 s gate times. The offset frequencies recorded in the scan are then converted into absolute frequencies by the applying corrections from the f_r data. Before applying corrections, repetition rate phase-lock breaks are detected and removed and the f_r data is low-passed as the point-to-point scatter is expected from the manufacturer specified Rb-timebase Allan deviation and is not likely due laser frequency excursions. An interpolation function for

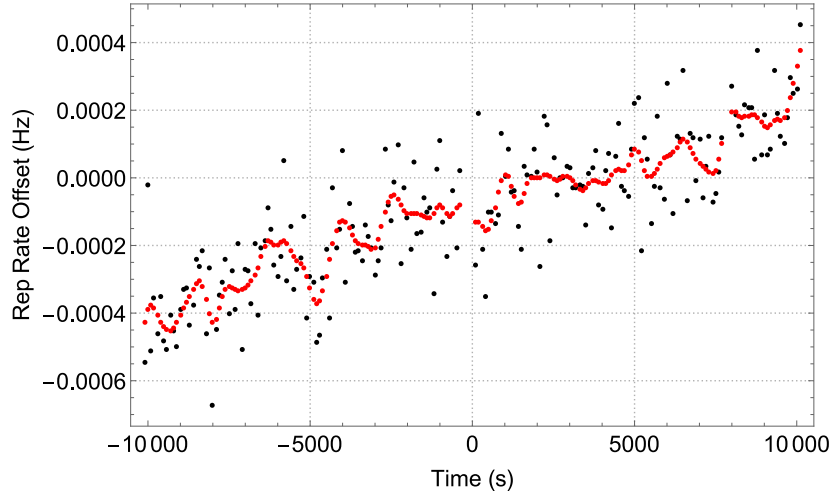


Figure 6.13: Example of f_r data collected in a day with an offset subtracted. The individual f_r measurements are displayed in black and the low-passed data is in red (low-pass corner of ≈ 1 mHz)

the low-passed f_r data generates an $f_r(t)$ function that applies a time-dependent correction to the recorded spectroscopy beat frequencies, as each frequency point in a line scan is also timestamped. The extrapolated frequencies in a day are insensitive to this low-pass corner. A typical days worth of data gives about 5000-20000 s of f_r counting.

Calculation of laser noise shifts

Noise on the laser light exciting a transition can shift, distort, and broaden the lineshape depending on the relative distribution of noise within the optical spectrum. Generically the presence

of laser noise will broaden the transition in question, but an asymmetric distribution of noise can induce shifts. We will quickly present how the noise present on a laser may be diagnosed via a beat note with another stable laser, and then apply that analysis to our 778 nm and 243 nm laser systems.

The noise on a laser may be diagnosed via investigation of a beat between that laser and a stable oscillator. Here we quickly derive the relation between the measured noise properties of that beat note with the noise properties of the laser itself. We make a three basic assumptions in this treatment: 1) that the noise on the laser is sufficiently small that higher order sidebands do not participate 2) that the finite noise frequency analysis applied here can be generalized to a continuous distribution of frequencies 3) All the noise measured on the beat note originates from the "non-stable" laser. The last assumption indicates that, in general, this procedure will provide an overestimate of the true noise of the laser in question.

A beat note between two lasers is typically measured by an RF spectrum analyzer, which reports the electronic power in a signal as a function of frequency. Consider the field of two lasers given by

$$E_1(t) = E_1 e^{-i\omega_1 t - i\beta(t)}, \quad (6.21)$$

$$E_2(t) = E_2 e^{-i\omega_2 t}, \quad (6.22)$$

and

$$\beta(t) = \beta \sin(\Omega t), \quad (6.23)$$

where $\omega_{1,2}$ are the coherent laser frequencies, and Ω is some modulation frequency on laser 1. Let us denote $\omega_0 = \omega_1 - \omega_2$, representing the beat frequency between these two lasers. The $\beta(t)$ modulation function will represent the noise on laser 1 due to a single perturbing frequency. The beat note between these two lasers is

$$I(t) \propto |E_1 + E_2|^2 = E_1^* E_2 + E_1 E_2^*, \quad (6.24)$$

where we have dropped the DC terms because they do not contribute further in this analysis. This can be expanded and gives

$$I(t) \propto E_1 E_2 (e^{-i\omega_1 t - i\beta(t)} e^{i\omega_2 t} + e^{i\omega_1 t + i\beta(t)} e^{-i\omega_2 t}). \quad (6.25)$$

We can then apply the Jacobi-Anger expansion

$$e^{-i\omega t - i\beta \sin(\Omega t)} = \sum_{n=-\infty}^{\infty} J_n(\beta) e^{-i(\omega + n\Omega)t}, \quad (6.26)$$

where J_n is the n^{th} Bessel function of the first kind. In our experiment, that the peak phase excursion caused by our noise source is much less than a radian, and therefore we are justified in only keeping the first order terms of Eq. (6.26):

$$e^{-i\omega t - i\beta \sin(\Omega t)} \approx J_0(\beta) e^{-i\omega t} + J_1(\beta) e^{-i(\omega + \Omega)t} - J_1(\beta) e^{-i(\omega - \Omega)t} \quad (6.27)$$

Using this series expansion we see right away that phase noise manifests as sidebands to the carrier. Applying this approximation and making some simplifications we arrive with

$$I(t) \propto 2E_1 E_2 (J_0(\beta) e^{-i\omega_0 t} + J_1(\beta) e^{-i(\omega_0 + \Omega)t} - J_1(\beta) e^{-i(\omega_0 - \Omega)t}), \quad (6.28)$$

where ω_0 is given by $\omega_1 - \omega_2$. This is our time-dependent beat-frequency signal now that would be detected. Presumably, the detection of this time dependent intensity signal is done by a photodiode, which provides current proportional to optical power (intensity). The RF spectrum analyzer converts this time dependent signal into a frequency dependent signal, and then measures the power in each frequency component. In other words, the resultant beat note measured by the spectrum analyzer is of the form $(I(\omega))^2$

$$(I(\omega))^2 = k(J_0^2(\beta)\delta(\omega - \omega_0) + J_1^2(\beta)\delta(\omega - (\omega_0 - \Omega)) + J_1^2(\beta)\delta(\omega - (\omega_0 + \Omega))) \quad (6.29)$$

where the cross terms drop out because they contain terms of $\delta(\omega - \omega_0)\delta(\omega - (\omega_0 \pm \Omega))$, etc. which are zero everywhere. We are interested in a driving two-photon transition in our spectroscopy. This is a nonlinear process and is best considered in the time domain. The amplitude of a nonlinear process is proportional to the electric field squared. The electric field squared is given by

$$E_1^2(t) = E_1^2[J_0^2(\beta)e^{-i2\omega_0 t} + 2J_0(\beta)J_1(\beta)e^{-i(2\omega_0+\Omega)t} - 2J_0(\beta)J_1(\beta)e^{-i(2\omega_0-\Omega)t} + \mathcal{O}(J_1(\beta)^2)]. \quad (6.30)$$

Taking the Fourier transform of this result, we find that the new spectral content is at 2ω (as expected) with sidebands still appearing at $\pm\Omega$. The total population driven in a two photon process will be proportional to the amplitude squared, so the population driven by frequency ω is given by

$$\rho_{ee}(\omega) = k[\delta(\omega - 2\omega_0) + 4\frac{J_1^2(\beta)}{J_0^2(\beta)}\delta(\omega - (2\omega_0 + \Omega)) + 4\frac{J_1^2(\beta)}{J_0^2(\beta)}\delta(\omega - (2\omega_0 - \Omega))]. \quad (6.31)$$

So the conversion of an RF beat note to an effective power distribution for a single two-photon process requires multiplying up the noise in the sidebands by a factor of 4 as compared to the original RF beatnote. This may be generalized to processes involving multiple nonlinear processes. For instance, when applied to driving the 1S-2S transition the noise in the beat note measured between the frequency comb and the 972 ECDL light requires a multiplication of 64.

Phase noise on a laser does not necessarily shift the observed transition frequency in a spectroscopy measurement. In general, the recovered atomic resonance will be a convolution of the atomic response with the laser spectrum. In the case of a highly coherent, monochromatic laser, the observed resonance will be the convolution of the atomic resonance with a Delta-function – we recover exactly the atomic resonance. If instead the spectroscopy laser has a non-negligible linewidth, we will recover a slightly broader line. Only in the case of an asymmetric distribution of laser power will the recovered resonance be shifted.

We apply our analysis detailed above to quantify potential shifts and line broadening due to the phase noise distribution on the Ti:Sapphire laser. Fig (6.14) shows the beat note between the Ti:Sapphire and the frequency comb. Since the 2S-8D is a two photon transition, the noise in this

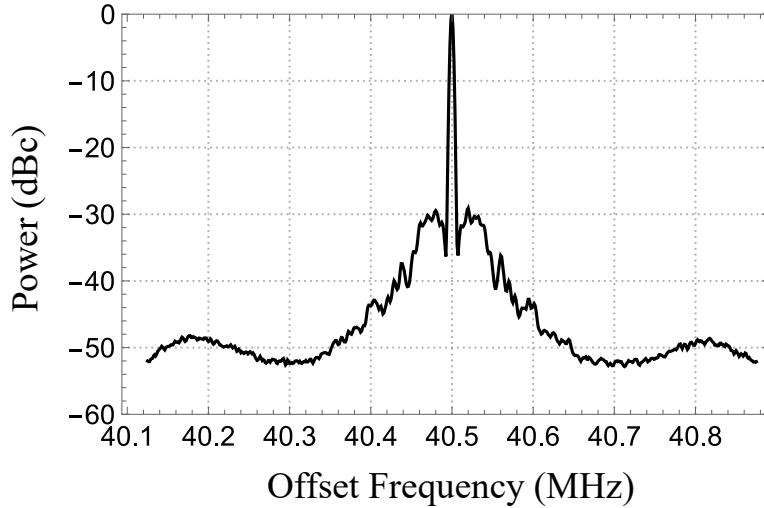


Figure 6.14: Ti:Sapphire-Frequency Comb beat note, 3 kHz resolution bandwidth

beat note is multiplied up by four in the excitation. The convolution of this spectral distribution with our fit function (fixed parameters), in laser frequency, provides a good estimate of the potential broadening and shifts due to the noise on the Ti:Sapphire laser. We estimate a shift on the order of 5 Hz, with a 10 Hz uncertainty in the shift due to laser noise, and a broadening of 2 kHz, which is an insignificant contribution at our current level of precision.

The beat note between the frequency comb and the 972 nm ECDL is shown in Fig. (6.15a). Unlike the 778 nm beatnote, the light at 972 nm undergoes three nonlinear processes to drive the 1S-2S transition, and is much more sensitive to the overall noise performance at the fundamental. At the same time, the 243 nm light is only used to generate the metastable hydrogen, and small shifts and broadening due to the noise performance of the laser system is not critical to the 2S-8D experiment.

Nevertheless, we investigated the broadening of the 1S-2S transition due to laser noise, and find excellent agreement between our calculations and the observed lineshape. The 1S-2S natural linewidth is ≈ 1 Hz, and we expect ~ 150 kHz transit time broadened lines from the 243 nm Gaussian profile. Due to the nature of the 243 nm enhancement cavity lock (we dither the cavity mirrors to generate an error signal) we also expect sidebands at 480 kHz with a Gaussian profile. In Fig (6.15b) we show an example of a recovered 1S-2S line (dotted black). To estimate the contribution of noise from the 972 laser to the lineshape, we convolve the estimated noise distri-

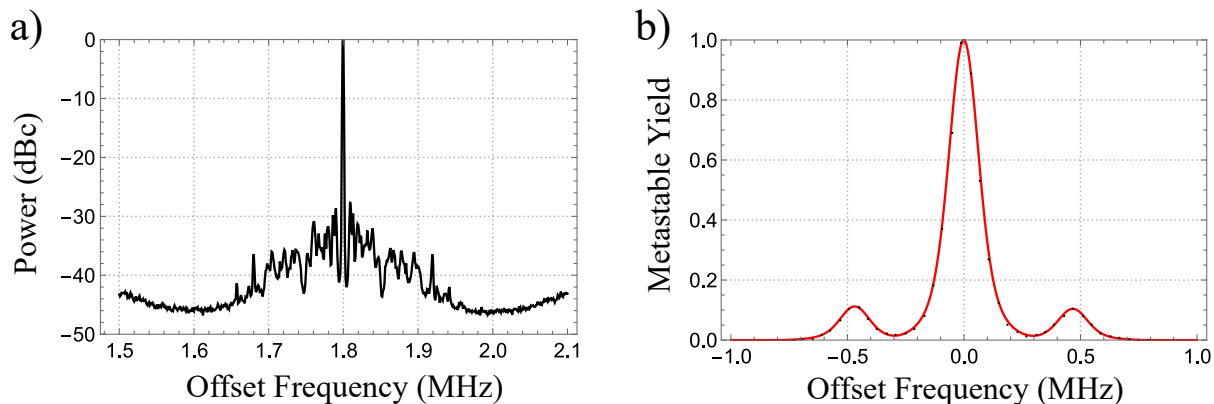


Figure 6.15: a) 972 nm ECDL-Frequency comb beatnote 1 kHz resolution bandwidth b) Comparison of convolved line (red) with 1S-2S measured lineshape (black)

tribution from the 972 nm beatnote with a set of three Gaussians with a width to match the transit time width. The red curve in Fig. (6.15b) shows the result of this convolution, which indicates excellent agreement in the recovered lineshape and the expected lineshape from 972 laser noise. The asymmetric phase noise on the 972 laser amounts to 580 ± 120 Hz (atomic) shift. This shift is independent of the sidebands, omitting them from the fit estimates a shift of 580 ± 350 Hz.

Verification of Absolute Frequency Calibration

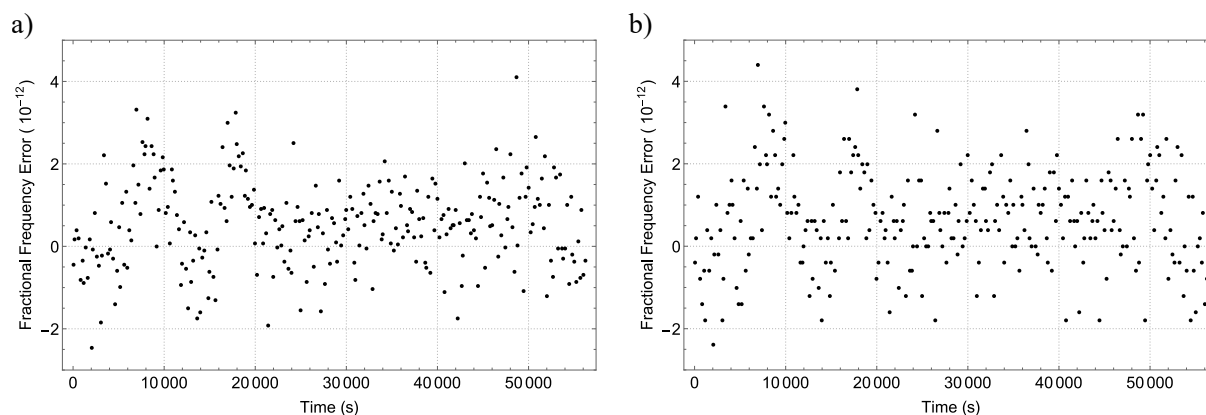


Figure 6.16: Frequency counting of NIST WWVB 5 MHz signal. a) Counted by the FS740 frequency counter. b) Counted by the HP 53131A

While we have determined that our measured lineshapes are in good agreement with the estimated noise of our lasers and there are no substantial shifts associated with that noise, we wish to verify the accuracy of our frequency metrology system. To verify our absolute frequency calibration, we instead compare our RF-frequency counter against a known RF standard. The National Institute of Standard and Technology (NIST) provides absolute frequency standards to the US via the WWV and WWVB radio stations located just North of Fort Collins Colorado. The WWV station provides a 2.5 MHz, 5 MHz, 10 MHz, 15 MHz, and 20 MHz broadcast signal to provide radio frequency standards across the United States, and are traceable to the National Standard at NIST. To verify the accuracy of our RF frequency metrology, we transported our RF-standard and frequency counters to the WWV station and counted a high fidelity 5 MHz signal provided. In Fig. 6.16, we show the counted fractional frequency difference by the SRS FS740 and Hewlett-Packard 53131A frequency counter, both of which referenced to the Rb-time base within the FS740. The SRS counter, which is the primary RF frequency counter, shows a mean fractional frequency offset of 0.53×10^{-12} and the HP counter a mean fractional frequency offset of 0.64×10^{-12} . The scatter of the frequency time series is expected from the the Allan deviation quoted by SRS for the FS740 for a gate time of 200s. The Allan deviation we measured for our timebase is given in Fig. 6.17 up to 18600 s.

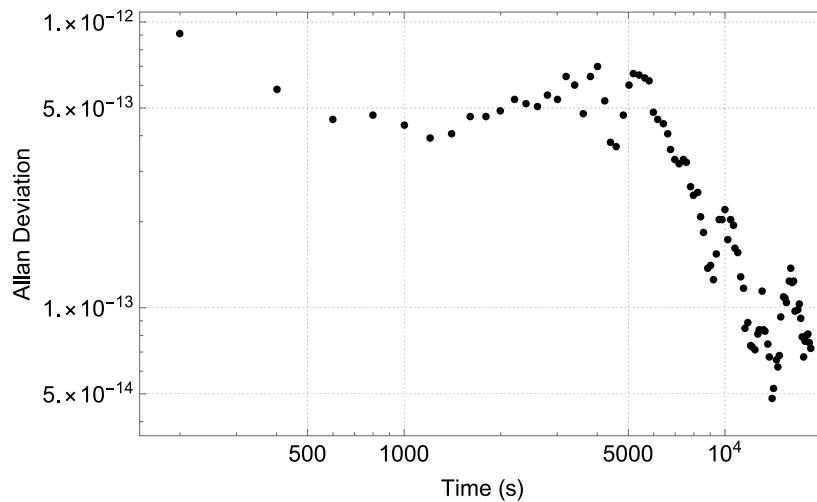


Figure 6.17: Calculated Allan deviation of the FS740 from data presented in Fig. 6.16 a).

Of particular importance is the timescale in which the frequency scatter in the logged f_r 's during 2S-8D spectroscopy becomes limited by frequency drift of the comb and ultra-stable cavity system as opposed to the stability of the Rb-timebase. For timescales in which the frequency scatter of the logged f_r 's is limited by the Rb-timebase, we are justified in averaging over these excursions because they do not represent true scatter in the frequency of the spectroscopic light. This is no longer true once the frequency drift of optical metrology system is appreciable over that time scale. A straightforward approach to estimate this timescale is to compare the Allan deviation of the FS740 and the logged repetition rate. At long time scales the unbounded drifts of the optical cavity become apparent whereas the FS740 is disciplined by GPS. In Fig. 6.18, we display an Allan deviation of f_r (black) compared to the Allan deviation of the FS740 (red). Apparently, for timescales below 1000 s, the frequency scatter of f_r is limited by the performance of the FS740, and above 1000 s the drift of the ultra-stable optical cavity becomes appreciable. As previously indicated, the logged f_r data is low-passed in the analysis of the 2S-8D spectroscopy. The corner frequency of this low-pass corner is set by this timescale of the ultra-stable cavity drift, $f_c \approx 1$ mHz.

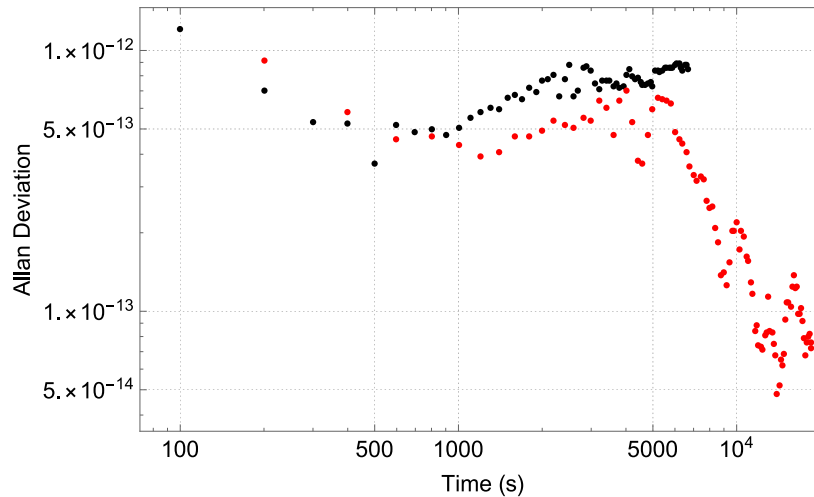


Figure 6.18: An example of the Allan deviation of f_r during spectroscopy compared to Allan deviation of the FS740. The Allan deviations are in reasonable agreement until averaging times of about 1000 s, after which the drift of the USC becomes apparent.

A fractional frequency offset of the FS740 of 5.3×10^{-13} corresponds to a shift of 410 Hz on the $2S_{1/2}-8D_{5/2}$ line and 1.2 kHz on the 1S-2S line. A mean offset of 5.3×10^{-13} from just under one day's averaging is apparently typical of many GPS disciplined Rb-oscillators [193], indicating it is likely that this counter offset is due to the relatively short time scale of a day in which the FS740 was locked to the GPS reference at the NIST WWV station. Aside from this measured frequency offset, there is also the fact that the precision of the absolute frequency metrology is limited by the measurement time. Since the repetition rate of the comb is measured for an average of 10000 s in a day of data, this also limits the achievable precision of the measurement. The stability of our time standard in 10000 s is $\approx 3 \times 10^{-13}$, which corresponds to an absolute frequency precision of ≈ 250 Hz in a day's scan. We apply a -400 ± 400 Hz shift associated with the measured frequency offset, and assume that the frequency stability and potential offsets are correlated. This corresponds to a final shift of -400 ± 650 Hz associated with our frequency metrology system, with negligible contribution from laser noise.

6.4.4 Second-Order Doppler Shift

The 2S-8D transitions are two-photon transitions and the first-order Doppler shift is heavily suppressed. However, second-order Doppler shifts remain. Second-order Doppler effects shift the resonance frequency by $\delta\nu = \frac{1}{2}(v/c)^2\nu_0$, where ν_0 is the rest frame resonance frequency of the transition, v is the velocity of the atom in the lab frame, and c is the speed of light. We have characterized the velocity distribution of the metastable hydrogen beam from our chopped-beam, time-of-flight measurements [3]. While a Maxwellian distribution is naively expected, this ignores effects that can modify the functional form of the measured distribution, in particular the dynamics of the 1S-2S optical excitation and the metastable atom detector. The overall modification to the metastable velocity distribution is the reduction in slow moving atoms [3], with the overall velocity distribution more closely matching a functional form of $P(v) \propto v^4 e^{-\beta v^2}$, with $\beta = m/2k_b T$. This shift to faster atoms is dominantly due to the ionization dynamics in the metastable generation and

the preference for faster atoms to reach the metastable detector. Currently, the temperature of the atomic beam is estimated by a silicon temperature probe mounted on the cryogenic nozzle.

Investigation with the numeric lineshape model indicates that the presence of a velocity distribution as opposed to a single velocity class does not strongly affect the associated Doppler shift. From data gathered in [3], the uncertainty in the most probable velocity class for a given temperature reading is quite low (< 10 m/s). Fitting the time-of-flight measurements shown in Fig. 2.4.2 gives a second-order Doppler shift of 1475 ± 25 Hz at 9.5 K and 930 ± 11 Hz at 5.9 K. We typically performed spectroscopy when the temperature readings were between 4.5-4.9 K, which corresponds to a shift of 730 ± 85 Hz.

6.4.5 Blackbody Radiation

Background blackbody radiation from nearby surfaces perturbs hydrogen atoms. This perturbation can be thought of as two-separate effects. The off-resonant blackbody spectrum perturbs the hydrogen atom analogously to the ac-Stark shift considered previously, albeit with a far weaker field and with much larger spectral bandwidth. On the other hand, since blackbody radiation is quite broad it can resonantly drive many dipole-allowed transitions, effectively reducing the lifetime of states in consideration. This resonant interaction will primarily affect the 8D state, as the density of nearby states within the spectrum of the blackbody radiation will be much greater than that of the 2S state. Blackbody radiation effects, while small, require consideration in precision spectroscopic or atomic clock experiments [194, 195].

In atomic hydrogen, the shift induced by blackbody radiation, $\Delta\nu_{BB}$, asymptotically approaches the value

$$\Delta\nu_{BB} = \frac{\alpha(k_b T)^2}{6\hbar mc^2} \quad (6.32)$$

as $n \rightarrow \infty$, which corresponds to a shift of about 2.4 kHz at 300 K [196]. As the spacing between adjacent states becomes large, $\hbar\omega_{ij} > k_b T$, the shift correspondingly decreases. In other words, as n decreases, the state becomes less sensitive to blackbody radiation. An estimation for which values of n Eq. (6.32) is expected to be applicable gives $n > 13$. Numeric calculation of

the blackbody shift at 300 K on the 8D state is 490 Hz. The previous measurement of the 2S-8D transitions [45] measured the transitions at 300 K and 330 K by heating their magnetic shields surrounding the spectroscopic volume and found an expected shift of 650(160) Hz and a broadening of 5.5(.5) kHz, which is in good agreement with the theoretical calculations presented in [196]. We therefore assume a 490 Hz shift due to blackbody radiation in our measurement, and assign 160 Hz as the uncertainty.

6.4.6 Hyperfine Structure

The hyperfine structure of the 8D manifold is unresolved, and therefore we have opted to include the hyperfine structure into the line fitting function. In contrast, the 2S hyperfine structure is resolved with a splitting of 177.556838 MHz and the $2S_{1/2}^{F=0}$ state does not participate appreciably in the spectroscopy. The measured $2S_{1/2}^{F=1}$ - $8D_{5/2}$ resonance frequency can be converted the $2S_{1/2}$ - $8D_{5/2}$ centroid frequency by including the hyperfine structure of the 2S state, which amounts to a shift of +44.38922 MHz, with the uncertainty in the 2S hyperfine splitting contributing negligibly [33, 197]. The 8D hyperfine splitting of 142430 Hz, calculated, is known to 140 Hz [5, 45]. Applying ± 140 Hz corrections to the hyperfine splitting in Eq. (4.39) amounts to ± 30 Hz shifts, which we take as the uncertainty.

6.4.7 Cross-Damping

The contribution of quantum interference, also known as cross-damping, on the experimental lineshape has been of great interest in recent high precision spectroscopic measurements [23, 29, 30]. This effect can be understood as the interference between different decay paths in the atom [106, 198]. It should be noted that this systematic, while present on recent fluorescence-detection measurement, is unlikely to be significant in this measurement or the previous measurements of the $2S_{1/2}$ - $8D_{5/2}$ transition, which could be ascertained through a careful study of publications on the phenomenon [106, 174, 199, 200].

A classical toy model may be constructed to help build intuition for this effect. The atom may be treated as a pair of classical dipoles driven by the spectroscopy light at frequency ω_L [199].

In this case, the dipole emitters are two transitions within the atom – presumably the on-resonant transition of interest and a nearby off-resonant transition that both decay to state $|f\rangle$. We may assume that the two dipoles have resonances ω_0 and $\omega_0 + \Delta$ for the resonant and off resonant transitions respectively. In that case, the net dipole moment of this classical dipole may be written as

$$\vec{\mu} = \frac{\vec{\mu}_0}{(\omega - \omega_L) + i\gamma/2} + \frac{\vec{\mu}_1}{(\omega - \omega_L + \Delta) + i\gamma/2}. \quad (6.33)$$

As the emission pattern is given by $|\vec{\mu}|^2$, the relative orientation of the two emitters and their detuning leads to a spatial dependence in the maximal response due to the interference term between the resonant and off resonant dipole, $\vec{\mu}_0 \cdot \vec{\mu}_1$. This spatial dependence can cause asymmetric line shapes due to the finite size of the detection geometries, which shifts the line.

To properly capture this effect, quantum considerations must be taken into account. For instance, determining the magnitude of the dipole moments, $\vec{\mu}_i$, and taking into account the discrete nature of the energy levels requires a quantum mechanical treatment. In the density matrix formulation, the dynamics of the atom in an electromagnetic field are given by

$$\frac{\partial \rho}{\partial t} = [H, \rho] - \mathcal{L}\rho, \quad (6.34)$$

with \mathcal{L} the Lindblad operator. Following the treatments of [106, 199], we denote initial, excited, and final states in the optical excitation and following decay $|i\rangle, |e\rangle, |f\rangle$ respectively. The matrix element $(\mathcal{L}\rho)_{e'e'}$ gives the decay term from excited state $|e'\rangle$ and it can be shown that

$$(\mathcal{L}\rho)_{e'e'} = \frac{1}{2} \sum_{ef\eta} \frac{\mu_{fe'}^\eta \mu_{fe}^\eta \omega_{ef}^3}{3\pi\epsilon_0 \hbar c^3} (\rho_{ee'} + \rho_{e'e}) \quad (6.35)$$

for splitting $\omega_{ij} = (E_i - E_j)/\hbar$, and matrix element $\mu_{fe}^\eta = q \langle f | \vec{\epsilon}_\eta \cdot \vec{r} | e \rangle$, for elementary charge q and spherical unit vectors $\vec{\epsilon}_\eta$, see [106, 200, 201]. Eq. (6.35) indicates that the decay rate out of state $|e'\rangle$ depends on both the population in state $|e'\rangle$ (normal damping) and state $|e\rangle$ (cross damping). The sum over η is related to the general detection geometry of the measurement. If fluorescence

is being measured by a finite sized detector, this leads to a partial summation over η whereas a full 4π solid angle detection corresponds to a complete summation over η . Similarly, measuring populations instead of fluorescence is also akin to a 4π detection as no decay channel is detected in exclusion to any other.

Applying the Wigner-Eckart theorem allows the matrix element μ_{fe}^η to be decomposed into a geometric factor sensitive to \vec{e}_η and a reduced matrix element. For completeness, we now introduce the proper quantum numbers to label states $|f\rangle$ and $|e\rangle$. As such, the dipole matrix element hyperfine basis can be written

$$\mu_{ef}^\eta \propto \xi \begin{Bmatrix} L' & J' & S \\ J & L & 1 \end{Bmatrix} \begin{Bmatrix} J' & F' & I \\ F & J & 1 \end{Bmatrix} \begin{pmatrix} F' & 1 & F \\ -m'_F & \eta & m_F \end{pmatrix}, \quad (6.36)$$

where $\xi = \sqrt{(2J+1)(2J'+1)(2F'+1)(2F+1)}(-1)^{L'+S+J+J'+I+F+F'-m'_F}$ with the unprimed quantum number corresponding to the $|e\rangle$ state. Equality is reached when the above expression is multiplied by the proper reduced matrix element. To evaluate the sum in Eq. (6.35) we first investigate $\mu_{fe_1}^\eta \mu_{fe_2}^\eta$, which is proportional to

$$\begin{aligned} \mu_{fe_1}^\eta \mu_{fe_2}^\eta &\propto (2J'+1)(2F'+1) \sqrt{(2J_1+1)(2J_2+1)(2F_1+1)(2F_2+1)} \\ &(-1)^{2(L'+J'+F'-m'_F)} (-1)^{S_1+J_1+I_1+F_1+S_2+J_2+I_2+F_2} \begin{Bmatrix} L' & J' & S_1 \\ J_1 & L_1 & 1 \end{Bmatrix} \begin{Bmatrix} L' & J' & S_2 \\ J_2 & L_2 & 1 \end{Bmatrix} \\ &\begin{Bmatrix} J' & F' & I \\ F_1 & J_1 & 1 \end{Bmatrix} \begin{Bmatrix} J' & F' & I \\ F_2 & J_2 & 1 \end{Bmatrix} \begin{pmatrix} F' & 1 & F_1 \\ -m'_F & \eta & m_{F_1} \end{pmatrix} \begin{pmatrix} F' & 1 & F_2 \\ -m'_F & \eta & m_{F_2} \end{pmatrix}. \end{aligned} \quad (6.37)$$

We now sum over f (i.e. L', J', m'_F) and η ,

$$\begin{aligned} \sum_{f\eta} \mu_{fe_1}^\eta \mu_{fe_2}^\eta &\propto \sum_{L', J', F'} (2J'+1)(2F'+1) \begin{Bmatrix} L' & J' & S_1 \\ J_1 & L_1 & 1 \end{Bmatrix} \begin{Bmatrix} L' & J' & S_2 \\ J_2 & L_2 & 1 \end{Bmatrix} \\ &\begin{Bmatrix} J' & F' & I \\ F_1 & J_1 & 1 \end{Bmatrix} \begin{Bmatrix} J' & F' & I \\ F_2 & J_2 & 1 \end{Bmatrix} \sum_{m'_F, \eta} \begin{pmatrix} F' & 1 & F_1 \\ -m'_F & \eta & m_{F_1} \end{pmatrix} \begin{pmatrix} F' & 1 & F_2 \\ -m'_F & \eta & m_{F_2} \end{pmatrix}. \end{aligned} \quad (6.38)$$

The 3– j symbols have a sum rule such that

$$(2j_3 + 1) \sum_{m_2 m_3} \begin{pmatrix} j_1 & j_2 & j_3 \\ m_1 & m_2 & m_3 \end{pmatrix} \begin{pmatrix} j_1 & j_2 & j'_3 \\ m_1 & m_2 & m'_3 \end{pmatrix} = \delta_{j_3, j'_3} \delta_{m_3, m'_3} \{j_1, j_2, j_3\} \quad (6.39)$$

which means that

$$\begin{aligned} \sum_{f\eta} \mu_{fe_1}^\eta \mu_{fe_2}^\eta &\propto \sum_{L', J'} \frac{(2J' + 1)}{2F_1 + 1} \begin{Bmatrix} L' & J' & S_1 \\ J_1 & L_1 & 1 \end{Bmatrix} \begin{Bmatrix} L' & J' & S_2 \\ J_2 & L_2 & 1 \end{Bmatrix} \\ &\left(\sum_{F'} (2F' + 1) \begin{Bmatrix} J' & F' & I \\ F_1 & J_1 & 1 \end{Bmatrix} \begin{Bmatrix} J' & F' & I \\ F_2 & J_2 & 1 \end{Bmatrix} \delta_{F_1, F_2} \delta_{m_{F_1}, m_{F_2}} \{F', 1, F_1\} \right). \end{aligned} \quad (6.40)$$

There is a sum rule for the six– j symbols that corresponds to the term in the parenthesis in the above equation,

$$\begin{aligned} &\left(\sum_{F'} (2F' + 1) \begin{Bmatrix} J' & F' & I \\ F_1 & J_1 & 1 \end{Bmatrix} \begin{Bmatrix} J' & F' & I \\ F_2 & J_2 & 1 \end{Bmatrix} \delta_{F_1, F_2} \delta_{m_{F_1}, m_{F_2}} \{F', 1, F_1\} \right) \\ &= \frac{\delta_{J_1, J_2}}{(2J_1 + 1)} \{J', 1, J_1\} \{F_1, I, J_1\}. \end{aligned} \quad (6.41)$$

This leaves us with

$$\begin{aligned} \sum_{f\eta} \mu_{fe_1}^\eta \mu_{fe_2}^\eta &\propto \sum_{L', J', F', m'_{F'}} \frac{(2J' + 1)}{(2F_1 + 1)(2J_1 + 1)} \begin{Bmatrix} L' & J' & S_1 \\ J_1 & L_1 & 1 \end{Bmatrix} \begin{Bmatrix} L' & J' & S_2 \\ J_2 & L_2 & 1 \end{Bmatrix} \\ &\delta_{J_1, J_2} \delta_{F_1, F_2} \delta_{m_{F_1}, m_{F_2}} \{F', 1, F_1\} \{J', 1, J_1\} \{F_1, I, J_1\}. \end{aligned} \quad (6.42)$$

Finally, applying the same six– j sum rule and the equality of a 6– j symbol under exchange of a pair of columns we arrive with

$$\sum_{f\eta} \mu_{fe_1}^\eta \mu_{fe_2}^\eta \propto \sum \frac{\delta_{L_1, L_2} \delta_{J_1, J_2} \delta_{F_1, F_2} \delta_{m_{F_1}, m_{F_2}}}{(2F_1 + 1)(2J_1 + 1)(2L_1 + 1)} \{F', 1, F_1\} \{J', 1, J_1\} \{F_1, I, J_1\} \{L', 1, L_1\} \quad (6.43)$$

which means that

$$\sum_{f\eta} \mu_{fe}^\eta \mu_{fe'}^\eta = 0 \quad (6.44)$$

unless $|e\rangle$ and $|e'\rangle$ have the same angular momentum quantum numbers, which requires they differ in principle quantum number. Since there are usually no states near the $|e\rangle$ manifold that meet this condition, excepting some circumstances like high Rydberg states, the contribution of such states is negligible due to the minimal population driven to such detuned states. If the splitting between the states in the $|f\rangle$ manifold are small, then we may approximate Eq. (6.35) as

$$(\mathcal{L}\rho)_{ee} \approx \sum_{f\eta} \frac{(\mu_{fe}^\eta)^2 \omega_{ef}^2}{3\pi\epsilon_0 \hbar c^3} \rho_{ee}. \quad (6.45)$$

In emission spectroscopy, typically the fluorescence detection does not cover the whole 4π solid angle around the emitting atoms, leading to only a partial summation over η . This leads to the distortion of the lineshape on detector geometry. However, if the entire 4π solid angle is detected, the cross damping effect becomes negligible. Detecting the populations in either $|g\rangle$ or $|e\rangle$ instead of detecting the fluorescence from $|e\rangle$ is analogous to a 4π detection, see for instance the introduction of [106], the cross damping section in [29], or the Lamb shift discussion in [199]. Therefore, this measurement is insensitive to this effect and we assign no corresponding shift or uncertainty.

6.4.8 Incoherent Line Pulling

Nearby atomic resonances can pull the line incoherently as well, as opposed to coherent line pulling in the quantum interference effect discussed above [199]. This effect is due to the tail of the nearby resonance having nonzero slope within the resonance of interest. The $8D_{3/2}$ states is the most nearby (60 MHz), allowed state that can contribute. These lines have smaller dipole matrix elements, but we will treat them as having the same magnitude – the lifetime of the $8D$ states is the same. We can estimate this effect by fitting a single Lorentzian function to a pair of Lorentzian separated by 44 MHz. As the off-resonant transition is about 80 linewidths away, we expect that this effect is quite small; a simple numerical test finds a < 1 Hz shift due to incoherent line pulling.

Additionally, the presence of the modulation sidebands of the 778 nm cavity can pull the line in a similar way, although this requires an asymmetry of the sidebands. The modulation frequency is ~ 8 MHz. In the case of two equally large Lorentzian resonances of width 200 kHz separated by 8 MHz results in a line shift of 1.5 Hz, corresponding to a 50/50 power split between the resonance and a single sideband (one should note that this represent an upper limit and the true effect is much smaller), so this is also a negligible effect.

6.4.9 Residual First Order Doppler shifts

Mismatched wave fronts at the spectroscopic volume of the oppositely propagating traveling waves in the 778 nm power enhancement cavity could lead to residual first-order Doppler shifts by driving the 2S-8D transition with off-resonant light. Additionally, some fraction of the input light may be coupled into the cavity far off the enhancement cavity resonance. The first-order Doppler shift is estimated to be close to 1 GHz if totally unmitigated.

We expect that the cavity suppresses modes whose phase fronts are not perfectly matched, strongly reducing the likelihood of mismatched wave fronts in the spectroscopic volume. However, we investigate the potential size of such an effect. The first-order Doppler shift is proportional to v/λ , so we can estimate the shift due to mismatched wavefronts as

$$\Delta\nu_{FODS} \approx \frac{1}{2\pi} (\vec{k}_+ - \vec{k}_-) \cdot \vec{v}, \quad (6.46)$$

where \vec{k}_\pm are the k -vectors of the forward and backward propagating traveling waves in the cavity, and v is the atom velocity. A fraction of the light power circulating in a higher-order spatial mode can be responsible for mismatched wave fronts, via the Gouy phase, particularly the TEM_{01} as it is the most degenerate with the TEM_{00} .

The geometry of the metastable beam/778 nm beam overlap permits about 10 cm sampling along the 778 nm axis, as the hydrogen beam is about 1 cm wide and the beams are 6° from collinear. If we assume that atoms sample symmetrically about the beam waist, where the Gouy phase most rapidly varies, and the Rayleigh range of the cavity mode is about 1.5 m, then $\Delta\phi_{\text{Gouy}} \approx$

65 mrad between the TEM_{00} and TEM_{01} . The atoms traverse the beam in 10^{-5} s, so the frequency shift experienced by the atoms is $\frac{1}{2\pi} \frac{\Delta\phi_{\text{Gouy}}}{\Delta t} \approx 750$ Hz. However, the TEM_{01} mode is 30 MHz separated from the TEM_{00} . The finesse of the 778 nm cavity is about 1000, which corresponds to a resonance full-width-half-maximum value of 200 kHz. We typically have mode-matching fractions between 50%-80%. In the high finesse limit, the shape of the cavity resonances are closely approximated with Lorentzian functions, so we expect a suppression of that mode by a factor of 5×10^{-6} . Therefore, we expect that residual first order Doppler shifts are negligible at our current level of precision.

6.4.10 4th Order ac-Stark Shift

While the treatment of the ac-Stark shift in [68] is a 2nd order perturbation of the atom, higher order perturbations may also contribute (see, for instance, the supplementary materials of [23]). The 4th order effects are the next largest term in perturbation theory. As a general order of magnitude estimate, perturbation theory is valid when the internal electric fields of the atom are much larger than the perturbing electric field. In the $|8D\rangle$ state of the atom, $\langle r \rangle \approx 100a_0$ so we expect that average electric field within the atom is on the order of $\mathcal{E} \sim \frac{1}{4\pi\epsilon_0} \frac{2e}{(100a_0)^2} = 10^8$ V/m. For comparison, the largest ac-field seen by the atoms is on the order of 3×10^5 V/m, which corresponds to ac-Stark shifts close to 500 kHz. One can expect then that the 4th order contribution comes in as $\Delta\nu_{ac}^{(4)} \sim (500\text{kHz}) \left(\frac{5 \times 10^5}{10^8}\right)^2 = 3$ Hz correction to our highest powers in our extrapolations – that is negligible at our current level of precision.

6.4.11 Recoil Shifts

The recoil of the atom upon absorption shifts of the resonance frequency by:

$$\Delta\nu = \frac{h}{M} \left(\frac{\nu^2}{c^2} \right) \quad (6.47)$$

Where ν is the frequency of the absorbed photon and M is the mass of the atom (see supplementary materials for [29]). Since this is a two photon transition, we have instead:

$$\Delta\nu = \frac{h}{M} \left(\frac{\nu_+^2}{c^2} \right) - \frac{h}{M} \left(\frac{\nu_-^2}{c^2} \right) \quad (6.48)$$

Where $\nu_{+/-}$ corresponds to the blue and red shifted photon respectively. As one may expect, this results in a very small recoil shift of ~ 0.03 Hz, as the fractional frequency difference between the blue and red shifted light is a few ppm.

6.4.12 Light Force Shift

Metastable atoms are deflected by the 778 nm light due to the 2S energy levels being modified by the ac-Stark effect. This spatially dependent energy shift corresponds to a force. Here, we define the z direction to be in the direction of the beam height. The atoms and beam length are in the $x - y$ plane. The energy shift is given by

$$\Delta E(2S) = h\beta_{ac}(2S)I(z). \quad (6.49)$$

Therefore, the z component of this force is

$$F = -\frac{\partial E}{\partial z} = -h\beta_{ac}(2S)\frac{\partial I}{\partial z}. \quad (6.50)$$

The maximal deflection possible from this force may be estimated as

$$\Delta z \leq \frac{1}{2}a|_{max}(\Delta t)^2. \quad (6.51)$$

For 50 W in a 600 μm beam waist, we find maximal deflections of less than 30 nm, which is amounts to about 20 ppm variation in the intensity, which corresponds to a < 1 Hz shift due to the ac-Stark shift. Corrections to the population driven out of the 2S will be on the order of the intensity variation due to the light force shift, which is also negligible.

6.4.13 Photodiode Offsets

The photodiode and DAC reading the 778 nm cavity transmission has a small offset, ~ 5 mV, that can vary slightly over time. This shifts the apparent zero-intensity resonance frequency. Given that the nonlinear coefficient in the ac-extrapolations is $\approx 10^4$ times smaller than the linear part, we may quickly estimate the associated uncertainty from this small offset. The ac-Stark shift is about 300 kHz for a voltage of 6V, so the uncertainty introduced by this photodiode offset is about 250 Hz.

6.4.14 Parasitic Etalons

As discussed at length in preceding sections, optical cavities, or etalons, act as frequency discriminators due to the natural resonances of the optical cavity. In the case of intentional etalons, these resonances are of tremendous benefit. However, unintentional etalons can be formed between any pair of optical surfaces that are “parallel enough” where interference fringes are produced. Typically, these unintentional etalons produce very low contrast fringes due to their low reflectivity/high loss surfaces. Parasitic etalons can modify the determination of the 778 nm power as a function of frequency, which would skew the ac-extrapolation results. This is primarily an issue for etalons between the 778 nm cavity and the transmission photodiode. Fortunately, checking for etalons is straightforward, as they would lead to a clear correlation between laser frequency and recorded voltage during line scans. We have checked for such a correlation, and we have found no evidence of problematic etalons in our system.

6.5 Preliminary $2S_{1/2}$ - $8D_{5/2}$ Results

From our ac-extrapolation data set, we found the $2S_{1/2}$ - $8D_{5/2}$ resonance frequency to be 770649561574.91 ± 1.20 kHz, including only statistical uncertainty. For this value, no correction due to the ac-Stark shift is necessary – the extrapolation accounts for the ac-Stark shift. From this point, we correct for the dc-Stark effect, which amounts to a weighted shift of -3.95 ± 1.28 kHz. Since the cross-talk between the Stark effects introduces a correlation, the ac- and dc-Stark

effect errors cannot only be added in quadrature, and we find a total dc-Stark corrected hyperfine centroid value of 770649561570.95 ± 1.82 kHz (see Chapter 6.3). Now we correct for the remaining minor systematic shifts, which are listed in Table 6.1. We obtain a centroid value of 770649561570.79 ± 1.96 kHz once the systematics are accounted for, corresponding to a relative value of -13.14 ± 1.96 kHz from previous determination of the $2S_{1/2}$ - $8D_{5/2}$ transition. For any individual correction determined to be less than 10 Hz, we apply no shift to the final centroid value. The dominant contribution of our uncertainty budget arises from the combined statistical uncertainty of ac-Stark shift extrapolations and the dc-Stark shift, with the remaining systematics contributing relatively little contribution to the total uncertainty of the measurement.

Table 6.1: Compilation of minor corrections and uncertainties of the extrapolated $2S_{1/2}$ - $8D_{5/2}$ hyperfine centroid. The uncorrected extrapolated frequency is 770649561574.90 ± 1.20 kHz. Correcting for the dc-Stark effect we find 770649561570.95 ± 1.82 kHz, with the uncertainty including the correlation between the Stark effects. Our reported value for the transition frequency is found at the bottom of the table.

	$\Delta\nu$ (kHz)	σ (kHz)
2 nd Order Doppler	0.73	0.10
Zeeman Effect	0	0.07
Frequency Metrology	-0.4	0.65
Blackbody Radiation	-0.49	0.16
Pressure Shifts	0	10^{-3}
Hyperfine Structure $8D_{5/2}$	0	0.03
4 th Order ac-Stark	0	10^{-4}
Photodiode offsets	0	0.25
Cross Damping	0	0
Residual Doppler Shifts	0	4×10^{-6}
Incoherent Line Pulling	0	5×10^{-4}
Recoil Shifts	0	3×10^{-5}
Light Force Shift	0	0
dc-Stark Corrected Centroid	770649561570.95	1.82
Minor corrections	-0.16	0.73
Hyperfine Centroid	770649561570.79	1.96

Since we are interested in the corresponding proton radius, we combine our obtained value for the $2S_{1/2}$ - $8D_{5/2}$ transition with the 1S-2S transition frequency [1] to compute the proton radius and compare to the CODATA2014 and muonic proton value. It is worth mentioning that the current

CODATA suggested value of the proton radius is $r_p = 0.8414 \pm .0019$ fm, which is in excellent agreement with the r_p obtained from muonic hydrogen. It is also notable to mention that the CODATA2014 r_p includes electron-proton scattering measurements in its calculation. There is a trend in the most recent results in hydrogen to discuss only the r_p obtained from the available hydrogen data. This is in part due to the updated CODATA-recommended value of r_p , but also some authors contend that it electron-proton scattering measurements is testing the same physics as spectroscopy – one is a scattering experiment and the other is testing bound state QFT calculations [23]. That said, we are highlighting the CODATA2014 value in this discussion due to its historical significance in the proton radius puzzle.

As a matter of scale, the discrepancy between the CODATA2014 proton radius and the muonic proton radius corresponds to about a 20 kHz shift on the 2S-8D transition. With our value, we find a proton charge radius of 0.8581 ± 0.0050 fm. In Fig. 6.19, we display our value of the proton charge radius in comparison to recent determinations of the proton radius, the muonic charge radius, the CODATA 2014 value, and the previous measurement of the $2S_{1/2}$ - $8D_{5/2}$ transition. Our determination of the proton charge radius is 3.4σ discrepant with the muonic proton charge radius and 2.2 combined σ with the CODATA 2014 value. In contrast, our determination of the proton radius is only 1.6σ combined discrepant with the recent 1S-3S measurement. We may also make a determination of the Rydberg constant, R_∞ , using our 2S-8D transition frequency combined with the 1S-2S measurement, $R_\infty = 10973731.568330 \pm .000052$ m⁻¹, though there is a strong correlation between the r_p and R_∞ obtained in this way (nearly 99%).

Our result lands in a somewhat inconclusive though potentially suggestive space. On one hand, the result does not strongly favor either the CODATA2014 value or the muonic value. First and foremost, this could indicate the presence of currently unknown experimental systematics within our measurement. For instance, it is suggested that either or both of the recent 1S-3S measurements, which are 2.1σ discrepant and have different leading systematic effects, are subject to a undiscovered systematic [23]. On the other hand, the slight disagreement between the weighted mean of the 1S-3S and our value of the proton radius puzzle is interesting. There exist proposals

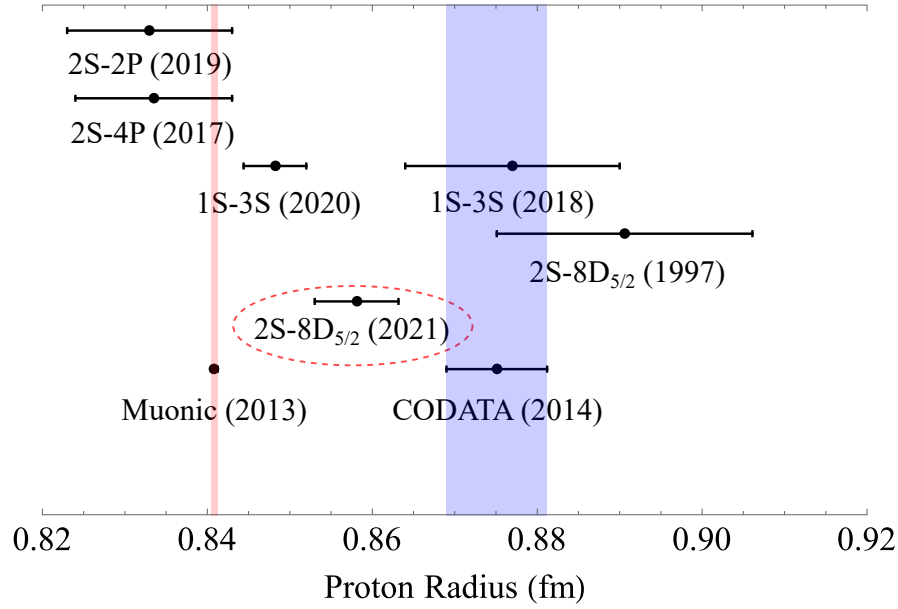


Figure 6.19: A selection of result determination of the proton radius when combined with the 1S-2S transition [1], with our determination circled.

which suggest extensions to the standard model that include a massive boson that couples leptons and quarks [35,37], causing an additional Yukawa potential to appear in the hydrogen Hamiltonian. As the Yukawa potential rapidly dies off a large distances away from the nucleus, high principle quantum number vs low principle quantum number states would be differently affected. While the existence of the proposed massive boson would not explain the current disagreement between the two 1S-3S measurements, it could provide an explanation for an apparent n -dependence appearing for the proton radius and R_∞ as they are currently calculated. There is the possibility that the muonic proton charge radius determination is subject to currently unaccounted for physics. The recent Fermilab muon $g-2$ measurement is anomalously large as compared to predictions from the standard model, with 4.2σ confidence levels [202]. At the time of this writing, the new $g-2$ result is new and articles suggesting connections between the muon proton radius and new muon ($g-2$) value have already begun appearing on the arXiv [203], though such proposals should be taken with a grain of salt. In fact, such a suggestions are not new. For instance, [204] suggested the presence of a force carrying boson at the MeV level that could explain the anomalous muon $g-2$ and proton radius in 2011. It should be noted that the work of [205] rejects the possibility of vector

massive photons at the MeV level explaining the anomalous muon $g - 2$ at the 99% confidence level, though axial dark photons causing this anomaly are not excluded.

6.6 Conclusion

In this section, we have discussed our $2S_{1/2}$ - $8D_{5/2}$ spectroscopy and data analysis. We have also investigated and quantified the potential systematic shifts and uncertainties to give our final value of the transition frequency. Finally, we combined our result with the 1S-2S transition to obtain a value for the proton radius and Rydberg constant which 3.4σ discrepant with the muonic value and 2.2σ discrepant with the CODATA 2014 value. We briefly discuss some possible explanation for this tension, which includes uncontrolled experimental systematic error and the presence of new physics.

Summary and Outlook

Spectroscopy on the hydrogen atom has a illustrious history pushing quantum theories forward over the past century. As the precision of the measurements in hydrogen increased, so did the subtlety of the theories necessary to properly capture the full physics told by the spectroscopic signals. Hydrogen spectroscopy provides an excellent testing bed for proper application of bound state Q.E.D. theory as well as a method to provide precise determination of fundamental constants, e.g. the Rydberg constant [1, 19]. Furthermore, comparison of high precision measurements in hydrogen and more exotic hydrogen-line species can provide stringent tests of CPT symmetry [11] by comparison with anti-hydrogen [13, 17].

More generally, searches for physics beyond the Standard Model in atomic systems offer a distinct approach from the high-energy collider experiments of particle physicists, and generally probe distinct energy scales. For instance, there are proposals regarding corrections to Coloumb's law from new physics observable with spectroscopy [206], measuring the electroweak mixing angle in parity non-conservation experiments [207–209], tests for temporal and/or spatial variation of the fine-structure constant [210, 211], and searches for an electron dipole moment [212–214]. The work of [205] is an example of the role precision AMO experiments can play in the search for physics beyond the Standard Model, excluding a particular classes of proposed dark boson candidates.

These highly refined AMO experiments, in particular precision spectroscopy, would not be possible if not for the continued advancement of technology, particularly laser development. The creation of the optical frequency comb has particularly benefited the entire field of spectroscopy by vastly simplifying absolute frequency metrology [55, 56]. Additionally, the development of high-power, coherent UV sources removes several technical difficulties in accessing transitions of hydrogen that do not involve its ground state, which previously required collisional techniques.

The work presented in this thesis follows in the long tradition of hydrogen spectroscopy: pushing laser technology and using this new technology to achieve a more refined result. A large

portion of the work detailed in this thesis deals with the creation of several different subsystems all necessary to probe the $2S_{1/2}$ - $8D_{5/2}$ transition: a high-power coherent 243.1 nm source, an optical frequency metrology system involving a frequency comb and ultra-stable cavity, a cryogenic hydrogen beam source, a frequency stabilized Ti:Sapphire laser, and a spectroscopy vacuum chamber where the subsystems come together. Each of these system provided their own engineering challenge, and often required breaking new ground [2–4, 48, 88]. This system as a whole provides a robust sandbox for further experiments in hydrogen and deuterium.

For the proton radius, this work lands in a rather interesting place. The tension amongst the recent high-precision measurements in hydrogen suggests yet-understood effects under the surface. While it is of course possible that these disparate results arise from underlying experimental systematics or comparatively uninteresting miscalculation of QED corrections to bound systems (see for instance [215]), the discrepancies also leave the possibility for discovering new physics. In particular, there are extensions to the standard model that include new forces with length scales comparable to the size of a hydrogen atom, $\sim .1a_0 - 50a_0$ [35]. In a sense, [35] is an investigation of modifications to Coloumb’s law in a specific parameter space where hydrogen spectroscopy is sensitive [206]. These modifications of Coloumb’s law, instead of introducing a photon rest mass [216], propose a slight mixing between the electromagnetic force and a new force mediated by a massive boson. As it stands, our work adds further tension to the the hydrogen data set, indicating that the proton radius puzzle is yet-to-be resolved.

As the leading systematics of the $2S$ - $8D$ measurement are due to the ac-Stark and dc-Stark shifts, further measurements on the $2S$ - $8D$ line would greatly benefit from mitigating one or both of these systematics. Reducing the perturbations from the ac-field require careful consideration. For instance, using a larger 778 nm beam radius would allow for smaller intensities/shifts with similar signal sizes, the nonlinearity in the extrapolation due to the metastable distribution becomes correspondingly more difficult to fit accurately. Similarly, a change of beam geometry so that the transit time is increased presents a similar problem and also increases the sensitivity to dc-fields as the interaction region becomes larger. In contrast, a reduction of the stray dc-fields would be

a benefit. It is possible that more active approaches to the cancellation of the dc-field is required, for instance using a three-axis electrode surrounding the spectroscopic volume. In that case, the applied voltages may be tweaked to reduce line distortions in high lying n -states before collecting 2S-8D data. This approach does introduce another knob to turn, increasing the experimental complexity, but it appears to be a fruitful path forward.

There is also the possibility that probing lines of narrower natural linewidth is an attractive option, for instance the high nS states. The S states are less sensitive to stray dc-fields and have narrower linewidths than the D states. Additionally, the hyperfine structure of the 8S state is resolved. However, they also have smaller two-photon matrix elements and thus requires much larger light intensities. Unfortunately, when the ac-Stark shift magnitude is close to the transition linewidth or greater, the line becomes heavily distorted. This technical problem could be overcome with the introduction of another off-resonant beam with intensity and wavelength chosen to cancel or heavily reduce the magnitude of the ac-Stark shift. Like the active cancellation of the dc-fields mentioned above, this would greatly increase the experimental complexity but the improvement in statistics from splitting a narrow line may well make the juice worth the squeeze. There is also the possibility of switching to detecting the fluorescence which allows for measuring much smaller metastable extinction ratios, potentially removing the ac-Stark shift distortion issue. Of course this approach reintroduces quantum interference, but it is more palatable in S states over D states as S states have resolved hyperfine structure.

The infrastructure surrounding the 2S-8D measurement may also be readily adapted for other experiments. A differential measurement between the hyperfine splitting of the 1S and 2S states greatly reduces contributions due to nuclear effects and therefore is an excellent test for QED theory [19]. At this time, such calculations are currently limited by the precision of 2S HFS measurements. As our apparatus already generates substantial metastable flux at cryogenic temperature, a few modifications can allow for a new measurement of the 2S hyperfine splitting. In a similar way, access to the 2S state opens the door for typical AMO experimental games. For instance, an 486 nm beam could be used to off-resonantly drive the 2S-4P transition. By applying temporal

and spatial variations to the 486 nm beam, the velocity distribution of the metastable beam may be manipulated. Due to the technical difficulty in traditional laser cooling of hydrogen, such a velocity manipulation may be an attractive route to reduce velocity systematics in hydrogen experiments.

While atomic physics and spectroscopy was crucial to the development of fundamental physics theory in the early 20th century, large collider-based experiments eventually took up the mantle in the decades following, culminating in the detection of the Higgs boson. The Higgs represented the final piece of the Standard Model theory, and now the search for physics beyond the Standard model have come in full swing. Such searches are not limited to high energy experiments, and precision AMO experiments provide another way to search for new physics, e.g. [11, 20, 35, 207, 208, 212, 216]. It is rather exciting to see that experimental physics exploring atoms and molecules has the possibility to contribute in the search for physics beyond the Standard Model in the beginning of the 21st century.

Bibliography

- [1] C. G. Parthey, A. Matveev, J. Alnis, B. Bernhardt, A. Beyer, R. Holzwarth, A. Maistrou, R. Pohl, K. Predehl, T. Udem, T. Wilken, N. Kolachevsky, M. Abgrall, D. Rovera, C. Salomon, P. Laurent, T. W. Hänsch, Improved Measurement of the Hydrogen 1S-2S Transition Frequency, *Phys. Rev. Lett.* **107**, 203001 (2011).
- [2] Z. Burkley, A. D. Brandt, C. Rasor, S. F. Cooper, D. C. Yost, Highly coherent, watt-level deep-UV radiation via a frequency-quadrupled Yb-fiber laser system, *Appl. Opt.* **58**, 1657–1661 (2019).
- [3] S. F. Cooper, A. D. Brandt, C. Rasor, Z. Burkley, D. C. Yost, Cryogenic atomic hydrogen beam apparatus with velocity characterization, *Rev. Sci. Instrum.* **91**, 013201 (2020).
- [4] A. D. Brandt, S. F. Cooper, Z. Burkley, D. C. Yost, Reduced phase noise in an erbium frequency comb via intensity noise suppression, *Opt. Express* **25**, 18175–18181 (2017).
- [5] A. E. Kramida, A critical compilation of experimental data on spectral lines and energy levels of hydrogen, deuterium, and tritium, *At. Data Nucl. Data Tables* **96**, 586–644 (2010).
- [6] S. G. Karshenboim, F. S. Pavone, G. F. Bassani, M. Inguscio, T. W. Hänsch, *Introduction to Simple Atoms* (Springer, 2007).
- [7] M. Inguscio, L. Fallani, *Atomic Physics: Precise Measurements & Ultracold Matter* (Oxford University Press, 2013).
- [8] L. de Broglie, Waves and Quanta, *Nature* **112**, 540 (1923).
- [9] E. Schrodinger, An Undulatory Theory of the Mechanics of Atoms and Molecules, *Phys. Rev.* **28**, 1049–1070 (1926).
- [10] W. E. Lamb, R. C. Retherford, Fine structure of the hydrogen atom by a microwave method, *Phys. Rev.* **72**, 241–243 (1947).

- [11] R. Bluhm, V. A. Kostelecký, N. Russell, CPT and Lorentz tests in hydrogen and antihydrogen, *Phys. Rev. Lett.* **82**, 2254–2257 (1999).
- [12] M. G. Boshier, S. Dhawan, O. van Dyck, P. Egan, X. Fei, M. G. Perdekamp, V. W. Hughes, M. Janousch, K. Jungmann, D. Kawall, W. Liu, F. G. Mariam, C. Pillai, R. Prigl, G. zu Putlitz, Precise microwave spectroscopy measurement of the muonium ground state: Hyperfine structure interval and muon magnetic moment, *Phys. Rev. Lett.* **82**, 711–714 (1999).
- [13] G. Gabrielse, N. S. Bowden, P. Oxley, A. Speck, C. H. Storry, J. N. Tan, M. Wessels, D. Grzonka, W. Oelert, G. Schepers, T. Sefzick, J. Walz, H. Pittner, T. W. Hänsch, E. A. Hessels, Background-Free Observation of Cold Antihydrogen with Field-Ionization Analysis of Its States, *Phys. Rev. Lett.* **89**, 213401 (2002).
- [14] M. Hori, A. Dax, J. Eades, K. Gomikawa, R. S. Hayano, N. Ono, W. Pirkel, E. Widmann, H. A. Torii, B. Juhász, D. Barna, D. Horváth, Determination of the antiproton-to-electron mass ratio by precision laser spectroscopy of $p\text{He}^+$, *Phys. Rev. Lett.* **96**, 40801 (2006).
- [15] C. Frugiuele, J. Pérez-Ríos, C. Peset, Current and future perspectives of positronium and muonium spectroscopy as dark sectors probe, *Phys. Rev. D* **100**, 15010 (2019).
- [16] L. Gurung, T. J. Babij, S. D. Hogan, D. B. Cassidy, Precision Microwave Spectroscopy of the Positronium $n=2$ Fine Structure, *Phys. Rev. Lett.* **125**, 73002 (2020).
- [17] C. J. Baker, W. Bertsche, A. Capra, C. Carruth, C. L. Cesar, M. Charlton, A. Christensen, R. Collister, A. C. Mathad, S. Eriksson, A. Evans, N. Evetts, J. Fajans, T. Friesen, M. C. Fujiwara, D. R. Gill, P. Grandemange, P. Granum, J. S. Hangst, W. N. Hardy, M. E. Hayden, D. Hodgkinson, E. Hunter, C. A. Isaac, M. A. Johnson, J. M. Jones, S. A. Jones, S. Jonesell, A. Khramov, P. Knapp, L. Kurchaninov, N. Madsen, D. Maxwell, J. T. K. McKenna, S. Menary, J. M. Michan, T. Momose, P. S. Mullan, J. J. Munich, K. Olchanski, A. Olin, J. Peszka, A. Powell, P. Pusa, C. Rasmussen, F. Robicheaux, R. L. Sacramento, M. Sameed, E. Sarid, D. M. Silveira, D. M. Starko, C. So, G. Stutter, T. D. Tharp, A. Thibeault, R. I.

- Thompson, D. P. van der Werf, J. S. Wurtele, Laser cooling of antihydrogen atoms, *Nature* **592**, 35–42 (2021).
- [18] S. G. Karshenboim, Precision physics of simple atoms: QED tests, nuclear structure and fundamental constants, *Phys. Rep.* **422**, 1–63 (2005).
- [19] S. G. Karshenboim, V. G. Ivanov, Hyperfine structure of the ground and first excited states in light hydrogen-like atoms and high-precision tests of QED, *Eur. Phys. J. D* **19**, 13–23 (2002).
- [20] M. S. Safronova, D. Budker, D. Demille, D. F. Kimball, A. Derevianko, C. W. Clark, Search for new physics with atoms and molecules, *Rev. Mod. Phys.* **90**, 025008 (2018).
- [21] S. G. Karshenboim, F. Pavone, G. F. Bassani, M. Inguscio, T. W. Hänsch, *Precision Spectroscopy of Atomic Hydrogen* (Springer, 2007).
- [22] P. J. Mohr, D. B. Newell, B. N. Taylor, CODATA recommended values of the fundamental physical constants: 2014, *Rev. Mod. Phys.* **88**, 035009 (2016).
- [23] A. Grinin, A. Matveev, D. C. Yost, L. Maisenbacher, V. Wirthl, R. Pohl, T. W. Hänsch, T. Udem, Two-photon frequency comb spectroscopy of atomic hydrogen, *Science* **370**, 1061–1066 (2020).
- [24] T. W. Hänsch, S. A. Lee, R. Wallenstein, C. Wieman, Doppler-free two-photon spectroscopy of hydrogen 1S-2S, *Phys. Rev. Lett.* **34**, 307–309 (1975).
- [25] B. De Beauvoir, F. Nez, L. Julien, B. Cagnac, F. Biraben, D. Touahri, L. Hilico, O. Acef, A. Clairon, J. J. Zondy, Absolute frequency measurement of the 2S-8S/D transitions in hydrogen and deuterium: New determination of the rydberg constant, *Phys. Rev. Lett.* **78**, 440–443 (1997).
- [26] C. Schwob, L. Jozefowski, B. De Beauvoir, L. Hilico, F. Nez, L. Julien, F. Biraben, O. Acef, A. Clairon, Optical frequency measurement of the 2S-12D transitions in hydrogen and deu-

- terium: Rydberg constant and lamb shift determinations, *Phys. Rev. Lett.* **82**, 4960–4963 (1999).
- [27] M. Niering, R. Holzwarth, J. Reichert, P. Pokasov, T. Udem, M. Weitz, T. W. Hänsch, P. Lemonde, G. Santarelli, M. Abgrall, P. Laurent, C. Salomon, A. Clairon, Measurement of the hydrogen 1S-2S transition frequency by phase coherent comparison with a microwave cesium fountain clock, *Phys. Rev. Lett.* **84**, 5496–5499 (2000).
- [28] O. Arnoult, F. Nez, L. Julien, F. Biraben, Optical frequency measurement of the 1S-3S two-photon transition in hydrogen, *Eur. Phys. J. D* **60**, 243–256 (2010).
- [29] A. Beyer, L. Maisenbacher, A. Matveev, R. Pohl, K. Khabarova, A. Grinin, T. Lamour, D. C. Yost, T. W. Hänsch, N. Kolachevsky, T. Udem, The Rydberg constant and proton size from atomic hydrogen, *Science* **358**, 79–85 (2017).
- [30] H. Fleurbaey, S. Galtier, S. Thomas, M. Bonnaud, L. Julien, F. Biraben, F. Nez, M. Abgrall, J. Guéna, New Measurement of the 1S-3S Transition Frequency of Hydrogen: Contribution to the Proton Charge Radius Puzzle, *Phys. Rev. Lett.* **120**, 183001 (2018).
- [31] N. Bezginov, T. Valdez, M. Horbatsch, A. Marsman, A. C. Vutha, E. A. Hessels, A measurement of the atomic hydrogen Lamb shift and the proton charge radius, *Science* **365**, 1007–1012 (2019).
- [32] P. J. Mohr, B. N. Taylor, D. B. Newell, CODATA recommended values of the fundamental physical constants: 2006, *Rev. Mod. Phys.* **80**, 1187 (2008).
- [33] U. D. Jentschura, V. A. Yerokhin, Quantum electrodynamic corrections to the hyperfine structure of excited S states, *Phys. Rev. A - At. Mol. Opt. Phys.* **73**, 062503 (2006).
- [34] T. Udem, Quantum electrodynamics and the proton size, *Nat. Phys.* **14**, 632 (2018).
- [35] M. P. A. Jones, R. M. Potvliege, M. Spannowsky, Probing new physics using Rydberg states of atomic hydrogen, *Phys. Rev. Res.* **2**, 13244 (2020).

- [36] U. D. Jentschura, Fifth force and hyperfine splitting in bound systems, *Phys. Rev. A* **101**, 062503 (2020).
- [37] S. G. Karshenboim, Precision physics of simple atoms and constraints on a light boson with ultraweak coupling, *Phys. Rev. Lett.* **104**, 40801 (2010).
- [38] R. Pohl, A. Antognini, F. Nez, F. D. Amaro, F. Biraben, J. M. R. Cardoso, D. S. Covita, A. Dax, S. Dhawan, L. M. P. Fernandes, A. Giesen, T. Graf, T. W. Hänsch, P. Indelicato, L. Julien, C. Y. Kao, P. Knowles, E. O. Le Bigot, Y. W. Liu, J. A. M. Lopes, L. Ludhova, C. M. B. Monteiro, F. Mulhauser, T. Nebel, P. Rabinowitz, J. M. F. Dos Santos, L. A. Schaller, K. Schuhmann, C. Schwob, D. Taqqu, J. F. C. A. Veloso, F. Kottmann, The size of the proton, *Nature* **466**, 213–216 (2010).
- [39] A. Antognini, F. Nez, K. Schuhmann, F. D. Amaro, F. Biraben, J. M. R. Cardoso, D. S. Covita, A. Dax, S. Dhawan, M. Diepold, L. M. P. Fernandes, A. Giesen, A. L. Gouvea, T. Graf, T. W. Hänsch, P. Indelicato, L. Julien, C. Y. Kao, P. Knowles, F. Kottmann, E. O. Le Bigot, Y. W. Liu, J. A. M. Lopes, L. Ludhova, C. M. B. Monteiro, F. Mulhauser, T. Nebel, P. Rabinowitz, J. M. F. Dos Santos, L. A. Schaller, C. Schwob, D. Taqqu, J. F. C. A. Veloso, J. Vogelsang, R. Pohl, Proton structure from the measurement of 2S-2P transition frequencies of muonic hydrogen, *Science* **339**, 417–420 (2013).
- [40] E. Peters, D. C. Yost, A. Matveev, T. W. Hänsch, T. Udem, Frequency-comb spectroscopy of the hydrogen 1S-3S and 1S-3D transitions, *Ann. Phys.* **525**, 29–34 (2013).
- [41] J. Arrington, I. Sick, Evaluation of the proton charge radius from electron-proton scattering, *J. Phys. Chem. Ref. Data* **44**, 31204 (2015).
- [42] W. Xiong, A. Gasparian, H. Gao, D. Dutta, M. Khandaker, N. Liyanage, E. Pasyuk, C. Peng, X. Bai, L. Ye, K. Gnanvo, C. Gu, M. Levillain, X. Yan, D. W. Higinbotham, M. Meziane, Z. Ye, K. Adhikari, B. Aljawrneh, H. Bhatt, D. Bhetuwal, J. Brock, V. Burkert, C. Carlin, A. Deur, D. Di, J. Dunne, P. Ekanayaka, L. El-Fassi, B. Emmich, L. Gan, O. Glamazdin,

- M. L. Kabir, A. Karki, C. Keith, S. Kowalski, V. Lagerquist, I. Larin, T. Liu, A. Liyanage, J. Maxwell, D. Meekins, S. J. Nazeer, V. Nelyubin, H. Nguyen, R. Pedroni, C. Perdrisat, J. Pierce, V. Punjabi, M. Shabestari, A. Shahinyan, R. Silwal, S. Stepanyan, A. Subedi, V. V. Tarasov, N. Ton, Y. Zhang, Z. W. Zhao, A small proton charge radius from an electron–proton scattering experiment, *Nature* **575**, 147–151 (2019).
- [43] F. Biraben, J. C. Garreau, L. Julien, Détermination of the rydberg constant by doppler-free two-photon spectroscopy of hydrogen rydberg states, *Epl* **2**, 925–932 (1986).
- [44] J. C. Garreau, M. Allegrini, L. Julien, F. Biraben, High resolution spectroscopy of the hydrogen atom. I. Method and experiment, *J. Phys.* **51**, 2263–2273 (1990).
- [45] B. De Beauvoir, C. Schwob, O. Acef, L. Jozefowski, L. Hilico, F. Nez, L. Julien, A. Clairon, F. Biraben, Metrology of the hydrogen and deuterium atoms: Determination of the Rydberg constant and Lamb shifts, *Eur. Phys. J. D* **12**, 61–93 (2000).
- [46] N. Kolachevsky, J. Alnis, S. D. Bergeson, T. W. Hänsch, Compact solid-state laser source for 1S-2S spectroscopy in atomic hydrogen, *Phys. Rev. A - At. Mol. Opt. Phys.* **73**, 22513 (2006).
- [47] N. Kolachevsky, J. Alnis, C. G. Parthey, A. Matveev, R. Landig, T. W. Hänsch, Low phase noise diode laser oscillator for 1S–2S spectroscopy in atomic hydrogen, *Opt. Lett.* **36**, 4299–4301 (2011).
- [48] Z. Burkley, C. Rasor, S. F. Cooper, A. D. Brandt, D. C. Yost, Yb fiber amplifier at 972.5 nm with frequency quadrupling to 243.1 nm, *Appl. Phys. B Lasers Opt.* **123**, 6583–6589 (2017).
- [49] G. Hagel, R. Battesti, F. Nez, L. Julien, F. Biraben, Observation of a Motional Stark Effect to Determine the Second-Order Doppler Effect, *Phys. Rev. Lett.* **89**, 203001 (2002).
- [50] T. Udem, J. Reichert, R. Holzwarth, T. W. Hänsch, Accurate measurement of large optical frequency differences with a mode-locked laser, *Opt. Lett.* **24**, 881–883 (1999).

- [51] R. Holzwarth, T. Udem, T. W. Hänsch, J. C. Knight, W. J. Wadsworth, P. S. J. Russell, Optical frequency synthesizer for precision spectroscopy, *Phys. Rev. Lett.* **85**, 2264–2267 (2000).
- [52] D. J. Jones, S. A. Diddams, J. K. Ranka, A. Stentz, R. S. Windeler, J. L. Hall, S. T. Cundiff, Carrier-envelope phase control of femtosecond mode-locked lasers and direct optical frequency synthesis, *Science* **288**, 635–639 (2000).
- [53] S. T. Cundiff, J. Ye, Colloquium: Femtosecond optical frequency combs, *Rev. Mod. Phys.* **75**, 325–342 (2003).
- [54] L. Hollberg, C. W. Oates, G. Wilpers, C. W. Hoyt, Z. W. Barber, S. A. Diddams, W. H. Oskay, J. C. Bergquist, Optical frequency/wavelength references, *J. Phys. B At. Mol. Opt. Phys.* **38**, 469–495 (2005).
- [55] P. Maddaloni, P. Cancio, P. De Natale, Optical comb generators for laser frequency measurement, *Meas. Sci. Technol.* **20**, 52001 (2009).
- [56] S. A. Diddams, The evolving optical frequency comb [Invited], *J. Opt. Soc. Am. B* **27**, 51–62 (2010).
- [57] S. Koke, C. Grebing, H. Frei, A. Anderson, A. Assion, G. Steinmeyer, Direct frequency comb synthesis with arbitrary offset and shot-noise-limited phase noise, *Nat. Photonics* **4**, 462–465 (2010).
- [58] N. Picqué, T. W. Hänsch, Frequency comb spectroscopy, *Nat. Photonics* **13**, 146–157 (2019).
- [59] T. Fortier, E. Baumann, 20 years of developments in optical frequency comb technology and applications, *Commun. Phys.* **2**, 153 (2019).
- [60] T. Udem, R. Holzwarth, T. W. Hänsch, Optical frequency metrology, *Nature* **416**, 233–237 (2002).

- [61] D. A. Jennings, C. R. Pollock, F. R. Petersen, R. E. Drullinger, K. M. Evenson, J. S. Wells, Direct frequency measurement of the 1-stabilized He-Ne 473- THz (633-nm) laser, *Opt. Lett.* **8**, 136–138 (1983).
- [62] H. Schnatz, B. Lipphardt, J. Helmcke, F. Riehle, G. Zinner, First Phase-Coherent Frequency Measurement of Visible Radiation, *Phys. Rev. Lett.* **76**, 18–21 (1996).
- [63] T. Udem, A. Huber, B. Gross, J. Reichert, M. Prevedelli, M. Weitz, T. W. Hänsch, Phase-Coherent Measurement of the Hydrogen 1 S -2 S Transition Frequency with an Optical Frequency Interval Divider Chain, *Phys. Rev. Lett.* **79**, 2646–2649 (1997).
- [64] C. L. Cesar, D. G. Fried, T. C. Killian, A. D. Polcyn, J. C. Sandberg, I. A. Yu, T. J. Greytak, D. Kleppner, J. M. Doyle, Two-photon spectroscopy of trapped atomic hydrogen, *Phys. Rev. Lett.* **77**, 255–258 (1996).
- [65] O. J. Luiten, H. G. C. Werij, I. D. Setija, M. W. Reynolds, T. W. Hijmans, J. T. M. Walraven, *AIP Conf. Proc.* (1993), vol. 275, p. 167.
- [66] V. Zehnlé, J. C. Garreau, Continuous-wave Doppler cooling of hydrogen atoms with two-photon transitions, *Phys. Rev. A - At. Mol. Opt. Phys.* **63**, 21402 (2001).
- [67] J. T. Walraven, I. F. Silvera, Helium-temperature beam source of atomic hydrogen, *Rev. Sci. Instrum.* **53**, 1167–1181 (1982).
- [68] M. Haas, U. D. Jentschura, C. H. Keitel, N. Kolachevsky, M. Herrmann, P. Fendel, M. Fischer, T. Udem, R. Holzwarth, T. W. Hänsch, M. O. Scully, G. S. Agarwal, Two-photon excitation dynamics in bound two-body Coulomb systems including ac Stark shift and ionization, *Phys. Rev. A - At. Mol. Opt. Phys.* **73**, 052501 (2006).
- [69] Z. N. Burkley, High-Power Deep-UV Laser for Improved and Novel Experiments on Hydrogen, Ph.D. thesis (2019).

- [70] C. Zimmermann, V. Vuletic, A. Hemmerich, T. W. Hänsch, All solid state laser source for tunable blue and ultraviolet radiation, *Appl. Phys. Lett.* **66**, 2318–2320 (1995).
- [71] C. J. Mackechnie, W. L. Barnes, D. C. Hanna, J. E. Townsend, High power ytterbium (Yb³⁺)-doped fibre laser operating in the 1.12 μm region, *Electron. Lett.* **29**, 52–53 (1993).
- [72] R. Paschotta, J. Nilsson, A. C. Tropper, D. C. Hanna, Ytterbium-doped fiber amplifiers, *IEEE J. Quantum Electron.* **33**, 1049–1056 (1997).
- [73] M. N. Zervas, High power ytterbium-doped fiber lasers - Fundamentals and applications, *Int. J. Mod. Phys. B* **28**, 1442009 (2014).
- [74] F. Roeser, C. Jauregui, J. Limpert, A. Tünnermann, 94 W 980 nm high brightness Yb-doped fiber laser, *Opt. Express* **16**, 17310–17318 (2008).
- [75] J. Bouillet, Y. Zaouter, R. Desmarchelier, M. Cazaux, J. Saby, R. Bello-doua, E. Cormier, Level Photonic Crystal Fiber Laser, *Society* **16**, 17891–17902 (2008).
- [76] R. Selvas, J. K. Sahu, L. B. Fu, J. N. Jang, J. Nilsson, A. B. Grudinin, Three-Level Fiber Sources At 980 Nm, *Opt. Lett.* **28**, 1093–1095 (2003).
- [77] R. Royon, J. Lhermite, L. Sarger, E. Cormier, High power, continuous-wave ytterbium-doped fiber laser tunable from 976 to 1120 nm, *Opt. Express* **21**, 12823–13818 (2013).
- [78] R. W. Boyd, *Nonlinear Optics* (Elsevier, 2003), third edn.
- [79] D. A. Kleinman, Theory of Second Harmonic Generation of Light, *Phys. Rev.* **15**, 1761–1775 (1962).
- [80] G. D. Boyd, A. Ashkin, J. M. Dziedzic, D. A. Kleinman, Second-harmonic generation of light with double refraction, *Phys. Rev.* **137**, 1305–1320 (1965).
- [81] G. D. Boyd, D. A. Kleinman, Parametric interaction of focused Gaussian light beams, *J. Appl. Phys.* **39**, 3597–3639 (1968).

- [82] R. C. Eckardt, J. Reintjes, Phase Matching Limitations of High Efficiency Second Harmonic Generation, *IEEE J. Quantum Electron.* **20**, 1178–1187 (1984).
- [83] A. V. Smith, D. J. Armstrong, W. J. Alford, Increased acceptance bandwidths in optical frequency conversion by use of multiple walk-off-compensating nonlinear crystals, *IEEE J. Opt. Soc. Am. B* **15**, 122–141 (1998).
- [84] R. W. P. Drever, J. L. Hall, F. V. Kowalski, J. Hough, G. M. Ford, A. J. Munley, H. Ward, Laser phase and frequency stabilization using an optical resonator, *Appl. Phys. B Photo-physics Laser Chem.* **31**, 97–105 (1983).
- [85] R. R. Kunz, V. Liberman, D. K. Downs, Experimentation and modeling of organic photo-contamination on lithographic optics, *J. Vac. Sci. Technol. B Microelectron. Nanom. Struct.* **18**, 1306–1313 (2000).
- [86] J. Hollenshead, L. Klebanoff, Modeling radiation-induced carbon contamination of extreme ultraviolet optics, *J. Vac. Sci. Technol. B Microelectron. Nanom. Struct.* **24**, 64–82 (2006).
- [87] D. Gangloff, M. Shi, T. Wu, A. Bylinskii, B. Braverman, M. Gutierrez, R. Nichols, J. Li, K. Aichholz, M. Cetina, L. Karpa, B. Jelenković, I. Chuang, V. Vuletić, Preventing and reversing vacuum-induced optical losses in high-finesse tantalum (V) oxide mirror coatings, *Opt. Express* **23**, 18014 (2015).
- [88] S. F. Cooper, Z. Burkley, A. Brandt, C. Rasor, D. Yost, Cavity-enhanced deep ultraviolet laser for two-photon cooling of atomic hydrogen, *Opt. Lett.* **43**, 1375–1378 (2018).
- [89] J. L. Hall, M. Zhu, *Laser Manip. Atoms Ions* (1992), pp. 671–701.
- [90] L. Willmann, Bose-Einstein condensation of atomic hydrogen, *Appl. Phys. B Lasers Opt.* **69**, 357–361 (1999).
- [91] T. C. Killian, 1S-2S spectrum of a hydrogen Bose-Einstein condensate, *Phys. Rev. A - At. Mol. Opt. Phys.* **61**, 33611 (2000).

- [92] F. C. Fehsenfeld, K. M. Evenson, H. P. Broida, Microwave discharge cavities operating at 2450 MHz, *Rev. Sci. Instrum.* **36**, 294–298 (1965).
- [93] S. C. Jain, K. S. Krishnan, The thermionic constants of metals and semi-conductors, *Proc. R. Soc. A* **213**, 143–157 (1952).
- [94] P. Gill, Optical frequency standards, *Metrologia* **42**, 125–137 (2005).
- [95] N. Poli, C. W. Oates, P. Gill, G. M. Tino, Optical atomic clocks, *Riv. del Nuovo Cim.* **36**, 555–624 (2013).
- [96] A. Foltynowicz, P. Maśłowski, T. Ban, F. Adler, K. C. Cossel, T. C. Briles, J. Ye, Optical frequency comb spectroscopy, *Faraday Discuss.* **150**, 23–31 (2011).
- [97] M. C. Stowe, M. J. Thorpe, A. Pe’er, J. Ye, J. E. Stalnaker, V. Gerginov, S. A. Diddams, Direct frequency comb spectroscopy, *Adv. At. Mol. Opt. Phys.* **55**, 1–60 (2008).
- [98] M. L. Weichman, P. B. Changala, J. Ye, Z. Chen, M. Yan, N. Picqué, Broadband molecular spectroscopy with optical frequency combs, *J. Mol. Spectrosc.* **355**, 66–78 (2019).
- [99] N. R. Newbury, Searching for applications with a fine-tooth comb, *Nat. Photonics* **5**, 186–188 (2011).
- [100] L. C. Sinclair, I. Coddington, W. C. Swann, G. B. Rieker, A. Hati, K. Iwakuni, N. R. Newbury, Operation of an optically coherent frequency comb outside the metrology lab, *Opt. Express* **22**, 6996–7006 (2014).
- [101] L. C. Sinclair, J. D. Deschênes, L. Sonderhouse, W. C. Swann, I. H. Khader, E. Baumann, N. R. Newbury, I. Coddington, Invited Article: A compact optically coherent fiber frequency comb, *Rev. Sci. Instrum.* **86**, 81301 (2015).
- [102] W. C. Swann, E. Baumann, F. R. Giorgetta, N. R. Newbury, Microwave generation with low residual phase noise from a femtosecond fiber laser with an intracavity electro-optic modulator, *Opt. Lett.* **36**, 24387–24395 (2011).

- [103] F. Krausz, M. Ivanov, Attosecond physics, *Rev. Mod. Phys.* **81**, 163–234 (2009).
- [104] H. Leopardi, J. Davila-Rodriguez, F. Quinlan, J. Olson, J. A. Sherman, S. A. Diddams, T. M. Fortier, Single-branch Er: fiber frequency comb for precision optical metrology with 10^{-18} fractional instability, *Optica* **4**, 879–885 (2017).
- [105] R. Lange, N. Huntemann, J. M. Rahm, C. Sanner, H. Shao, B. Lipphardt, C. Tamm, S. Weyers, E. Peik, Improved Limits for Violations of Local Position Invariance from Atomic Clock Comparisons, *Phys. Rev. Lett.* **126**, 11102 (2021).
- [106] D. C. Yost, A. Matveev, E. Peters, A. Beyer, T. W. Hänsch, T. Udem, Quantum interference in two-photon frequency-comb spectroscopy, *Phys. Rev. A - At. Mol. Opt. Phys.* **90**, 012512 (2014).
- [107] D. C. Yost, A. Matveev, A. Grinin, E. Peters, L. Maisenbacher, A. Beyer, R. Pohl, N. Kolachevsky, K. Khabarova, T. W. Hänsch, T. Udem, Spectroscopy of the hydrogen 1S-3S transition with chirped laser pulses, *Phys. Rev. A* **93**, 42509 (2016).
- [108] P. Del’Haye, A. Schliesser, O. Arcizet, T. Wilken, R. Holzwarth, T. J. Kippenberg, Optical frequency comb generation from a monolithic microresonator, *Nature* **450**, 1214–1217 (2007).
- [109] T. J. Kippenberg, R. Holzwarth, S. A. Diddams, Microresonator-based optical frequency combs, *Science* **332**, 555–559 (2011).
- [110] C. H. Li, A. J. Benedick, P. Fendel, A. G. Glenday, F. X. Kärtner, D. F. Phillips, D. Sasselov, A. Szentgyorgyi, R. L. Walsworth, A laser frequency comb that enables radial velocity measurements with a precision of 1 cm s^{-1} , *Nature* **452**, 610–612 (2008).
- [111] A. Bartels, D. Heinecke, S. A. Diddams, 10-GHz self-referenced optical frequency comb, *Science* **326**, 681 (2009).

- [112] L. Lorini, N. Ashby, A. Brusch, S. Diddams, R. Drullinger, E. Eason, T. Fortier, P. Hastings, T. Heavner, D. Hume, W. Itano, S. Jefferts, N. Newbury, T. Parker, T. Rosenband, J. Stalnaker, W. Swann, D. Wineland, J. Bergquist, Recent atomic clock comparisons at NIST, *Eur. Phys. J. Spec. Top.* **163**, 19–35 (2008).
- [113] N. Huntemann, B. Lipphardt, C. Tamm, V. Gerginov, S. Weyers, E. Peik, Improved limit on a temporal variation of m_p/m_e from comparisons of Yb⁺ and Cs atomic clocks, *Phys. Rev. Lett.* **113**, 210802 (2014).
- [114] T. R. Schibli, I. Hartl, D. C. Yost, M. J. Martin, A. Marcinkevicius, M. E. Fermann, J. Ye, Optical frequency comb with submillihertz linewidth and more than 10 W average power, *Nat. Photonics* **2**, 355–359 (2008).
- [115] N. Scharnhorst, J. B. Wübbena, S. Hannig, K. Jakobsen, J. Kramer, I. D. Leroux, P. O. Schmidt, High-bandwidth transfer of phase stability through a fiber frequency comb, *Opt. Express* **23**, 19771–19776 (2015).
- [116] H. R. Telle, D. Meschede, T. W. Hansch, Realization of a new concept for visible frequency division : phase locking of harmonic and sum frequencies, *Opt. Lett.* **15**, 532–534 (1990).
- [117] S. A. Diddams, D. J. Jones, J. Ye, S. T. Cundiff, J. L. Hall, B. Laboratories, L. Technologies, M. Avenue, M. Hill, R. Holzwarth, T. Udem, T. W. Hänsch, Direct Link between Microwave and Optical Frequencies with a 300 THz Femtosecond Laser Comb, *Phys. Rev. Lett.* **84**, 5102–5105 (2000).
- [118] C.-C. Lee, C. Mohr, J. Bethge, S. Suzuki, M. E. Fermann, I. Hartl, T. R. Schibli, Frequency comb stabilization with bandwidth beyond the limit of gain lifetime by an intracavity graphene electro-optic modulator, *Opt. Lett.* **37**, 3084–3086 (2012).
- [119] N. Kuse, C.-C. Lee, J. Jiang, C. Mohr, T. R. Schibli, M. E. Fermann, Ultra-low noise all polarization-maintaining Er fiber-based optical frequency combs facilitated with a graphene modulator, *Opt. Express* **23**, 24342–24350 (2015).

- [120] E. Baumann, F. R. Giorgetta, J. W. Nicholson, W. C. Swann, I. Coddington, N. R. Newbury, High-performance, vibration-immune, fiber-laser frequency comb, *Opt. Lett.* **34**, 638–640 (2009).
- [121] S. Droste, G. Ycas, B. R. Washburn, I. Coddington, N. R. Newbury, Optical Frequency Comb Generation based on Erbium Fiber Lasers, *Nanophotonics* **5**, 196–213 (2016).
- [122] T. M. Fortier, D. J. Jones, S. T. Cundiff, Phase stabilization of an octave-spanning Ti : sapphire laser, *Opt. Lett.* **28**, 2198–2200 (2003).
- [123] H. A. Haus, Mode-locking of lasers, *IEEE J. Sel. Top. Quantum Electron.* **6**, 1173–1185 (2000).
- [124] E. P. Ippen, Principles of passive mode locking, *Appl. Phys. B Laser Opt.* **58**, 159–170 (1994).
- [125] H. A. Haus, Theory of Mode Locking with a Slow Saturable Absorber, *IEEE J. Quantum Electron.* **11**, 736–746 (1975).
- [126] F. X. Kärtner, I. D. Jung, U. Keller, Soliton mode-locking with saturable absorbers, *IEEE J. Sel. Top. Quantum Electron.* **2**, 540–556 (1996).
- [127] R. Paschotta, U. Keller, Passive mode locking with slow saturable absorbers, *Appl. Phys. B Lasers Opt.* **73**, 653–662 (2001).
- [128] C. Hönninger, R. Paschotta, F. Morier-Genoud, M. Moser, U. Keller, Q-switching stability limits of continuous-wave passive mode locking, *America (NY)*. **16**, 46–56 (1999).
- [129] F. X. Kärtner, J. Aus Der Au, U. Keller, Mode-locking with slow and fast saturable absorbers - What's the difference?, *IEEE J. Sel. Top. Quantum Electron.* **4**, 159–168 (1998).
- [130] L. E. Nelson, D. J. Jones, K. Tamura, H. A. Haus, E. P. Ippen, Ultrashort-pulse fiber ring lasers, *Appl. Phys. B Lasers Opt.* **65**, 277–294 (1997).

- [131] J. Kim, Y. Song, Ultralow-noise mode-locked fiber lasers and frequency combs: principles, status, and applications, *Adv. Opt. Photonics* **8**, 465 (2016).
- [132] R. Paschotta, Noise of mode-locked lasers (Part I): Numerical model, *Appl. Phys. B Lasers Opt.* **79**, 153–162 (2004).
- [133] R. Paschotta, Noise of mode-locked lasers (Part II): Timing jitter and other fluctuations, *Appl. Phys. B Lasers Opt.* **79**, 163–173 (2004).
- [134] S. Namiki, H. A. Haus, Noise of the stretched pulse fiber laser: Part I - Theory, *IEEE J. Quantum Electron.* **33**, 649–659 (1997).
- [135] R. Paschotta, Timing jitter and phase noise of mode-locked fiber lasers, *Opt. Express* **18**, 5041–5054 (2010).
- [136] J. P. Gordon, H. A. Haus, Random walk of coherently amplified solitons in optical fiber transmission, *Opt. Lett.* **11**, 665–667 (1986).
- [137] R. H. Stolen, L. F. Mollenauer, Observation of pulse restoration at the soliton period in optical fibers, *Opt. Lett.* **8**, 186–188 (1983).
- [138] N. Kuse, J. Jiang, C. C. Lee, T. R. Schibli, M. E. Fermann, *2016 Conf. Lasers Electro-Optics, CLEO 2016* (2016).
- [139] W. Hänsel, H. Hoogland, M. Giunta, S. Schmid, T. Steinmetz, R. Doubek, P. Mayer, S. Dobner, C. Cleff, M. Fischer, R. Holzwarth, All polarization-maintaining fiber laser architecture for robust femtosecond pulse generation, *Appl. Phys. B Lasers Opt.* **123**, 41 (2017).
- [140] R. Ell, U. Morgner, F. X. Kärtner, J. G. Fujimoto, E. P. Ippen, V. Scheuer, G. Angelow, T. Tschudi, M. J. Lederer, A. Boiko, B. Luther-Davies, Generation of 5-fs pulses and octave-spanning spectra directly from a Ti:sapphire laser, *Opt. Lett.* **26**, 373–375 (2001).
- [141] I. N. Duling, All-fiber ring soliton laser mode locked with a nonlinear mirror, *Opt. Lett.* **16**, 539–541 (1991).

- [142] H. Lin, D. K. Donald, W. V. Sorin, Optimizing Polarization States in a Figure-8 Laser Using a Nonreciprocal Phase Shifter, *J. Light. Technol.* **12**, 1121–1128 (1994).
- [143] J. W. Nicholson, M. Andrejco, A polarization maintaining, dispersion managed, femtosecond figure-eight fiber laser, *Opt. Express* **14**, 8160–8167 (2006).
- [144] O. Boyraz, T. Indukuri, B. Jalali, Self-phase-modulation induced spectral broadening in silicon waveguides, *Opt. Express* **12**, 829–834 (2004).
- [145] J. W. Nicholson, P. S. Westbrook, K. S. Feder, A. D. Yablon, Supercontinuum generation in ultraviolet-irradiated fibers **29**, 2363–2365 (2004).
- [146] J. M. Dudley, G. Genty, S. Coen, Supercontinuum generation in photonic crystal fiber, *Rev. Mod. Phys.* **78**, 1135–1184 (2006).
- [147] L. Yin, Q. Lin, G. P. Agrawal, Soliton fission and continuum generation in silicon waveguides, *Opt. InfoBase Conf. Pap.* **32**, 391–393 (2006).
- [148] A. Bétourné, A. Kudlinski, G. Bouwmans, A. Mussot, Y. Quiquempois, Supercontinuum generation in solid-core photonic bandgap fibers, *Opt. InfoBase Conf. Pap.* **34**, 3083–3085 (2009).
- [149] N. R. Newbury, W. C. Swann, Low-noise fiber-laser frequency combs (Invited), *J. Opt. Soc. Am. B* **24**, 1756–1770 (2007).
- [150] J. J. McFerran, W. C. Swann, B. R. Washburn, N. R. Newbury, Suppression of pump-induced frequency noise in fiber-laser frequency combs leading to sub-radian f ceo phase excursions, *Appl. Phys. B Lasers Opt.* **86**, 219–227 (2007).
- [151] E. Benkler, H. R. Telle, A. Zach, F. Tauser, Circumvention of noise contributions in fiber laser based frequency combs, *Opt. Express* **13**, 5662–5668 (2005).

- [152] K. L. Corwin, N. R. Newbury, J. M. Dudley, S. Coen, S. A. Diddams, K. Weber, R. S. Windeler, Fundamental Noise Limitations to Supercontinuum Generation in Microstructure Fiber, *Phys. Rev. Lett.* **90**, 113904 (2003).
- [153] R. Paschotta, A. Schlatter, S. C. Zeller, H. R. Telle, U. Keller, Optical phase noise and carrier-envelope offset noise of mode-locked lasers, *Appl. Phys. B Lasers Opt.* **82**, 265–273 (2006).
- [154] A. Cingöz, D. C. Yost, T. K. Allison, A. Ruehl, M. E. Fermann, I. Hartl, J. Ye, Broadband phase noise suppression in a Yb-fiber frequency comb, *Opt. Lett.* **36**, 743–745 (2011).
- [155] J. Alnis, A. Matveev, N. Kolachevsky, T. Udem, T. W. Hänsch, Subhertz linewidth diode lasers by stabilization to vibrationally and thermally compensated ultralow-expansion glass Fabry-Pérot cavities, *Phys. Rev. A - At. Mol. Opt. Phys.* **77**, 53809 (2008).
- [156] A. D. Ludlow, X. Huang, M. Notcutt, T. Zanon-Willette, S. M. Foreman, M. M. Boyd, S. Blatt, J. Ye, Compact, thermal-noise-limited optical cavity for diode laser stabilization at 1×10^{15} , *Opt. Lett.* **32**, 641–643 (2007).
- [157] D. G. Matei, T. Legero, S. Häfner, C. Grebing, R. Weyrich, W. Zhang, L. Sonderhouse, J. M. Robinson, J. Ye, F. Riehle, U. Sterr, 1.5 μ m Lasers with Sub-10 mHz Linewidth, *Phys. Rev. Lett.* **118**, 213401 (2017).
- [158] E. Bava, G. Galzerano, C. Svelto, Amplitude and frequency noise sensitivities of optical frequency discriminators based on Fabry-rot interferometers and the frequency modulation technique, *Rev. Sci. Instrum.* **77**, 1–9 (2006).
- [159] Y. N. Zhao, J. Zhang, A. Stejskal, T. Liu, V. Elman, Z. H. Lu, L. J. Wang, A vibration-insensitive optical cavity and absolute determination of its ultrahigh stability, *Opt. Express* **17**, 8970–8982 (2009).
- [160] S. A. Webster, M. Oxborrow, S. Pugla, J. Millo, P. Gill, Thermal-noise-limited optical cavity, *Phys. Rev. A - At. Mol. Opt. Phys.* **77**, 33847 (2008).

- [161] B. Argence, E. Prevost, T. Lévêque, R. Le Goff, S. Bize, P. Lemonde, G. Santarelli, Prototype of an ultra-stable optical cavity for space applications, *Opt. Express* **20**, 25409–25420 (2012).
- [162] J. M. Robinson, E. Oelker, W. R. Milner, W. Zhang, T. Legero, D. G. Matei, F. Riehle, U. Sterr, Ye, J.U.N., J. Ye, Crystalline optical cavity at 4 K with thermal noise limited instability and ultralow drift, *Optica* **6**, 240–243 (2019).
- [163] K. Numata, A. Kemery, J. Camp, Thermal-noise limit in the frequency stabilization of lasers with rigid cavities, *Phys. Rev. Lett.* **93**, 250602 (2004).
- [164] M. Notcutt, L. S. Ma, A. D. Ludlow, S. M. Foreman, J. Ye, J. L. Hall, Contribution of thermal noise to frequency stability of rigid optical cavity via Hertz-linewidth lasers, *Phys. Rev. A - At. Mol. Opt. Phys.* **73**, 022513 (2006).
- [165] D. Z. Anderson, Alignment of resonant optical cavities, *Appl. Opt.* **23**, 2944–2949 (1984).
- [166] E. D. Black, An introduction to Pound–Drever–Hall laser frequency stabilization, *Am. J. Phys.* **69**, 79–87 (2001).
- [167] J. Millo, D. V. Magalhães, C. Mandache, Y. Le Coq, E. M. L. English, P. G. Westergaard, J. Lodewyck, S. Bize, P. Lemonde, G. Santarelli, Ultrastable lasers based on vibration insensitive cavities, *Phys. Rev. A - At. Mol. Opt. Phys.* **79**, 53829 (2009).
- [168] D. W. Allan, Atomic Frequency Standards, *Proceedings IEEE* **54**, 221–230 (1966).
- [169] T. Kessler, C. Hagemann, C. Grebing, T. Legero, U. Sterr, F. Riehle, M. J. Martin, L. Chen, J. Ye, A sub-40-mHz-linewidth laser based on a silicon single-crystal optical cavity, *Nat. Photonics* **6**, 687–692 (2012).
- [170] F. Nez, M. D. Plimmer, S. Bourzeix, L. Julien, F. Biraben, R. Felder, O. Acef, J. J. Zondy, P. Laurent, A. Clairon, M. Abed, Y. Millerioux, P. Juncar, Precise Frequency Measurement

- of the 2S-8S/8D Transitions in Atomic Hydrogen: New Determination of the Rydberg Constant, *Phys. Rev. Lett.* **69**, 2326–2329 (1992).
- [171] K. D. Bonin, T. J. McIlrath, K. D. Bonin, T. J. McIlrath, Two-photon electric-dipole selection rules, *J. Opt. Soc. Am. B* **1**, 52–55 (1984).
- [172] F. Bloch, Nuclear induction, *Phys. Rev.* **70**, 460–474 (1946).
- [173] R. G. DeVoe, R. G. Brewer, Experimental Test of the Optical Bloch Equations for Solids, *Phys. Rev. Lett.* **50**, 1269–1272 (1983).
- [174] A. A. Buchheit, G. Morigi, Master equation for high-precision spectroscopy, *Phys. Rev. A* **94**, 42111 (2016).
- [175] S. H. Autler, C. H. Townes, Stark Effect in Rapidly Varying Fields, *Phys. Rev.* **100**, 703–722 (1955).
- [176] R. A. Swainson, G. W. Drake, A unified treatment of the non-relativistic and relativistic hydrogen atom: III. The reduced Green functions, *J. Phys. A. Math. Gen.* **24**, 1801–1824 (1991).
- [177] P. S. Epstein, The Stark effect from the point of view of Schroedinger’s quantum theory, *Phys. Rev.* **28**, 695–710 (1926).
- [178] J. R. Taylor, *An Introduction to Error Analysis: The Study of Uncertainties in Physical Measurements* (University Science Books, 1982), second edn.
- [179] B. H. Porter, Research applications of colloidal graphite, *Rev. Sci. Instrum.* **7**, 101–106 (1936).
- [180] L. I. Schiff, H. Snyder, Theory of the quadratic zeeman effect, *Phys. Rev.* **55**, 59–63 (1939).
- [181] D. Hanneke, S. Fogwell, G. Gabrielse, New measurement of the electron magnetic moment and the fine structure constant, *Phys. Rev. Lett.* **100**, 120801 (2008).

- [182] T. Aoyama, M. Hayakawa, T. Kinoshita, M. Nio, Tenth-order QED contribution to the electron $g-2$ and an improved value of the fine structure constant, *Phys. Rev. Lett.* **109**, 111807 (2012).
- [183] P. Elleaume, O. Chubar, J. Chavanne, Computing 3D magnetic fields from insertion devices, *Proc. IEEE Part. Accel. Conf.* **3** (1998).
- [184] H. M. Foley, The pressure broadening of spectral lines, *Phys. Rev.* **69**, 616–628 (1946).
- [185] L. Galatry, Simultaneous effect of doppler and foreign gas broadening on spectral lines, *Phys. Rev.* **122**, 1218–1223 (1961).
- [186] U. D. Jentschura, C. M. Adhikari, R. Dawes, A. Matveev, N. Kolachevsky, Pressure Shifts in High-Precision Hydrogen Spectroscopy: I. Long-Range Atom-Atom and Atom-Molecule Interactions, *J. Phys. B At. Mol. Phys.* **52**, 1–18 (2019).
- [187] J. Cooper, Broadening of isolated lines in the impact approximation using a density matrix formulation, *Rev. Mod. Phys.* **39**, 167–177 (1967).
- [188] C. M. Adhikari, V. Debierre, A. Matveev, N. Kolachevsky, U. D. Jentschura, Long-range interactions of hydrogen atoms in excited states. I. 2S-1S interactions and Dirac- δ perturbations, *Phys. Rev. A* **95**, 22703 (2017).
- [189] A. Matveev, N. Kolachevsky, C. M. Adhikari, U. D. Jentschura, Pressure shifts in high-precision hydrogen spectroscopy: II. Impact approximation and Monte-Carlo simulations, *J. Phys. B At. Mol. Opt. Phys.* **52**, 75006 (2019).
- [190] J. C. De Vries, A precision millimeter-wave measurement of the Rydberg frequency, Ph.D. thesis (1993).
- [191] S. A. Clough, Y. Beers, G. P. Klein, L. S. Rothman, Dipole moment of water from Stark measurements of H₂O, HDO, and D₂O, *J. Chem. Phys.* **2254**, 2254–2259 (1973).

- [192] A. Matveev, (private communication).
- [193] M. A. Lombardi, The Use of GPS Disciplined Oscillators as Primary Frequency Standards for Calibration and Metrology Laboratories, *NCSLI Meas.* **3**, 56–65 (2008).
- [194] K. Beloy, U. I. Safronova, A. Derevianko, High-accuracy calculation of the blackbody radiation shift in the Cs133 primary frequency standard, *Phys. Rev. Lett.* **97**, 40801 (2006).
- [195] M. S. Safronova, M. G. Kozlov, C. W. Clark, Precision calculation of blackbody radiation shifts for optical frequency metrology, *Phys. Rev. Lett.* **107**, 40801 (2011).
- [196] J. W. Farley, W. H. Wing, Accurate calculation of dynamic Stark shifts and depopulation rates of Rydberg energy levels induced by blackbody radiation. Hydrogen, helium, and alkali-metal atoms, *Phys. Rev. A* **23**, 2397–2424 (1981).
- [197] N. E. Rothery, E. A. Hessels, Measurement of the 2S atomic hydrogen hyperfine interval, *Phys. Rev. A - At. Mol. Opt. Phys.* **61**, 44501 (2000).
- [198] H. Fleurbaey, F. Biraben, L. Julien, J. P. Karr, F. Nez, Cross-damping effects in 1S-3S spectroscopy of hydrogen and deuterium, *Phys. Rev. A* **95**, 52503 (2017).
- [199] T. Udem, L. Maisenbacher, A. Matveev, V. Andreev, A. Grinin, A. Beyer, N. Kolachevsky, R. Pohl, D. C. Yost, T. W. Hänsch, Quantum Interference Line Shifts of Broad Dipole-Allowed Transitions, *Ann. Phys.* **531**, 1900044 (2019).
- [200] D. A. Cardimona, M. G. Raymer, Spontaneous radiative coupling of atomic energy levels, *Phys. Rev. A* **27**, 2456–2461 (1983).
- [201] D. A. Cardimona, M. G. Raymer, C. R. Stroud, Steady-state quantum interference in resonance fluorescence, *J. Phys. B At. Mol. Phys.* **15**, 55–64 (1982).
- [202] B. Abi, T. Albahri, D. Allspach, L. P. Alonzi, A. Anastasi, A. Anisenkov, F. Azfar, K. Badgley, Measurement of the Positive Muon Anomalous Magnetic Moment to 0.46 ppm, *Phys. Rev. Lett.* **126**, 141801 (2021).

- [203] B. Zhu, X. Liu, Probing light dark matter with scalar mediator: muon (g-2) deviation, the proton radius puzzle, *arXiv* **2104.03238** (2021).
- [204] D. Tucker-Smith, I. Yavin, Muonic hydrogen and MeV forces, *Phys. Rev. D - Part. Fields, Gravit. Cosmol.* **83**, 101702 (2011).
- [205] R. H. Parker, C. Yu, W. Zhong, B. Estey, H. Müller, Measurement of the fine-structure constant as a test of the Standard Model, *Science* **360**, 191–195 (2018).
- [206] J. Jaeckel, S. Roy, Spectroscopy as a test of Coulomb’s law: A probe of the hidden sector, *Phys. Rev. D - Part. Fields, Gravit. Cosmol.* **82**, 015010 (2010).
- [207] W. J. Marciano, J. L. Rosner, Atomic parity violation as a probe of new physics, *Phys. Rev. Lett.* **65**, 2963–2966 (1990).
- [208] C. S. Wood, S. C. Bennett, D. Cho, B. P. Masterson, J. L. Roberts, C. E. Tanner, C. E. Wieman, Measurement of parity nonconservation and an anapole moment in cesium, *Science* **275**, 1759–1763 (1997).
- [209] C. Rasor, D. C. Yost, Laser-based measurement of parity violation in hydrogen, *Phys. Rev. A* **102**, 032801 (2020).
- [210] J. K. Webb, V. V. Flambaum, C. W. Churchill, M. J. Drinkwater, J. D. Barrow, Laboratory search for the time variation of the fine structure constant, *Phys. Rev. Lett.* **82**, 884–887 (1999).
- [211] E. Peik, B. Lipphardt, H. Schnatz, T. Schneider, C. Tamm, S. G. Karshenboim, *AIP Conf. Proc.* (2005), vol. 770, pp. 103–111.
- [212] S. M. Barr, A. Zee, Electric dipole moment of the electron and of the neutron, *Phys. Rev. Lett.* **65**, 21–24 (1990).

- [213] W. B. Cairncross, D. N. Gresh, M. Grau, K. C. Cossel, T. S. Roussy, Y. Ni, Y. Zhou, J. Ye, E. A. Cornell, Precision Measurement of the Electron's Electric Dipole Moment Using Trapped Molecular Ions, *Phys. Rev. Lett.* **119**, 40801 (2017).
- [214] V. Andreev, D. G. Ang, D. DeMille, J. M. Doyle, G. Gabrielse, J. Haefner, N. R. Hutzler, Z. Lasner, C. Meisenhelder, B. R. O'Leary, C. D. Panda, A. D. West, E. P. West, X. Wu, B. R. O'Leary, C. D. Panda, A. D. West, E. P. West, X. Wu, Improved limit on the electric dipole moment of the electron, *Nature* **562**, 355–360 (2018).
- [215] A. Czarnecki, R. Szafron, Light-by-light scattering in the Lamb shift and the bound electron g factor, *Phys. Rev. A* **94**, 60501 (2016).
- [216] L. C. Tu, J. Luo, Experimental tests of Coulomb's Law and the photon rest mass, *Metrologia* **41**, 136–146 (2004).